"If the fool would continue his folly, he would become wise."

- William Blake (~ 1790)

“Research, whilst greatly enhancing our understanding of fusion welding, has also revealed the scientific complexity of the process with the result that more and more variables require to be controlled in production.”

- Richard Weck, 1977

University of Alberta

Effects of Submerged Arc Weld (SAW) Parameters on Bead Geometry and Notch-Toughness for X70 and X80 Linepipe Steels

by

Joel Todd Pepin

A thesis submitted to the Faculty of Graduate Studies and Research
in partial fulfillment of the requirements for the degree of

Master of Science
in
Materials Engineering

Department of Chemical and Materials Engineering

Fall 2009
Edmonton, Alberta

Examining Committee

H. Henein (Supervisor), Chemical and Materials Engineering

D.G. Ivey (Supervisor), Chemical and Materials Engineering

A. Gerlich, Chemical and Materials Engineering

P. -Y. Ben Jar, Mechanical Engineering

For my parents, Denis and Lois,
Who instilled in me the desire
To pursue higher education.

For my wife, Stefanie, for
Supporting me, inspiring me,
And tolerating me throughout
This pursuit.

Abstract

For the manufacture of higher strength pipelines to be feasible, a better understanding of the effects of welding on toughness is necessary. Bevel submerged arc welds were performed on X80 grade steel. The subsequent Charpy V-notch (CVN) test results indicated that the notch placement in the various heat affected zone regions, and hence the bead geometry, affected the test results. A series of bead-on-plate (BOP) submerged arc welds then were performed on X70 grade steel plate to determine the effects of current, voltage, heat input, polarity, and waveform manipulation (i.e., balance, offset, and frequency) on both single and tandem weld bead geometry. A new bead profile characteristic, the SP ratio, is proposed to describe weld bead geometry, and its relationship with welding parameters is discussed. Sub-size CVN specimens, pulled from many of the BOP weld coupons, were then tested. The greatest sub-size CVN fracture energies were achieved when the bead was produced using lower heat input, and when the bead profile possessed a greater SP ratio.

ACKNOWLEDGEMENTS:

I would like to acknowledge and thank my supervisors, Dr. Douglas Ivey and Dr. Hani Henein, for sharing their wisdom, perspectives, and friendship. The stimulating questions and advice from Dr. Barry Wiskel and Dr. Douglas Boyd also helped shape this research project. I also am grateful for the continued support and advice from my fellow graduate students.

Financial support provided to this project by the Natural Sciences and Engineering Research Council (NSERC) of Canada and EVRAZ Inc. NA is gratefully acknowledged. I also would like to thank the entire EVRAZ Inc. NA Research Group for their technical expertise, especially Christopher Penniston, Fathi Hamad, and Laurie Collins.

I would like to acknowledge the Alberta Research Council for the use of their facilities. In particular, I would like to thank Matthew Yarmuch and Dr. Gary Fisher for their advice, ideas, and support. I would like to thank Wanda Griesheimer from Qualimet Inc., for ensuring that my many sub-size Charpy V-Notch specimens were prepared in record time. I also would like to thank Dr. John Nychka and Dr. Adrian Gerlich, who gave me extensive access to their micro-Vickers hardness tester.

I would like to thank my parents, Lois and Denis, for their continuous love and support, and their unwavering confidence in me. My sister, Alexis, and her husband, Fil, both of whom had survived graduate studies themselves, also offered tremendous support and encouragement.

Most importantly, to my wife, Stefanie: Through my ramblings, I am certain you learned more about welding than you ever wanted. Furthermore, for your love and tolerance, your thesis proofreading, and that one night you helped me with metallurgical sample preparation, I am forever indebted to you. I love you.

TABLE OF CONTENTS:

LIST OF TABLES:

LIST OF FIGURES:

ACRONYMS:

AC	alternating current
AC-SQ	square-wave alternating current
BM	base metal
BOP	bead-on-plate (refers to welding)
CC	constant current (refers to power source welding mode)
CGHAZ	coarse grain heat affected zone
CV	constant volage (refers to power source welding mode)
CVN	Charpy V-notch
DBTT	ductile-to-brittle transition temperature
DCEN	direct current electrode negative
DCEP	direct current electrode positive
DJ	double-jointer (refers to a pipe-joining welding process)
FGHAZ	fine grain heat affected zone
FL	fusion line (refers to the Charpy V-notch specimen vertical notch placement, such that equal lengths of the notch are above the fusion line, in the weld metal, and below the fusion line, in the heat affected zones and base metal)
FL + 2	refers to a Charpy V-notch specimen vertical notch location, which is located 2 mm from the “FL” location, away from the weld metal
FL + 5	refers to a Charpy V-notch specimen vertical notch location, which is located 5 mm from the “FL” location, away from the weld metal
GMAW	gas metal arc welding
GTAW	gas tungsten arc welding
HAZ	heat affected zone
HI	heat input
ICHAZ	inter-critical heat affected zone
ID	inner diameter (refers to pipe face)
LPA	longitudinal to the pipe axis (refers to spiral-welded pipe test specimen orientation)

LRA	longitudinal to the rolling axis (refers to spiral-welded pipe test specimen orientation)
M-A phase	a microstructure phase, consisting of martensite with retained austenite
OD	outer diameter (refers to pipe face)
PWHT	post weld heat treatment
RMS	root mean square
SAW	submerged arc welding
SMYS	specified minimum yield strength
SP Ratio	semi-penetration ratio (refers to a shape characterization technique, explained in section 5.2.4)
SS-CVN	sub-size Charpy V-notch (refers to the CVN test specimen)
TMCP	thermo-mechanical controlled processed
TPA	transverse to the pipe axis (refers to spiral-welded pipe test specimen orientation)
TRA	transverse to the rolling axis (refers to spiral-welded pipe test specimen orientation)
WFS	wire feed speed
WM	weld metal
X60	a grade of pipeline steel, with toughness requirements, and a specified minimum yield strength of 413.6 MPa (60 ksi)
X70	a grade of pipeline steel, with toughness requirements, and a specified minimum yield strength of 482.6 MPa (70 ksi)
X80	a grade of pipeline steel, with toughness requirements, and a specified minimum yield strength of 551.5 MPa (80 ksi)
X100	a grade of pipeline steel, with toughness requirements, and a specified minimum yield strength of 689.4 MPa (100 ksi)
X120	a grade of pipeline steel, with toughness requirements, and a specified minimum yield strength of 827.3 MPa (120 ksi)

SYMBOLS:

A	amperage (amperes)
A_p	bead penetration area (mm^2)
A_r	bead reinforcement area (mm^2)
J	energy (joules)
p	bead penetration depth (mm)
r	bead reinforcement height (mm)
V	voltage (volts)
w	bead width (mm)
λ	frequency (Hz)

CHAPTER 1: INTRODUCTION

1.1: Pipeline Economic and Technical Considerations

As hydrocarbon fuel reserves continue to be consumed worldwide, it is critical to identify and exploit new sources responsibly. However, many new sources are remotely situated, and hence require the production and installation of extensive (and expensive) pipelines. With gas pipelines in particular, greater operating pressures allow for higher gas throughput, making the use of high-strength pipe materials economically advantageous [1].

Traditional pipelines may be built above the ground on anchored structures, or buried beneath the ground surface. In both cases, it is typical for stress-based design to be used, in which a specified minimum yield strength (SMYS) must be met or exceeded by all piping material. With stress-based design, a higher gas throughput may be easily addressed by using stronger piping material or increased pipe wall thickness. Gas pipeline design in arctic regions is complicated by the cyclical melting of permafrost (thaw settlement) and freezing of the ground (frost heave), which can induce significant pipeline deformation [10, 15]. As a result, strain-based design is applied, in which the pipelines must withstand plastic strain without rupture [10]. While greater gas throughput still may be addressed with either stronger piping material or thicker walled pipe, the potential for plastic strain must be addressed by ensuring adequate piping material toughness. Material toughness becomes even more critical because of the lower ambient temperatures of the arctic. As a final complication, arctic pipelines must be economically feasible: the improved strength and toughness must be achieved without the use of expensive alloying additions.

The successful integration of thermo-mechanical controlled processing (TMCP) with microalloying techniques, therefore, can be used to produce the ideal arctic pipeline material. The resulting high-strength steel possesses a fine-grained microstructure with lean chemistries (i.e., with low levels of alloying additions)

that are relatively inexpensive. As additional benefits, the fine microstructure yields high toughness values, and the low carbon contents dramatically improve the ability to weld the steel without cracking, even without the use of preheat or post weld heat treatment. The microstructure, however, cannot be recreated through heat treatment alone. Only the combined application of mechanical straining with specific thermal cycles can achieve the desired microstructure characteristics (and hence the improved mechanical properties) [5]. This poses a technical challenge, because TMCP microalloyed steel sheets must be welded into individual pipes, which then undergo additional girth-welding to form extensive pipelines. During any welding process, some of the base metal (BM) is melted, and the adjacent unmelted metal is subjected to thermal gradients. Such unmelted material that undergoes changes to the microstructure as a result of the thermal gradients is referred to as heat affected zone (HAZ). It is its proximity to the molten metal (i.e., weld metal, WM) that dictates the HAZ's heating and cooling rates, as well as its maximum temperature achieved [9, 46].

With steels in particular, several metallurgically-distinct bands of HAZ material form adjacent to the weld fusion lines. Because each HAZ band consists of a variety of microstructures, the different HAZ bands may possess a wide range of mechanical properties (including strength and toughness). It was previously mentioned that both adequate strength and toughness must be maintained throughout all of the material used to make the pipeline. Because of the thermal effects of welding, the designer must therefore consider the distinct mechanical properties of the BM, WM, and every HAZ layer. It is critical for the mechanical properties of every region to meet the minimum strength and toughness requirements for the pipeline's strain-based design.

1.2: Project Scope

The project focuses on the investigation of how various submerged arc welding (SAW) parameters affect the corresponding weld bead geometry. In turn,

additional testing is performed to determine the effects of weld bead geometry on notch-toughness fracture energy values of the weld HAZ.

Material physical properties (i.e., thermal coefficients of expansion, conductivity, etc.) were not considered, nor was material resistance to pipeline degradation mechanisms (including corrosion, fatigue, erosion, or fluid transients). While it is important to note that high-pressure pipelines require adequate toughness, calculations used to determine exact mechanical requirements were not investigated. The effects of any external forces upon the pipeline, including those considered for strain-based design, were not addressed either, nor were the special requirements for buried or subsea pipelines.

On a final note, there are many different welds involved for the fabrication of pipelines from steel sheet (including spiral and circumferential welds). However, the following study is more general, making many of its conclusions (and in particular those related to bead geometry) transferrable to the submerged arc welding of most TMCP microalloyed steels.

1.3: Overall Project Objectives

The main objective of this research was to improve the understanding of how submerged arc welding parameters affect the HAZ toughness of TMCP microalloyed pipeline steels.

Chapter 2 begins with a general literature review that outlines pipe and pipeline mechanical requirements, TMCP steels, and welding metallurgy. The literature review continues with an investigation of arc welding processes and power sources, as well as welding thermal considerations, welding variables, and waveform manipulation, and their effects on weld bead geometry. Charpy V-notch testing is briefly summarized at the end of the chapter.

Chapter 3 summarizes initial experiments performed to directly determine the effects of current polarity on the Charpy V-Notch (CVN) toughness (at -20°C) of X80 steel after undergoing a tandem weld process (i.e., using two in-line welding arcs). Weld bead and heat affected zone cross-section profiles were investigated, and micro-Vickers hardness testing and optical microscopy were used to supplement the CVN fracture energy values. Chapter 4 summarizes a supplementary literature review that further explores the effects of individual welding parameters on weld bead geometry. In Chapter 5, a series of bead-on-plate welds, performed on available X70 steel, was explored to confirm the literature review results, as well as to further investigate the effects of waveform manipulation variables. In Chapter 6, an extensive group of sub-size CVN specimens were tested at -20°C to determine the effects of either welding parameters or bead geometry characteristics on notch-toughness. Overall discussion and conclusions are summarized in Chapter 7, and future work is recommended in Chapter 8.

CHAPTER 2: BACKROUND INFORMATION

The present work was initiated to investigate the effects of welding parameters on toughness. As such, a literature survey was performed in the following areas:

- Pipe and pipeline mechanical requirements
- Thermo-mechanical controlled processed (TMCP) steels
- Welding metallurgy
- Arc welding processes
- Arc welding thermal considerations
- Power sources and waveform manipulation
- Charpy V-notch (CVN) testing

2.1: Pipes and Pipelines

Pipelines are an efficient means of transporting gas over long distances. A common form of pipe is the spiral-welded pipe, which was the initial focus of this investigation.

2.1.1 Spiral Pipe Assembly & Orientations

To manufacture spiral-welded pipes, steel is rolled into sheets (Figure 2-1a) that are formed into a spiral-shape (Figure 2-1b), which then is welded to produce an individual pipe (Figure 2-1c). The pipes then are girth-welded (Figure 2-1d), to join shorter lengths of pipe. In Figure 2-1, spiral-welds (colored green), are illustrated, and a girth-weld (colored red) is shown with a circumferential orientation around the joint pipe.

Girth welding may be performed at the steel plant to form longer pipes prior to shipment, to reduce the number of field welds required to complete the pipeline. As subsequent sections will explain, submerged arc welding (SAW) is an

excellent process for performing welds in the mill, and gas metal arc welding (GMAW) is the field-welding process of choice.

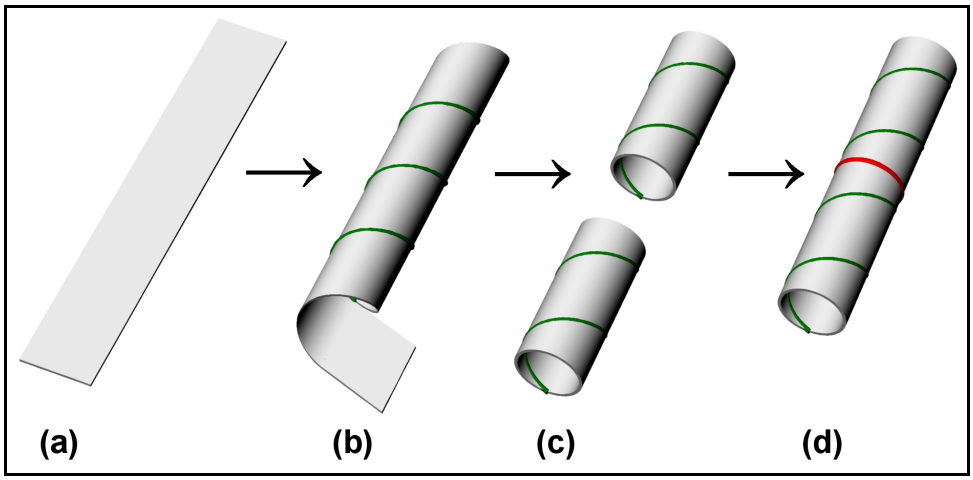

Figure 2-1: Schematics of Spiral-Welded Pipeline Fabrication Steps

During test coupon extraction from a spiral-welded pipe, the longitudinal and transverse directions may be considered, relative to either the original plate-rolling direction or the final pipe axis (Figure 2-2). Test coupons may be oriented LPA (longitudinal to the pipe axis), TPA (transverse to the pipe axis), LRA (longitudinal to the rolling axis), and TRA (transverse to the rolling axis).

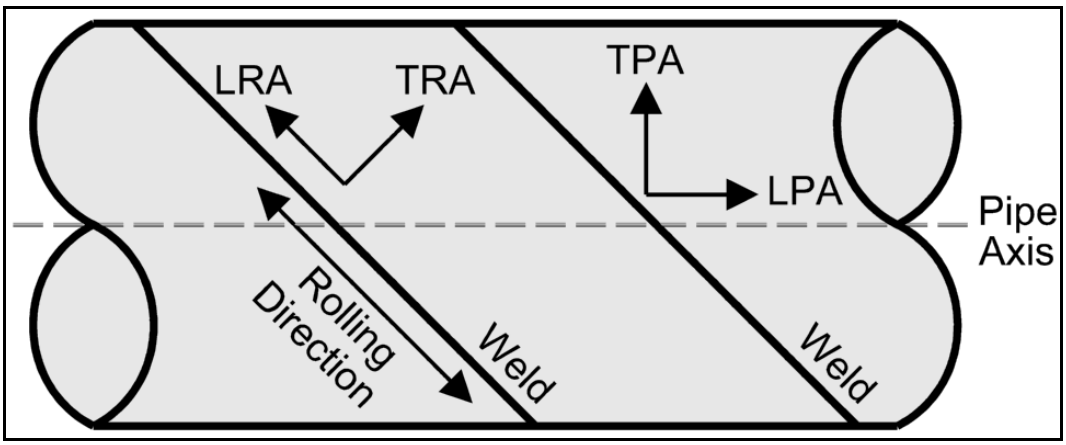

Figure 2-2: Pipe Specimen Orientations (Adapted from Shehata & Boyd [50])

2.1.2 Pipeline Mechanical Requirements

For a gas pipeline, operating pressure may be increased to improve product throughput [1]. While economically attractive, this requires either thicker pipe walls or pipe material with a greater specified minimum yield strength (SMYS). While the use of increased pipe wall-thickness may seem promising, it is accompanied by increased overall costs due to additional material costs, transportation costs, welding filler consumables required, and welding time. It is therefore attractive to develop stronger pipe materials [1, 12 – Pg. 289, 19, 30].

Typical steel strengthening mechanisms may include grain refinement, solid solution strengthening, precipitation strengthening, and work hardening [12 – Pg. 28]. While grain refinement improves both strength and the impact transition temperature, other strengthening mechanisms may come at the expense of reduced material toughness [12 – Pg. 61]. Consequently, to conform to the requirements of strain-based design, a balance must be set between improved strength and toughness.

EVRAZ Inc. NA personnel noted that previous multiple-pass welds had achieved minimum notch toughness values of 90 Joules, at a -20°C testing temperature (66.4 ft-lbs at -4°F), while still maintaining an SMYS of 550 MPa (80 ksi) [8]. The mechanical properties were maintained throughout the weld metal (WM), heat affected zone (HAZ), and base metal (BM) notch locations. However, because of the additional time and money required to perform multiple-pass welds, it was noted that achieving the same minimum requirements using only a single fill pass would be beneficial [8].

2.2: Thermo-Mechanical Controlled Processing (TMCP) Steels

Recent developments to reduce costs and improve material performance have led to the fabrication of microalloyed steels via thermo-mechanical control-processing (TMCP). The resulting steel contains carbon and total alloying

contents each typically less than 0.1 weight percent. The low carbon content also improves the ability to weld the steel without cracking, even without the use of preheat or post weld heat treatment [12 – Pg. 3]. The resulting microstructure possesses a fine bainitic and/or ferritic microstructure with a high dislocation concentration and a dispersion of fine precipitates.

Steel microstructure (i.e., phase and grain size) dictates the macroscopic mechanical properties. Separate thermal and mechanical processing operations are typically used to control the resulting microstructure [5]. Steel strength may be enhanced by the formation of precipitates. For effective precipitation strengthening, the precipitates must collectively constitute a sufficiently large volume fraction of the steel, while independently being very fine. If a precipitate has a higher formation temperature (e.g., TiN), the volume fraction will be large, but the individual precipitates will be too coarse. Nb, V, and Ti are used to react with C and/or N to produce desirable finer precipitating particles in microalloyed steels (the exception, of course, being TiN, most of which forms at high temperatures) [5]. However, these finer precipitates, formed at lower temperatures, do not typically constitute large enough volume fractions to increase the steel's strength considerably [5].

It may then seem appropriate to re-heat the steel to form the necessary quantities of fine precipitates. However, not only is this uneconomical, but it also coarsens matrix material grains (detrimentally affecting material toughness). Alternatively, the steel may be mechanically deformed within specific temperature ranges during fabrication to improve precipitation kinetics through increased dislocation density.

Figure 2-3 is a schematic of the overall thermo-mechanical process used to produce high-strength micro-alloyed steel. The steel is first held at a high enough temperature to fully dissolve all precipitation strengthening elements (Figure 2-3, point 22), before being deformed mechanically (Figure 2-3, point 24) to induce recrystallization for initial austenite grain refining (Figure 2-3, point 26). The

steel is then rolled above the austenite-ferrite transformation temperature, but below the recrystallization temperature, to produce a heavily pancaked austenite structure (Figure 2-3, point 30) [5]. When rapidly cooled below the transformation temperature, the high grain-boundary fraction produced by the pancaked austenite structure increases the number of ferrite grain nucleation sites, further refining the microstructure. The rapid-quench (Figure 2-3, point 32) also inhibits the formation of precipitates at high temperatures. The steel undergoes final deformation between 350°C and 450°C (660°F and 840°F) to increase the final dislocation volume fraction to assist with the formation of fine precipitates [5]. The final rolling operation also can produce sub-grains to increase strength and induce texture development [12 – Pg. 290].

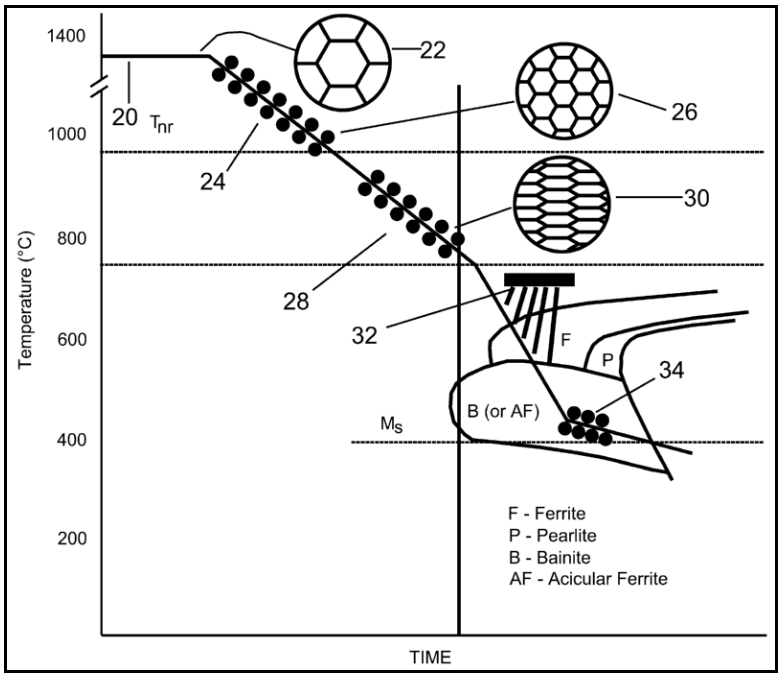

Figure 2-3: TMCP Steel Process Diagram (Adapted from US Patent 6,682,613 B2, Fig. 1) [5]

The intimate combination of thermal and mechanical processing thus produces a microstructure that cannot be reproduced through thermal processing alone. The favorable microstructure provides TMCP microalloyed steels with improved

strength and toughness, making it a suitable, and economical, material choice for pipeline applications.

2.3: Welding Metallurgy

When a weld is performed, the BM closest to the arc will melt. If the welding process is autogenous, the BM will then solidify to form the weld metal (WM). If the process is non-autogenous, the molten BM will mix with deposited molten metal to form a mixed WM. In both cases, the interface separating the WM from the un-melted BM is referred to as the fusion line.

The heat from the welding process creates thermal gradients that travel through the base metal, perpendicular to the fusion line. If the BM is close enough to the fusion line that the thermal gradients affect the microstructure, this material is then referred to as the heat affected zone (HAZ). The energy supplied by the welding process, combined by the HAZ material's proximity to the fusion line, dictate the heating rates, maximum temperatures, and cooling rates to which that HAZ material will be exposed. As a result, distinct bands of HAZ material form perpendicular to the fusion line, each with different microstructures and corresponding mechanical properties.

Figure 2-4 illustrates a schematic of a welded steel plate. The solid curve connecting points A and B illustrates the range of maximum temperatures achieved in the material, moving away from the fusion line. The iron-iron carbide phase diagram is included in the schematic to illustrate how these temperatures correspond to changes in the HAZ microstructure.

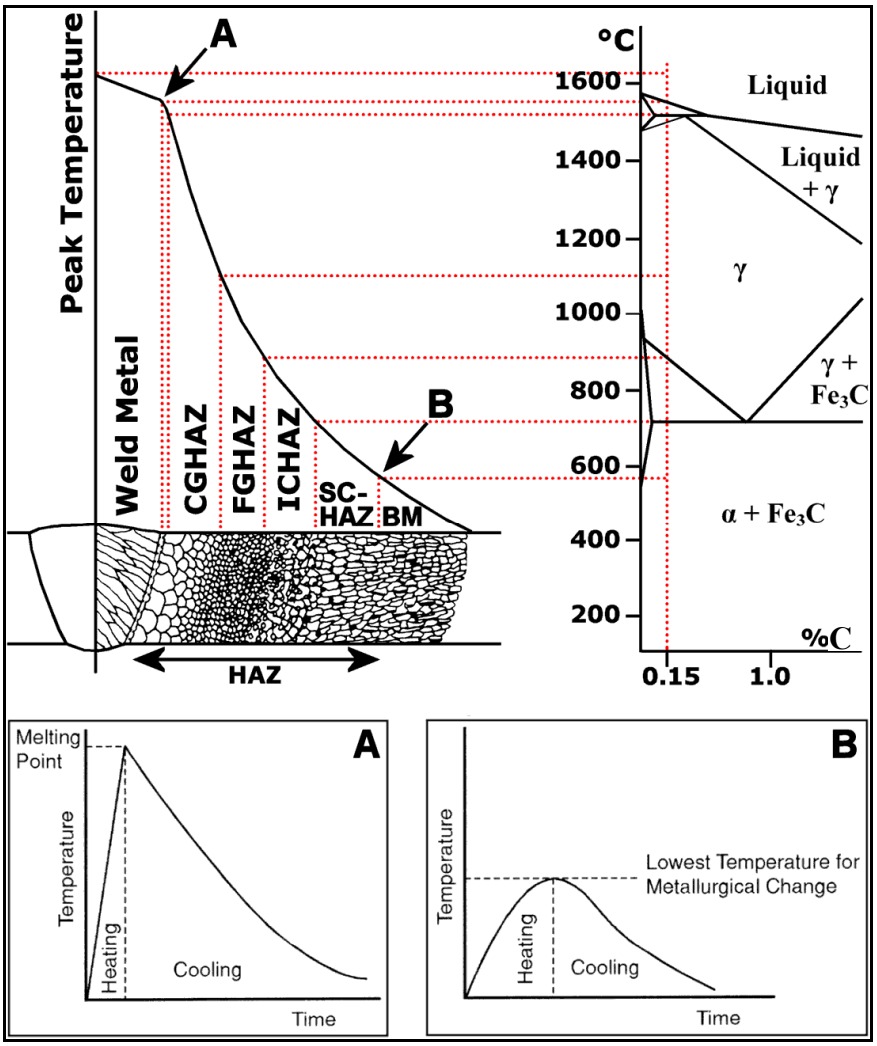

Figure 2-4: Single-Pass Weld Thermal Gradients and Corresponding Heat Affected Zones (based upon original images by Easterling, pg. 126, and Patchet) [9, 46]

Figure 2-4 shows that four distinct HAZ regions form when steel is welded. Moving away from the weld bead, the HAZ regions are designated the coarse grain, fine grain, intercritical, and sub-critical HAZ regions respectively (CGHAZ, FGHAZ, ICHAZ, and SCHAZ). Both the CGHAZ and FGHAZ regions become fully austenitic from the weld's thermal cycles. The grains in the CGHAZ grow significantly due to greater maximum temperatures achieved, whereas FGHAZ grains recrystallize but do not coarsen. As a result, FGHAZ material typically displays reasonable toughness, whereas reduced toughness is expected in the CGHAZ [2, 36]. ICHAZ regions partially-austenitize during

welding, producing carbon- and manganese-rich austenite. Due to its enhanced hardenability, the new austenite can sometimes form martensite-retained austenite regions (M-A phase) upon cooling [49]. M-A phase formation may be a source of high localized hardness and reduced toughness. The SCHAZ undergoes stress relieving, but undergoes no microstructure transformations. Throughout the HAZ regions, steel precipitate size and distributions are also affected [9, 48, 36]. If multiple-pass welds are performed, the combination of several separate thermal gradients can further complicate HAZ microstructures.

Microalloyed TMCP steel microstructure is optimized through a series of carefully-selected metallurgical processes and parameters. As a result, the effects of welding on the HAZ microstructures are typically unwanted. It therefore is necessary either to minimize the detrimental effects to the steel HAZ microstructure, or to repair it.

Many grades of metal undergo a post-weld heat treatment (PWHT) following welding, in an attempt to return HAZ microstructures to their pre-welded conditions. However, because TMCP microalloyed steel microstructures cannot be achieved without utilizing a combination of thermal and mechanical processing techniques, PWHT cannot be used to repair their HAZ microstructures. In fact, the PWHT of microalloyed TMCP steel would likely coarsen the steel's grains, effectively damaging the steel's microstructure further.

Because microstructure repair is therefore not possible, it becomes necessary to determine how to minimize the detrimental effects to the HAZ microstructure. A common approach is to reduce the energy supplied by the welding arc, thereby minimizing the effects of the corresponding HAZ thermal cycles. Not only does such an approach not necessarily work, but it also neglects potential negative consequences including poor penetration and loss in productivity. However, there is a wide range of available welding processes and variables that can be manipulated. By optimizing the welding variables, it should be possible to determine how to minimize the detrimental effects on the mechanical properties

throughout the HAZ. The wide range of welding processes and parameters will be reviewed next.

2.4: Arc Welding Process Overview

Arc welding processes use the electric arc's intense energy to generate the heat necessary for fusion [58]. Spiral welding is typically performed via a high-productivity (i.e., high heat input) submerged arc welding (SAW) process, with one pass from the inside and one from the outside [31]. When two short pipe lengths are girth-welded at the mill, a "double jointer" (DJ) weld is performed using the SAW process. This is done either by using multiple passes around the outer diameter (OD), or by using a single pass from the inner diameter (ID) and one from the OD (similar to the process used for the spiral weld). Girth welds performed in the field (during pipeline assembly) typically use a lower heat input gas metal arc welding (GMAW) process, using multiple passes around the OD [31]. A brief introduction to the primary arc welding processes, and their relation to SAW, follow.

2.4.1 Gas Tungsten Arc Welding (GTAW)

While the role of GTAW in fabrication is often limited to root passes, GTAW also has been a helpful research tool. A non-consumable electrode (typically tungsten) is used to establish a welding arc by means of thermionic emission. A consumable filler metal is then supplied separately, and fed into the arc for deposition (Figure 2-5). The autogenous GTAW process (i.e., GTA welding without filler metal) is the simplest form of arc welding from a scientific standpoint, making it crucial for developing a better understanding of arc welding physics principles.

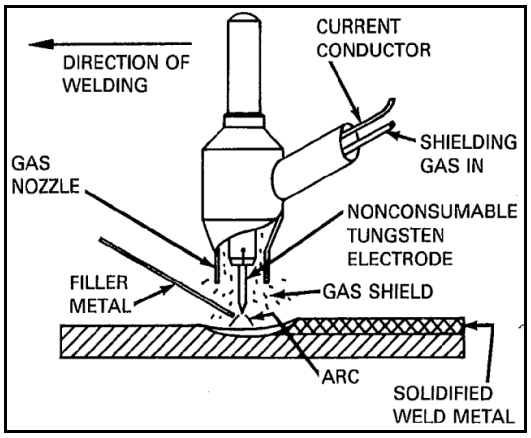

Figure 2-5: Schematic of GTAW Equipment Layout & Process [18 - Pg. 74]

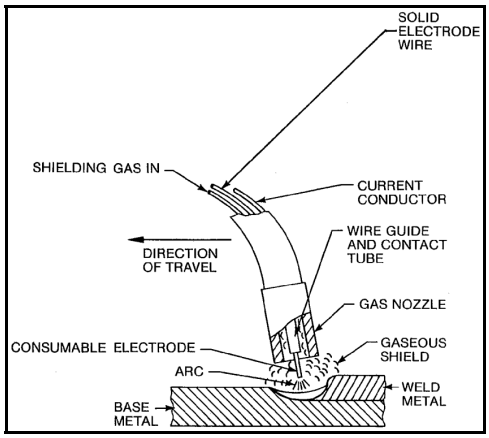

Figure 2-6: Schematic of GMAW Equipment Layout & Process [21 - Pg. 111]

2.4.2 Gas Metal Arc Welding (GMAW)

Unlike GTAW, GMAW uses a consumable electrode that also acts as the filler metal. Once again, gas is used as a shielding medium to protect the welding pool from the open atmosphere (Figure 2-6). GMAW is typically a manual welding process, and can be used in all orientations. This flexibility and portability, along with relatively high deposition rates (for a manual welding process), make it an attractive option for field welding (i.e., for assembling pipelines). Also, literature focusing on the GMAW process can often be helpful in better understanding SAW, because the GMAW arc and metal transfer modes can be visually recorded (unlike the SAW arc, which is hidden beneath the surface of the solid flux).

2.4.3 Submerged Arc Welding (SAW)

Submerged arc welding (SAW) is similar in principle to GMAW, in that the electrode is a consumable-wire, typically fed from a spool. However, instead of gas shielding, the arc and weld puddle are shielded using a solid flux. The arc is 'submerged' beneath the solid flux surface, hence the process's name. A SAW system setup and process schematic is illustrated in Figure 2-7.

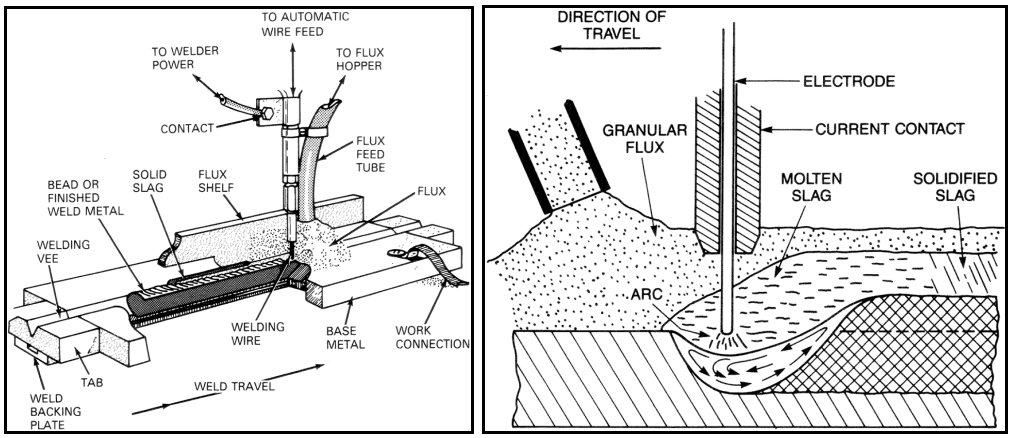

Figure 2-7: Schematic of SAW Equipment Layout and Process [45 – Pg. 193, 41 - Pg. 505]

The process typically uses large diameter wire and high currents, resulting in a fast continuous welding process capable of welding together thick base materials in a single pass. The process can be used only in the flat position, and it has poor portability (therefore making it a poor choice for field-welding). It also requires more initial capital investment than other processes. However, the high level of automation allows for the process to be adequately performed by welding operators (instead of by expensive highly skilled welders). Higher travel speeds also are possible. On a final note, SAW produces no visible arc, and produces less fume generation than other processes, making it attractive from environmental and safety perspectives [28 – Pg. 8].

Overall, SAW is a welding process with high efficiency, high deposition rates, and a reduced dependence upon highly skilled personnel, making it an attractive process for in-house pipe welding at steel mills [35].

2.4.4 Summary of Arc Welding Processes

The two welding processes most commonly used for pipeline fabrication are SAW and GMAW. SAW was considered the better welding process with which to begin an investigation on the effects of welding parameters on toughness, primarily because it is not a manual welding process and hence does not introduce

many variables associated with manual welding (e.g., variation in the contact tip angle and the distance between the welding torch and base metal).

2.5: Arc Welding Thermal Considerations

Before a production weld may be performed and used for its desired application, the proposed combination of welding parameters, base material, and welding technique must pass a battery of tests. Such testing is performed to ensure that both the WM and HAZ regions can meet all required material properties.

For oil and gas applications, it is common for welding variable controls to be administered to enforce acceptable strength [3], toughness [3], and hardness values [44] throughout the WM and HAZ. WM and HAZ thermal cycles control the microstructure, which in turn controls mechanical properties. Preheat, heat input, and post-weld heat treatment (PWHT) are three welding variables that affect the thermal cycles of the WM and HAZ material.

A preheat may be enforced to slow the cooling rate after welding. The greater the preheat temperature, the slower the cooling rate. Preheating is, therefore, especially helpful when welding large components that act as efficient heat-sinks, rapidly increasing the cooling rates of the WM and HAZ regions. Unfortunately, preheating adds additional cost into production.

A PWHT may also be used, sometimes merely to stress-relieve the welded component, and other times to completely austenitize or solution-anneal the welded component. However, due to the aforementioned microstructure of TMCP steels, and the complicated processing necessary to produce them, a PWHT actually would be detrimental to welded TMCP steels [29, pg. 117]. Therefore, because of technical or economic limitations, it becomes even more critical to understand the effects of heat input when welding TMCP steels.

2.5.1 Heat Input

"Heat input" refers to a man-made welding variable, calculated with equation (1).

$$Heat\ Input = \left[\frac{(Voltage) \times (Current)}{(Travel\ Speed)} \right] \quad \textbf{(1)}$$

Calculating heat input is a simple way to compare the amount of energy (Joules) used to form a specific length of weld (typically measured in mm or inches). Voltage is measured in volts, current is measured in amperes, and travel speed is typically measured in "mm per second" (or sometimes inches per second). Due to the large numbers produced, heat input is often converted to the units kJ/mm or kJ/inch.

The theoretical heat input equation, (1), does not take into account arc inefficiencies, which later are described in more detail (refer to section 2.6.4). However, for SAW, the arc efficiency is approximately 85% [32, Pg. 40].

When current is increased, deposition, penetration, and overall molten volume increase during welding. Voltage has little effect on deposition rates, but if a greater voltage is used, the arc length will increase [23]. As the arc shape is typically conical, the increased arc length can result in a wider deposited bead. Conversely, a lower voltage will reduce arc length, increasing electrode stickout, which in turn will increase resistive heating within the wire. As a result, deposition should increase [20, 56]. Resistive heating is more critical in smaller diameter wire processes; the relatively large electrode diameters used in SAW may reduce the measurable effects of resistive heating [14]. Additionally, with the contact-tip-to-work distance less than 25 mm, resistive heating should not play a significant role in controlling bead geometry.

If travel speeds are too low, the molten metal cushions the penetrating force of the arc, which actually reduces penetration [53 - Pp. 278-280]. However, if the

puddle is not leading the arc, both the cross-section penetration and reinforcement areas will reduce as the travel speed is increased.

Overall greater heat input is often associated with increased penetration, deposition, and heat affected zone size, along with slower cooling rates (due to increased heating of the adjacent base metal). While the slower cooling rates can sometimes reduce the likelihood of forming rapidly-quenched microstructures (which may be beneficial), the greater heat affected zone size can increase the volume of coarse-grained microstructures [52, 36].

When a tandem welding process is used, the overall heat input may be calculated using Equation 2. Equation 2 was derived simply by adding the heat inputs from each electrode.

$$Heat\ Input = \left[\frac{(Voltage \times Amperage)_{LEAD} + (Voltage \times Amperage)_{TRAIL}}{Travel\ Speed} \right] \quad \textbf{(2)}$$

2.5.2 Polarity

Polarity refers to the direction of electron flow of a welding process. During welding, the electric arc is formed between the electrode and the base material. When electrons flow from the base material to the electrode, the negatively-charged electrons are attracted to a positive electrode; this polarity is referred to as direct current electrode positive (DCEP, EP, or DC+). When the electrons flow from the electrode to the base material, the electrons flow away from a negative electrode; this polarity is referred to as direct current electrode negative (DCEN, EN, or DC-). Refer to the schematic illustrated in Figure 2-8.

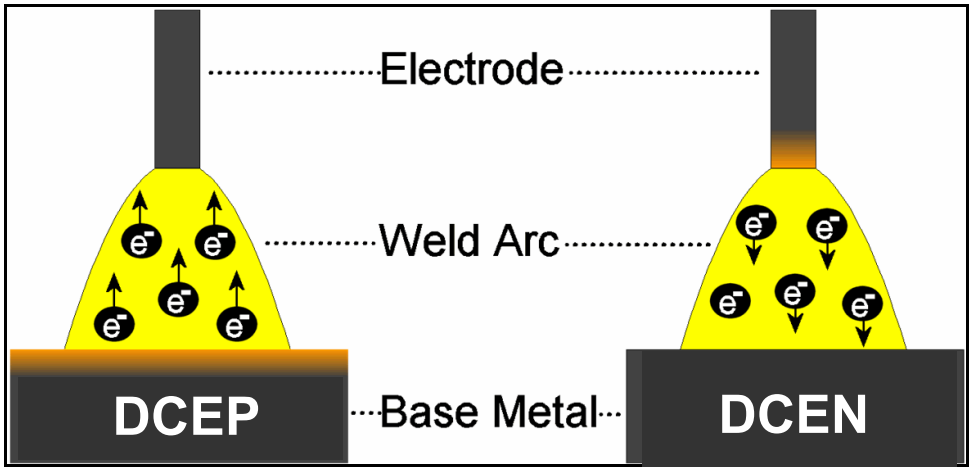

Figure 2-8: Schematic of Polarity for a Consumable Electrode Welding Process

Though not included in the standard heat input formula, polarity significantly affects weld bead shapes and sizes (including deposition rates and penetration depths). As stated earlier, autogenous GTAW in particular is a welding process suitable for scientific research. As such, it has been well-documented [57, 17, 26] that maximum penetration is achieved with GTAW using DCEN polarity, and maximum deposition is achieved using DCEP. Unfortunately, it has become a common misconception that polarity affects consumable-electrode processes (i.e., SAW) in a similar manner. This point will be addressed in the subsequent investigation.

When GTAW is supplied with a DCEN current, electron production is achieved via thermionic emission. This mechanism however is applicable only for materials with high melting points and low work-functions, such as carbon, molybdenum, tantalum, or tungsten" [57]. When electrons are produced from a material with a lower melting point and a greater work function (e.g., steel consumable electrodes used for SAW), a field-emission mechanism occurs in which electrons are emitted from highly-mobile cathode spots that typically are found at inclusions of lower work function, and not at the metallic phase [57]. The field-emission mechanism, therefore, concentrates additional energy at the cathode spots for consumable-electrode welding processes [57]. As a result,

when DCEN polarity is used for SAW, additional filler wire should melt, which should increase the deposition height and area. Alternatively, when DCEP polarity is supplied for SAW, additional base metal should melt, resulting in increased penetration area and depth. DCEP polarity will increase the bead width too, as the mobile cathode spots increase the emission area from the base metal [57, 14]. Bead width increase may also be attributed to cathode heating (i.e., resistive heating in the base material) [14]. Figure 2-8 graphically represents the effects of polarity on electrode and base material heating, by coloring regions of increased melting rates orange.

While DCEP polarity allows for emission area increases by widening the arc at the base metal, DCEN polarity emission areas increase by means of the arc plasma climbing the electrode [26, 14]. As a result, additional molten metal flows down the wire surface, joining the formed droplet at the electrode's tip [26, pg. 201]. Consequently, DCEN droplets are larger, and there is an overall increase in melting rate. Researchers have reported that changing polarity from DCEP to DCEN can increase GMAW deposition rates by 40% to 50%, and improve SAW deposition rates by 10% to 40% due to electromagnetic forces and plasma interactions [26, 14].

However, DCEP droplet flight times across the arc are typically only 1 ms (compared to 5.25 ms for DCEN droplet transfer), indicating a greater force towards the weldment [26]. Such an increase in force would further increase bead penetration. Jiluan finally notes that due to increased melting rates, it can be inferred that DCEN droplet temperatures would be lower than those of DCEP droplets. This would further reduce effective heat input into the base material (and penetration) [26].

From a more empirical perspective, Fisher agrees that DCEN directs more energy into the electrode than DCEP, allowing for greater deposition rates, effectively reducing heat input to the workpiece, resulting in reduced base metal dilution and

distortion [11]. However, Fisher does caution that without an increased welding current, DCEN may lead to reduced or insufficient penetration.

2.6: Arc Welding Power Sources & Waveform Manipulation

2.6.1 Conventional Arc Welding Power Sources

Traditional power sources consist of transformers, rectifiers, transistors, and inductors, supplying voltages in the range of 20 V to 80 V, and currents ranging from 30 A to 1500 A [43 – Pg. 2]. The transformer is used to convert voltage and current, depending upon the number of coils within it. The silicon-controlled rectifier (SCR, a.k.a. a thyristor) is used to convert an AC waveform into a DC waveform. Finally, the inductor can be used to smooth the "output ripple" produced using a rectifier to convert an alternating current to a direct current [13].

As such, traditional welding power sources have been able to supply DCEP, DCEN (Figure 2-9), or sinusoidal AC (Figure 2-10, left).

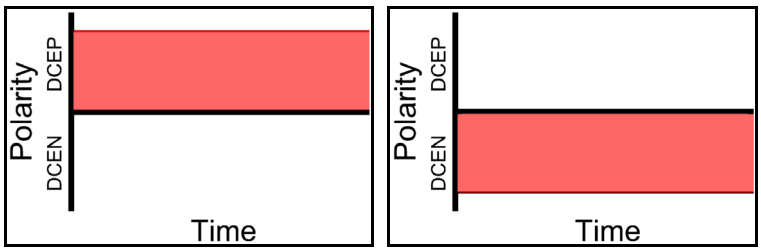

Figure 2-9: DCEP (left) and DCEN (right) Current Waveforms

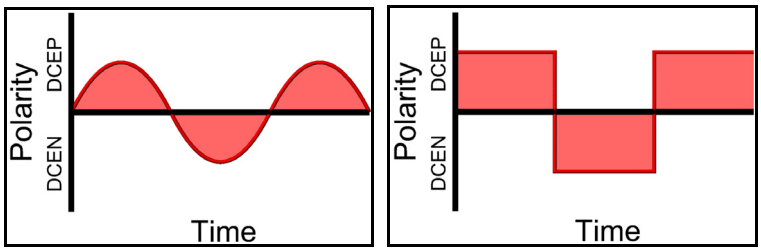

Figure 2-10: Sinusoidal AC (left) and Square-Wave AC (right) Current Waveforms

When using a conventional welding power source, the user typically chooses between DCEN or DCEP, at the respective expense of penetration or deposition. Sinusoidal AC has been attractive because it balances the advantages and disadvantages of DCEP and DCEN [11].

However, a sinusoidal AC wave takes a relatively long time to transition through the zero amp range [11]. Also, there is insufficient dwell time at peak amperages, resulting in inadequate penetration and deposition rates [11]. Modern power sources have allowed for the use of square-wave AC polarity (Figure 2-10, right), which transitions from positive to negative, and vice versa, much more quickly than sinusoidal polarity [11]. This reduces arc stability problems and increases peak current dwell time.

Fisher notes that variable balance AC squarewave submerged arc welding (SAW) technology overcomes the traditional problems or limitations SAW using DC electrode positive (DCEP), DC electrode negative (DCEN), or traditional sinusoidal AC [11]. Fisher explains that the variable balance SAW allows for significant deposition rate increases up to 59 per cent over DCEP using the same welding parameters and welding types [11]. Under different applications, travel speeds can be increased by as much as 2.75 mm/s (65 ipm) [11]. Fisher finally notes that variable balance AC SAW has improved deposition rates over DCEP welding, causes less warping, and is easier to configure for multiple torch welding by offsetting the AC squarewave waveform cycles [11].

2.6.2 Modern Welding Power Sources

The advent of the solid-state inverter has been extremely important for the welding industry. Transformer mass is inversely proportional to applied frequency [43 – Pg. 11], requiring very large transformers for typical line frequency of 50 Hz to 60 Hz. However, inverters can convert direct current into high-frequency alternating current, in the range of 20 kHz to 100 kHz [43 – Pg.

11]. By using an inverter to increase current and voltage frequency prior to using the transformer, a smaller transformer can be used, allowing for overall reductions of up to 75% in power source size and weight [43 – Pg. 11]. Figure 2-11 demonstrates a typical modern power source electrical schematic, with voltage waveform schematics illustrated at the top.

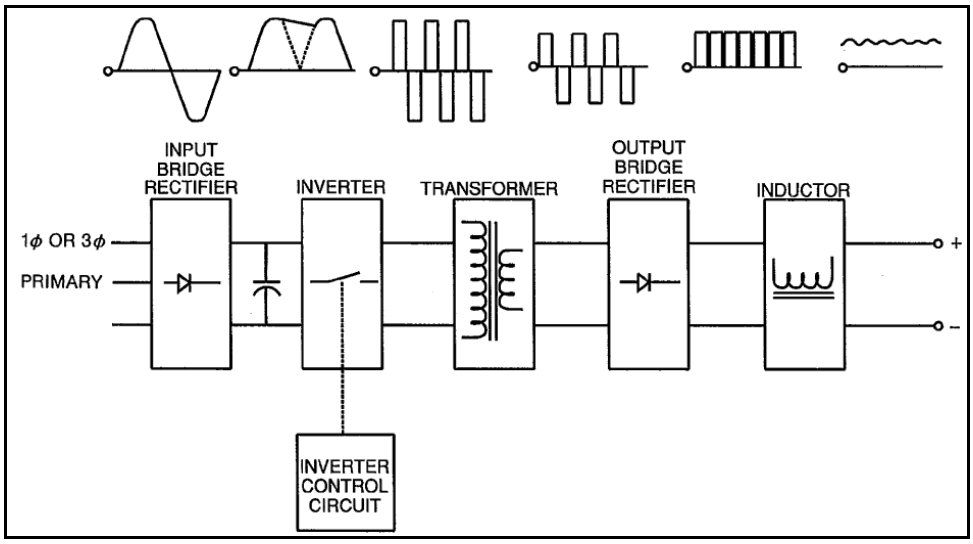

Figure 2-11: Schematic of a Welding Power Source Supplying Direct Current

Figure 2-11, therefore, uses an SCR to convert sinusoidal alternating current to a direct current waveform. The inverter is then used to produce a high-frequency waveform that can then be converted to appropriate voltage and current using a much smaller transformer. A second rectifier can then be used to produce a direct current (now with the appropriate voltage and current). An inductor may then be used to dampen any voltage variation produced by the SCR.

Either a memory core (used in conjunction with a synchronous rectifier) or a single DC constant-current source (used in conjunction with transistors) may be used to produce a square-wave current capable of polarity balance and frequency control. However, to be able to manipulate the DCEN and DCEP current amplitudes independently (i.e., manipulate wave offset), the power source will

actually consist of two distinct three-phase, adjustable-current, direct-current internal power sources in conjunction with several SCRs [43 - Pp. 28-30].

The two internal power sources use separate transformers, each set to a different polarity to allow for independent control of DCEP and DCEN dwell time (i.e., balance control) and offset control [11]. The power sources are then controlled digitally to manipulate frequency too. The welding arcs for all experiments in this study were produced using a pair of paralleled Lincoln Electric Power Wave® AC/DC 1000™ digitally-controlled inverter power sources (Figure 2-12), capable of outputting DCEN, DCEP, and square-wave AC current [39].

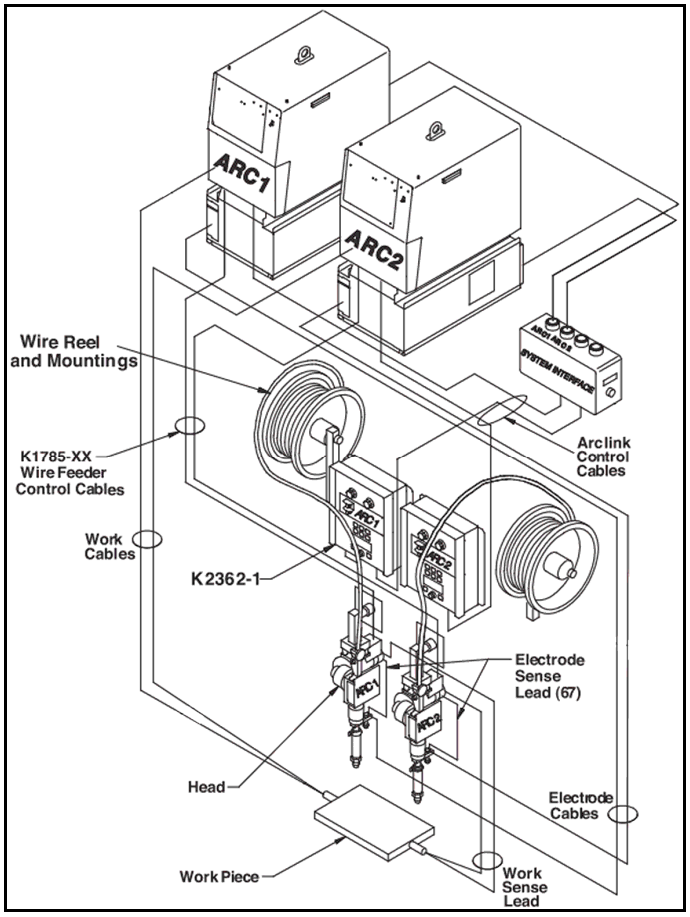

Figure 2-12: Lincoln Electric PowerWave AC/DC 1000 Power Sources and Wire Feeders for Tandem Welds [39]

The square-wave AC can also be manipulated to control positive and negative amplitude and time duration, as well as frequency. The power may be supplied as constant current or as constant voltage. Figure 2-12 illustrates a schematic of the test setup used throughout the investigation. The two Power Wave AC/DC 1000 power sources independently supply electricity to separate electrodes, thus allowing for the production of tandem welds. With tandem welds, it is common for the lead arc to use DCEP current, which promotes greater penetration. Historically, it has been common for the trail electrode to be supplied either DCEN or AC current, allowing for increased deposition [28 - Pg. 8, 40].

2.6.3 Waveform Manipulation

The Power Wave AC/DC 1000 is capable of supplying DCEN, DCEP, and square-wave AC (AC-SQ) current. All three polarities may be supplied with constant current or constant voltage. The AC current can be manipulated further by controlling various waveform variables: frequency (λ), balance (i.e., changing the relative time fraction at each polarity), and offset (i.e., changing the current amplitude at each polarity independently). Specifically, balance refers to the percentage of time that each complete waveform cycle is held at DCEP polarity (Figure 2-13).

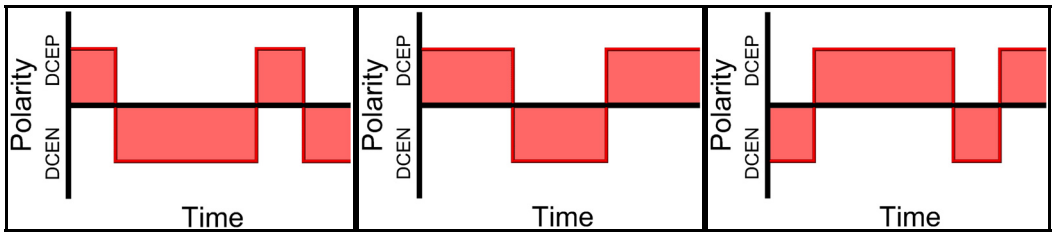

Figure 2-13: Current Waveform for 25% (left), 50% (middle), and 75% (right) Balance

The unbalanced AC-SQ waveform gives the user even further control over increased deposition or penetration. While not previously achievable, it now is

possible to combine good penetration with increased deposition, good penetration with lower heat input, or increased deposition with lower heat input [11].

2.6.4 Heat Input Efficiency (η)

Several welding parameters, including polarity, have interactive effects with each other, which can change the effective heat input during welding. Such interactions have often been lumped together as being a single factor referred to as "η," the welding heat efficiency. "η" is incorporated into the heat input equation as per Equation 3.

$$Heat\ Input = \left[\frac{(Voltage) \times (Current)}{(Travel\ Speed)} \right] \times \eta \qquad \textbf{(3)}$$

The welding heat efficiency is a function of the amount of heat produced by the power source that is actually used to melt base or filler metal. Variables including welding process, welding equipment, heat intensity, stick-out distance, metal transfer mechanism, voltage, current, and travel speed all affect the welding heat efficiency [48 - Pg. 31, 54, 51, 20]. While calorimetric effects would be the most accurate method of calculating heat input efficiency for a specific combination of welding variables [48 - Pg. 31], the change of any one variable would likely change the welding heat efficiency value. Ideally, the welding heat efficiency should be based upon scientific relationships instead of being measured empirically.

As a first step towards a more complete heat input formula, it may be helpful for the existing equation (1) to be modified to calculate heat input on the basis of current polarity. As such, the author recommends that the product of time fraction at each polarity be multiplied by the current amplitude at each polarity. The ratio of these products will be used to separate total heat input produced from DCEP polarity (4), and total heat input produced from DCEN polarity (5).

$$DCEP\ Heat\ Input = \left[\frac{(Current)\times(Voltage)}{Travel\ Speed}\right]\times(\%\ Balance)\times(1+\%\ Offset) \quad \textbf{(4)}$$

$$DCEN\ Heat\ Input = \left[\frac{(Current)\times(Voltage)}{Travel\ Speed}\right]\times(1-\%\ Balance)\times(1-\%\ Offset) \quad \textbf{(5)}$$

For a tandem welding process, the total DCEP or DCEN heat inputs may be calculated by adding the individual values for both electrodes.

2.6.5 Constant Current vs. Constant Voltage

As was previously noted, the Lincoln Power Wave AC/DC 1000 can supply power either using "constant current" or "constant voltage." During constant current, the operator selects the desirable current and voltage, and the wire feed speed (WFS) compensates for changes in arc length [39, pg. B-8]. For example, if the base material is uneven, the arc length varies with welding distance. However, the wire-feed speed will increase or decrease to hold the arc length constant (and hence keep the voltage near-constant).

When welding with constant voltage mode, the operator inputs WFS and voltage, and the current compensates for changes in arc length [39, pg. B-8]. For example, if the base material is uneven and the arc length increases, the current will reduce temporarily to slow the melt-off rate. The reduced current allows the welding wire to re-establish the desired arc length. Alternatively, if the arc length decreases, the current will increase to accelerate wire melt-off, once again re-establishing the desired arc length.

2.7: Charpy V-Notch Testing

Some reference thus far has been made to material toughness. However, for practical purposes, 'fracture toughness' will not be investigated in this project.

Rather, Charpy V-Notch (CVN) impact testing will be performed to determine CVN fracture energy values.

2.7.1 Charpy V-Notch (CVN) Impact Testing

While CVN testing cannot provide absolute fracture toughness values of a material, it can provide useful comparative data [42 - Pg. 35, 41 – Pg. 156]. A notched specimen (Figure 2-14) is inserted into a liquid bath held at the test temperature, before being inserted into an apparatus, where a hammer will impact it (Figure 2-15). Once removed from the liquid bath, the test sample must be impacted within five seconds to minimize test temperature variations [4].

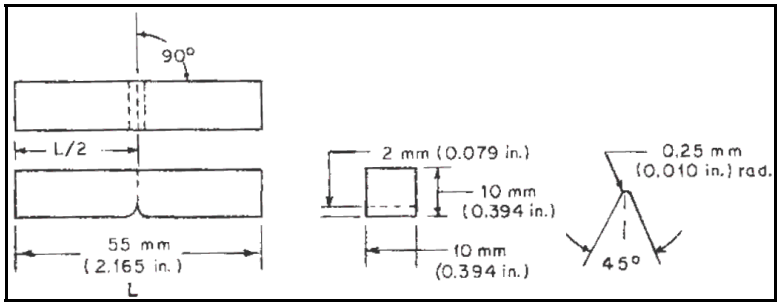

Figure 2-14: Schematic of Full-Size CVN Specimen Dimensions [4]

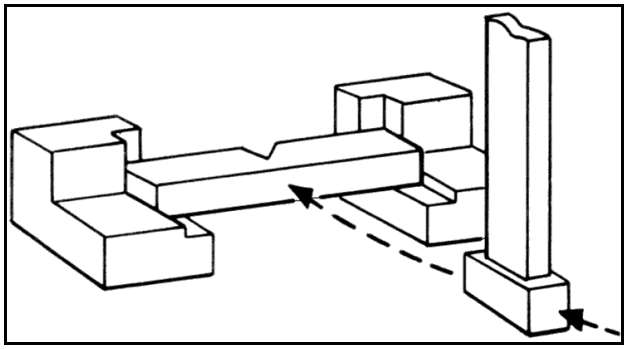

Figure 2-15: Schematic of CVN Equipment and Samples [25 - Pg. 1.2-5]

Notch positioning in the sample is critical, as position deviations as small as 0.5 mm can cause dramatic changes to the reported CVN fracture energy values. The

position of the notch becomes even more critical when weld HAZ material is being evaluated, due to the wide range of mechanical properties in the distinct HAZ regions [42, pg 35]. Therefore, even though the principles of the test are simple to explain, sample preparation is both critical and tedious. If the notch is located such that an increased portion of CGHAZ is sampled by the notch, CVN fracture energy values will be detrimentally affected [52].

By extension, the slope of the weld bead fusion line at the notch location is critical too. Figure 2-16 illustrates two weld beads with different fusion line slopes. The red lines represent the outlines and notches of two CVN test specimens. The CVN specimen notch at the steeper fusion line slope (Figure 2-16, left) passes through WM and CGHAZ, whereas the specimen notch passing through a shallower fusion line slope (Figure 2-16, right) samples WM, CGHAZ, and FGHAZ material. As a result, the specimen on the right is expected to achieve superior test results [36]. The effects of fusion line slope, therefore, will be considered when designing test matrices and evaluating CVN fracture energy values.

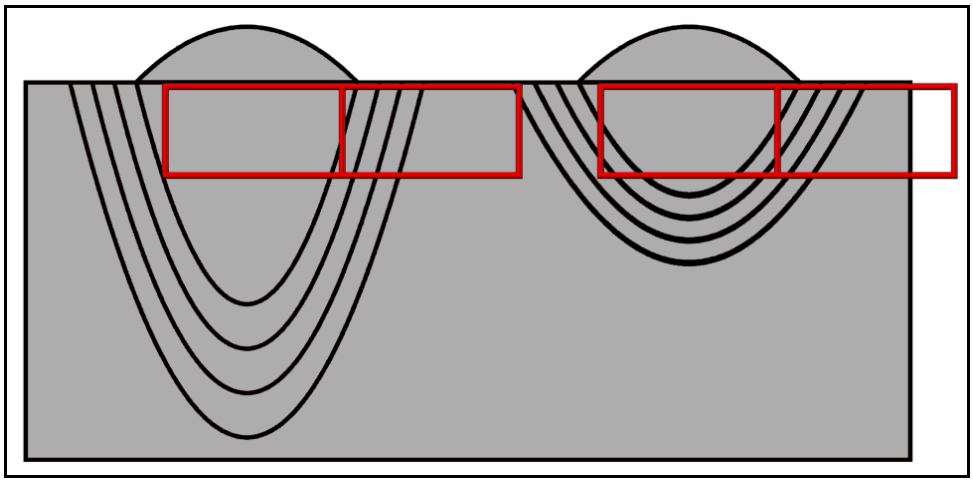

Figure 2-16: Weld Bead Fusion Line Slope and CVN Specimen Notch Placement

The mechanism of fracture, and the corresponding fracture test result, changes dramatically with testing temperature with ferritic steels. At lower temperatures,

steel becomes brittle and fails by cleavage. At higher temperatures, the material becomes ductile and fails by microvoid coalescence [2 - pg. 297].

The relationship between fracture mechanism (and impact energy) and test temperature is often illustrated in a characteristic S-shaped ductile-to-brittle transition temperature (DBTT) curve (Figure 2-17). The DBTT, which affects BCC metals such as steels, is a test temperature below which fracture becomes increasingly brittle. This curve can shift to the right (i.e., to higher temperatures) if the microstructure is coarser [52].

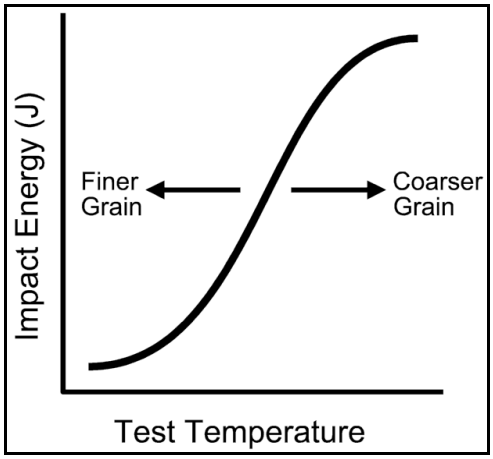

Figure 2-17: DBTT Schematic

However, using smaller CVN test specimens (Figure 2-18) often results in a decreased DBTT because the fracture mechanism shifts from one of plane strain to one of plane stress [29]. While it is preferable to use full-size CVN specimens, sub-size specimens are an acceptable practice, though a new DBTT curve should be developed for the new specimen size.

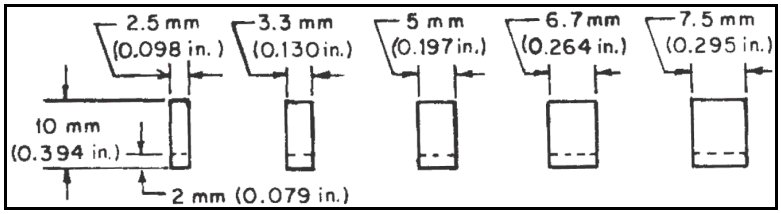

Figure 2-18: Schematic of Sub-Size CVN Specimen Dimensions [4]

2.8: Literature Review Summary

Microalloyed TMCP steels are ideal for high-pressure arctic gas pipelines, because of their combination of high strength, good toughness, and reasonable cost. For high-productivity spiral welding, the SAW process is utilized to join steel rolls into spiraled pipe. However, the steel's optimized microstructure, which is responsible for its excellent mechanical properties, can undergo significant modifications along the distinct HAZ regions that form adjacent to the WM fusion line. The best method of addressing the effects of welding on HAZ microstructure is to simply try to minimize such changes.

Heat input, equation (1), is a relationship between voltage, current, and travel speed, and represents the amount of energy supplied by the welding power source per linear weld distance. However, equation (1) does not address polarity, which does affect both welding wire deposition rates, and base metal melting rates. The author proposes that by comparing the ratio of heat input values supplied by DCEN and DCEP polarity (equations (4) and (5)), a better understanding of the effect of welding parameters on HAZ notch-toughness can be established. The waveform variable, balance, allows for precise control of the ratio of heat input supplied by each polarity. Finally, CVN sample extraction will be important in accurately determining CVN fracture energy values for weld HAZ. The notch placement relative to the distinct HAZ regions, in particular, will be critical.

CHAPTER 3: POLARITY AND TANDEM BEVEL WELD NOTCH-TOUGHNESS[*]

During pipe or pipeline fabrication, every welding pass induces thermal gradients upon the adjacent unmelted steel. Depending upon its proximity to the weld pool, the newly formed heat affected zone (HAZ) may undergo full recrystallization accompanied by grain coarsening, full recrystallization with grain refinement, or partial phase transformations. In all three conditions, secondary phases may undergo varying degrees of growth, dissolution, or dissolution and re-precipitation. The mechanical properties of the HAZ bands are affected by changes in size and distribution of both microstructure phases and precipitates.

When producing a multiple-pass weld, smaller beads are laid, whose thermal gradients partially refine each other's HAZ regions. This has allowed for thermo-mechanical controlled processed (TMCP) microalloyed steel HAZ to achieve or exceed EVRAZ Inc. NA's notch impact value targets of 90 J (66.4 ft-lbs) at -20°C (at the mid-wall fusion line). However, multiple pass welding procedures are less easily applied to spiral welding systems. Therefore, this work explores the use of new power-source technologies to achieve similar toughness values, while using only a single weld pass.

A tandem welding process was used with a pair of Lincoln Electric Power Wave AC/DC 1000 power sources, set at constant current for easier heat input and current waveform analysis. The first arc utilized DCEP polarity, and the second arc used square-wave AC. A basic flux was used to improve notch-toughness results. After welding parameters were set to allow for a single-pass bevel fill, a second tandem weld was performed manipulating waveform balance, which should affect the HAZ microstructure. Notch impact toughness tests were

[*] Some of the results and analysis in this chapter have been published at the 2008 International Pipeline Conference (paper IPC2008-64398), hosted in Calgary.

performed throughout the weld metal (WM) and HAZ regions of two promising sets of welding parameters, which, other than current balance, were produced using the same welding parameters.

3.1: Experimental Procedure

3.1.1 Base Material

Weld coupons were extracted from a 762 mm (30") outer diameter (OD) spiral-welded steel grade X80 pipe, with a wall thickness of 16.2 mm (0.638"). The pipe was designated #3039, and its nominal chemical composition is listed in Table 3-1.

Table 3-1: Chemical Composition (weight %) of X80 Steel (Pipe #3039)

C	Mn	S	Si	Al	Mo	Nb	N	Ti
0.06	1.6	0.002	0.15	0.02	0.2	0.03	0.005	0.012

EVRAZ Inc. NA provided base material Charpy V-notch (CVN) results at a range of temperatures (with three 10 mm x 10 mm test coupons broken at each temperature, in compliance with the current edition of ASTM A370 [4]). The results are plotted in Figure 3-1, though only two test results were accepted for the -60°C test temperature (the third value was considered an outlier).

Figure 3-1 illustrates the expected trend that CVN absorbed energy increases with increasing testing temperature. Because EVRAZ Inc. NA's CVN test targets are for fracture energies produced at -20°C [8], that temperature was selected for subsequent project tests. CVN specimens, tested at -20°C, indicated that the X80 base material from pipe #3039 should have a notch-toughness of 274 J, with a standard deviation of 22 J.

A Hypertherm corporation Powermax 1650 plasma cutter was used to extract weld coupons from the pipe. Coupons were approximately 500 mm (20") long

(parallel to the LPA orientation) and 250 mm (10”) wide. Samples were extracted from the pipe such that prior spiral welds were avoided; by doing so, it would not be possible to accidentally analyze a region where a new HAZ overlapped with a prior HAZ region. The resulting samples were curved (refer to Figure 3-2 and Figure 3-3), and were flattened by a hydraulic press prior to welding. Because the samples were removed from a pipe, the top and bottom surfaces are referred to as the “OD Surface” and the “ID Surface” (inner diameter) respectively (refer to Figure 3-3), even after being flattened.

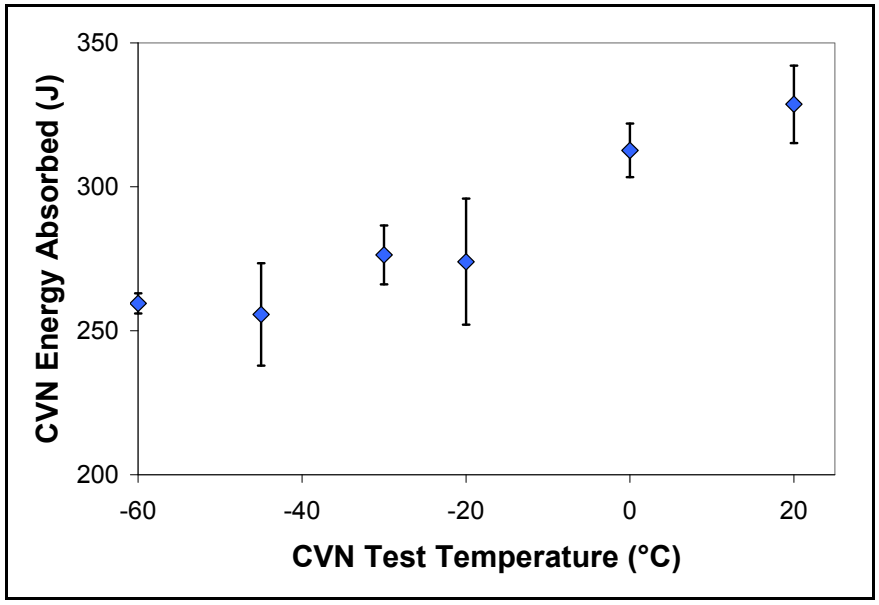

Figure 3-1: Pipe 3039 Full-Size CVN Results at Various Test Temperatures

Figure 3-2: Cut Weld Coupons, Illustrating Curved 250 mm (10”) Sides

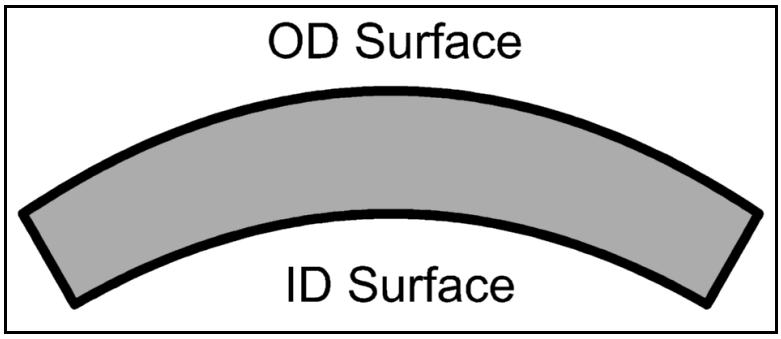

Figure 3-3: Schematic of Weld Coupon Cross-Section

Each weld coupon underwent beveling along one of its 500 mm (20") long faces. Modified V-groove bevels (not used for production welds), were selected to allow for a root opening large enough for electrode access, while steep enough to promote near-vertical HAZ regions that would be easier to individually evaluate with CVN testing (refer to Figure 3-4).

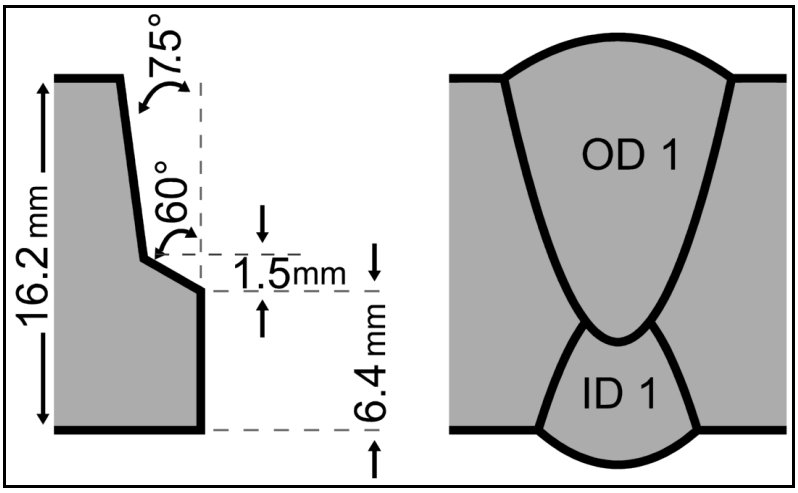

Figure 3-4: Single-Pass Bevel Design

3.1.2 Welding Process and Setup

Submerged arc welding was performed using two paralleled Lincoln Electric Power Wave® AC/DC 1000™ power sources. The two power sources were used for the two separate electrodes required for tandem welding. A schematic of the

welding heads and electrodes relative to the base metal (BM) is illustrated in Figure 3-5 (all units are in mm unless otherwise stated, and angular dimensions could vary by +/- 2°). At the start of each weld, the electrode stick-out distance was approximately 10 mm (0.4").

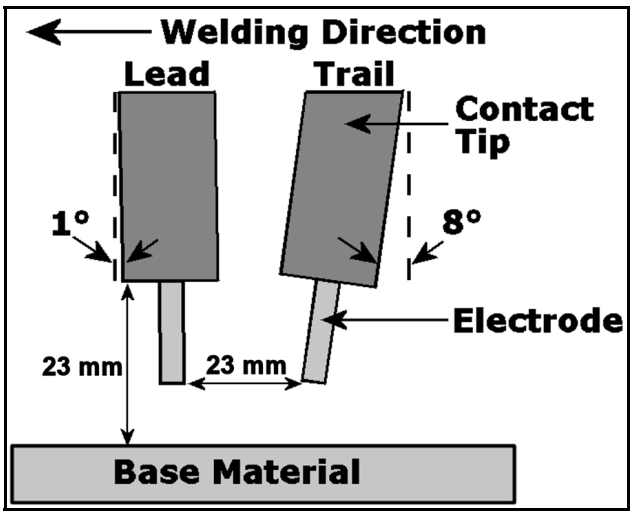

Figure 3-5: Electrode and Base Metal Setup Dimensions (units in mm)

An S3 NiCrMo2.5 wire (3.2 mm, 0.125 in. diameter) was used in conjunction with a basic flux (their chemical compositions are listed in Table 3-2 and Table 3.3). A basic flux was selected to produce cleaner weld metal (WM) with lower inclusion content. The primary goal for the choice of this combination of wire and flux was to measure HAZ toughness that may not be altered significantly by weld metal strength.

Table 3-2: Electrode Chemical Composition (Wt. %)

C	Si	Mn	Cr	Ni	Mo
0.11	0.2	1.4	0.7	2.4	0.5

Table 3-3: Flux System Chemical Composition (Wt. %)

SiO_2 +TiO_2	CaO + MgO	Al_2O_3 + MnO	CaF_2
20	20	35	20

3.1.3 Welding Parameters

As Figure 3-4 indicates, the weld sequence included a single-pass tandem ID root weld pass followed by a single-pass tandem OD fill weld pass. A combination of experimental welding parameters (voltage, current, and travel speed) was developed to allow for the bevel to be completely filled by a single OD pass. The welding parameters are listed in Table 3-4. To allow for simpler analysis of the effects of heat input and current-waveform manipulation, it was desirable to be able to maintain constant voltage and current values. Therefore, constant current was selected for all welds.

Table 3-4: Experimental Welding Arc Parameters

Weld Type	Lead Arc		Trail Arc		Travel Speed	
	Amps	Volts	Amps	Volts	ipm	mm/s
ID Pass	500	28	500	27	53	22.5
OD Pass	350	28	700	30	25	10.5

The ID root pass was used only to connect the separate pieces of steel together. Because no ID WM or HAZ underwent subsequent analysis, it will not be discussed further. As per the Section 2.5.1, the heat input for a tandem welding process may be determined using Equation 2 from section 2.5.1.

Because the two welds performed vary only in polarity, they both should possess identical heat inputs as calculated with (1). Using parameter values from Table 3-4, both welds should achieve a total OD heat input of 2.91 kJ/mm (73.92 kJ/in.).

Polarity is not included in the classical heat input equation (1), though it does affect penetration depth and deposition rates. If penetration depth is affected, it is reasonable to assume that heat affected zone microstructures also will be affected, and by extension, notch toughness along the weld and HAZ. Two welds were

produced (henceforth referred to as “I” and “II”), using the welding variables from Table 3-4, while varying electrode polarities.

In conformance with typical tandem welding strategies [22, 33, 40], the lead arc polarity was selected to promote deeper penetration, while the trail arc polarity was selected to increase deposition. For an initial investigation into the effects of balance on bevel weld parameters, the current polarity for WC2 was selected by reducing the time fraction at DCEP (i.e., balance) of both lead and trail electrodes by 25%.

Weld coupon “I” (WC1) used a direct current electrode positive (DCEP) lead arc, followed by an alternating current with a 50% balance (AC 50%) trail arc (Figure 3-6). Weld coupon “II” (WC2) used an alternating current with a 75% balance (AC 75%) lead arc, followed by an alternating current with a 25% balance (AC 25%) trail arc (Figure 3-7). Because the WC2 electrodes both used alternating current polarities, their current frequencies were offset by the recommended amount (90°) to reduce detrimental arc interactions during the welds (refer to Figure 3-7).

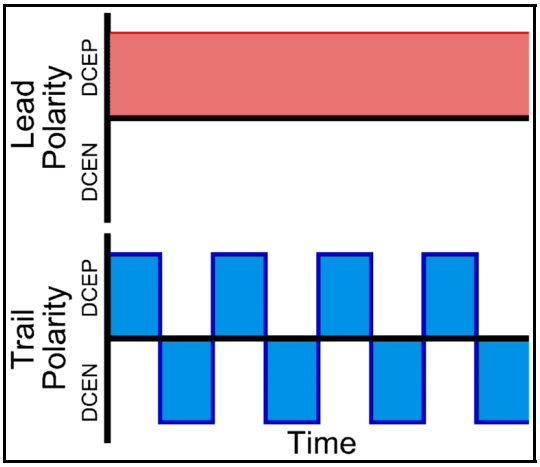

Figure 3-6: Polarity for Weld Coupon “I”

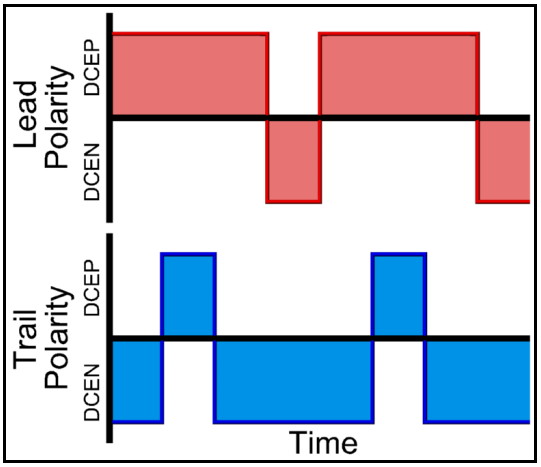

Figure 3-7: Polarity for Weld Coupon “II”

The heat input was then calculated in terms of kJ/mm for each polarity, by multiplying the total heat input for each weld by the time fraction at each polarity. The corresponding heat input values are summarized in Table 3-5.

Table 3-5: Heat Input (HI) as a Function of Polarity

	Heat Input (kJ / mm)	Heat Input (kJ / in.)	Heat Input Fraction
WC 1 - DCEP	1.92	48.72	0.66
WC 1 - DCEN	0.99	25.20	0.34
WC 1 - Total (DCEP + DCEN)	2.91	73.92	1.00
WC 2 - DCEP	1.19	30.24	0.41
WC 2 - DCEN	1.72	43.68	0.59
WC 2 - Total (DCEP + DCEN)	2.91	73.92	1.00

The table demonstrates that even though WC1 and WC2 will use essentially the same total heat input, 66% of the heat input for WC1 will be supplied as DCEP, whereas only 41% of the WC2 heat input will be supplied as DCEP. Based on the above percentages (and Section 2.5.2), it is expected that WC1 should behave more like a DCEP weld (i.e., deeper penetration, reduced electrode deposition, and greater effective heat input into the base material) while WC2 should behave more like a direct current electrode negative (DCEN) weld (i.e., reduced penetration, greater electrode deposition, and reduced effective heat input into the base material).

From Section 2.5, a greater heat input will allow for slower cooling rates, which will reduce the formation of localized brittle zones. However, the increased heat will also widen the HAZ regions, consequently yielding a greater CGHAZ. This would result in an overall reduction in notch toughness at the fusion line. The aforementioned fusion line slope effects on toughness may cause other effects on the notch-toughness.

3.1.4 Sample Preparation

Samples extracted for metallographic examination were mounted in 50.4 mm (2 in.) diameter Bakelite pucks. The specimens then were ground to a 600-grit finish, and polished to a 0.05 micron mirror finish. The etchant was a mixture of equal volumetric portions of 4% nitric acid dissolved in methanol, and 2% picric acid dissolved in methanol. The picric acid was used to improve contrast between individual HAZ regions. The etchant was applied to dry specimen surfaces, and rinsed off with running tap water.

Full-size CVN specimens (10 mm x 10 mm x 55 mm) were used to evaluate notch toughness of the welds and corresponding HAZ regions. Samples were extracted as close to the top metal surface as possible, to evaluate only the OD WM and HAZ (as illustrated by the red-outlines in Figure 3-8). By doing so, it was possible to extract CVN specimens free from ID WM and HAZ, as well as areas of overlap between OD and ID WM and HAZ. If ID WM or HAZ (or overlap regions) had been analyzed, it would have complicated subsequent analysis.

Figure 3-8 illustrates the various notch locations used for this investigation:

- WM: The notch is located along the WM centerline.
- FL: The notch is located such that its top half is located above the fusion line (i.e., in the WM) and the bottom half is located below the fusion line (i.e., in the HAZ and BM).
- FL+2: The notch is 2 mm from the FL location, away from the WM.
- FL+5: The notch is 5 mm from the FL location, away from the WM.

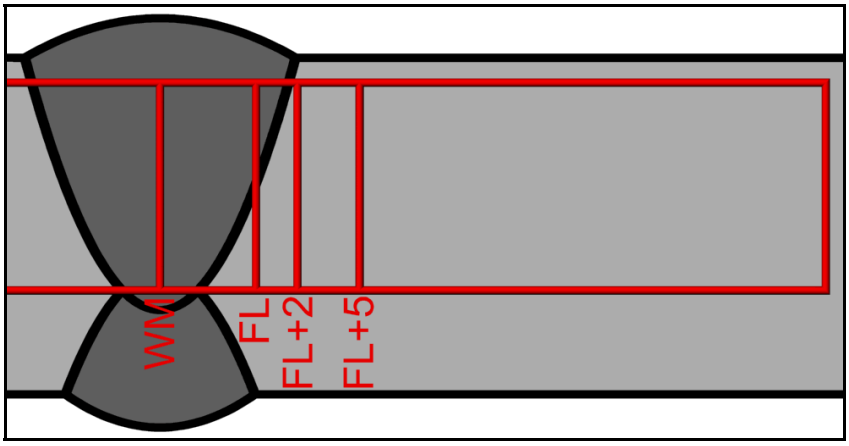

Figure 3-8: CVN Notch Placement

For accurate CVN notch placement, specimens were ground and etched using a methanol-based 4% Nital etchant to resolve the WM and fusion lines. Notches were oriented such that fracture propagation would run parallel to the welding direction (refer to the red outlines in Figure 3-9).

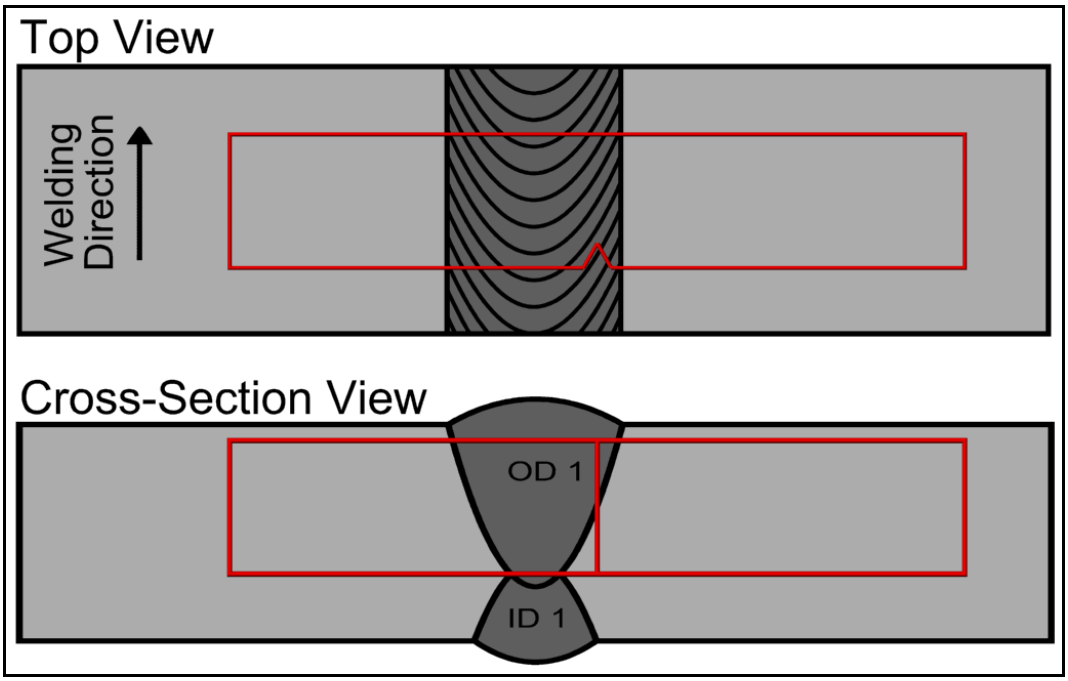

Figure 3-9: CVN Extraction and Notch Placement ("FL" Notch Location)

Figure 3-9 illustrates the specimen extracted from the weld, such that the notch is located at the fusion line (or "FL") location. To improve contrast when recording images of fusion lines and HAZ boundaries, distinct regions were typically outlined with pencil.

3.1.5 Testing Parameters

CVN testing, sample tolerances, and equipment calibrations were performed in compliance with ASTM A370-03a [4]. Specimens notched along the centers of the WM were tested at the Regina R&D facility of EVRAZ Inc. NA. All remaining CVN specimens (i.e., samples notched at the FL, FL+2, and FL+5 locations) were tested at the Alberta Research Council Millwoods Facility. Testing was performed at -20°C (-4°F).

Micro-Vickers hardness testing was performed with a 500 gram load, applied for 15 seconds per indentation. The large load and long loading time were selected to increase indentation sizes, thereby making it easier for the operator to accurately measure the hardness values.

3.2: Results

3.2.1 Macroscopic Evaluation

WC1 and WC2 were cross-sectioned, mounted in 50.4 mm diameter Bakelite pucks, ground, polished, and etched. Magnified macroscopic images illustrate the OD WM and various HAZ bands that formed (Figure 3-10 and Figure 3-11).

Figure 3-10: Weld Coupon "I" Cross-Section (5.5x magnification)

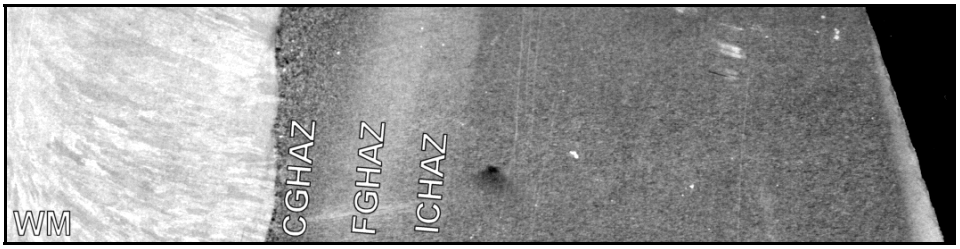

Figure 3-11: Weld Coupon "II" Cross-Section (5.5x magnification)

The boundaries for the OD WM and HAZ regions were then outlined and illustrated in Figure 3-12 and Figure 3-13. For WC1, the FGHAZ / ICHAZ boundary (i.e., the boundary between the CGHAZ and FGHAZ regions) on the right side was obscured by the ID weld bead. Both weld cross-sections demonstrated significant distortion (with the BM OD surfaces achieving concave curvature). As a result, additional care was needed during subsequent CVN test specimen extraction.

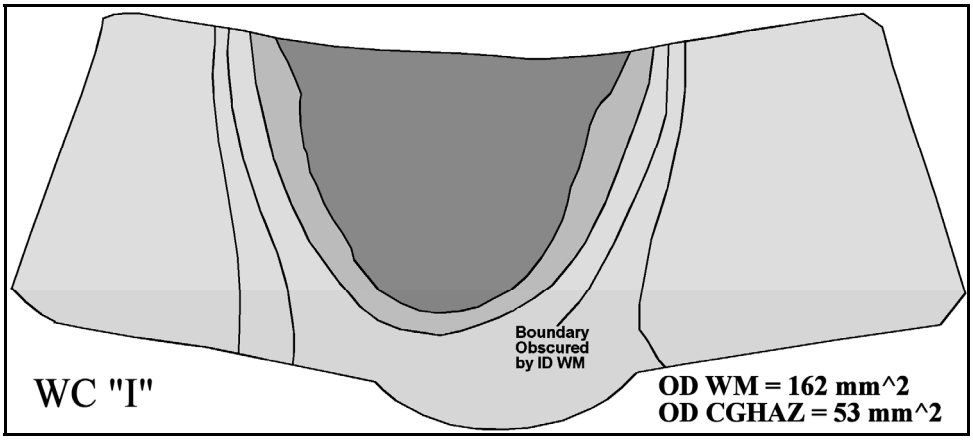

Figure 3-12: Weld Coupon "I" WM and HAZ Boundary Outlines (2.5x magnification)

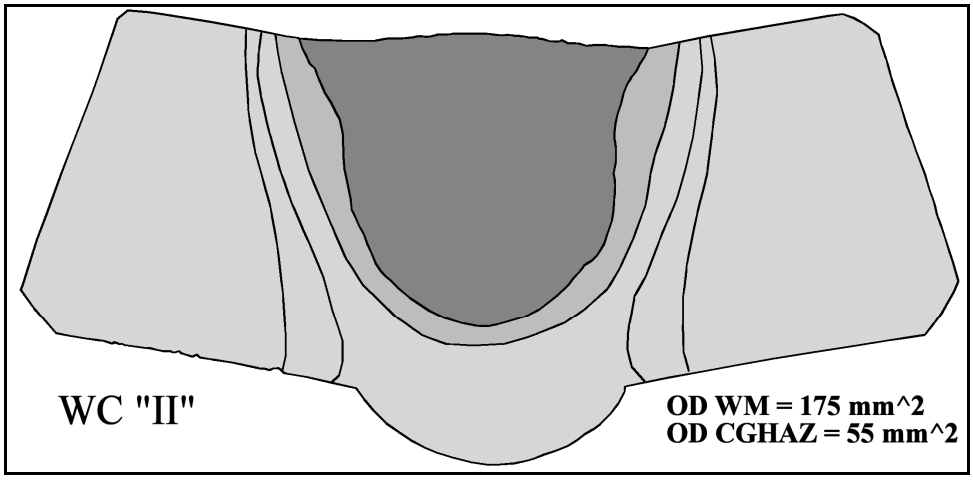

Figure 3-13: Weld Coupon "II" WM and HAZ Boundary Outlines (2.5x magnification)

Figure 3-12 and Figure 3-13 show that for both weld coupons, the CGHAZ / FGHAZ boundaries ran roughly parallel to the fusion lines. However, the FGHAZ / ICHAZ and ICHAZ / BM boundary paths deviated from the fusion lines. The shape of the CGHAZ regions resemble three-dimensional heat flow lines as described by Easterling, whereas the FGHAZ and ICHAZ regions resemble two-dimensional heat flow lines. Therefore, it is suspected that if thicker BM had been used, the FGHAZ and ICHAZ shapes (and areas) would have differed. As a result, only the WM and CGHAZ areas were measured for subsequent analysis.

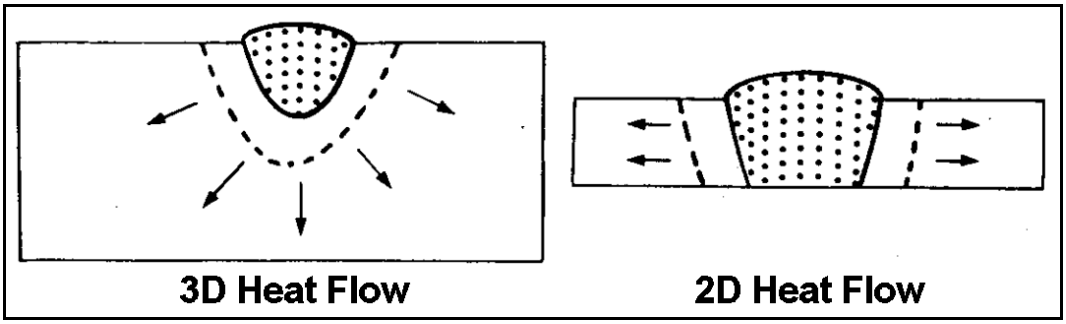

Figure 3-14: Three-Dimensional Heat Flow in a Thick BM, and Two-Dimensional Heat Flow in a Thin BM (adapted from Easterling [9 – Pg. 20])

The areas listed in Figure 3-12 and Figure 3-13 indicated that WC1 and WC2 possess CGHAZ areas that are very similar (each roughly 54 mm^2). The WC2 WM area (175 mm^2) is 8% greater than the WC1 WM area (162 mm^2). Area measurements were performed on the same plane used for subsequent hardness measurements (presented in the next section). This area difference corresponds to the WM shape: the WC1 bead top is flat or slightly concave, whereas the WC2 bead top is slightly convex. Additionally, WC2 possesses a more vertical fusion line than WC1.

3.2.2 Micro-Vickers Hardness Evaluation

A series of micro-Vickers hardness indentations were performed on each cross-section, running parallel to the top BM surface, and at a depth approximately half of the maximum OD weld bead penetration. Macroscopic images were recorded of indentations (Figure 3-15 and Figure 3-16), with the white dots being the hardness indentations. To the right of the WM, hardness indentations were spaced 0.25 mm apart, ensuring that a minimum of three full indentation lengths could fit between any two indentations.

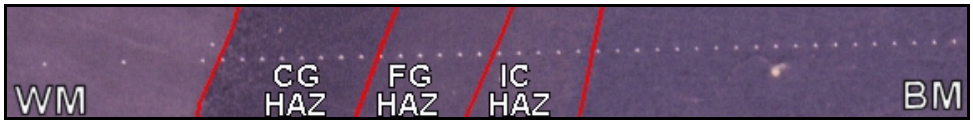

Figure 3-15: Weld Coupon "I" Hardness Traverse Locations

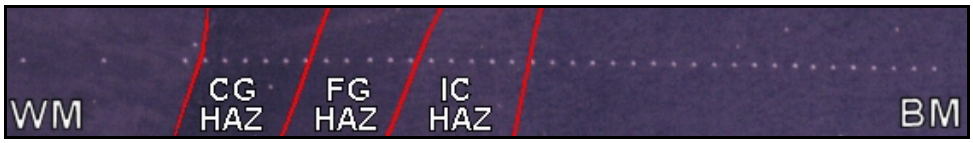

Figure 3-16: Weld Coupon "II" Hardness Traverse Locations

Using the previously-determined HAZ interfaces (which are near-vertical red lines in Figure 3-15 and Figure 3-16), it was possible to plot the hardness values with respect to their corresponding region (Figure 3-17 and Figure 3-18).

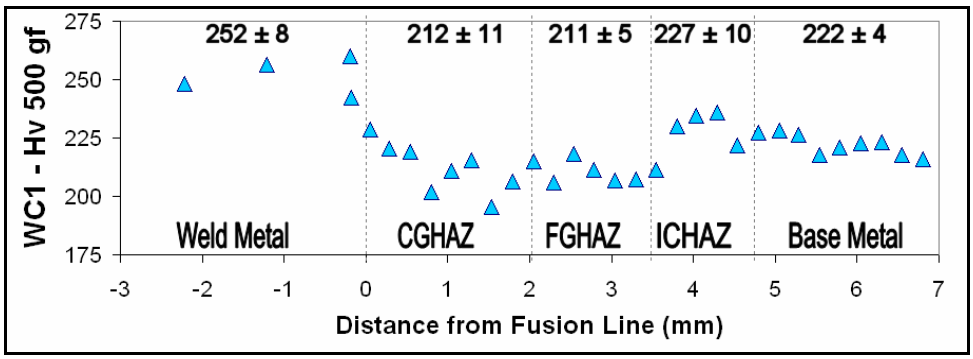

Figure 3-17: Weld Coupon "I" Hardness Traverse Results (Hv 500 gf, 15 s)

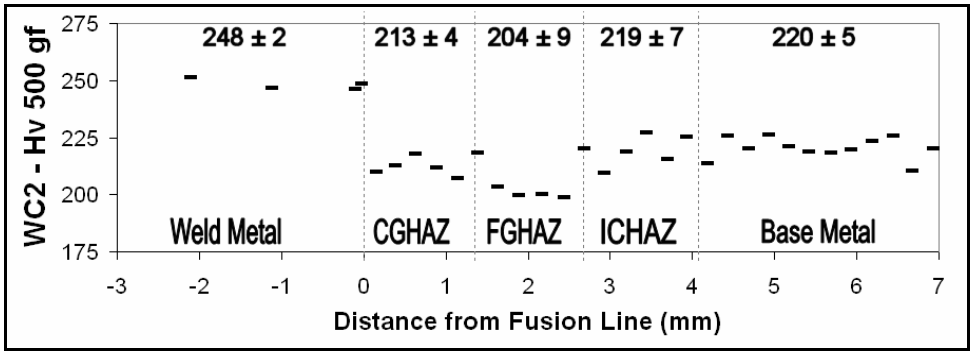

Figure 3-18: Weld Coupon "II" Hardness Traverse Results (Hv 500 gf, 15 s)

Figure 3-17 and Figure 3-18 both illustrate the hardness values with respect to the fusion line ("0" on the "x" axis). Hardness indentations were separated on the basis of metallurgical region (e.g., WM, CGHAZ, etc.). Additionally, the average hardness and tolerance (standard deviation) values are listed for each metallurgical region.

As Figure 3-12 and Figure 3-13 show, HAZ region widths vary significantly as a function of depth. As a result, the HAZ region widths in Figure 3-17 and Figure 3-18 vary too, even though both weld coupons demonstrated similar weld bead and HAZ geometries overall. When comparing the individual metallurgical regions of each weld coupon, WC1 and WC2 both demonstrate very comparable average hardness values and corresponding standard deviations. In each case, the highest hardness was achieved in the WM, followed by a sudden drop of hardness in the CGHAZ. The FGHAZ demonstrated comparable or slightly lower hardness than the CGHAZ, likely as a result of the increased grain boundary fraction that would have reduced overall hardenability (and hardness). The subsequent ICHAZ demonstrated an increase in hardness. The BM hardness was typically similar to the ICHAZ range, and it was fairly uniform.

While the two weld coupons appear to have quite comparable hardness ranges across the various metallurgical regions, there are two minor differences worth noting. First, WC2 demonstrates a slightly softer FGHAZ than WC1. Second, only WC1 demonstrated an ICHAZ region with hardness values exceeding those of the BM. These differences both fall within the ranges of the test standard deviations. Because the largest difference in hardness values is between the WM and the CGHAZ, that boundary became an obvious focus for subsequent investigation. As the following section will show, CVN test results further reinforced the importance of investigating the material along the fusion line.

3.2.3 Charpy V-Notch Test Results

CVN fracture energy values for WC1 and WC2 are plotted in Figure 3-19. The horizontal axis represents the notch placement (with FL, FL+2, and FL+5 plotted at 0, 2, and 5 mm, respectively), and the dashed line represents the fusion line. Three specimens were tested for each notch location for each weld coupon. The average test values at each location are summarized in Table 3-6, along with the standard deviation at each test location, represented as a percentage of the average

values. The percentage difference of WC2 results (relative to WC1 results) is also included in Table 3-6. WC1 and WC2 each had one significant outlier test value at the FL+5 test location. In Table 3-6, the average results and standard deviations were calculated both with and without the outlier values (corresponding to rows "FL+5" and "(FL+5)*" respectively).

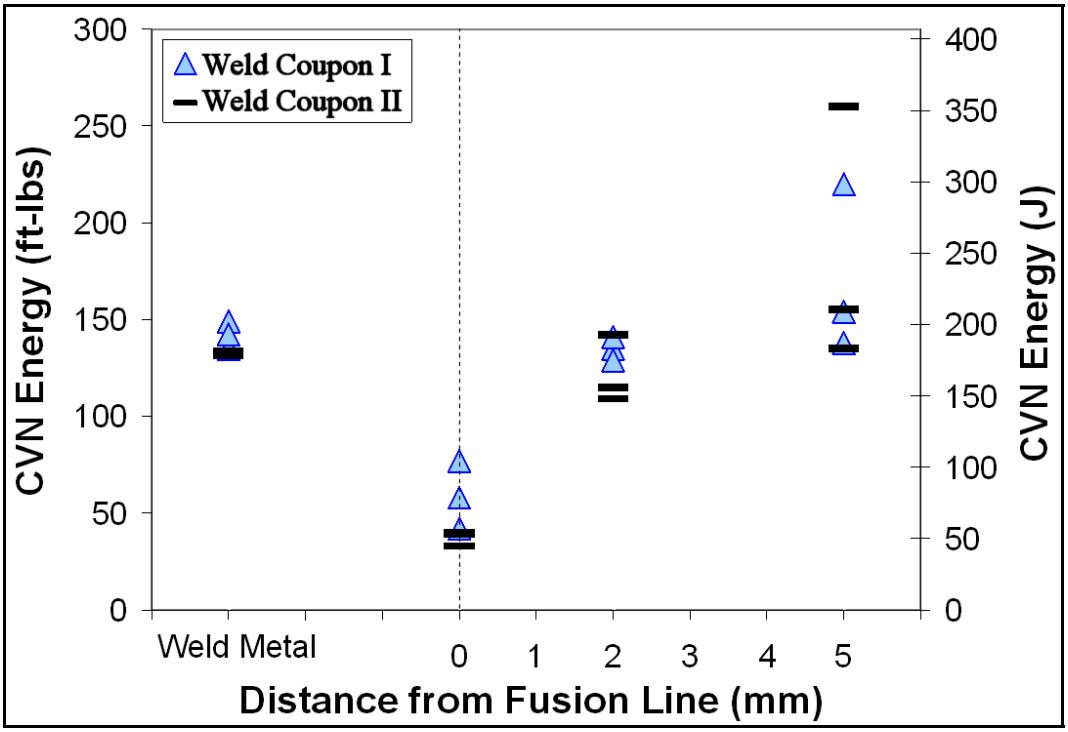

Figure 3-19: CVN Results at -20°C (-4°F) for Weld Coupons I and II

Table 3-6: Average CVN Results at Test Locations, and Standard Deviations

Notch Location	Weld Coupon I			Weld Coupon II			Percent Difference
	Ft-lbs	Joules	% Std. Dev.	Ft-lbs	Joules	% Std. Dev.	
WM	142	193	4.9%	132	179	1.0%	7.0%
FL	59	80	29.7%	37	51	10.3%	37.3%
FL+2	135	183	4.4%	122	165	14.4%	9.6%
FL+5	171	231	25.4%	183	249	36.7%	-7.0%
(FL+5)*	146	198	7.7%	145	197	9.7%	0.7%

The CVN test results for both coupons produced similar trends. For both coupons, placing the notch at the WM yielded moderate energy values, while placing the notch at the fusion line yielded lower values. As the notch was then moved further from the fusion line, towards the BM, the energy values steadily increased.

WC1 achieved greater average notch-toughness results than WC2. Furthermore, the greatest difference between WC1 and WC2 average values was achieved at the FL notch location. When the outlier values were not considered, average test results at the FL+5 notch location were nearly identical.

The standard deviation values for WM notch location results were very small, whereas the specimens with notches located in HAZ material displayed greater standard deviations (i.e., more test result variability).

It is worth repeating that the X80 base material achieved CVN fracture energy values of 274 Joules at -20°C, with a standard deviation of 22 Joules. It is therefore reasonable that the test specimens notched at the FL+5 location should demonstrate elevated test values, because a greater fraction of their notches presumably pass through unaffected BM. In other words, the notch lengths passing through different HAZ regions appears to strongly influence the CVN test results. On a final note, the outliers actually exceeded the expected BM toughness, which further indicates that they should truly be considered only outliers.

3.2.4 Microscopic Evaluation

Optical microscopy was performed, in close proximity with the hardness indentations, to allow for a comparison of the microstructures adjacent to the weld fusion lines. The following optical micrographs show a mixture of ferrite and bainite, with a range of grain sizes.

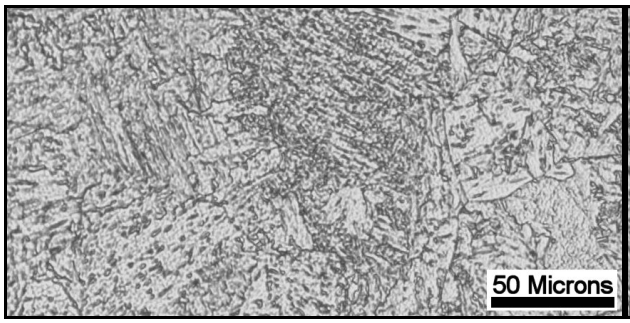

Figure 3-20: WC1 0.3 mm from the FL

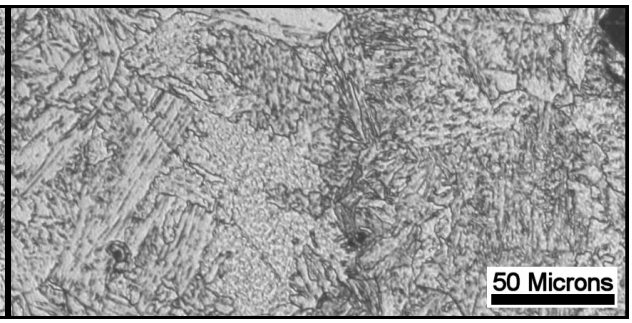

Figure 3-21: WC2 0.3 mm from the FL

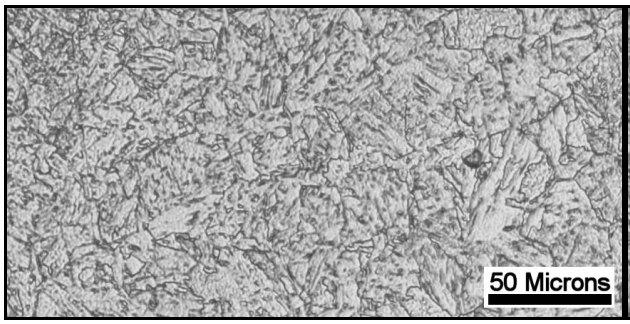

Figure 3-22: WC1 0.8 mm from the FL

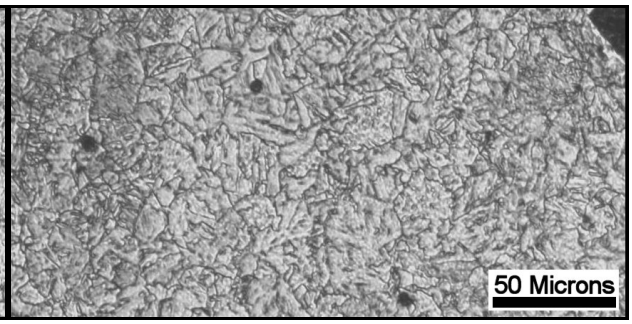

Figure 3-23: WC2 0.8 mm from the FL

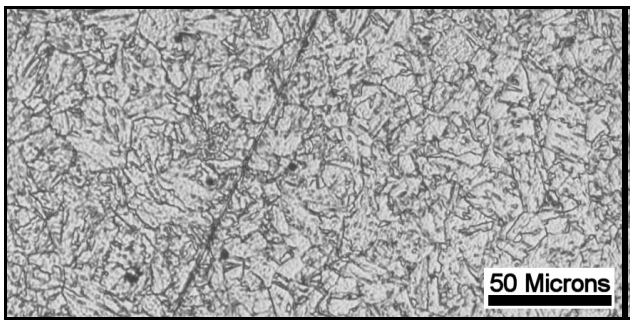

Figure 3-24: WC1 1.3 mm from the FL

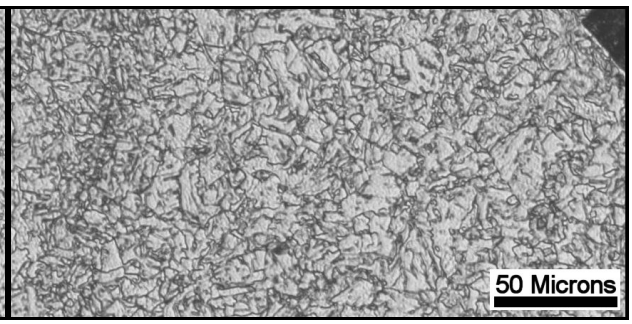

Figure 3-25: WC2 1.3 mm from the FL

Figure 3-20, Figure 3-22, and Figure 3-24 illustrate micrographs at various distances from the fusion line (and into the HAZ) for WC1, and Figure 3-21, Figure 3-23, and Figure 3-25 illustrate the corresponding micrographs for WC2. According to the measurements in Figure 3-17 and Figure 3-18, all six micrographs display CGHAZ material. Each corresponding pair of micrographs appears to demonstrate similar-looking phases and grain shapes, indicating that the HAZ regions of the two weld coupons contain comparable microstructures.

The sizes of the grains appear to be comparable too, which was expected, based upon the similar hardness values.

3.2.5 Charpy V-Notch Placement

The focus of this investigation was to determine how to best improve SAW HAZ toughness. The initial hardness or microstructures did not appear to strongly affect the CVN fracture energy values. However, the notch toughness was by far worst when the specimens were notched at the FL location. Therefore subsequent analysis was performed to help determine the source of the poor toughness.

Specimens notched at the FL location are expected to exhibit poor CVN fracture energy values, primarily because a large portion of the notch will pass through the coarse-grain HAZ. Both WC1 and WC2 demonstrated comparable microstructures (with WC2 demonstrating slightly finer microstructures in close proximity to the fusion line) and hardness. However, specimens notched at the FL location demonstrated that WC1 had superior notch-toughness to WC2. Due to this, the notch locations were investigated further.

When preparing the CVN specimens, sample faces were ground to 600 grit and etched lightly. Such preparation allowed for the WM and HAZ regions to be visible to the naked eye. Such boundaries were not detected adequately when they were digitally imported using a flatbed scanner. As a solution, specimen WM and HAZ boundaries were outlined with pencil prior to scanning (refer to Figure 3-26). The specimens were scanned a second time after notching, and the previously recorded HAZ outlines were then superimposed over the notch location (Figure 3-27).

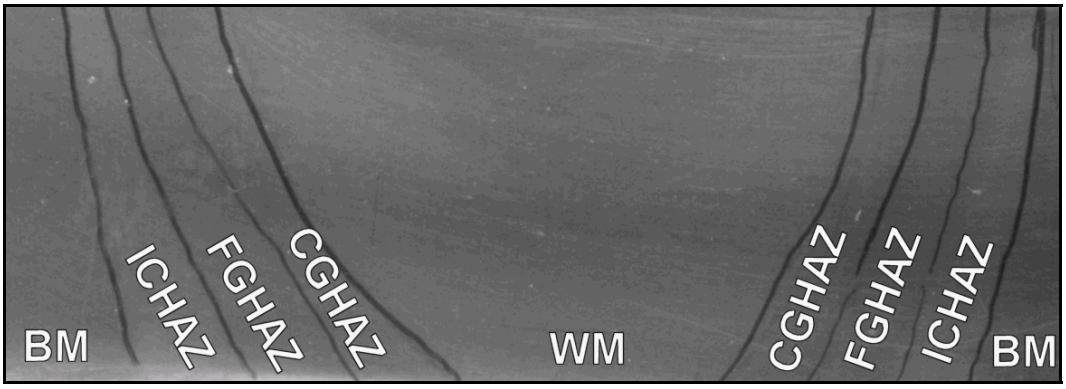

Figure 3-26: CVN WM and HAZ Regions

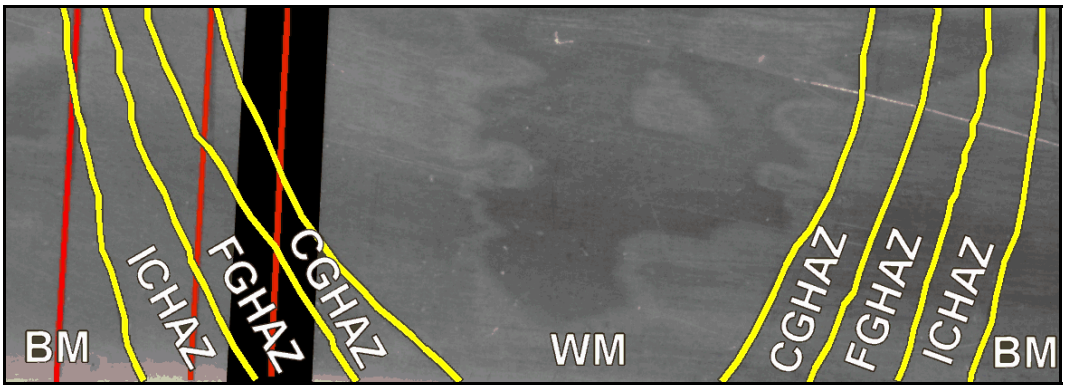

Figure 3-27: Notched CVN WM and HAZ Region[†]

Figure 3-27 demonstrates the notch (the black rectangle), the HAZ boundaries (highlighted in yellow), and the notch centerline location (the vertical red line furthest to the right[‡]). By measuring the lengths along the notch centerline, passing through the various WM and HAZ regions, it was possible to estimate the relative amounts of each region that would initiate fracture during CVN testing. It was expected that as greater portions of the centerline passed through regions of high toughness (i.e., FGHAZ), the CVN fracture energy values should increase. Alternatively, as the centerline length passing through the CGHAZ increases (a

[†] Even though the notch does not appear to run perfectly vertically, that is a result of scanning the specimen digitally. The actual specimen notch was correctly oriented.

[‡] The three red lines, from right to left, represent the three possible notch placement locations: FL, FL+2, and FL+5 respectively.

region of lower notch-toughness), it is expected that the CVN fracture energy value should decrease. The values were measured and averaged for all "FL" specimens for both WC1 and WC2 (refer to Figure 3-28). The error bars in Figure 3-28 represent one standard deviation (which were calculated using the measurements from the three "FL" specimens for each coupon).

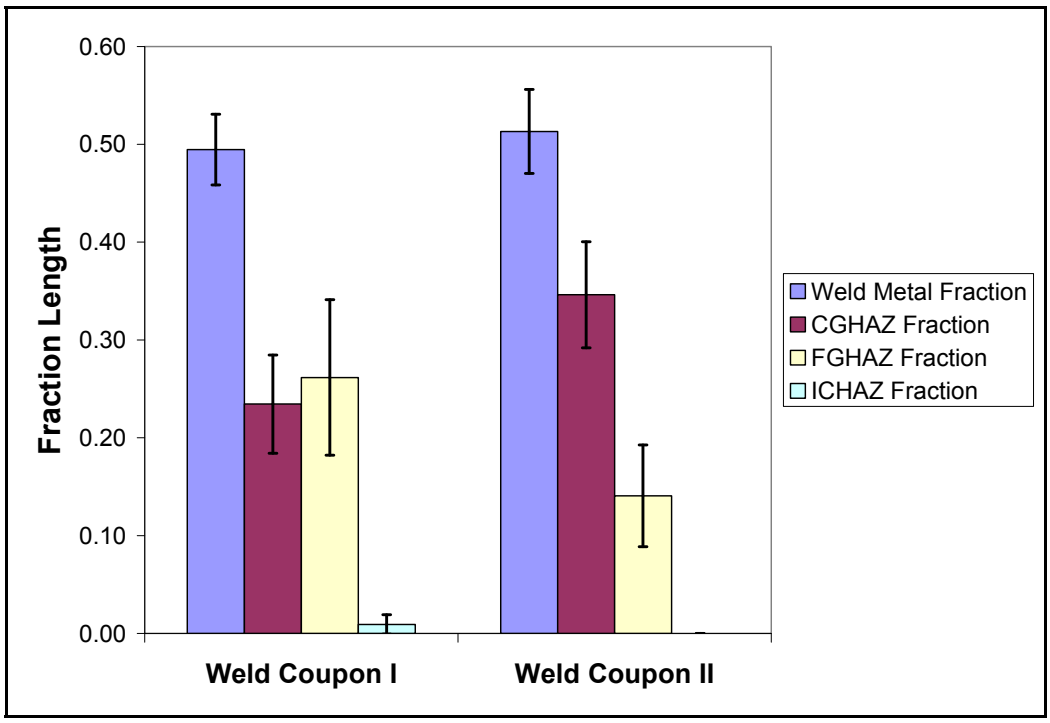

Figure 3-28: Average Notch Centerline Fraction for "FL" CVN Specimens

Both sets of CVN specimens demonstrated comparable WM fractions (as they should), and negligible quantities of ICHAZ material. However, due to the differences in curvature of the WM and HAZ bands, the WC1 and WC2 CVN specimens demonstrated different amounts of CGHAZ and FGHAZ material passing through their notch centerlines. WC1, which achieved higher notch-toughness at the FL location, had less CGHAZ and more FGHAZ passing along the notch centerline when compared with WC2. While the standard deviations in Figure 3-28 are high, the differences in average amounts of CGHAZ and FGHAZ is clear, and the trends confirm that as the amount of CGHAZ material running

along the notch centerline increases (and the amount of FGHAZ decreases) CVN tests achieve poorer results.

By superimposing CVN specimen outlines (with the central vertical line representing the notch, positioned at the FL notch location) onto the cross sections from Figure 3-12 and Figure 3-13, it becomes clear that a greater portion of the CVN test specimen notch for WC1 passes through CGHAZ, compared to the test specimen's notch for WC2, resulting in improved CVN fracture energy values for WC1 (Figure 3-29). However, both WC1 and WC2 demonstrate comparable weld metal cross-section areas, bead widths, and penetration depths. Because they share similar bead widths and penetration depths, their overall fusion line slopes should be similar. Furthermore, their individual HAZ cross-section areas appear to be similar, as are their respective hardness values (Figure 3-17 and Figure 3-18).

However, because of the weld bead shapes, the fusion lines demonstrate different changes in slope at different penetration depths. It is therefore only the fusion line slope directly at the notch that affects the amount of CGHAZ and FGHAZ passing through the two CVN test specimen notches. As a result, there is strong evidence that the geometry of the weld bead has an effect on HAZ CVN fracture energy values. It therefore became necessary to develop a better understanding of the relationships between welding variables and weld bead geometry.

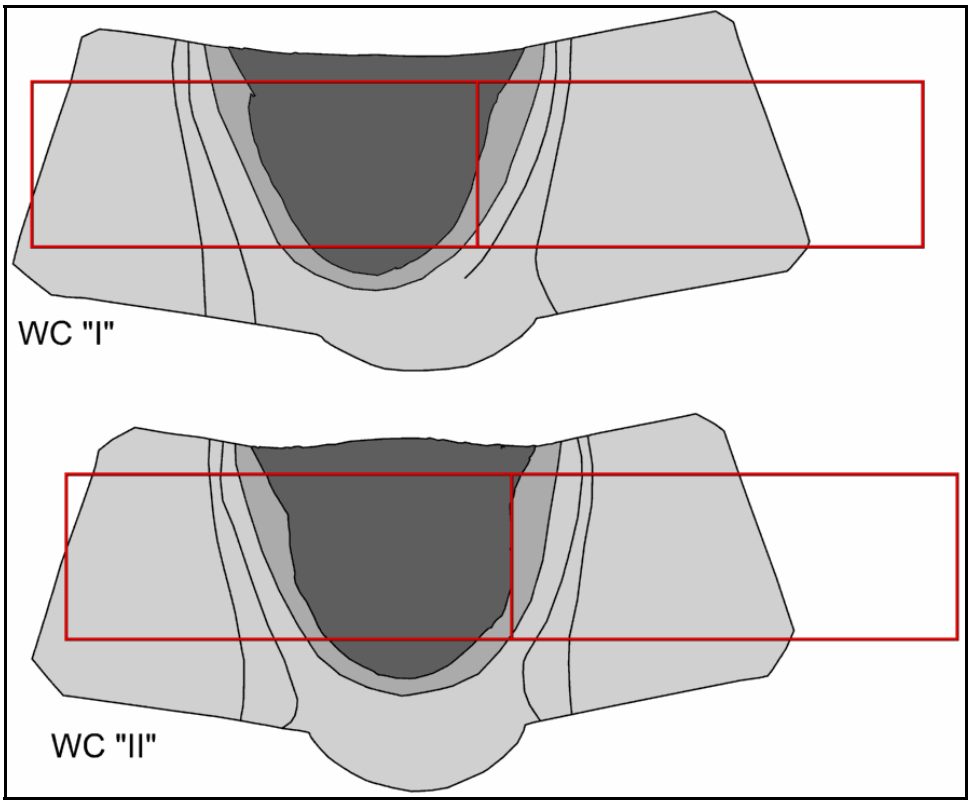

Figure 3-29: CVN Specimen Outlines Superimposed on Weld Coupon Cross-Section Profiles

3.3: Conclusions

Submerged arc welding was used to produce two tandem-arc weld coupons: WC1 and WC2. While both weld coupons were produced using identical total heat inputs, 66% of the heat input from WC1 was supplied as DCEP, whereas only 41% of the WC2 heat input was supplied as DCEP. DCEP is characterized by deeper penetration, whereas DCEN is characterized by reduced penetration but increased deposition. The corresponding weld bead cross-sections indicated a slight increase in WM area in WC2, which appears to correspond to a more convex bead cap (i.e., presumably caused by increased deposition). Meanwhile, WC2 clearly possesses a more vertical fusion line.

Hardness-testing demonstrated comparable HAZ hardness values for both welded coupons (indicating comparable microstructures), and optical metallography further reinforced these results by demonstrating that both coupons possessed

comparable grain sizes and shapes. Throughout the WM and HAZ regions, WC1 displayed higher notch-toughness than WC2. The FL notch location yielded the lowest results for both coupons, making it the focus of additional analysis.

Because WC2 possessed a different bead geometry than WC1, the WC1 FL CVN specimen notch centerlines possessed less CGHAZ material, and more FGHAZ material, than the WC2 FL CVN specimens. As a result, the WC1 test specimens achieved greater CVN fracture energy values. The WM geometry appears to have made a significant contribution to the notch-toughness test results. Subsequent weld beads were therefore required to investigate the relationships between welding parameters and weld bead geometry.

CHAPTER 4: SUPPLEMENTARY BACKGROUND INFORMATION

Based upon the Chapter 3 results, there appears to be a relationship between weld bead geometry and Charpy V-notch (CVN) test results. It was therefore necessary to develop a more in-depth understanding of the effects of welding variables on bead geometry. However, before more welds were performed, additional literature was reviewed to develop a better understanding in the following areas:

- Bead-on-plate (BOP) welding
- The effects of traditional "heat input variables" on bead geometry
- The effects of waveform manipulation on bead geometry
- Welding heat input efficiency

4.1: Bead-on-Plate (BOP) Welding

The previously-investigated bevel welds were resource-intensive, requiring much preparation time and expensive pipe flattening and bevel-machining. The tack and root welds further increased the time required per weld. Bead-on-plate (BOP) welding provides a simpler and faster testing methodology for screening a large number of welding parameters quickly. As such, a series of single-pass BOP welds were performed.

Not only are BOP welds fast and efficient, but they also are an excellent choice from a research standpoint. Simple cross-section analysis provides a quick understanding of the molten bead geometry, including reinforcement height, penetration depth, and bead width (r, p, and w, respectively in Figure 4-1). Understanding the relationships between these values and welding parameters can yield insight when trying to increase penetration (i.e., weld thicker components together with a single pass) or increase deposition (i.e., increase productivity) during bevel welds.

The reinforcement area, penetration area, and total molten area (A_r, A_p, and "A_r + A_p", respectively in Figure 4-1) also can be quickly determined. Due to the complications of accurately measuring true heat input, the total fused volume deposited per length of weld (i.e., the total molten area) is sometimes used as an alternative estimate of heat input [3]. The reinforcement area can be multiplied by travel speed to calculate the volume of metal deposited per second. Not only is the volume deposited per second an indication of productivity, but it also is an indication of wire feed speed and wire melt-off rates.

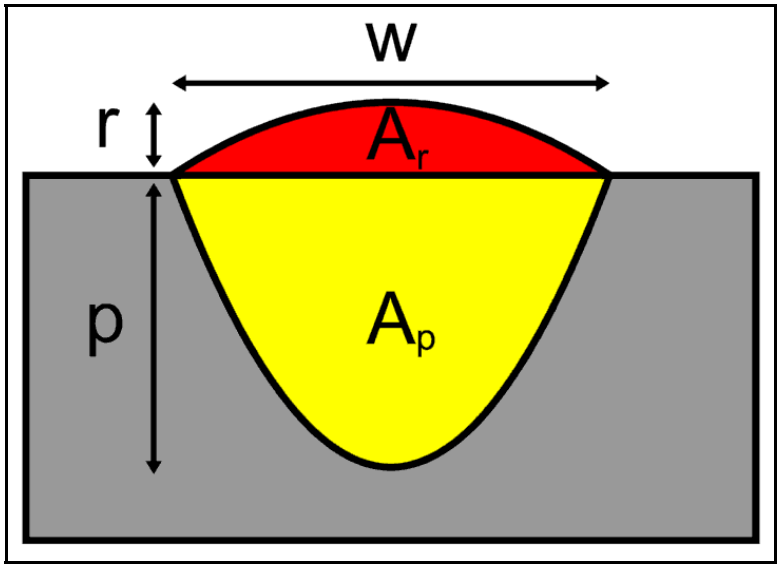

Figure 4-1: Bead-on-Plate Weld Metal Schematic

Finally, by removing additional variables (e.g., tack welding, bevel machining toleration, pipe-flattening), there are fewer sources of bead geometry variation introduced into the welds.

4.2: Traditional "Heat Input" Variables

It was noted in Chapter 2 that heat input is the result of a combination of current, voltage, and travel speed. As heat input increases, bead width, reinforcement height, and penetration depth should all increase. Additionally, while not included in the heat input equation, polarity also strongly influences weld bead characteristics. The following literature review focuses specifically on the effects, and interactions, of welding variables on BOP weld characteristics.

4.2.1 Amperage

From the Section 2.5.1, increasing current should increase the width, penetration, and reinforcement of the weld bead (Figure 4-2) [55, 37].

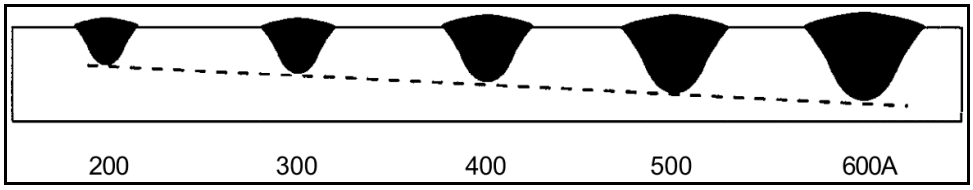

Figure 4-2: The Effect of Varying Current on SAW BOP Weld Cross Sections [55 - Pg. 74]

Melting rate (mass per unit time) is proportional to current. Therefore, reinforcement area is proportional to the current, divided by the travel speed. Furthermore, as current increases, more heat is supplied to the weld, and penetration increases accordingly [24].

As current is increased, bead width increases due to an increased deposition rate. As the current becomes greater (e.g., higher than 700 A), subsequent increases in current are accompanied by significantly greater penetration rates, and reductions in the rate of increase in weld width [14]. Therefore, at higher current values, penetration increases more than bead width. It has been postulated that if the current were to reach a critical value, additional increases would in fact reduce

bead width [14]. An opposing view is that a high current will produce a higher and narrower weld, with no critical current being required [55].

Based upon the geometry, increasing current will also increase weld bead dilution (i.e., the ratio of base metal melted to that of the total molten area) [24]. Such considerations are beneficial when determining welding parameters for either bevel weld root or fill passes.

4.2.2 Voltage

By controlling the arc length (Figure 4-3), the voltage can affect the bead width and deposition rates [56, 20].

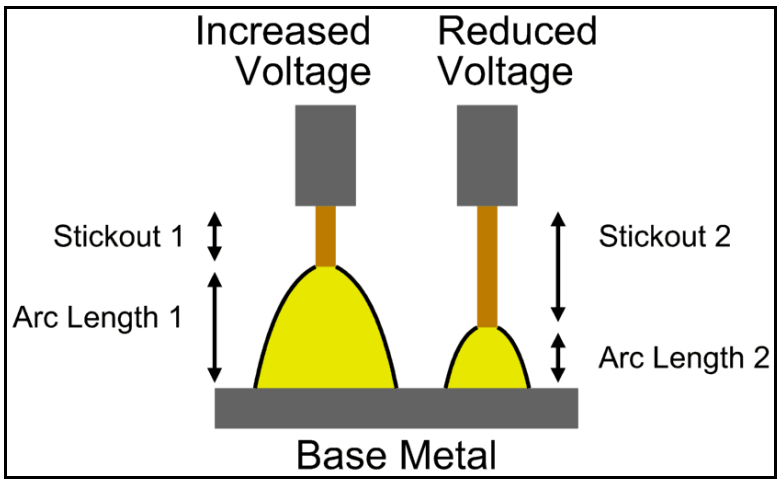

Figure 4-3: The Effects of Voltage on Stickout and Arc Length

A higher voltage is capable of sustaining a greater arc length, whereas a lower voltage will produce a stable arc only if it is shorter. With a constant-current (CC) power source, the wire feed speed (WFS) varies to hold both current and voltage constant. Therefore, a change in voltage will indirectly control both the arc length and the length of electrode between the arc and the contact tip (a.k.a. the "stickout") [55]. Deposition rate is best measured as electrode unit length

deposited per unit time (i.e., WFS). When a CC power source is used, WFS is variable. However, measuring the reinforcement cross-section areas for BOP welds can be a good estimate of actual deposition rates.

As voltage is reduced, the arc length will decrease, which in turn increases the electrode stick-out length (Figure 4-3, right). The arc width (and subsequently the bead width) is reduced as well [55]. The electrode between the contact tip and the arc is then heated resistively, effectively preheating the electrode. As a result, without changing the welding current, the electrode deposition rates will increase [56]. In extreme cases, the electrode melting rate will increase more than 500% , using the same current while increasing the electrode extension beyond the contact tip [20]. In combination with the reduced bead width associated with lower voltage, a significant increase in stickout will increase the reinforcement height considerably [27, 56].

When the voltage is increased, the arc length increases. Further voltage increases will reduce the arc forces until penetration begins to decrease [22, 24, 55].

4.2.3 Travel Speed

By manipulating the travel speed, the heat input is either increased or decreased significantly. Because heat input increases bead width, penetration depth, and reinforcement height, an increase in travel speed should simply reduce all three measurements (Figure 4-4). However, this generalization is not always accurate [55].

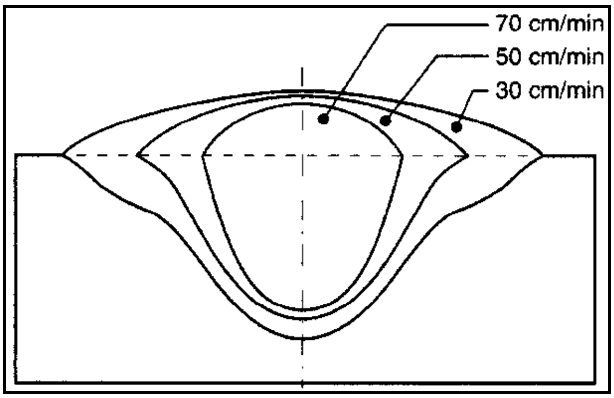

Figure 4-4: The Effect of Varying Travel Speed on SAW BOP Weld Cross Sections [55]

When the travel speed is quite low, the molten metal can pool ahead of the arc, insulating the unmelted base material. As a result, base metal melting rates decrease (effectively reducing weld bead dilution) and penetration is reduced [27, 55]. Bead penetration reduction becomes particularly noticeable at lower welding currents, due to reduced arc pressure, which normally would be able to help displace molten metal from the weld pool [14]. As travel speed is reduced further, the deposited metal will pool on the base metal's surface and spread out, increasing bead width. A shallow layer of the base metal in contact with the deposited molten puddle will melt, whereas penetration will be deeper at the bead centerline. Such 'T-shaped' profile is susceptible to thermal cracking [37, 55]. Because increases to voltage widen the arc, a greater voltage can further promote the formation of 'T-shaped' profile [37].

Conversely, as travel speed is increased, the weld bead dilution rate increases, the bead narrows, and penetration increases. As the speed is increased further, the bead narrows further, and the total fused material cross-section will decrease [22], even though melting rate should remain unaffected [24]. At even greater travel speeds, narrow weld beads are produced with low penetration [55].

4.2.4 Polarity

The Chapter 2 literature survey already established how and why bead width, bead penetration, and electrode deposition are affected by polarity changes in a consumable-electrode welding process: a shift from DCEN to AC-SQ to DCEP should increase penetration, increase bead width, and decrease deposition and reinforcement area (Figure 4-5). However, further investigation is required to better understand the interactions of weld parameter changes on polarity changes.

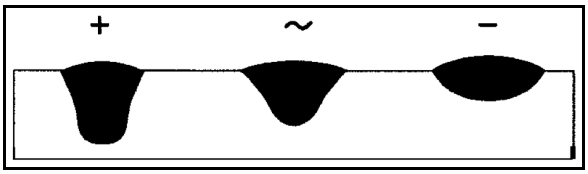

Figure 4-5: The Effect of Varying Polarity (DCEP left, AC middle, DCEN right) on SAW BOP Weld Cross Sections [55– Pg. 74]

A shift from DCEP to DCEN polarity increases deposition rates. This relationship becomes amplified as current is increased [14]. Such a current-dependency of the polarity-deposition rate relationship could conceivably be a source of the wide range of deposition rate changes reported in the literature [55, 26]. There has not been a similar reported connection between polarity, penetration, and voltage.

Gupta et al. suspected that at greater currents, the amplification of the polarity-deposition relationship is caused by more heating at the electrode. Based upon this reasoning, it seems logical that the polarity-penetration relationship also should be amplified at greater currents. In other words, as current is increased, DCEP polarity should achieve increasingly larger penetration areas in relation to DCEN polarity. Additionally, above 500 A, the increased arc plasma pressure is able to displace molten metal from the weld pool to expose base metal directly to the arc, thereby increasing the penetration [14].

With the change of polarity either increasing the reinforcement area at the expense of penetration area, or vice versa, it seems reasonable that polarity should not affect the total molten area. Work by Chandel et al. confirms this, except when current becomes very high (presumably greater than 700 A). In such instances, a shift from DCEN to DCEP will cause an increase in penetration that exceeds the reduction in deposition rate. Therefore, there is a net increase in molten area [7].

Finally, the shift from DCEP to DCEN increases bead reinforcement height. However, as the current increases, the reinforcement height difference between DCEP and DCEN increases. This is presumably because as current increases, the effect of polarity on bead width remains constant, while the effect of polarity on deposition increases [14].

4.2.5 Tandem Electrode Welding

In the previous experiments, tandem welds were performed, and the overall heat input was treated as a single value. However, careful consideration must be made regarding the interaction of the individual welding variables with tandem welds. A generalization that appears to be accurate is that the lead arc establishes penetration depth, and the trail arc establishes deposition and overall bead appearance (Figure 4-6). As a result, it is typical for the lead arc to use welding parameters that promote deeper penetration (e.g., increased current, DCEP polarity), whereas the trail arc's parameters should promote high deposition (e.g. DCEN polarity).

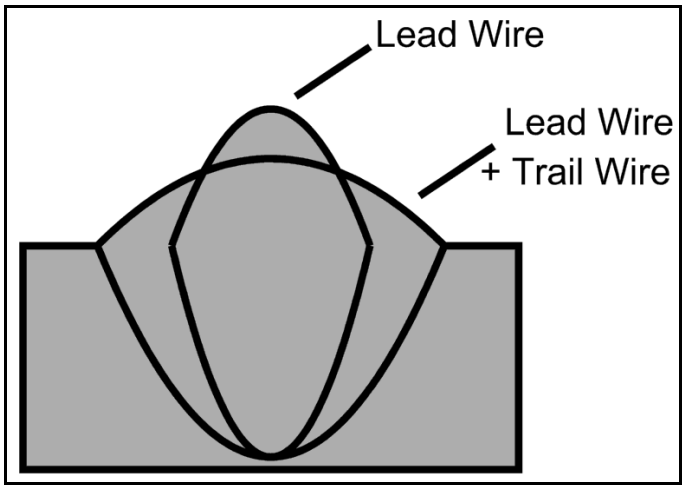

Figure 4-6: Function of Lead and Trail Wires in Multipower Welding (Adapted from Kubli & Shrubsall [33])

At higher travel speeds, a single electrode arc may run ahead of the molten pool, causing immediate solidification behind it. Newly deposited molten metal is then pushed backwards over the solidified bead, resulting in non-uniform solidification and a poor bead appearance. If a tandem arc setup is used instead, and the polarity (and phase offset) is set to attract the two arcs, the trail arc will be directed towards the welding direction. The trail arc's force will then push newly deposited molten metal forward, preventing the arc from running ahead of the welding pool. A superior bead appearance should result [22].

Based upon the relationships of the lead and trail arcs, it is therefore critical to properly adjust the lead and trail currents and voltages with respect to each other. If the trail arc voltage is significantly lower than the lead arc voltage, the trail arc will be too narrow. Accordingly, molten metal from the lead arc may be pushed backwards over the bead around the narrower arc, resulting in poor bead appearance. Alternatively, if the trail arc voltage is very high, the arc length will increase too much, and its arc forces will be inadequate to push the lead arc's molten metal forward. Accordingly, Ito et al. recommend that the trail voltage be 0 V to 6 V greater than that of the lead arc [22].

If the trail arc's current is too low, arc forces will once again be too low to push the lead arc's molten metal forward. However, if the trail arc's current is too great, the molten pool will be disturbed, and there will be forward overlapping of the bead [22]. Due to these concerns, Ito et al. recommend that the trail current be 0 A to 200 A less than the lead arc current, whereas Kubli et al. recommend a trail arc roughly 85% that of the lead arc [22, 33]. The above recommendations are for tandem welds, in which the lead and trail electrodes have the same diameter.

When two tandem electrodes supply current using opposite polarity, their arcs will repel each other; if the electrode polarities are in phase, their arcs will be attracted (Figure 4-7).

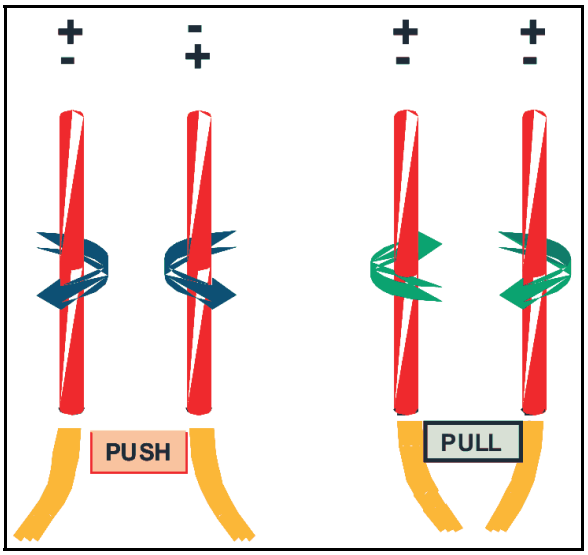

Figure 4-7: Tandem Electrodes with Opposite Polarity (left) & Same Polarity (right) [39]

When two tandem electrodes are both using AC-SQ, excessive attraction and repulsion (Figure 4-8a) can be detrimental to the weld. If the two AC waveforms are offset (Figure 4-8b), excessive attraction or repulsion can be avoided. Increased frequency also may reduce issues from excessive arc attraction or repulsion. The actual effects of phase offset on weld bead geometry are not well understood, and may be worth consideration for future work.

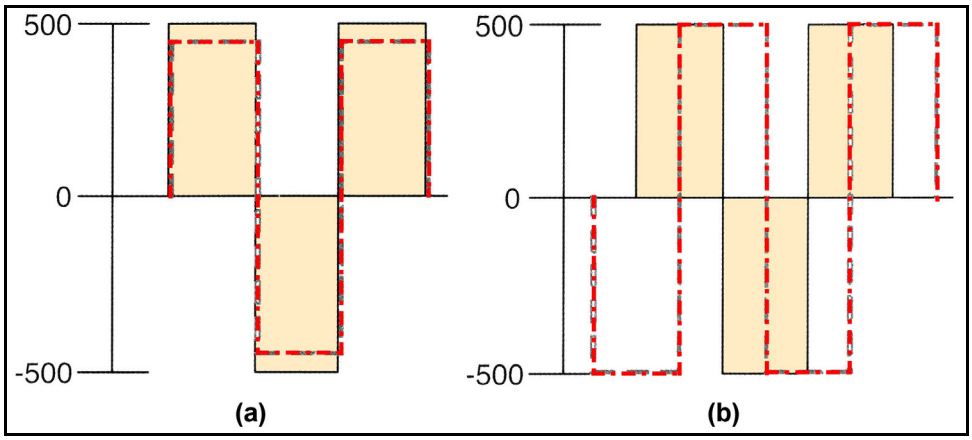

Figure 4-8: Phase Offset for Multiple AC-SQ Electrodes (Adapted from [39])

4.3: Waveform Manipulation Variables

As was previously mentioned, the Lincoln Electric Power Wave AC/DC 1000 is capable of supplying DCEN, DCEP, and AC-SQ current, while also allowing for AC-SQ current waveform manipulation. The following section of the literature review focuses on the effects of frequency, balance, and offset on BOP weld geometry.

4.3.1 Balance

As was previously discussed, balance refers to the percentage of time that each complete waveform cycle is held at DCEP polarity (Figure 4-9). By extension, DCEP can be considered to have 100% balance, and DCEN can be considered to have 0% balance.

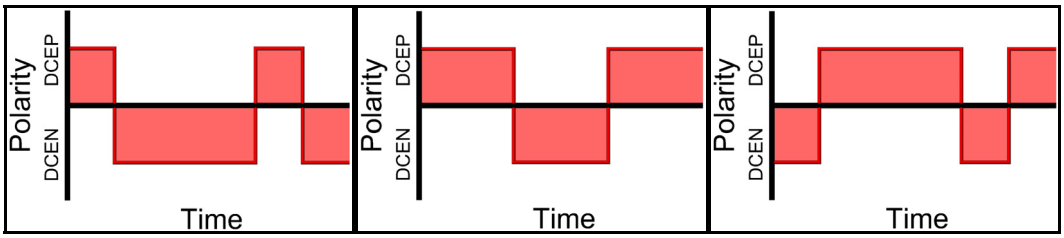

Figure 4-9: Current Waveform with 25%, 50%, and 75% Balance (left to right)

Balance control can be treated as manipulating polarity across the full spectrum (instead of just selecting the extremes, i.e., DCEN and DCEP). Therefore, increasing balance is expected to produce the same trends as shifting polarity from DCEN to DCEP:

- Penetration will increase (especially at higher welding current values).
- Deposition will decrease (especially at higher welding current values).
- Bead width should increase.
- Reinforcement height should decrease.

The second point, that deposition will decrease, has already been verified experimentally by the previous bevel welds.

4.3.2 Offset

The offset refers to the manipulation of DCEP and DCEN current amplitudes (Figure 4-10). By default, the offset is set at 0%, in which case the offset has no effect on the weld. If the offset is set to a positive value (e.g., +10%), the DCEP amplitude will increase by that percentage and the DCEN amplitude will decrease by that percentage. Alternatively, if the offset is set to a negative value, the DCEP will decrease by 10%, and the DCEN amplitude will increase by that percentage.

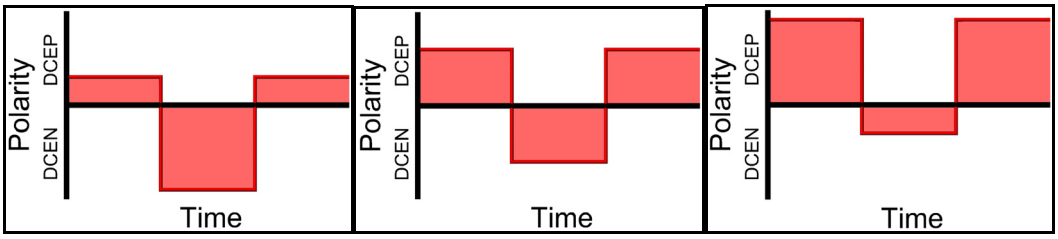

Figure 4-10: Current Waveform with -50% Offset, 0% Offset, and +50% Offset (left to right)

Based upon the previously established relationships between current, polarity, and bead shape, a few inferences can be made regarding the expected results of increasing offset:

- Penetration should increase.
- Deposition should decrease.
- Bead width increases with DCEP polarity, but increases only slightly with current. However, because the effets of polarity are amplified by increased current, it is reasonable that there could be a slight bead width increase. This would result also if the offset current increase is accompanied by a voltage increase.

Additionally, because balance increases are related to current amplitude, offset should produce interaction effects as well. However, at this time, no literature could be found that clearly illustrated the effect(s) of varying offset on weld bead geometry.

4.3.3 Frequency

AC-SQ frequency refers to the number of polarity shifts per second. Literature has indicated that increased frequency can improve arc stability (especially with low welding voltage, and at increased travel speeds for a given electrode diameter), reduce bead porosity, and improve bead appearance [11, 34]. While it has been noted that greater frequency reduces bead cross-section variations along

the weld bead [34], there is little information regarding the effects of current frequency on bead cross-section geometry.

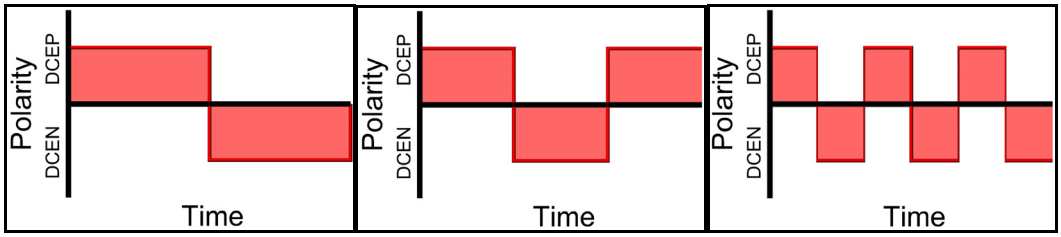

Figure 4-11: Current Waveform with Low, Medium, and High frequency (left to right)

In one study, using a balanced current waveform, beads were performed with frequency ranging from 20 to 240 Hz. It was noted that for a balanced 50% DCEP AC waveform, the frequency will not affect the weld's fusion characteristics [57]. However, it also was noted that additional work would be necessary to determine the effect of frequency on welds produced using unbalanced current waveforms [57].

4.4: Summary of Welding Variable Effects on Bead Geometry

The expected effects of welding variables on weld bead geometry is summarized in Table 4-1. Depending upon the combination of variables, an increase in travel speed could increase deposition (if the increase allowed for the electrode arc to move in front of the molten weld puddle), whereas a further increase could reduce penetration (by moving the arc too quickly past the base metal to allow for deep penetration). Presently, there was insufficient literature available to allow for a strong understanding of the effects of squarewave alternating current frequency and offset on weld bead geometry.

For tandem welds, the welding parameters of the two arcs should be set such that penetration is controlled by the lead arc, and bead width is controlled by the trail

arc. Both arcs contribute to the the reinforcement area (i.e., the deposited weld metal).

As penetration area increases, and bead width decreases, a steeper overall fusion line slope is expected, though the effects on the localized fusion line (where a CVN test specimen notch would be located) could vary based upon the fusion line profile.

Table 4-1: Expected Effects of Welding Variable Changes on Bead Geometry

Weld Parameter	Penetration Area	Reinforcement Area	Width
Increase in **Current**	+	+	+
Increase in **Voltage**	-	-	+
Increase in **Travel Speed**	variable	-	-
Increase in **Heat Input**	+	+	+
Shift from **DCEN to AC to DCEP**	+	-	+
Increase in **Frequency**	unknown	unknown	unknown
Inrease in **Balance**	+	-	+
Increase in **Offset**	unknown	unknown	unknown

CHAPTER 5: SAW WELDING PARAMETERS AND BEAD-ON-PLATE WELD GEOMETRY

The results from Chapter 3 indicate that the weld metal (WM) and heat affected zone (HAZ) geometries have an effect on notch-toughness test results. As a fusion line slope decreases, the amount of coarse grain heat affected zone (CGHAZ) passing through a Charpy V-notch (CVN) test specimen notch centerline is expected to decrease. As a greater amount of CGHAZ passes through the CVN specimen notch centerline, the CVN fracture energy should decrease. It, therefore, was important to investigate the effects many welding parameters have on weld bead geometry.

Bead-on-plate (BOP) weld geometry trends were compared with various input parameters (including voltage, current, travel speed, polarity, frequency, offset, balance, and number of electrodes). The power source included a software package, Command Center version 1.12.0.729, which was used primarily to record wire feed speed for each weld.

Microstructure analysis, hardness testing, and mechanical testing were not pursued during initial analysis of the BOP welds. Because the chemistry of X70 is close to that of X80 and the behaviour of both steels is likely to be similar in a bead on plate test [15]. X70 steel was available as a flat plate, thus requiring no additional machining or flattening. The X70 material was thinner (11.1 mm, 0.438 in.) than the previously investigated X80 material (16.2 mm, 0.638 in.), but it was not expected that such a variation would affect the general BOP cross-section geometry trends.

Finally, because X70 possesses slightly different alloying elements than X80, the BM, WM, and HAZ microstructures and secondary phases will differ also. However, such variations are quite minor, and X70 should melt in a similar manner and rate as X80, making it a suitable alternative for a macroscopic investigation on the interaction between the weld metal and the base metal.

5.1: Experimental Procedure

5.1.1 Base Material

All weld coupons were extracted from a 11.125 mm (0.438 in.) thick X70 steel plate (heat 593021A09). Its nominal chemical composition is listed in Table 5-1. A band saw was used to cut the plate into weld coupons, 330 mm wide (13 in.), and approximately 230 mm long (9 in.).

Table 5-1: Chemical Composition (Weight %) of X70 Steel (Plate, Heat 593021A09)

C	Mn	S	Si	Al	Mo	Nb	N	Ti
0.03	1.5	0.002	0.2	0.05	0.2	0.07	0.008	0.015

5.1.2 Welding Process and Setup

BOP welds were performed parallel to the 230 mm axis, corresponding to the original steel's longitudinal to the rolling axis (LRA) orientation. Six welds were performed on each weld coupon. However, the coupons were cooled below 38°C (100°F) between welds to avoid the introduction of preheating effects into subsequent beads. A contact thermocouple was used to measure the top of the weld coupon, at the starting location of the next weld bead. Beads were spaced 45 mm (1.75 in.) apart centre-to-centre, with the two outermost beads being spaced approximately 50 mm (2 in.) from the edges of the weld coupon. A sectioned schematic of a BOP weld coupon is illustrated in Figure 5-1.

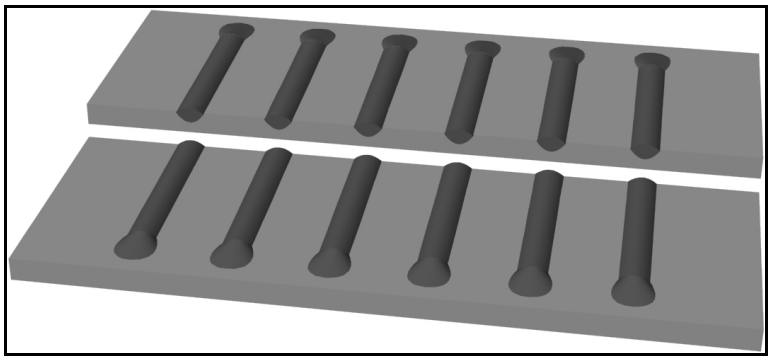

Figure 5-1: Schematic of a Sectioned Bead-on-Plate Weld Coupon with Weld Beads

BOP welding parameters have been classified as either "heat input variables" or "waveform manipulation variables." Heat input variables include the traditional variables used to calculate heat input (welding current, voltage, and travel speed), as well as polarity, whose effects on heat input have been discussed earlier in Sections 2.5 and 4.2. Waveform manipulation variables are those used to manipulate the weld current waveform, consisting of frequency, balance, and offset. All BOP welds were separated into four groups based upon the number of electrodes used, and the type of variables manipulated (Table 5-2). Each group was then investigated separately before final conclusions were drawn.

Table 5-2: BOP Weld Variable Groups

	Single Electrode	Tandem Electrode
Heat Input Variables	Group 1	Group 2
Waveform Manipulation Variables	Group 3	Group 4

Welding was performed at EVRAZ Inc. NA using two paralleled Lincoln Electric Power Wave® AC/DC 1000™ power sources. For single-wire welds, only the power source for the lead electrode was used, while both power sources were required for tandem welds. Constant current (CC) was used for all BOP welds. A schematic of the welding system is shown in Figure 2-12, and the setup of

welding torch angles and positions remain unchanged from previous studies (Figure 3-5). The same consumables from the prior bevel weld investigation (Chapter 3) were used for the BOP welds: 3.2 mm (0.125 in.) diameter S3NiCrMo.2.5 electrode with a basic flux.

5.1.3 Group 1 Welding Variables

The Group 1 welds were performed to confirm the effects of primary variables on single-electrode bead cross-sections. Weld coupon parameter combinations are listed in Table 5-3 through Table 5-5. Table 5-3 lists the welds produced using alternating current, while Table 5-4 and Table 5-5 list the welds produced using DCEP and DCEN polarity, respectively. Two additional welds (Table 5-6) were performed to produce idealized top-bead surfaces, after which neither weld underwent additional analysis. Because the initial scope of the investigation focused heavily on heat input, weld travel speeds were manipulated to control the heat input, while accommodating differences in voltage and current. The heat input values were set as close as possible to 0.5 kJ/mm, 1.5 kJ/mm, or 2.5 kJ/mm. The Group 1 welds were produced using default settings for frequency, balance, and offset (i.e., 60 Hz, 50%, and 0% respectively for AC-SQ; the settings are not applicable for direct current).

Table 5-3: Group 1 Single-Electrode AC Square-Wave Heat Input Welding Variables

Weld Bead	Polarity	Current (Amps)	Voltage (Volts)	Travel Speed (mm/s)	Heat Input (kJ/mm)
1	AC-SQ	400	28	22.4	0.50
2				7.4	1.51
3				4.4	2.52
4			32	25.2	0.51
5				8.5	1.51
6				5.1	2.52
7		550	28	30.9	0.50
8				10.6	1.46
9				6.2	2.47
10			32	34.3	0.51
11				11.9	1.48
12				7.0	2.52
13		700	28	39.4	0.50
14				13.5	1.45
15				7.8	2.50
16			32	44.9	0.50
17				14.8	1.51
18				8.9	2.52

Table 5-4: Group 1 Single Electrode DCEP Heat Input Welding Variables

Weld Bead	Polarity	Current (Amps)	Voltage (Volts)	Travel Speed (mm/s)	Heat Input (kJ/mm)
19	DCEP	400	28	22.4	0.50
20				4.4	2.52
21			32	25.2	0.51
22				5.1	2.52
23		700	28	39.4	0.50
24				7.8	2.50
25			32	44.9	0.50
26				8.9	2.52

Table 5-5: Group 1 Single Electrode DCEN Heat Input Welding Variables

Weld Bead	Polarity	Current (Amps)	Voltage (Volts)	Travel Speed (mm/s)	Heat Input (kJ/mm)
27	DCEN	400	28	22.4	0.50
28				4.4	2.52
29			32	25.2	0.51
30				5.1	2.52
31		700	28	39.4	0.50
32				7.8	2.50
33			32	44.9	0.50
34				8.9	2.52

Table 5-6: Additional Group 1 Single Electrode AC Square-Wave Heat Input Welding Variables

Weld Bead	Polarity	Current (Amps)	Voltage (Volts)	Travel Speed (mm/s)	Heat Input (kJ/mm)
35	AC-SQ	450	30	6.8	1.99
36		500	30	7.6	1.97

5.1.4 Group 2 Welding Variables

The Group 2 welds were performed to study the effects of primary variables on tandem weld bead cross-sections. Like the Group 1 welds, all waveform manipulation variables were left at their default settings. Weld coupon parameter combinations are listed in Table 5-7 through Table 5-10.

The four tables summarize the weld coupon parameters produced using AC-SQ/AC-SQ, AC-SQ/DCEN, DCEP/AC-SQ, and DCEP/DCEN lead and trail polarities respectively. To reduce the number of welds required, only one heat input (1.5 kJ/mm) and two current values (550 A and 632 A) were used. A minor increase in the voltage range (the maximum voltage was changed to 32.2 V instead of 32.0 V) was introduced to improve differentiation between the two voltage levels. Travel speed was varied between 20 and 25 mm/s to maintain heat input. Phase offset was left at a default 90° to help minimize interactions between two AC waveforms when applicable.

The primary objective of performing the Group 2 welds was to determine the individual effects of lead and trail electrode polarities. Investigating all possible combinations of wire polarity would have required too many welds. Following practices discussed in Section 4.2.5 (in which greater penetration is required from the lead arc and greater deposition is required from the trail arc), the lead electrode polarity was limited to either AC-SQ or DCEP and the trail electrode was limited to AC-SQ or DCEN. The Group 2 welds also were produced using default settings for frequency, balance, and offset.

Table 5-7: Group 2 AC/AC Tandem Electrode Heat Input Welding Variables

Weld Bead	LEAD ELECTRODE			TRAIL ELECTRODE			Travel Speed (mm/s)	Heat Input (kJ/mm)	Phase Offset (Deg.)
	Polarity	Current (Amps)	Voltage (Volts)	Polarity	Current (Amps)	Voltage (Volts)			
37	AC-SQ	550	28	AC-SQ	550	28	20.5	1.50	90
38		632	28		550	28	22.0	1.50	
39		550	28		632	28			
40		550	32.2		550	28			
41		550	28		550	32.2			
42		632	32.2		550	28	23.7	1.51	
43		550	28		632	32.2			
44		632	28		550	32.2		1.49	
45		550	32.2		632	28			

Table 5-8: Group 2 AC/DC- Tandem Electrode Heat Input Welding Variables

Weld Bead	LEAD ELECTRODE			TRAIL ELECTRODE			Travel Speed (mm/s)	Heat Input (kJ/mm)	Phase Offset (Deg.)
	Polarity	Current (Amps)	Voltage (Volts)	Polarity	Current (Amps)	Voltage (Volts)			
46	AC-SQ	550	28	DCEN	550	28	20.5	1.50	N/A
47		632	28		550	28	22.0	1.50	
48		550	28		632	28			
49		550	32.2		550	28			
50		550	28		550	32.2			
51		632	32.2		550	28	23.7	1.51	
52		550	28		632	32.2			
53		632	28		550	32.2		1.49	
54		550	32.2		632	28			

Table 5-9: Group 2 DC+/AC Tandem Electrode Heat Input Welding Variables

Weld Bead	LEAD ELECTRODE			TRAIL ELECTRODE			Travel Speed (mm/s)	Heat Input (kJ/mm)	Phase Offset (Deg.)
	Polarity	Current (Amps)	Voltage (Volts)	Polarity	Current (Amps)	Voltage (Volts)			
55	DCEP	550	28	AC-SQ	550	28	20.5	1.50	N/A
56		632	28		550	28	22.0	1.50	
57		550	28		632	28			
58		550	32.2		550	28			
59		550	28		550	32.2			
60		632	32.2		550	28	23.7	1.51	
61		550	28		632	32.2			
62		632	28		550	32.2		1.49	
63		550	32.2		632	28			

Table 5-10: Group 2 DC+/DC- Tandem Electrode Heat Input Welding Variables

Weld Bead	LEAD ELECTRODE			TRAIL ELECTRODE			Travel Speed (mm/s)	Heat Input (kJ/mm)	Phase Offset (Deg.)
	Polarity	Current (Amps)	Voltage (Volts)	Polarity	Current (Amps)	Voltage (Volts)			
64	DCEP	550	28	DCEN	550	28	20.5	1.50	N/A
65		632	28		550	28	22.0	1.50	
66		550	28		632	28			
67		550	32.2		550	28			
68		550	28		550	32.2			
69		632	32.2		550	28	23.7	1.51	
70		550	28		632	32.2			
71		632	28		550	32.2		1.49	
72		550	32.2		632	28			

5.1.5 Group 3 Welding Variables

The Group 3 welds were performed using a single-electrode welding process, but all primary welding parameters were held constant (550 A current, 28 V voltage, 1.46 kJ/mm heat input, using an AC square-wave polarity and a 10.6 mm/s travel speed). Table 5-11 lists the Group 3 welds, which were produced by varying frequency (30, 60, and 90 Hz), balance (25%, 50%, and 75%), and offset (-15%, 0%, and +15%). All possible waveform variable combinations were tested.

Table 5-11: Group 3 Single-Electrode Waveform Welding Variables

Weld Bead	Polarity	Frequency (Hz)	Balance (%)	Offset (%)
73	AC-SQ	60	50	0
74				15
75				-15
76			75	0
77				15
78				-15
79			25	0
80				15
81				-15
82		30	50	0
83				15
84				-15
85			75	0
86				15
87				-15
88			25	0
89				15
90				-15
91		90	50	0
92				15
93				-15
94			75	0
95				15
96				-15
97			25	0
98				15
99				-15

It was hoped that by performing the welds in Table 5-11, the effects of frequency, polarity, and offset on single-electrode weld bead cross-section profiles would be determined.

5.1.6 Group 4 Welding Variables

The Group 4 welds were performed using a tandem-electrode welding process, with all primary welding parameters held constant (550 A lead and trail current, 28 V lead and trail voltage, and 1.5 kJ/mm overall heat input, using a DCEP lead polarity and an AC-SQ trail polarity with a 20.6 mm/s travel speed). Table 5-12 lists the Group 4 welds, which were produced by varying trail frequency (30, 60,

and 90 Hz), balance (25%, 50%, and 75%), and offset (-15% and 0%). Because the use of a positive offset for the trail arc would essentially induce a greater current amplitude trailing the lead arc (which is not consistent with the Group 2 welds), positive offset was not investigated.

Table 5-12: Group 4 Tandem Electrode Waveform Welding Variables

Weld Bead	Lead Polarity	Trail Polarity	Trail Frequency (Hz)	Trail Balance (%)	Trail Offset (%)
102	DCEP	AC-SQ	60	50	-15
103				75	0
105					-15
106				25	0
108					-15
109			30	50	0
111					-15
112				75	0
114					-15
115				25	0
117					-15
118			90	50	0
120					-15
121				75	0
123					-15
124				25	0
126					-15

5.1.7 Sample Preparation

A typical weld coupon is illustrated in Figure 5-2. Cross-section specimens were removed from the weld coupons, approximately midway along the welding length. Samples were ground to a 600 grit finish, and etched with a 4% nitric acid solution. Weld beads (running along the outside perimeter above the plate top surface, and along the fusion line beneath the plate surface) were scanned, outlined using a Jasc PSP version 7.04, and measured using a CAD program (Figure 5-3). After the CAD images were scaled to proper dimensions, linear distances (i.e., bead width, reinforcement, and penetration), areas, and aspect ratios were measured.

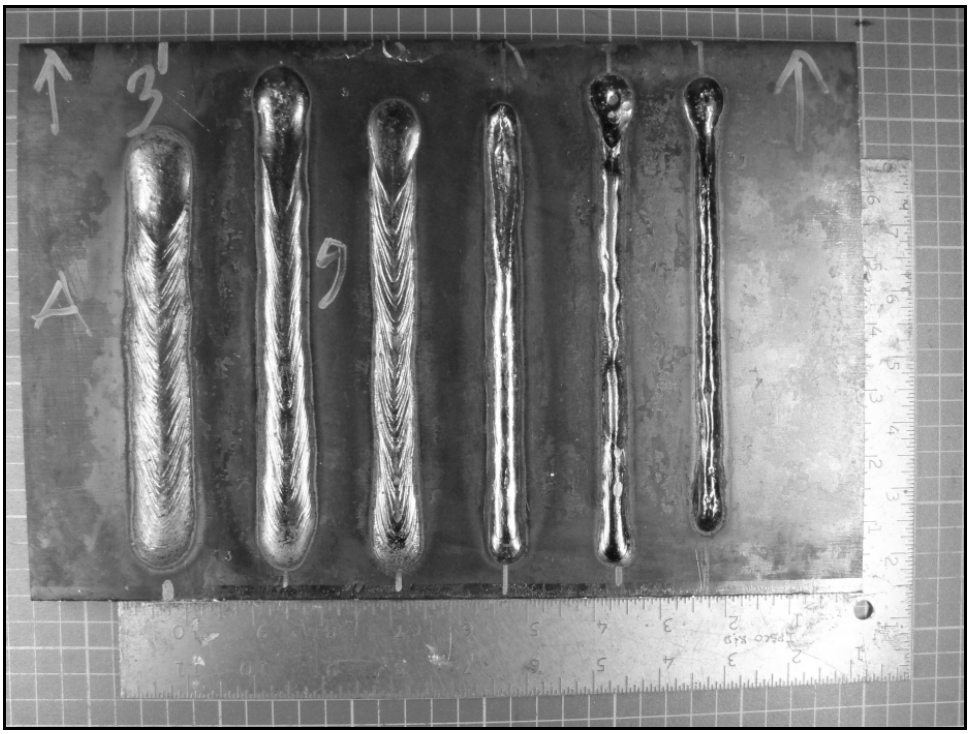

Figure 5-2: Typical Weld Coupon Displaying Six Bead-on-Plate Welds

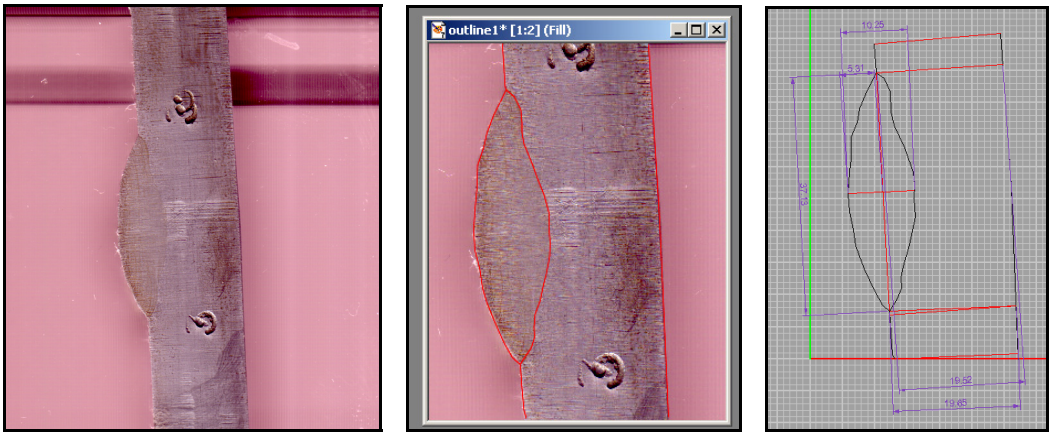

Figure 5-3: Etched Macro-Specimen (Left), Digitally-Outlined (Centre), and Measured (Right)

5.1.8 Quality Assurance

Over 150 BOP welds were performed, but not all of them were acceptable for subsequent analysis. The most prevalent issue was bead consistency. Some weld beads appeared to possess constant widths as a function of welding distance (e.g.,

the left weld bead in Figure 5-4), while others demonstrated considerable bead width variation along the welding direction (e.g., the right weld bead in Figure 5-4). When bead widths varied considerably, so did the reinforcement heights. If width and reinforcement height vary significantly, it is reasonable to expect that penetration depth would vary too, though future work would be required to confirm penetration variation.

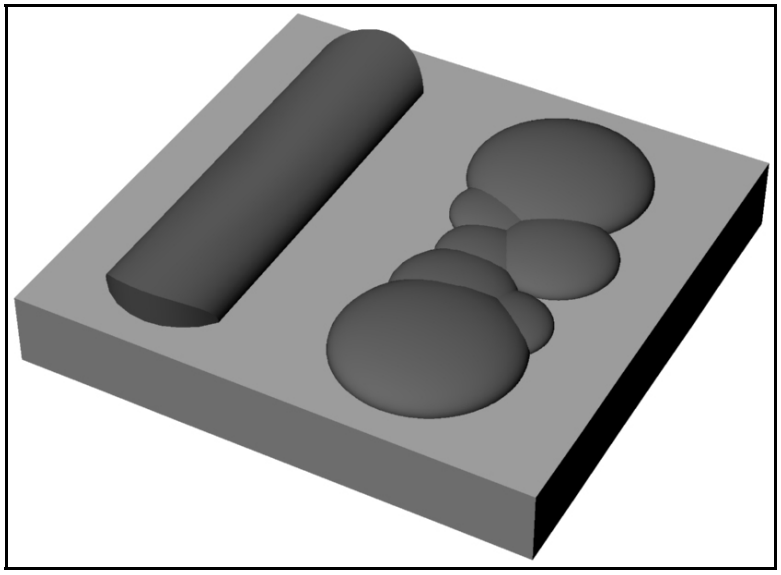

Figure 5-4: Stable (left) and Unstable (right) Bead Profiles

When two specimens are removed from each of the weld beads illustrated in Figure 5-4, their cross-sections are very different as illustrated in Figure 5-5.

Beads with inconsistent cross-section profiles would be difficult to analyze accurately. It was therefore crucial to first determine if a welding bead shape could be considered "stable" or "unstable." Qualitative sorting was performed first. As an example, weld coupons 35 and 36 (Figure 5-6 and Figure 5-7 respectively) demonstrated relatively uniform bead width consistency as a function of distance along the weld (and hence were considered to possess good bead width consistency). Weld coupons 25 and 33 (Figure 5-8 and Figure 5-9 respectively) demonstrated poor bead width consistency, whereas coupons 4 and

7 (Figure 5-10 and Figure 5-11) demonstrated bead width consistency that could not be readily classified as either good or bad.

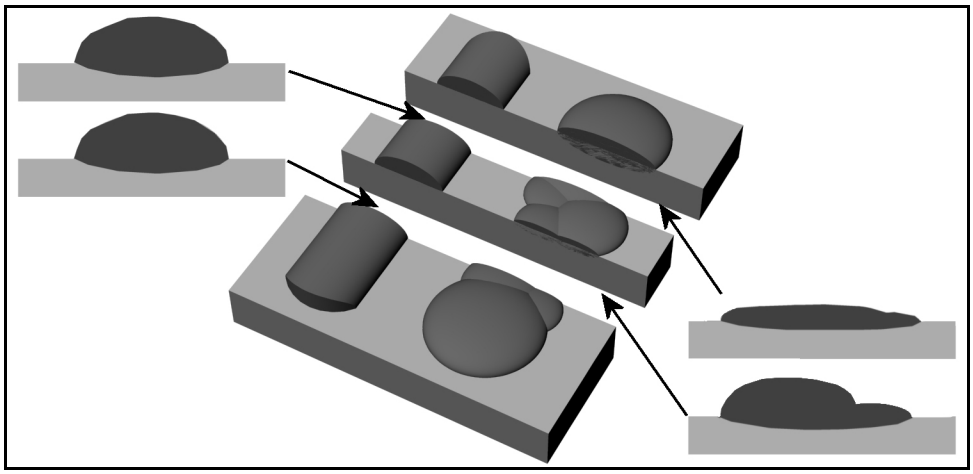

Figure 5-5: Sample Cross-Sections Profiles from Stable (left) and Unstable Weld Beads

Figure 5-6: Weld Coupon 35 (Good Bead Width Consistency)

Figure 5-7: Weld Coupon 36 (Good Bead Width Consistency)

Figure 5-8: Weld Coupon 25 (Poor Bead Width Consistency)

Figure 5-9: Weld Coupon 33 (Poor Bead Width Consistency)

Figure 5-10: Weld Coupon 4 (Intermediate Bead Width Consistency)

Figure 5-11: Weld Coupon 7 (Intermediate Bead Width Consistency)

Beads demonstrating either poor or undetermined bead width consistency only occurred with the Group 1 samples (beads 1 through 36 refer to Table 5-3, Table 5-4, Table 5-5, and Table 5-6. These welds underwent the most extreme voltage, current, and travel speed variations and, hence, were most likely to demonstrate bead instability. As a result, beads with poor bead width consistency included weld coupons 10, 13, 16, 21, 23, 25, and 33. Beads with intermediate bead width consistency included weld coupons 4, 7, 14, and 27. All other beads were considered to have good bead width consistency.

The variables responsible for producing the inconsistent weld beads were investigated. Using the criteria above, a total of seven beads had poor bead width consistency, making them clearly rejectable. An additional four beads with intermediate bead width consistency also were rejected.

Of the seven beads with poor bead width consistency, all were produced using low heat input (i.e., 0.5 kJ/mm). Three of the four beads displaying intermediate bead width consistency also were produced using a 0.5 kJ/mm heat input (the fourth bead was produced a 1.5 kJ/mm heat input). Most of the rejected beads also were produced using high current (i.e., 700 amps). If the product of current and travel speed was less than 8900 A*mm/s, there were no issues with bead width variation, whereas above that limit, only five of the sixteen weld beads were considered acceptable. There was no clear trend relating polarity or voltage to excessive bead width variation.

5.2: Group 1 Variable Weld Coupons

5.2.1 Effects of Input Parameters on Cross-Section Geometries

For the Group 1 welds, visual examination of the bead cross sections was performed first. Figure 5-12 illustrates the bead cross-section areas for the AC-SQ BOP welds. The tops of the weld beads (colored red) are the reinforcement areas, and the weld bead areas beneath the plate surface (colored yellow) are the penetration areas. The three columns of coupons represent the specimens with 0.5 kJ/mm, 1.5 kJ/mm, and 2.5 kJ/mm heat inputs, from left to right, and the current and voltage vary with row.

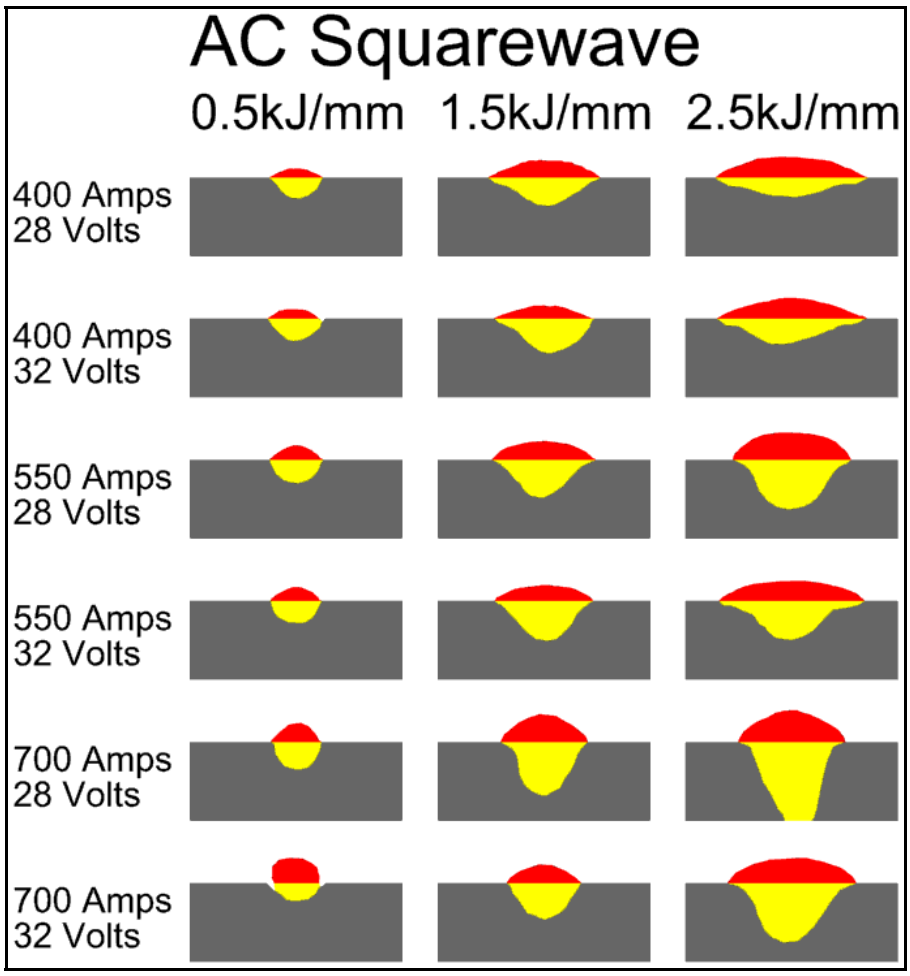

Figure 5-12: Group 1 AC-SQ Weld Bead Cross-Sections

Qualitatively, the bead profiles in Figure 5-12 indicate that as heat input increased, the total molten areas increased too. Also, at higher currents, increases in heat input clearly resulted in increased deposition and penetration height and areas. This trend is not always shown at lower current values. Bead width also increased with heat input. Finally, beads with the same heat input (i.e., from the same columns in Figure 5-12) demonstrated large variations in cross-sectional shape and size. Even though a greater heat input, calculated using equation (1), is often accompanied by an increase in weld bead cross-section area, the ratio of width and height is affected very much by fluid flow of the weld pool. Therefore, the heat input formula (Equation 1) is insufficient to predict weld bead geometry characteristics.

5.2.2 Effects of Current on Weld Bead Geometry Values

The use of multiple travel speeds to maintain heat input greatly complicated analysis of the welding variables. For instance, any two rows in Figure 5-12 (i.e., six weld beads) would be the result of two combinations of voltage and current, but also the result of six distinct travel speeds. Furthermore, the travel speed differences between columns change for each row. As a result, it was necessary to normalize the results based on travel speed.

A series of bar charts were produced for analysis. Unless otherwise noted, all error bars represent one standard deviation.

The effects of current on AC-SQ weld beads were plotted against penetration depth, reinforcement height, and bead width (Figure 5-13). The plot does illustrate some trends expected when the current is increased: penetration depth and reinforcement height both increase.

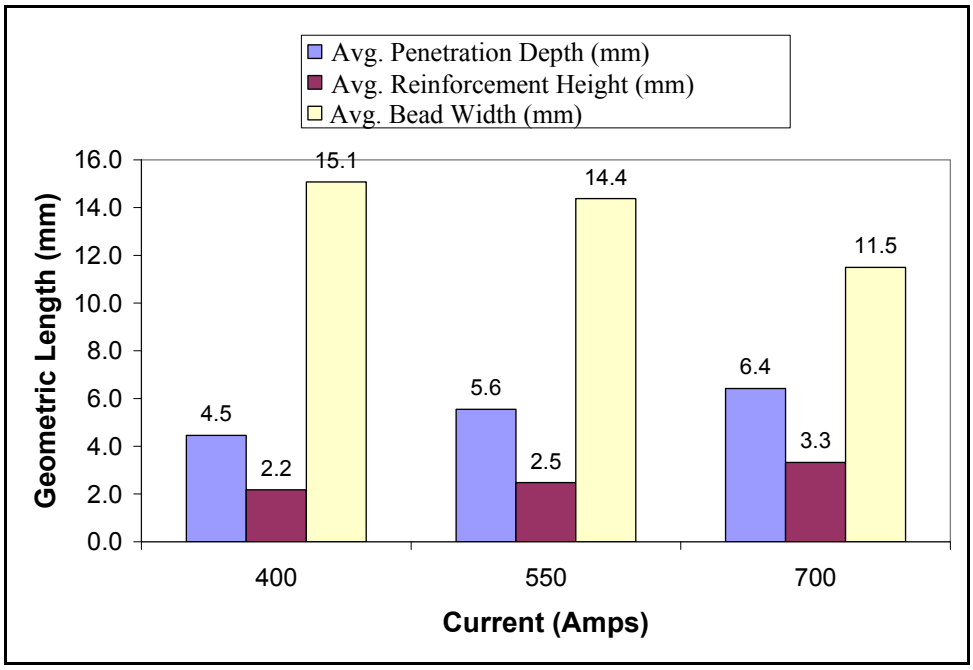

Figure 5-13: Effects of Current on Bead Geometric Lengths (1.5 kJ/mm heat input)

The literature review predicted an increased bead width as current is increased. The data in Figure 5-13 indicates that bead width actually decreased as current was increased. However, to maintain heat input, increases in current were accompanied by travel speed increases. For Figure 5-13, the average velocities corresponding to the three current values are 7.95, 11.25, and 14.15 mm/s. Therefore, while the greater current values should increase bead width, the accompanying increased travel speed values have caused a net decrease in bead width. This also would have affected penetration depth and reinforcement height.

The increase in travel speed should not significantly affect the amount of filler metal deposited. Also, depending upon the combination of other variables, the increased travel speed may have caused either a slight increase or decrease in the amount of base metal melted. Assuming the travel speed has a negligible effect on the amount of base metal melted, a decreased bead width should increase both the reinforcement height and penetration depth, regardless of the molten cross-section areas. In effect, the manipulation of travel speed throughout the welding trials may have significantly affected all three linear geometric values: bead

width, reinforcement height, and penetration depth. The weld bead cross-section areas were therefore investigated. Figure 5-14 investigates the effect of current on penetration area and reinforcement area (in addition to bead width).

Figure 5-14 demonstrates that when the current is increased to 550 Amps, penetration and reinforcement areas increase significantly. However, a further increase in current to 700 Amps does not result in further changes to either bead area. This is because the corresponding increase in travel speed is still counteracting the effects of current.

It therefore became apparent that when travel speed was variable, the penetration and reinforcement volume rates should be compared to welding parameters (and not areas or linear measurements). By multiplying the penetration and reinforcement cross-sectional areas by the travel speed, it was possible to calculate penetration and reinforcement volume rates produced per second of welding (i.e., volume rates, measured in mm^3/s). The above section, "Quality Assurance," demonstrates how weld beads with excessively variable bead widths were removed from the investigation. If the bead width variation was acceptable along the bead length, this implies that voltage and current variations along the weld length also should be acceptable. By extension, it was presumed that both reinforcement and penetration cross-section areas should be relatively constant along the welding length.

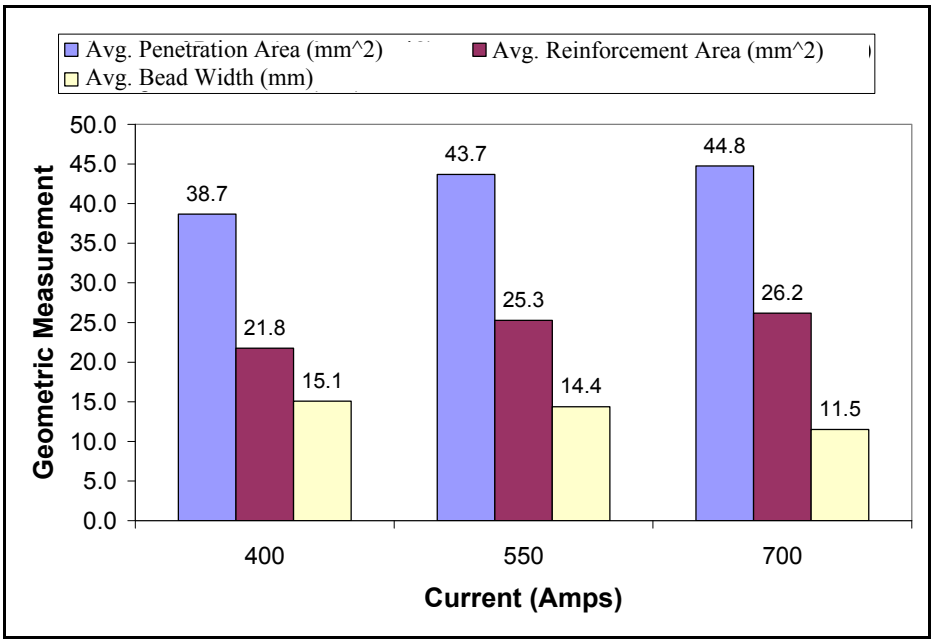

Figure 5-14: Effects of Current (and Travel Speed) on Bead Geometric Values (1.5 kJ/mm heat input)

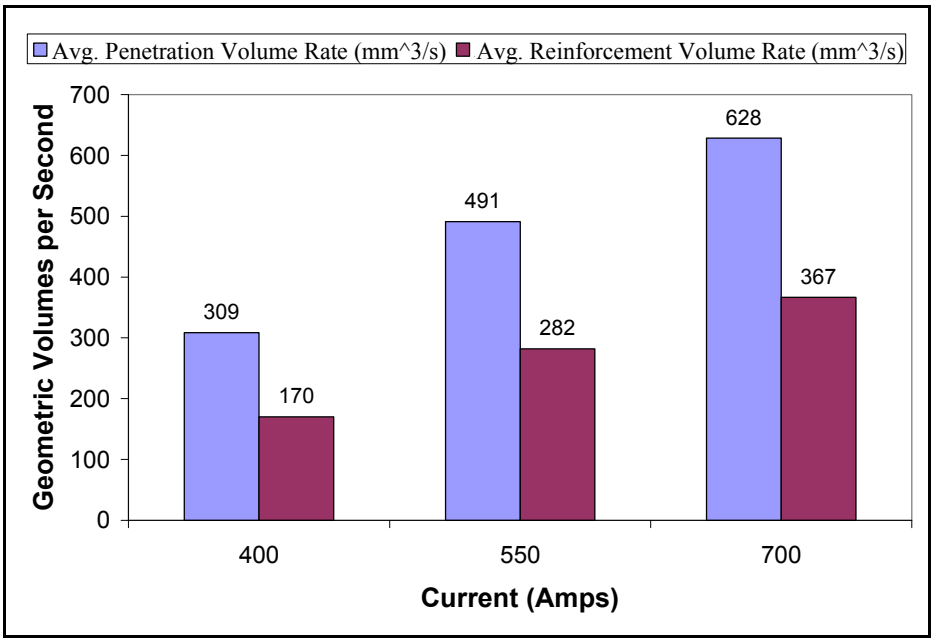

Figure 5-15: Effects of Current on Penetration and Reinforcement Volumes Deposited per Second (1.5 kJ/mm heat input)

Figure 5-15 gives a clearer indication of the true effect of current on reinforcement and penetration (i.e., an increase in current produces a clear

increase in both penetration and reinforcement). Figure 5-16 and Figure 5-17 illustrate that the trends linking current to penetration and reinforcement volume rates are maintained at different heat input values.

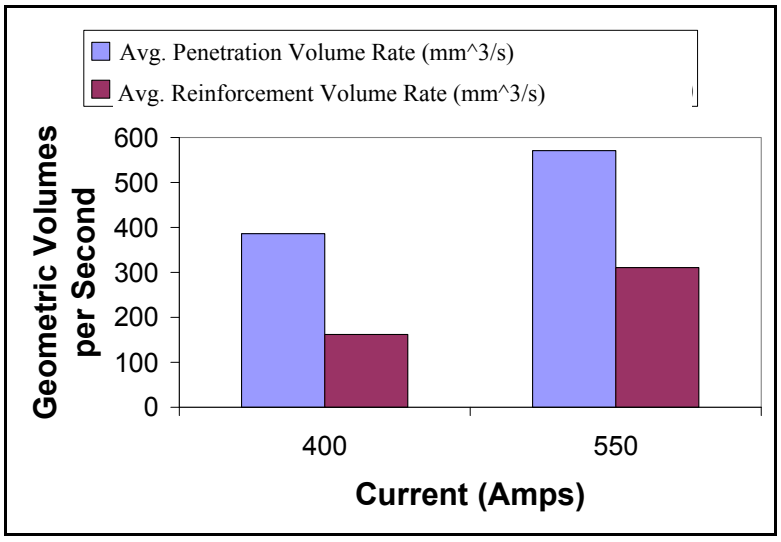

Figure 5-16: Effect of Current on Penetration andReinforcement Volumes per Second (0.5 kJ/mm heat input)

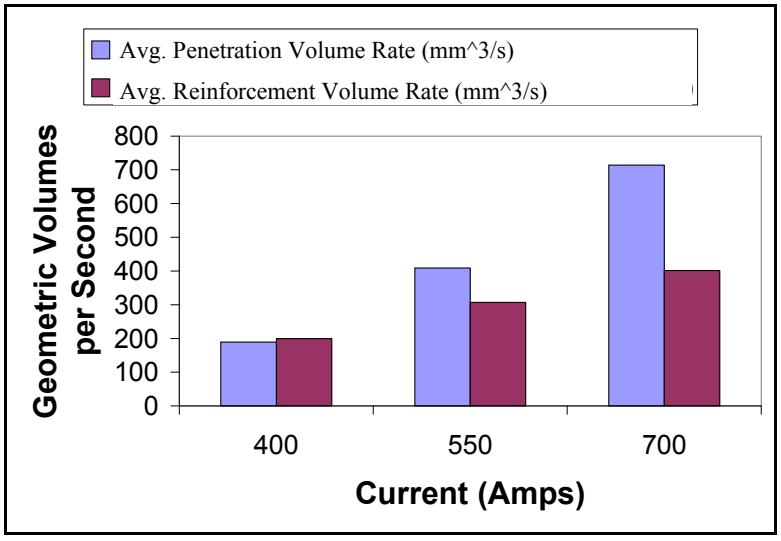

Figure 5-17: Effect of Current on Penetration and Reinforcement Volumes per Second (2.5 kJ/mm heat input)

5.2.3 Effects of Voltage on Weld Bead Geometry Values

The effects of voltage were compared to corresponding penetration and deposition volume rates (Figure 5-18).

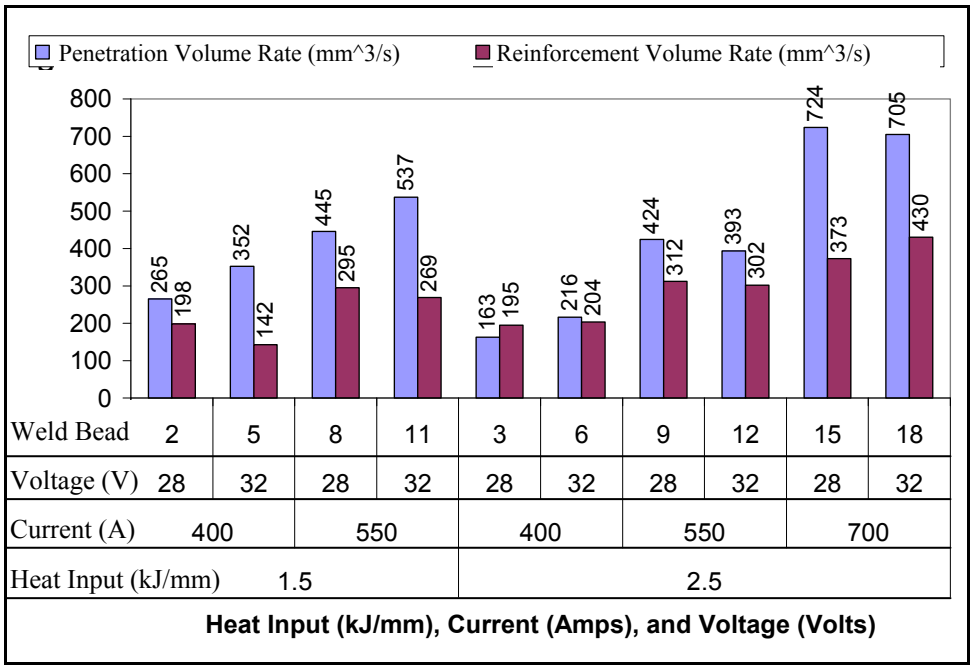

Figure 5-18: Effects of Heat Input, Current, and Voltage on Penetration and Reinforcement Volumetric Rates (mm^3/s)

At 1.5 kJ/mm heat input, an increase in voltage typically resulted in a decrease in reinforcement volume rate. When voltage is increased, arc length should increase, reducing electrode stickout. The lower stickout diminishes the resistive preheat, which in turn should reduce the metal deposition rate. A reduced reinforcement volume rate should result.

Weld beads 15 and 18 formed the only pair to strongly oppose the expected relationship between voltage and reinforcement volume rate. However, the software supplied with the welding power sources, Lincoln Command Center version 1.12.0.729, indicated that beads 15 and 18 had WFS values of 60 mm/s and 52 mm/s respectively. According to this, 18 should have achieved lower deposition rates than 15, resulting in a reduced reinforcement volume rate.

However, when bead 15's bead cross-section was investigated again (Figure 5-12, 2.5 kJ/mm, 700 Amps and 28 Volts), it became clear that the bead melted through the plate. Additional molten material burnt through the plate (Figure 5-19, illustrating the underside of the weld coupon), but was removed during sample preparation. This additional deposited material accounts for the low reinforcement volume rate measurement for bead 15. Unfortunately, because the burn-through was inconsistent, it was not possible to correct the measured reinforcement volume rate value. The slight increase in reinforcement volume rate between beads 3 and 6 cannot be explained satisfactorily at this time.

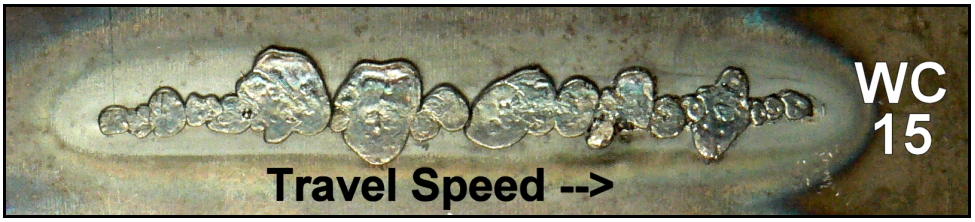

Figure 5-19: Photograph of the Underside of Weld Bead 15

The relationship between voltage and penetration volume rate cannot be explained satisfactorily. As per the discussion in Sections 2.5 and 4.2, increases in voltage are accompanied by increases in arc length, resulting in reduced plasma forces and, in turn, reduced penetration. However, three pairs of the beads (2 and 5, 8 and 11, and 3 and 6) in Figure 5-18 oppose this expected relationship When voltage is increased, assuming travel speed remains constant, bead width should increase and penetration should decrease (refer to Sections 2.5 and 4.2). However, the three aforementioned pairs of beads demonstrate a decrease in bead width and an increase in penetration volume rate with an increase in voltage (Figure 5-20). The two other pairs of beads (9 and 12, and 15 and 18) demonstrate bead widths that increase and penetration volume rates that decrease as voltage is increased (Figure 5-20).

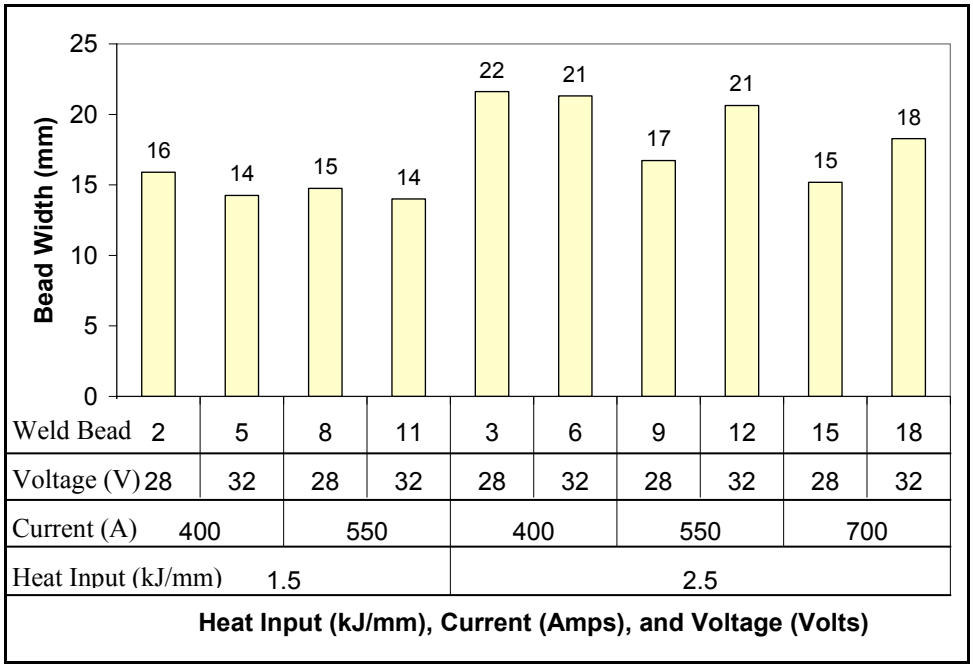

Figure 5-20: The Effect of Heat Input, Current, and Voltage on Bead Width

When voltage is increased, bead width increases. However, when travel speed is increased, bead width decreases. To maintain the heat input, a voltage increase from 28 V to 32 V would have been accompanied by a faster travel speed. As travel speed increases (under certain conditions), the arc moves forward within the molten pool. This causes less molten metal to insulate the base material from the arc. As a result, a slight increase in travel speed may actually result in an increase in penetration.

The relationship between voltage and penetration has been complicated by variable travel speeds. Future work would be necessary to determine critical travel speeds beyond which penetration increases or decreases, for various combinations of other weld variables.

5.2.4 Effects of Polarity on Weld Bead Geometry Values

Beads using direct current polarity were welded using heat inputs of either 0.5 kJ/mm or 2.5 kJ/mm (Figure 5-21). Voltages were either 28 V or 32 V, and amperages were either 400 A or 700 A.

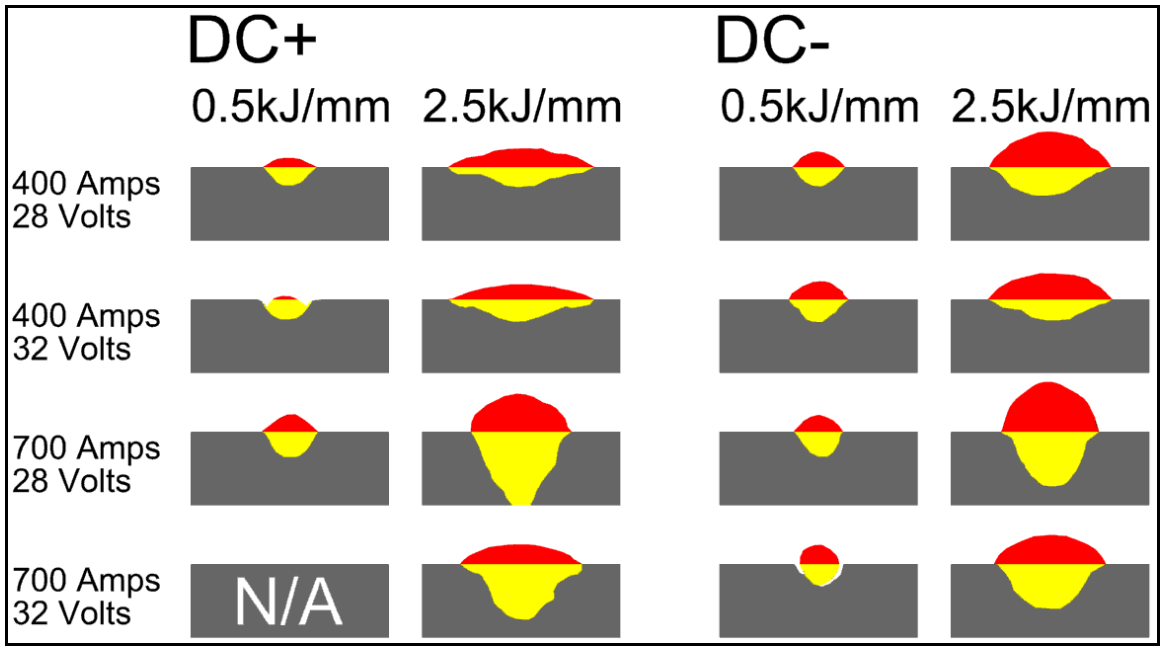

Figure 5-21: Group 1 DCEP and DCEN Weld Bead Cross-Sections

Because so many beads with 0.5 kJ/mm heat inputs had inconsistent bead widths, the effects of polarity were investigated only with specimens with 2.5 kJ/mm of heat input. The effects of polarity were compared with corresponding penetration and deposition volume rates (Figure 5-22). Any bead demonstrating penetration through the entire plate depth will have a misleading low reinforcement volume rate measurement.

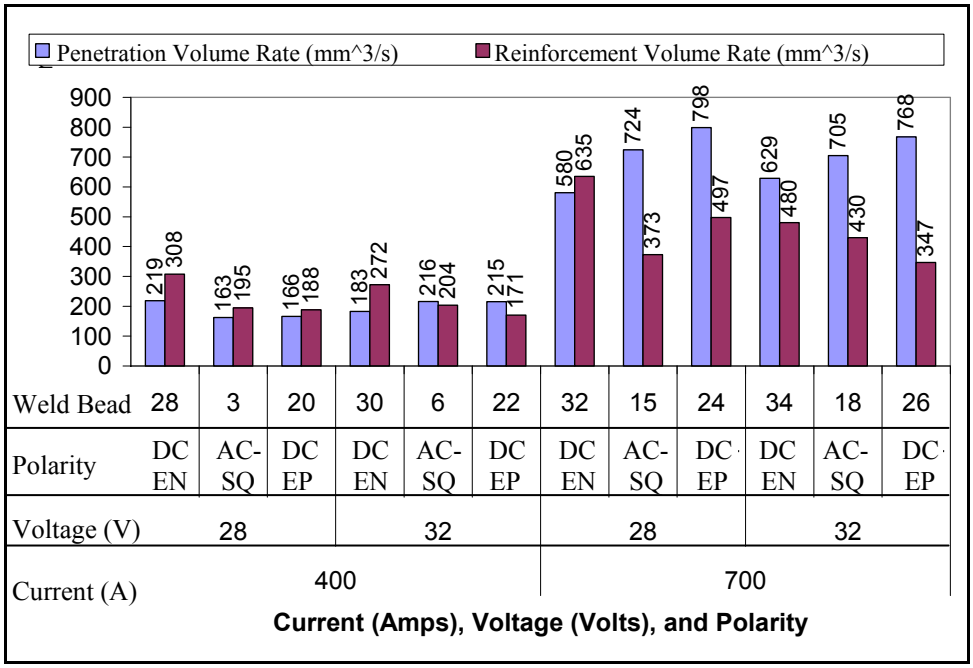

Figure 5-22: The Effect of Current, Voltage, and Polarity on Penetration & Reinforcement

Overall, Figure 5-22 demonstrates that a polarity shift from DCEN to AC-SQ to DCEP reduces reinforcement volume rate. It is worth repeating that weld bead 15 should have a greater reinforcement volume rate, but some of the deposited metal melted through and was removed during sample preparation (refer to Figure Figure 5-19). This confirms the literature review in Section 2.5.2 and Section 4.2.4, which indicated that a DCEN polarity should achieve the greatest electrode melting rates because of field emission and "arc climb" at the electrode. When the amperage was set at 700 A, the same shift in polarity produced a clear increase in penetration. When welded using 400 A, the penetration trends either were not visible or were inconsistent with those welded using 700 A. The literature review in Sections 4.2 indicated that at lower current values, the same trends should exist, though the effects from polarity changes would be reduced.

To achieve a heat input of 2.5 kJ/mm with 400 A, much lower travel speeds were necessary. As such, it is expected that the weld puddle should shield the base metal from the arc, resulting in reduced penetration (refer to Section 4.2.3). Upon

re-examination of Figure 5-21, it appears that the weld beads using 400 Amps with 2.5 kJ/mm heat inputs either had formed the characteristic shallow 'T-shaped' bead cross-section profile due to extremely low travel speeds, or they would have with any further decrease in travel speed. Such a formation of T-shaped beads complicated analysis of penetration and reinforcement volume rates. Accordingly, no further analysis was performed to link the effects of polarity on 400 A bead molten volume rates.

Finally, the effects of polarity on bead width were measured (Figure 5-23). In agreement with the literature review, shifting the polarity from DCEN to AC-SQ to DCEP increased bead width.

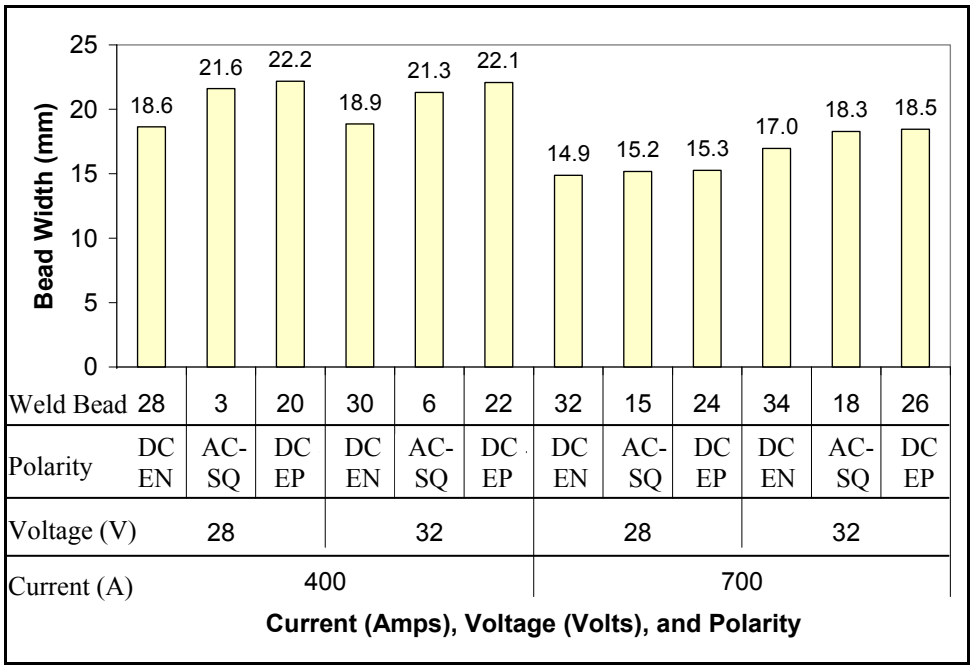

Figure 5-23: The Effect of Current, Voltage, and Polarity on Bead Width

5.2.5 Bead Shape

Both the literature and the initial analysis indicate that in addition to measurable cross-section values (e.g., bead width, penetration area, reinforcement volume rate

deposited per second, etc.), the shapes of the weld beads vary. This also can be seen clearly by referring to Figure 5-12 and Figure 5-21. In both figures, it is easy to distinguish the shape of the weld beads looking at each bead individually. While the naked eye will remain a quick and useful method of evaluating weld bead shape, the ability to plot a numerical shape factor can be helpful when dealing with large numbers of weld beads. Such a numerical shape factor was developed, and while only in its initial stages of development, it was applied to the single electrode welds, which demonstrated greater variations in weld bead geometry shapes and sizes than the other weld bead groups.

Typically, the shapes of the reinforcement areas are quite consistent (Figure 5-12). Some are taller or shorter, some are wider or narrower, but they all are roughly parabolic in shape. The penetration areas however display significant shape differences.

Figure 5-24 demonstrates an idealized bulbous penetration bead on the left, and a T-shaped penetration on the right. Assuming that for each bead, "p_1" and "p_2" are equal, the ratio of "w_2/w_1" will decrease as the bead becomes less bulbous and more "T-shaped."

Because this method compares the full width to the width at half (or semi) penetration (i.e., "w_2/w_1"), this measurement was named the "SP Ratio." The bead cross-sections (demonstrating stable bead widths) were superimposed on a chart demonstrating increasing SP ratio values (Figure 5-25).

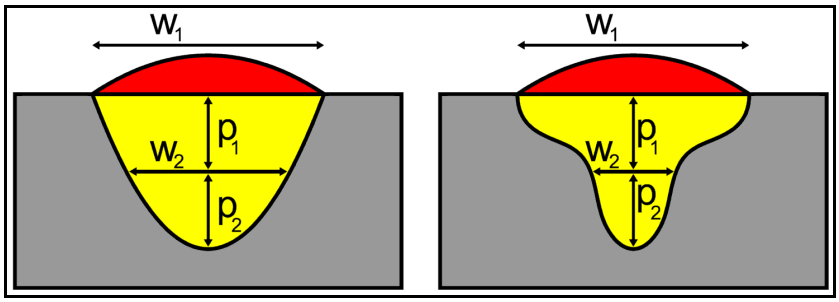

Figure 5-24: Schematics Demonstrating Bulbous (left) & T-shaped (right) Profiles

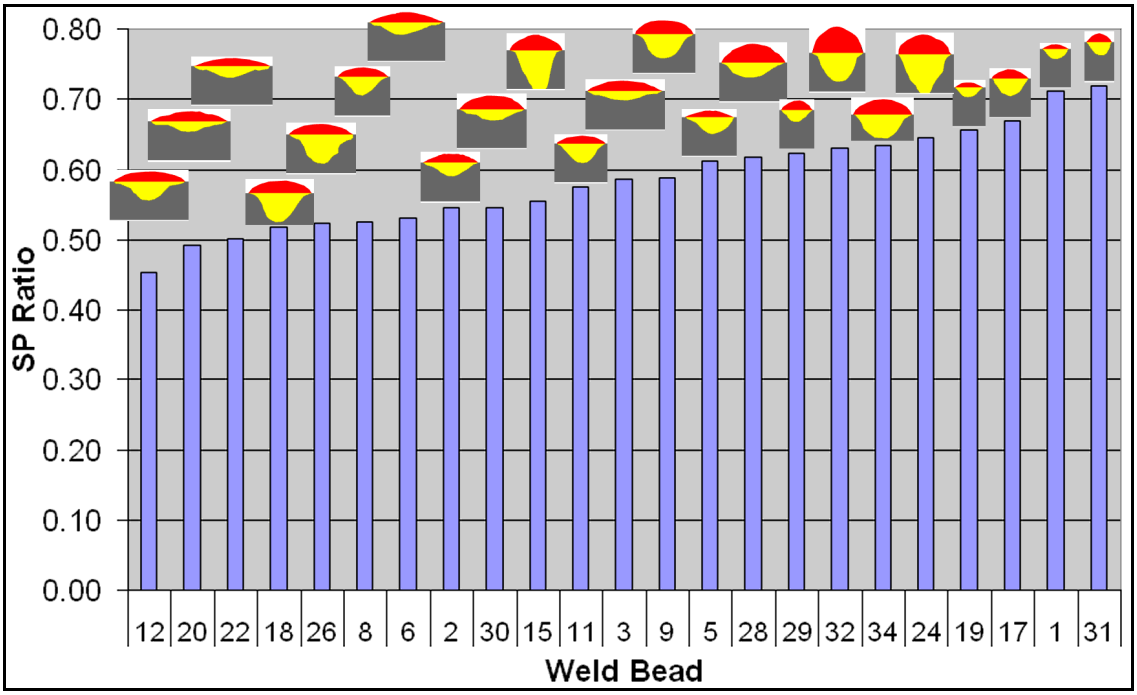

Figure 5-25: The Effect of SP Ratio (w_2/w_1) on Cross-Section Appearance

Figure 5-25 clearly demonstrates that T-shaped beads possess lower SP ratios than bulbous beads. When combined with bead width and penetration depth, the SP ratio provides a new means of defining bead penetration characteristics numerically. The SP ratio was compared against current, voltage, and polarity (refer to Figure 5-26, which demonstrates values for beads produced with a 2.5 kJ/mm heat input).

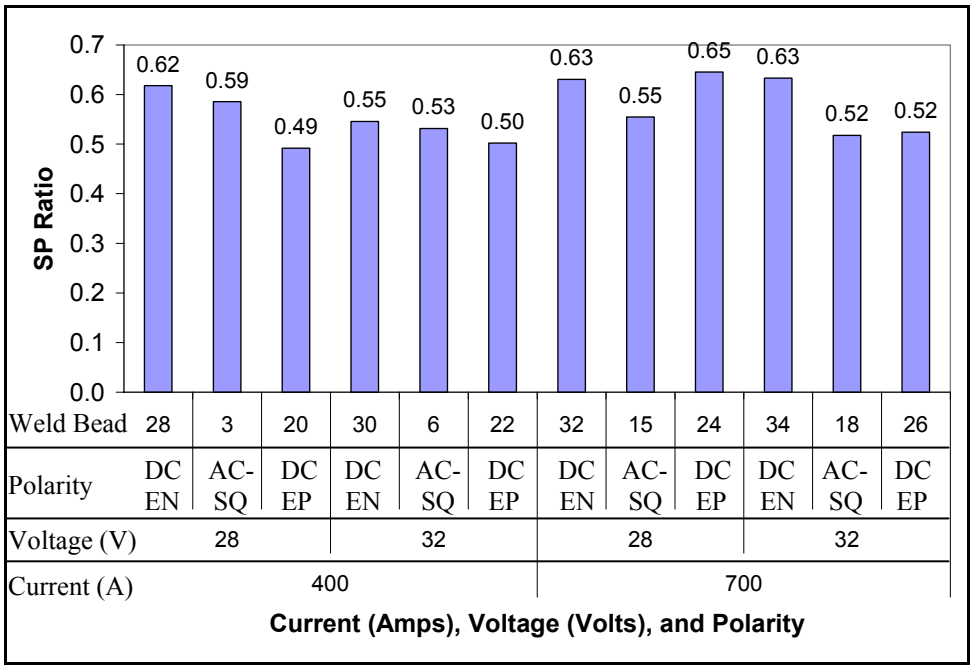

Figure 5-26: The Effect of Current, Voltage, and Polarity on SP Ratio

Figure 5-26 demonstrates a few trends. Most prominent is that as polarity is shifted from DCEN to AC-SQ to DCEP, the SP ratio typically decreases. This is probably because when DCEP is used, non-metallic inclusions act as electron field emitters. For enough electrons to be emitted, the arc is typically wider than it is with DCEN. As a result, the bead width typically increases too. However, most of the penetration will occur at the centre of the bead, while the outer-edges of the bead will have only shallow penetration. The result is a decreased SP ratio.

Figure 5-26 also appears to demonstrate relationships between voltage, current, and SP ratio. Voltage increases appear to reduce SP ratios, while changes in current do not appear to cause significant changes to the SP ratio. The extent of such relationships cannot be measured quantitatively unless future beads are performed, using constant travel speeds. Figure 5-27 was plotted to address the relationship between travel speed and SP ratio. The values for weld beads 1 through 34 were included, meaning that the trend transcends polarity, voltage, current, and heat input variation. As travel speed increases, there is a strong

correlation for the SP ratio to increase too. This implies that travel speed affects the fusion line shape very strongly compared to other welding parameters.

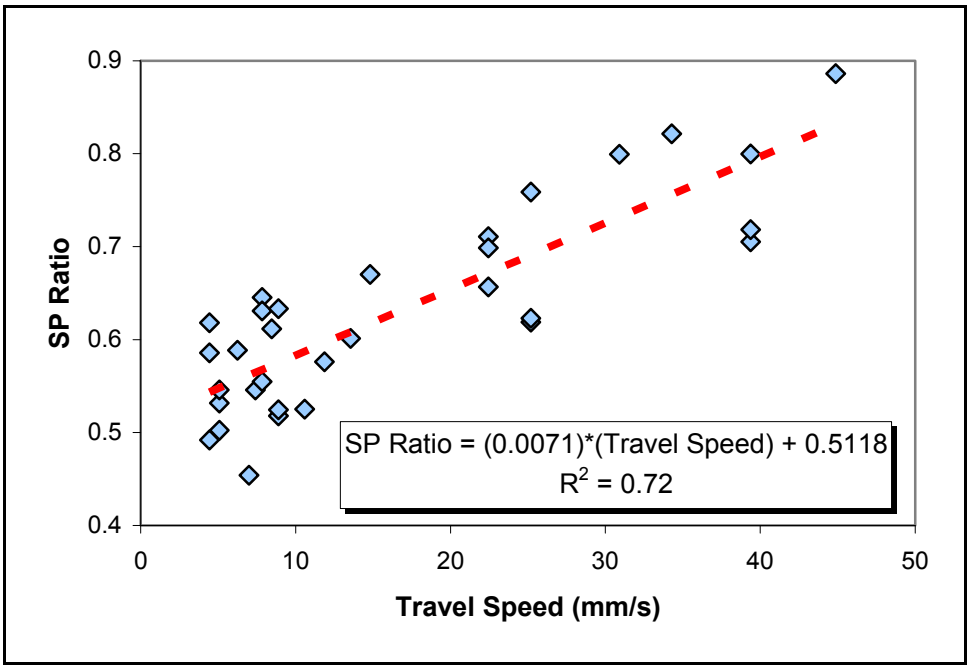

Figure 5-27: The Effect of Travel Speed on Group 1 SP Ratio Values

To be thorough, Figure 5-27 was re-plotted, such that the scatter points were separated on the basis of the various welding variables: current, voltage, polarity, and heat input. When the data points were separated on the basis of heat input (Figure 5-28), it was reinforced that heat input was manipulated by controlling the travel speed. As a result, the question was posed whether heat input truly had an effect on SP ratio, or if SP ratio was just related to the travel speed. As a result, the scatter plot was plotted again on the basis of power (i.e., current x volts) (Figure 5-29). These trends have been observed in industrial trials where weld profile was improved by increasing travel speed [47].

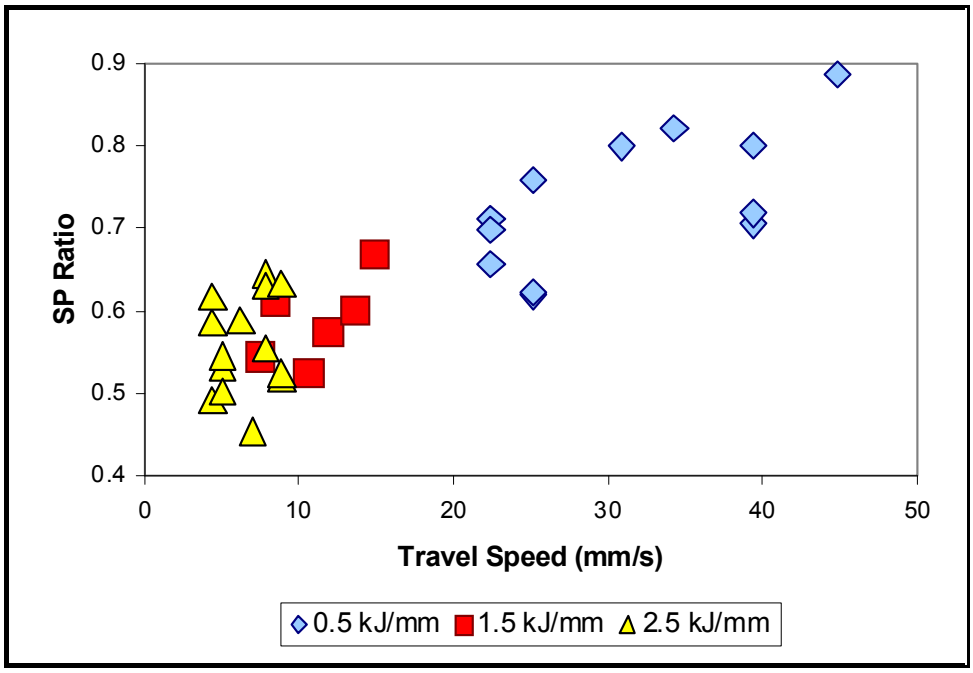

Figure 5-28: The Effect of Heat Input and Travel Speed on SP Ratio

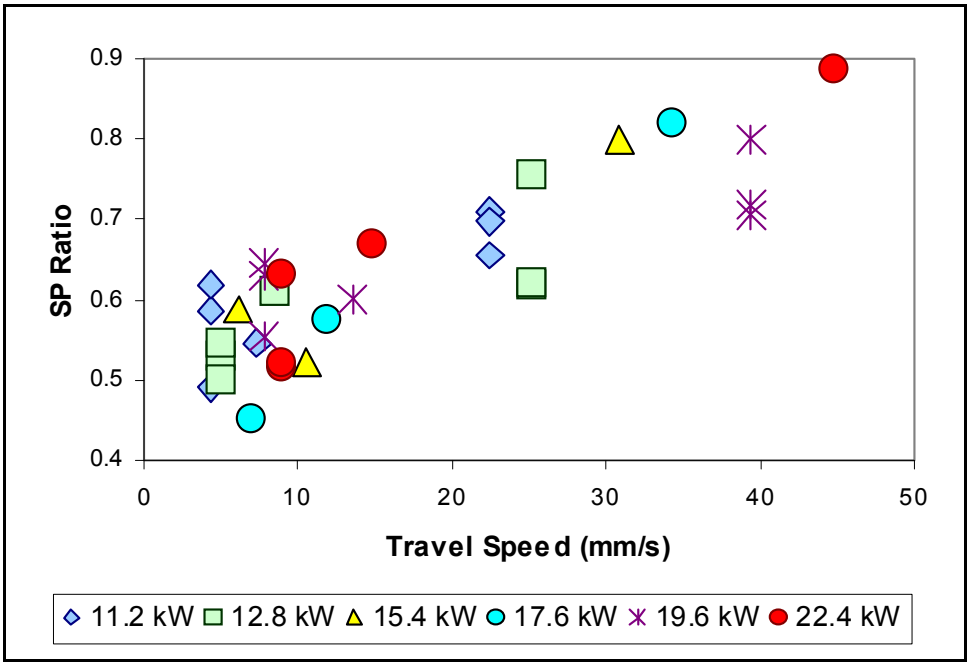

Figure 5-29: The Effect of Power and Travel Speed on SP Ratio

Because Figure 5-29 does not appear to show a strong trend that illustrates differences in trends based on power, it can be concluded that there is no clear trend linking arc power to SP ratio shape. By extension, there is no strong trend linking heat input to SP ratio shape.

5.3: Group 2 Variable Weld Coupons

5.3.1 Effects of Input Parameters on Cross-Section Geometries

Analysis of the BOP welds began with visual examination of the Group 2 bead cross-sections (Figure 5-30 through Figure 5-33). By limiting the heat input and current ranges, the Group 2 bead cross-section geometry variations were more minor than those of the Group 1 weld beads.

All Group 2 beads were deemed to have stable widths with respect to welding direction. Because travel speed was still varied to maintain the overall heat input, only the volume rates deposited and penetrated were investigated. It also is clear that the penetrated beads for the DCEP lead arc, DCEN trail arc beads are typically offset to the left. Because of their constant polarity, they would be more susceptible to having grounding systems affect the bead shape.

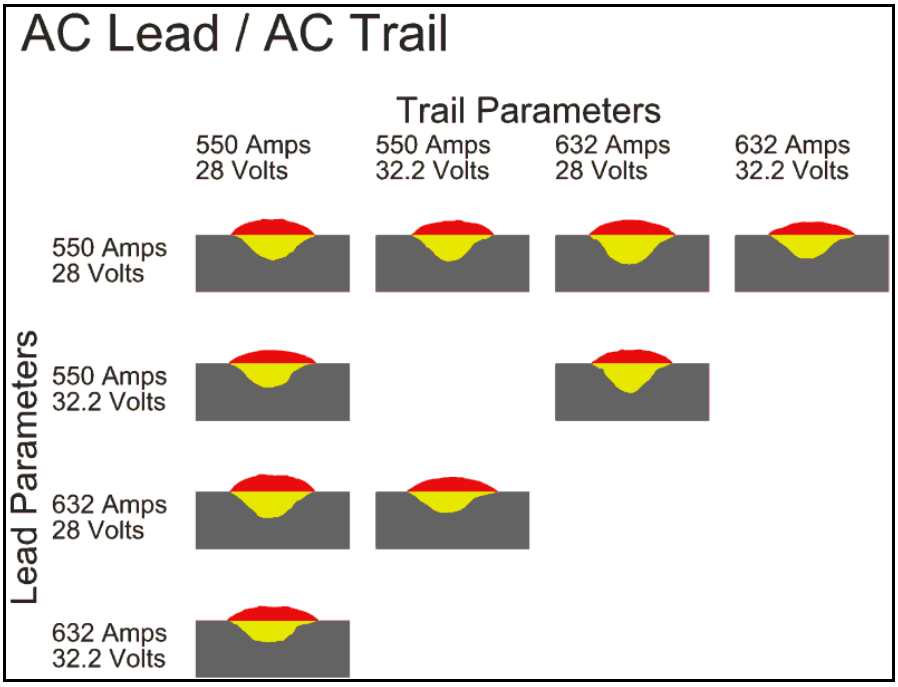

Figure 5-30: Group 2 AC-SQ Lead and Trail Tandem Weld Bead Cross-Sections

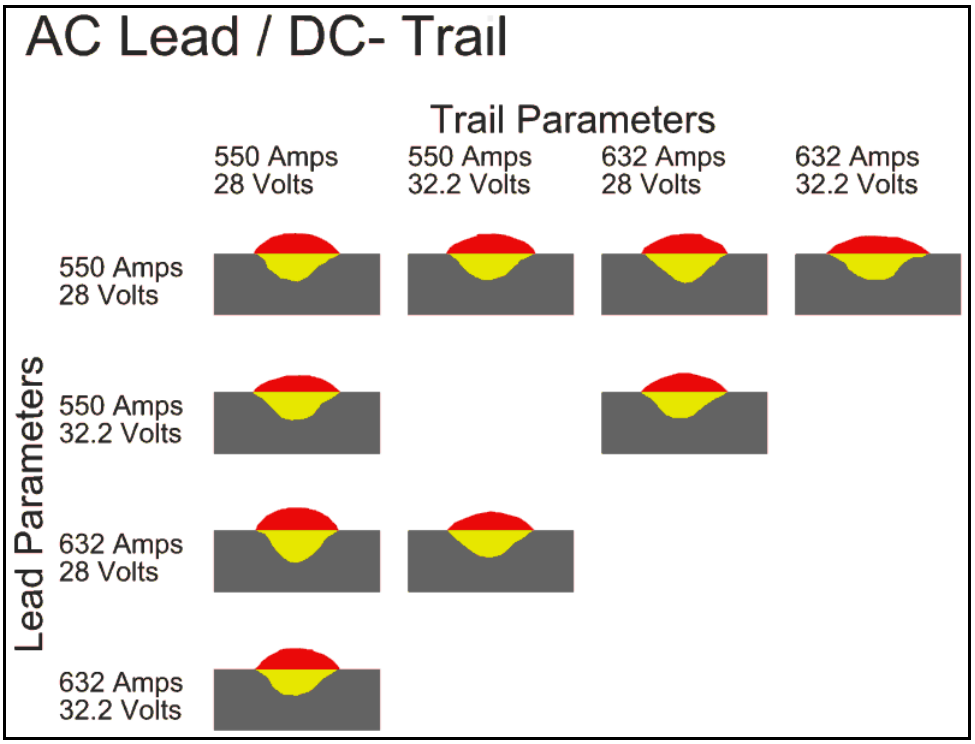

Figure 5-31: Group 2 AC-SQ Lead, DCEN Trail Tandem Weld Bead Cross-Sections

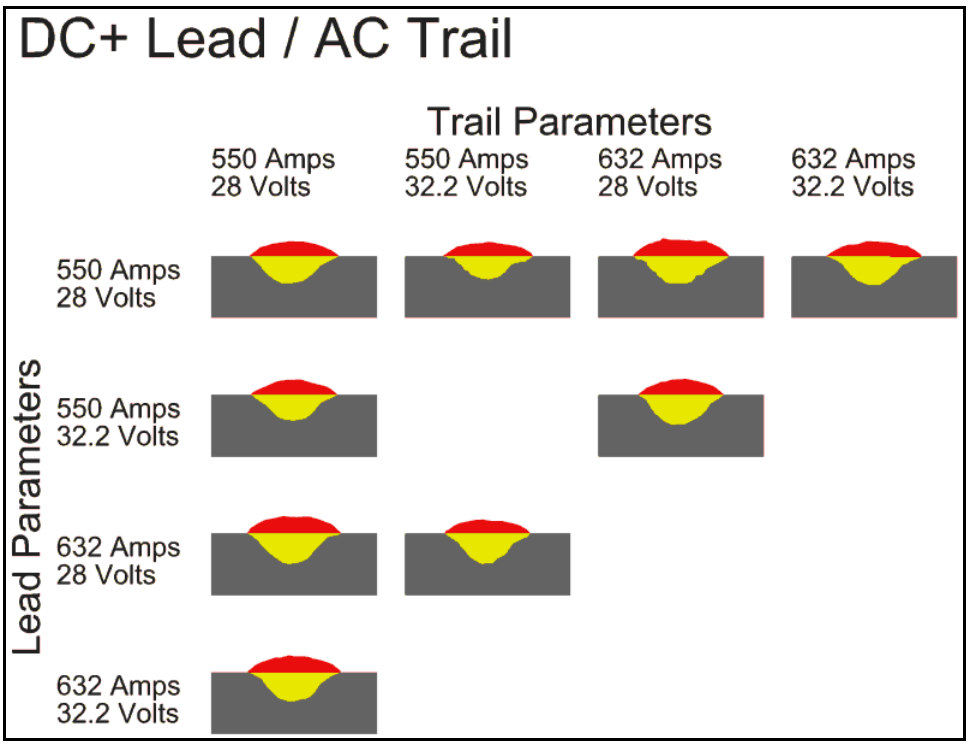

Figure 5-32: Group 2 DCEP Lead, AC-SQ Trail Tandem Weld Bead Cross-Sections

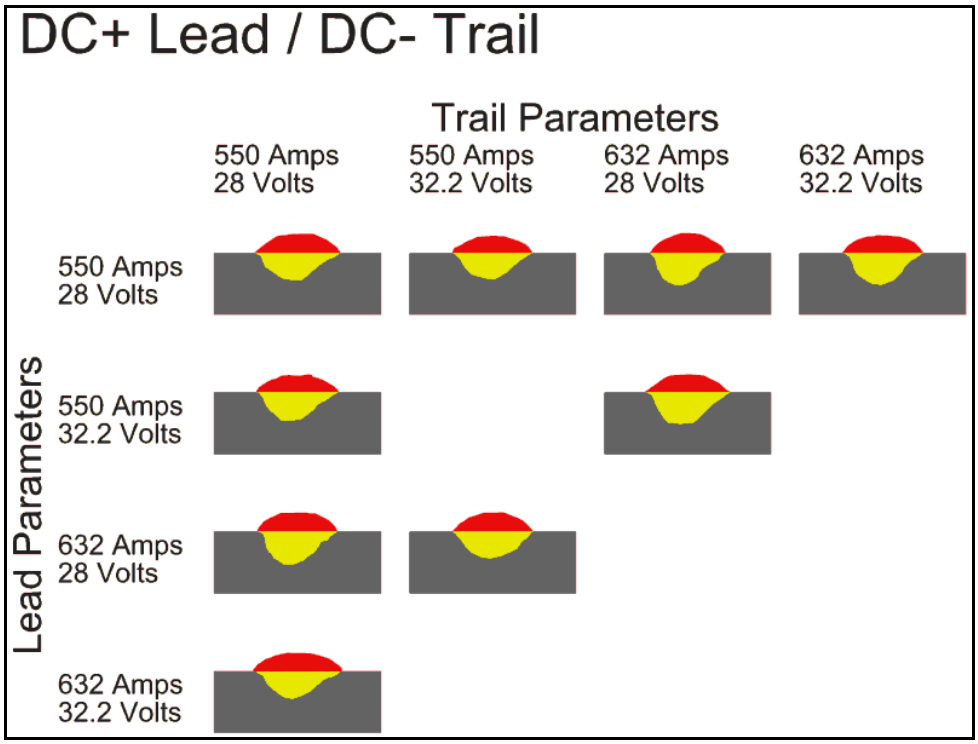

Figure 5-33: Group 2 DCEP Lead, DCEN Trail Tandem Weld Bead Cross-Sections

5.3.2 Overall Polarity Trends

Analysis was started by investigating the average effect of modifying lead and trail arc polarity (Figure 5-34). Figure 5-34 demonstrates that regardless of the lead polarity, a shift from AC-SQ to DCEN trail polarity resulted in a small increase in penetration, and a significant increase in reinforcement. Likewise, a shift from the AC-SQ to DCEP lead polarity resulted in an increase in penetration, and a decrease in reinforcement. To better understand the effects on reinforcement, the wire feed speeds for both the lead and trail arcs were plotted against the lead and trail arc polarities (Figure 5-35).

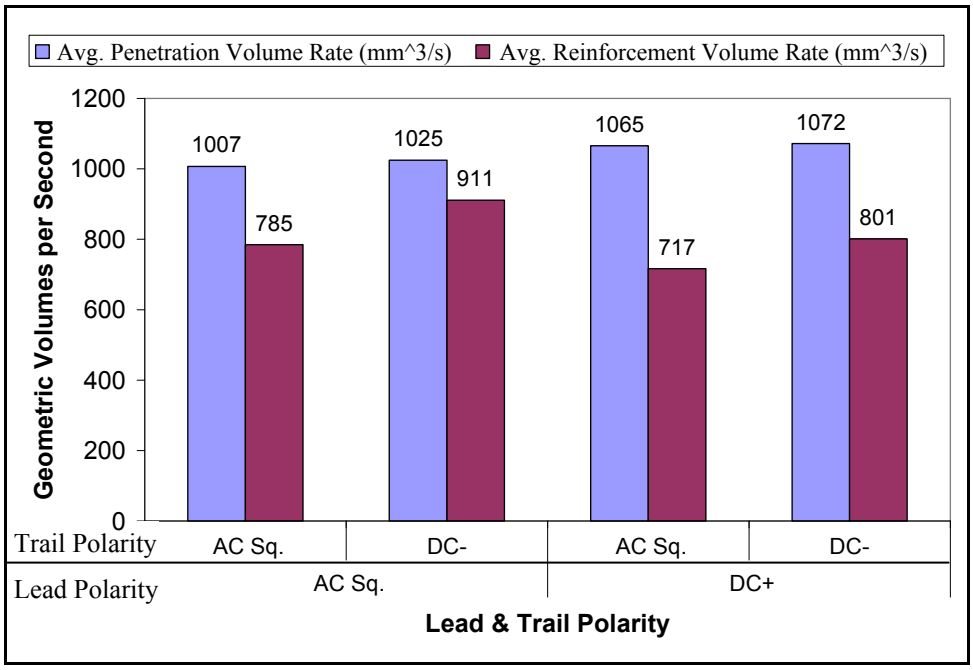

Figure 5-34: The Effect of Lead and Trail Polarity on Penetration and Reinforcement

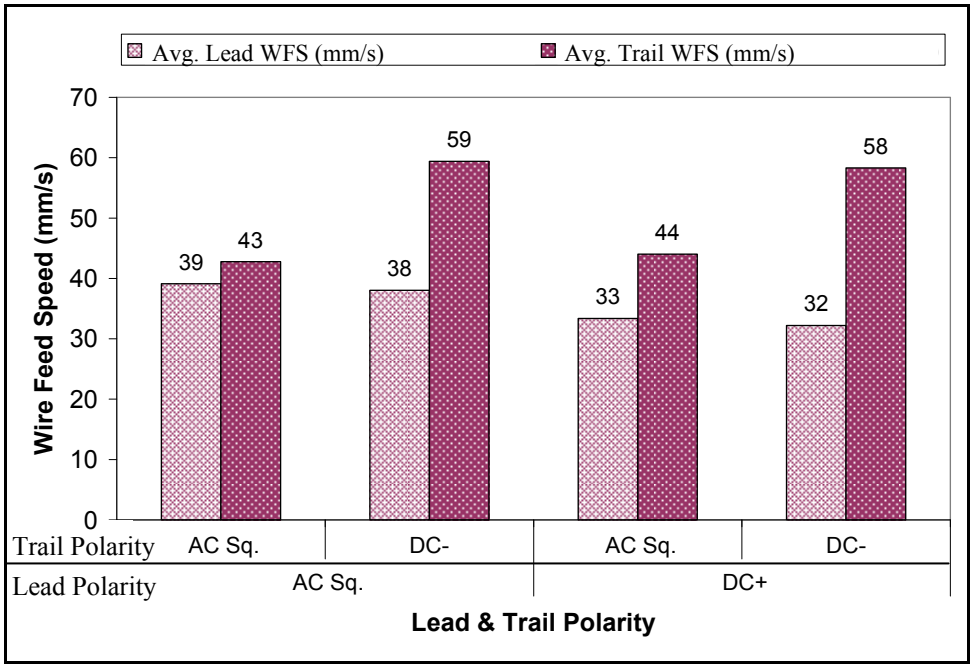

Figure 5-35: The Effect of Lead and Trail Polarity on Lead and Trail Arc Wire Feed Speed

Figure 5-35 demonstrates that there is a strong relationship between the lead and trail arc polarities, and their corresponding wire feed speeds (i.e., their deposition

rates). When the lead arc polarity was changed from AC-SQ to DCEP, there was a reduction in lead electrode WFS from 39 mm/s to 33 mm/s. Likewise, when the trail arc polarity was changed from AC-SQ to DCEN, there was an increase in trail electrode WFS from 44 mm/s to 58 mm/s. The WFS is changed more noticeably when the trail electrode polarity is manipulated. There does not seem to be any relationship between one electrode's polarity and the WFS of the other electrode.

If the total WFS values from Figure 5-35 are considered (i.e., the sum of both lead and trail WFS values), the ratio between total WFS values matches the ratios between reinforcement volume rates from Figure 5-34. Therefore, the effect of lead and a trail polarity on reinforcement volume rates is quite straightforward: as either polarity is shifted from DCEN to AC-SQ to DCEP, the reinforcement volume rate will increase.

The penetration trends in Figure 5-34 can be explained also. When the lead arc polarity was shifted from AC-SQ to DCEP, there was a clear increase in penetration depth. This trend was predicted in the literature review. However, when the trail arc polarity was shifted from AC-SQ to DCEN, there was no decrease in penetration. In fact, the penetration volume rate increased slightly. This may have been caused by phase offset.

As per Section 4.2.5, arcs in close proximity, with various polarities, will either attract or repel each other. Arcs with the same polarity attract, and those with opposite polarity repel. When tandem welding, the weld pool is fed by both electrodes. Figure 5-36 demonstrates the repulsion and attraction times of tandem arcs, depending upon their relative polarities.

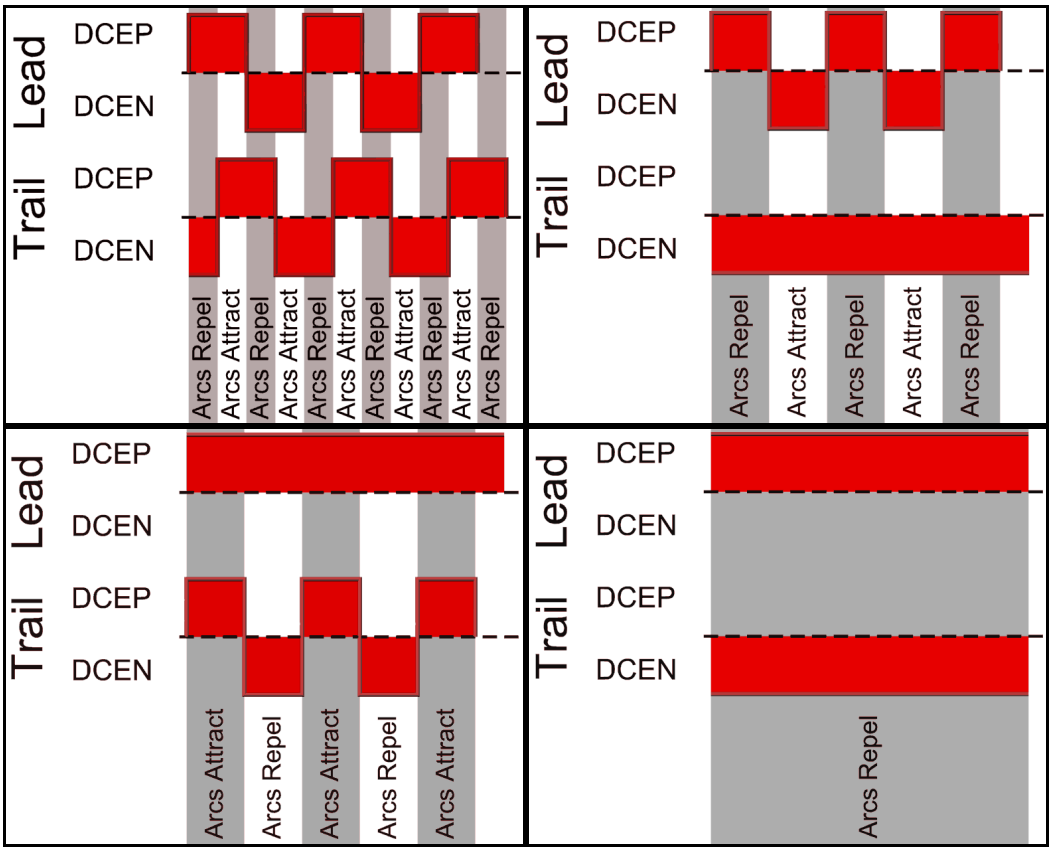

Figure 5-36: The Effect of Tandem Electrode Polarity on Arc Attraction or Repulsion

Figure 5-36 clearly demonstrates that when the trail arc polarity is shifted from AC-SQ to DCEN, the arcs repel and attract one another with lower frequency. With a DCEP lead arc and a DCEN trail arc, the relative arc positions should be constant, further increasing arc penetration. There appears to be a link between arc attraction / repulsion frequency and penetration.

As current is increased, the arc force can push molten metal aside to expose base metal during welding. Because molten metal thermally insulates base material during welding, exposing the base metal directly to the arc increases penetration.

When the arcs attract and repel each other rapidly, the arc oscillation relative to the weld pool may cause agitation (i.e., "sloshing") of the molten metal. It is therefore proposed that increased agitation hinders an arc's ability to push aside molten metal. Therefore, as the oscillation of arc attraction and repulsion is

reduced, it is expected that there should be a slight increase in bead penetration (even though the shift to DCEN is predicted to decrease bead penetration). With the current weld beads, it appears that such an increase in penetration overcame the expected results of a trail arc polarity shift from AC-SQ to DCEN, which was expected to decrease penetration.

5.3.3 Bead Shape

The SP ratio was calculated for the Group 2 weld beads (Figure 5-37). However, the strong relationship to travel speed displayed by the Group 1 welds was not present for the Group 2 welds. Just as before, the scatter plots were re-plotted, such that the individual welding variables (i.e., lead and trail current, voltage, polarity, and power) could be evaluated. In all cases, there were no clear trends.

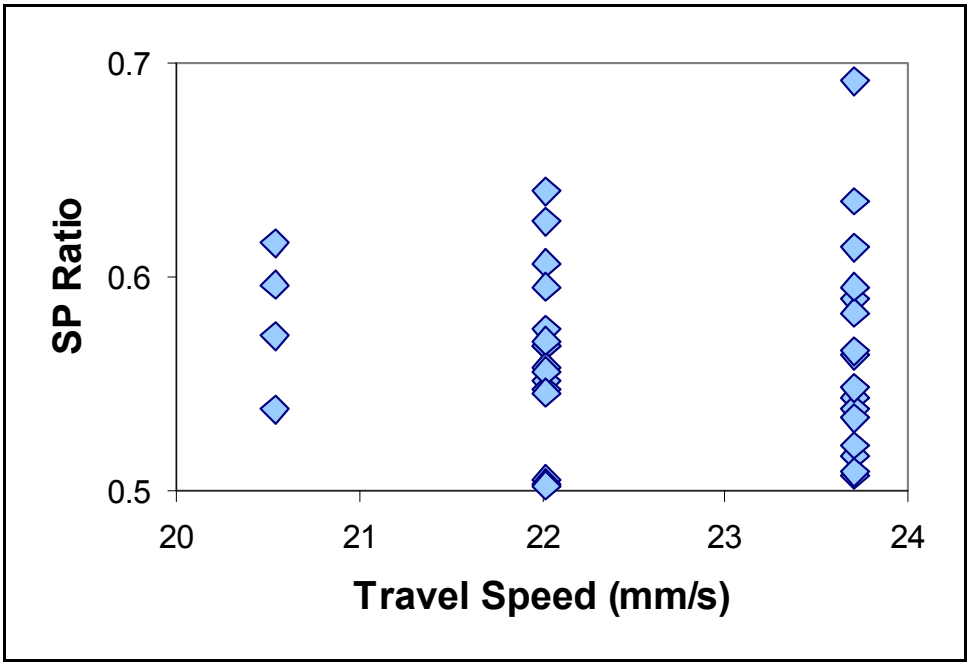

Figure 5-37: The Effect of Travel Speed on Group 2 SP Ratio Values

The only visible trend was that as travel speed increased, the range of SP ratio values increased. However, upon re-evaluation of Table 5-7 through Table 5-10, it became clear that the range increased because the welding variable ranges used increased too. At the lowest travel speeds, four welds were produced, each with the same voltage, current, and travel speed, but with different polarities. Because the range of SP ratio values at the lowest travel speed (nearly 0.1) was attributed only to different combinations of polarity, the data was re-plotted to reflect the effects of the tandem arc polarity combinations.

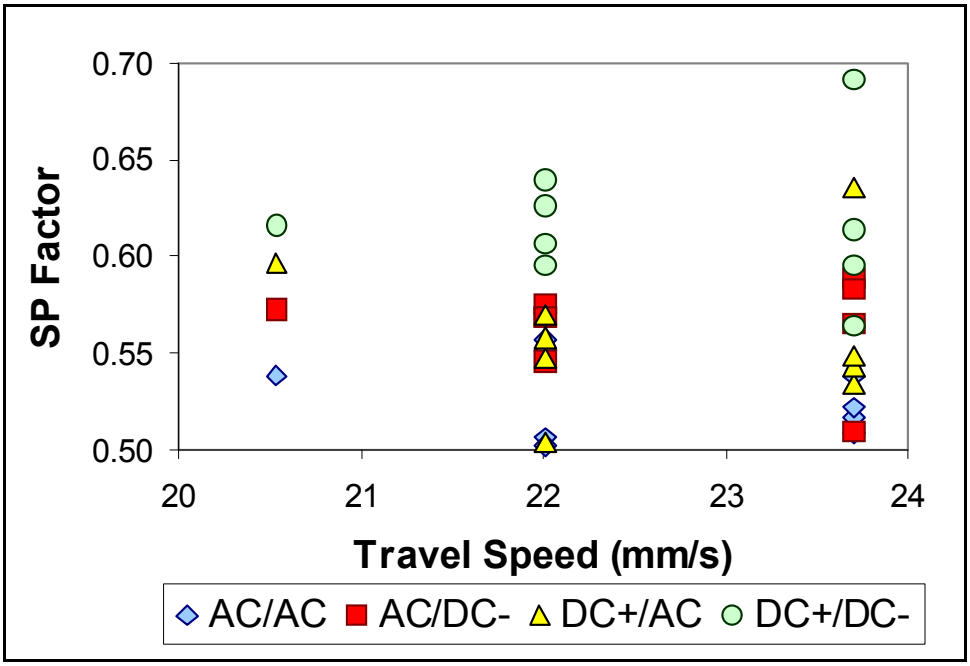

Figure 5-38: The Effect of Tandem Arc Polarity Combination and Travel Speed on Group 2 SP Ratio Values

Figure 5-38 clearly shows that the highest SP ratio values (i.e., the beads had the most bulbous shapes) were achieved with the combination of a lead DCEP polarity with a trail DCEN polarity (henceforth referred to as the DCEP/DCEN welds), regardless of travel speed. When AC-SQ polarity was used for both arc polarities (henceforth referred to as the AC-SQ/AC-SQ welds), the SP ratio tended to be lower (i.e., the beads were more T-shaped). However, the bead cross-section profiles of the four beads produced at the lowest travel speed

(Figure 5-39) do not appear to be significantly different. All four cross-sections demonstrate comparable penetration depth and bead width. The symmetry of the beads, however, does vary.

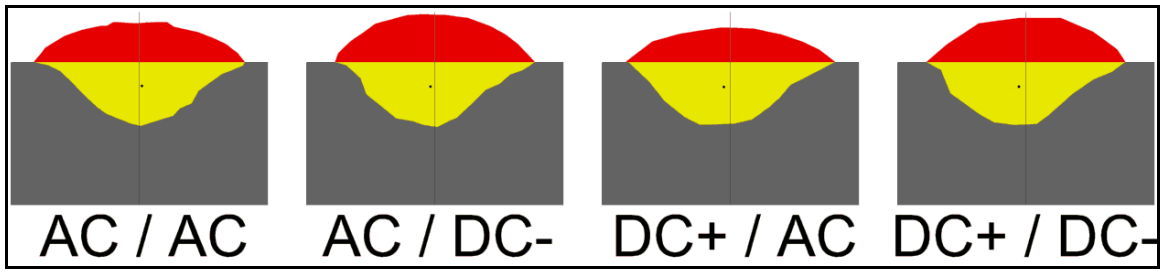

Figure 5-39: Cross-Section Profiles of Weld Beads Produced Using Minimum Travel Speed

In Figure 5-39, the bead cross-sections have been overlaid by vertical lines, running along the centres of the weld beads. Each bead also has been overlaid by a small black dots, representing the centre of the penetration areas. The dots are extremely close to the vertical line for the AC (0.21 mm to the right), whereas when the polarity combinations were changed (moving from left to right), the dots move further to the left (0.34 mm, 0.51 mm, and 0.55 mm to the left respectively). In other words, the cross-section bead profile at the left is the most symmetric, while the cross-section bead profile at the right is the most asymmetric. It is suspected that this could be the result of grounding issues, because alternating current arcs should be less likely to deflect due to such issues. Regardless of the source of the bead symmetry variations, there is evidence that the SP ratio method of comparing bead profile shapes is valid only for relatively symmetric cross-section bead profiles.

Amongst the Group 2 welds, sixteen were produced using the greatest weld travel speed: four beads for each polarity combination. Both the AC-SQ/AC-SQ and DCEP/DCEN high travel speed weld bead cross-section profiles were investigated further (Figure 5-40 and Figure 5-41). Overall, it appears as though the AC-SQ/AC-SQ weld beads (Figure 5-40) display a more pronounced T-shape profile than the DCEP/DCEN weld beads (Figure 5-41).

Based upon the earlier results, it is clear that a single DCEN polarity arc will produce increased deposition but reduced penetration (compared to both DCEP and AC-SQ polarity). Therefore, it is suspected that when welding with an AC-SQ/AC-SQ tandem weld beads, the trail arc has a greater propensity to further increase penetration. As a result, it seems reasonable that there should be a primary rounded profile, with a deeper central penetration at the middle (forming the characteristic T-shape). As Figure 5-40 illustrates, the beads demonstrating the most severe T-shaped profiles (i.e., the beads labeled '43' and '45') were those with the greater trail arc current values. However, Figure 5-41 shows that a distinct T-shape profile was achieved when a high-current lead arc was combined with a low-current trail arc (i.e., the bead labeled '69'). It therefore is still uncertain how the lead and trail current and voltage settings control the bead shape for a tandem weld. The combination of the lead and trail variables does affect the weld bead cross-section profile, but the exact relationships between the variables has not yet been determined. As such, multi-variable statistical modeling analysis of the data may be helpful for future work.

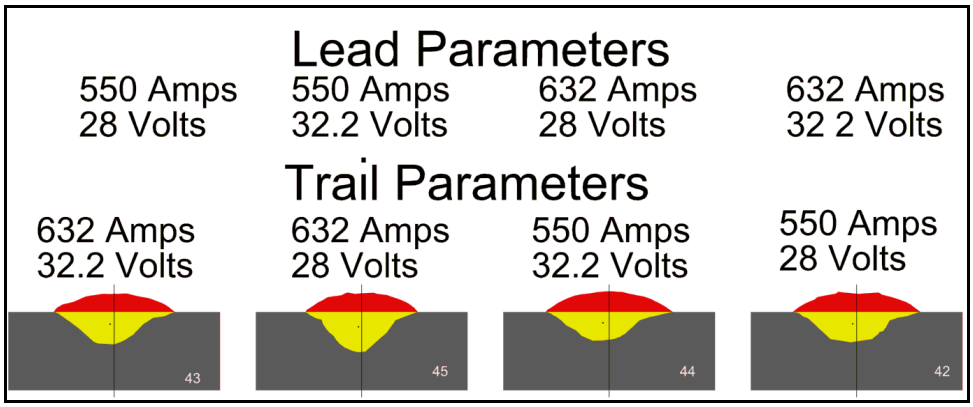

Figure 5-40: Cross-Section Profiles of AC-SQ/AC-SQ Weld Beads Produced Using Maximum Travel Speed

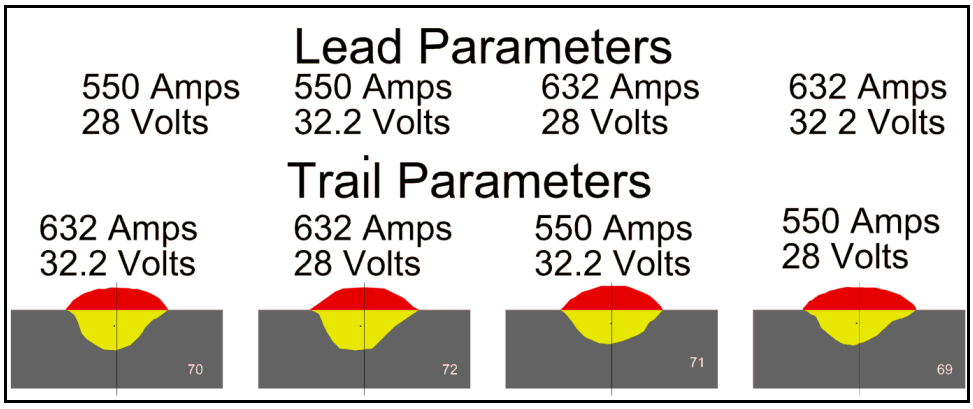

Figure 5-41: Cross-Section Profiles of DCEP/DCEN Weld Beads Produced Using Maximum Travel Speed

5.4: Group 3 Variable Weld Coupons

5.4.1 Effects of Input Parameters on Cross-Section Geometries

Analysis of the BOP welds began with a visual examination of the Group 3 bead cross-sections (Figure 5-42). All beads used the same voltage, current, and travel speed.

There were no visible trends caused by the variations in balance, offset, and frequency. Figure 5-42 clearly demonstrates that compared to the heat input parameters, the waveform variables caused only minor effects on bead cross-section geometry. Bar charts initially were generated, but they were discarded because no trends were visible between beads. It is suspected that the bead cross-section variations (as functions of welding distance), though small, were of a comparable magnitude to the minute cross-section variations caused by the waveform variables. As a result, only the reinforcement trends were considered, as they could be linked directly to the wire feed speed (WFS), which was measured with high accuracy using Lincoln Electric Command Center software.

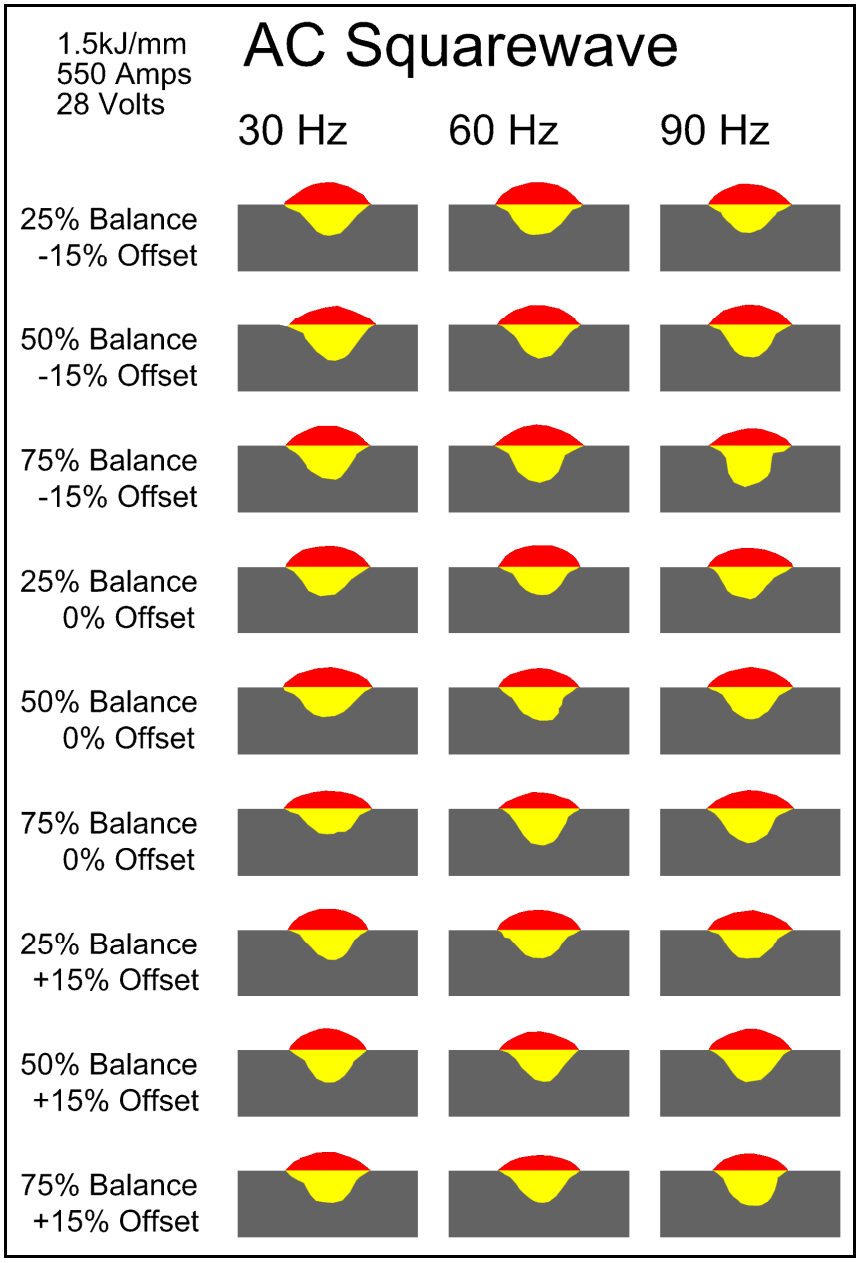

Figure 5-42: Group 3 Weld Bead Cross-Sections

5.4.2 The Effects of Balance (%)

Balance is the percentage of time that the square-wave current is held at DCEP polarity. The effect of current balance on WFS is illustrated in Figure 5-43.

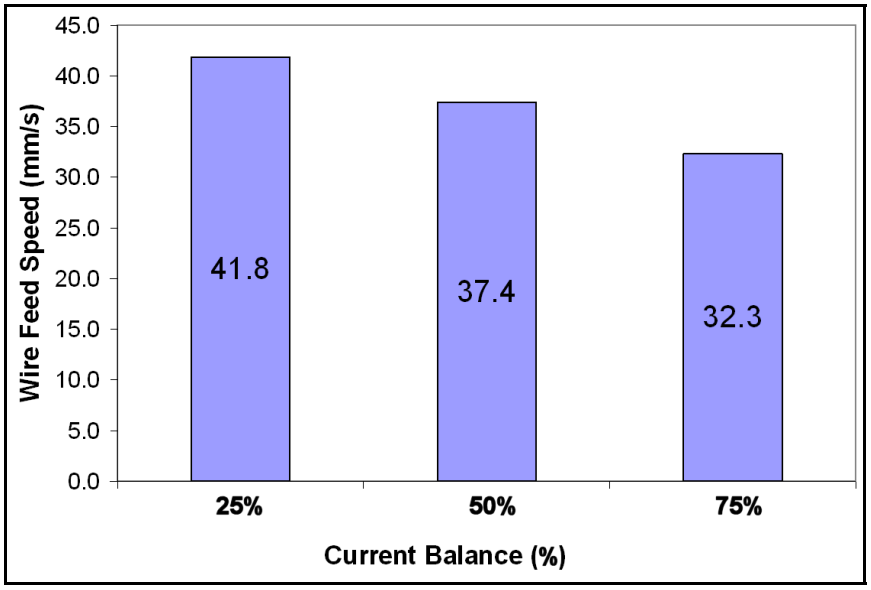

Figure 5-43: The Effect of Current Balance on WFS

Figure 5-43 shows that as balance increases, WFS (and hence reinforcement) decreases. This was expected, because a shift in polarity from DCEN to DCEP typically decreases reinforcement. The relationship appears to be linear.

5.4.3 The Effects of Offset (%)

Offset is the percentage by which the DCEP current amplitude is increased (and the same percentage by which the DCEN current amplitude is decreased). The effect of current offset on WFS is illustrated in Figure 5-44.

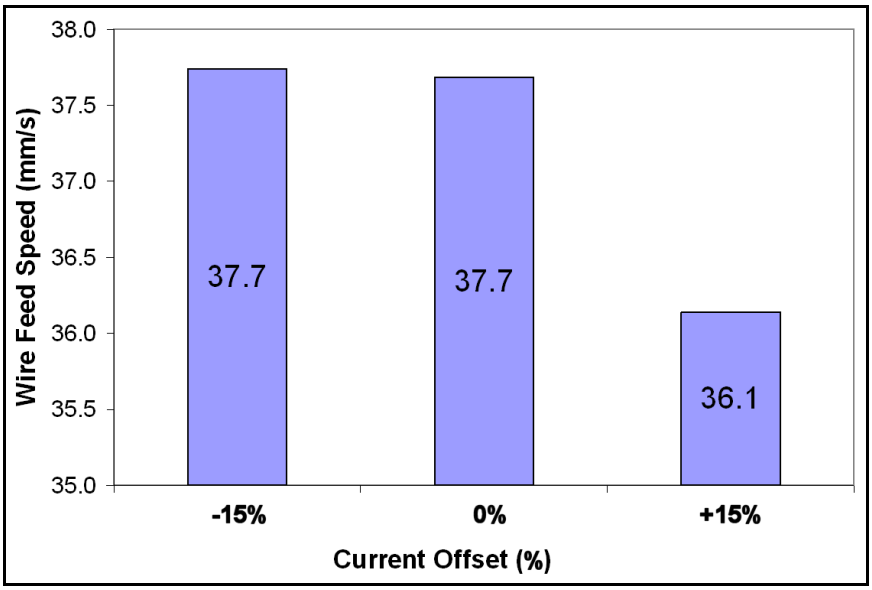

Figure 5-44: The Effect of Current Offset on WFS

Figure 5-44 indicates that an offset change, from -0.15 to 0, had virtually no effect on WFS (and hence reinforcement) for a single electrode weld bead. There was a slight reduction in WFS when the offset was increased to 0.15. With a greater offset, the WFS was expected to decrease, primarily due to reduced DCEN current amplitude. However, the shift from -0.15 to 0 was expected to cause a reduction in WFS too. The use of an oscilloscope on future welds may be beneficial in better determining the relationship between offset and WFS. It also is worth considering that the shift from 36.1 to 37.7 mm/s represents only a 3% difference.

5.4.4 The Effects of Frequency (Hz)

Frequency controls the number of polarity shifts between DCEN and DCEP per second. Assuming the current polarity shifts instantaneously, frequency should have no effect on a single electrode weld bead cross-section geometry. However, if the polarity shift is not instantaneous, the time at peak current should decrease,

resulting in decreased penetration and reinforcement. The effect of frequency on WFS is shown in Figure 5-45.

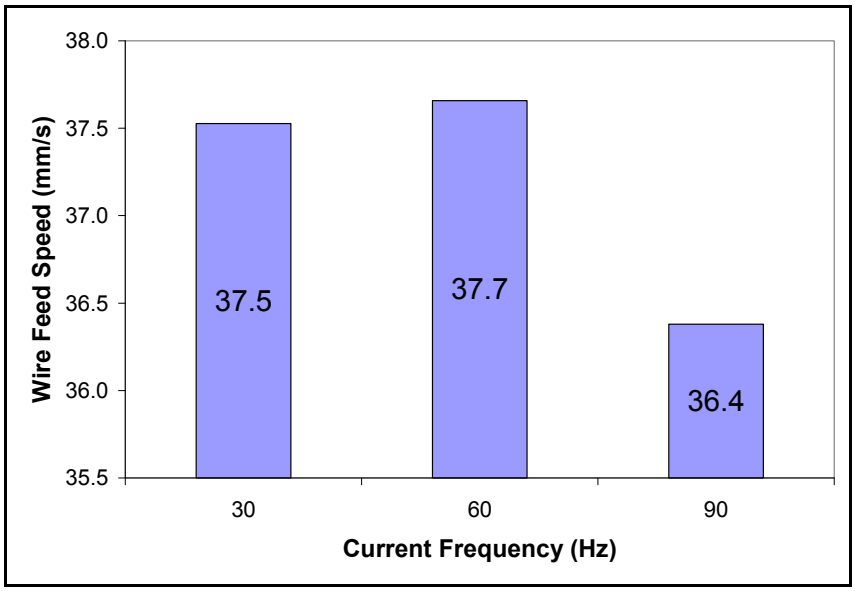

Figure 5-45: The Effect of Current Frequency on WFS

Figure 5-45 indicates that a frequency change, from 30 Hz to 60 Hz, had virtually no effect on WFS (and hence reinforcement) for a single electrode weld bead. There was a slight reduction in WFS when the frequency was increased to 90 Hz. Welding at such a high frequency may have resulted in either a reduced peak current with a near-instantaneous polarity shift, or a slower polarity shift with a maintained peak current. Confirmation with an oscilloscope on future welds would be beneficial. It also is worth noting that the WFS decrease from 37.7 to 36.4 mm/s represents only a 3% difference.

Overall, no strong trends, linking waveform variables to cross-section geometries, were found. Waveform parameters are strongly related to the effects of polarity variation on bead geometry. It, therefore, is suspected that using a greater arc current (i.e., 700 A or greater) may result in more noticeable trends linking waveform variables to bead geometry.

5.4.5 Effects of Waveform Variables on Bead SP Ratio

SP ratios for the Group 3 weld bead cross-section profiles were measured, in the hopes of identifying trends relating balance, offset, and frequency to bead shape (Figure 5-46, Figure 5-47, and Figure 5-48 respectively). None of the three charts illustrate strong trends relating the respective waveform variables to SP ratio values. It is, however, suspected that using a greater arc current (i.e., 700 A or greater) may result in more noticeable trends linking waveform variables to bead shape (i.e., SP ratio).

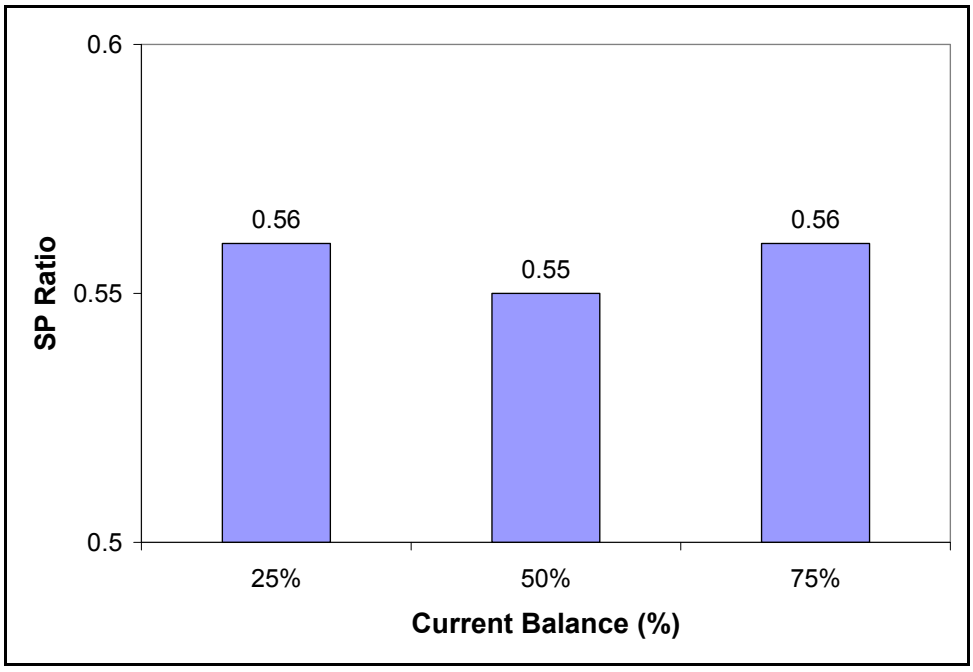

Figure 5-46: The Effect of Current Balance on SP Ratio

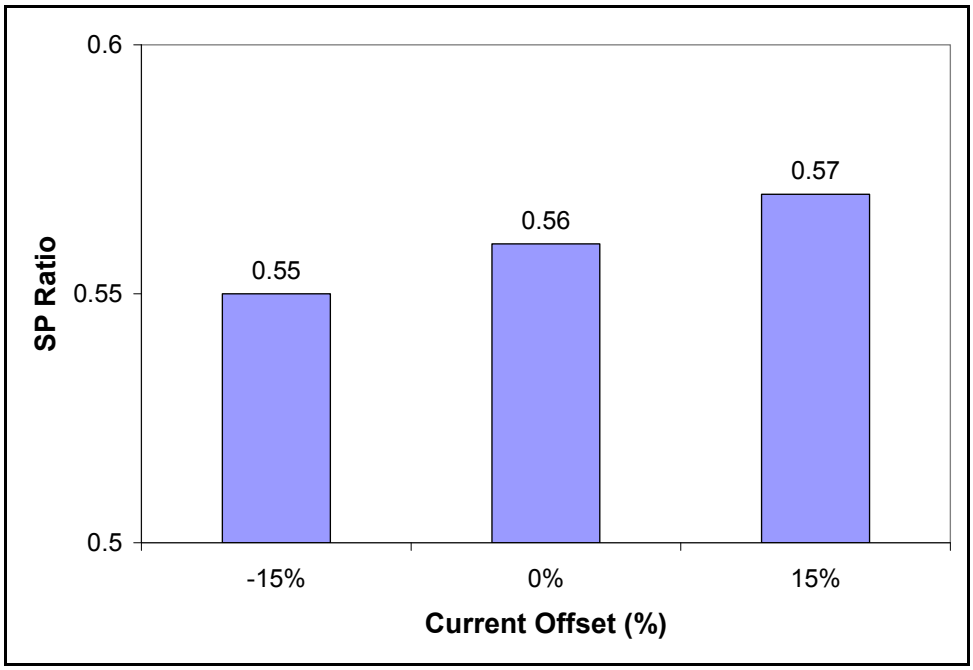

Figure 5-47: The Effect of Current Offset on SP Ratio

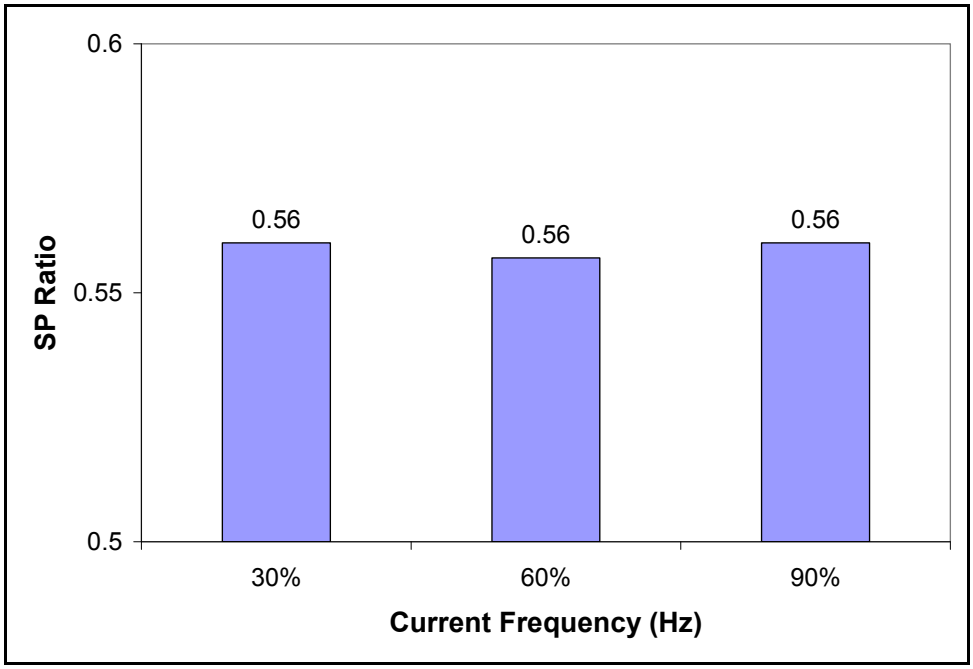

Figure 5-48: The Effect of Current Frequency on SP Ratio

5.5: Group 4 Variable Weld Coupons

5.5.1 Effects on Input Parameters on Cross-Section Geometries

Analysis of the BOP welds began with visual examination of the Group 4 bead cross-sections (Figure 5-49). Weld bead 55B, from the Group 2 welds, was the weld bead using an AC-SQ trail 60 Hz frequency, 50% balance, and 0% offset. There were no visible trends linking variations in balance, offset, and frequency to weld bead geometry. Pivot charts initially were generated, but once again were discarded because no trends were determined. Again, it is suspected that bead cross-section variations (as functions of welding distance) were of a comparable magnitude to the minute cross-section variations caused by the waveform variables. Therefore, the trends were hidden. However, WFS should be proportional to the reinforcement volume because increases in WFS result in increases in electrode deposition. While the WFS values can not provide the insight available from cross-section measurements (i.e., bead width to reinforcement ratios, etc.), they were recorded with a high precision, making it possible to at least detect subtle differences in reinforcement volume. Therefore, the welding variables were plotted against the corresponding WFS output values.

The effects of trail current balance, offset, and frequency were compared to trail WFS (Figure 5.39, Figure 5-51, and Figure 5-52, respectively). The trends for trail arc balance and offset and corresponding WFS were consistent with the trends determined in Section 5.4. As trail current balance was increased, WFS decreased. As trail current offset was increased from -0.15 to 0, the WFS remained virtually unchanged. Increasing trail frequency reduced trail WFS a very small amount, but unlike the results from Section 5.4, there was no sudden WFS decrease when 90 Hz was selected.

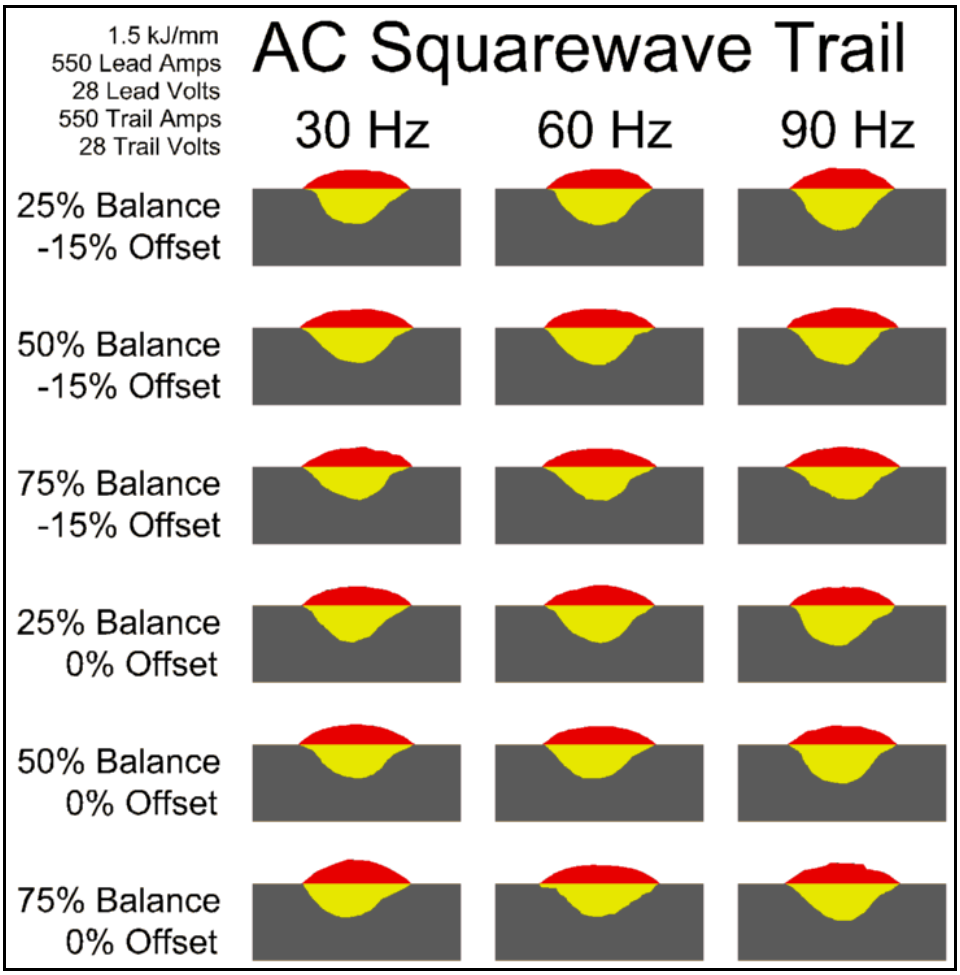

Figure 5-49: Group 4 Weld Bead Cross-Sections

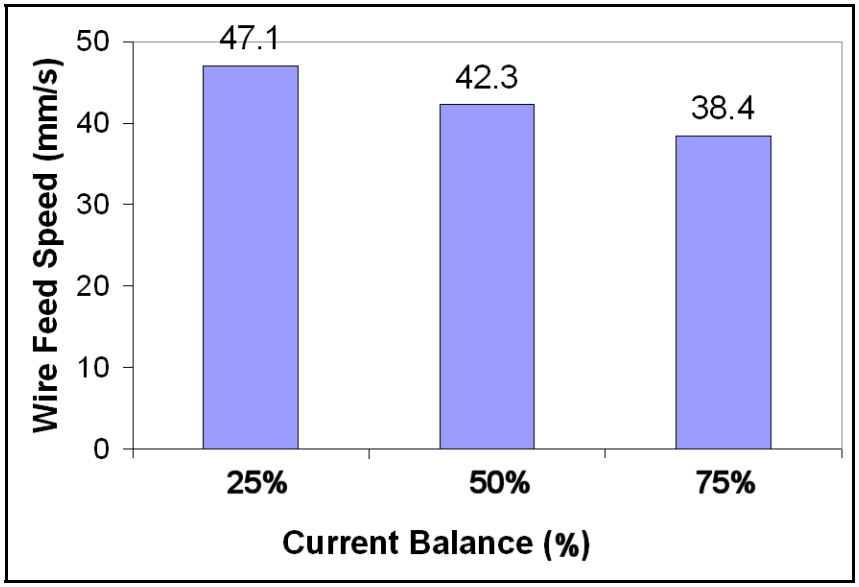

Figure 5-50: The Effect of Trail Current Balance on Wire Feed Speed

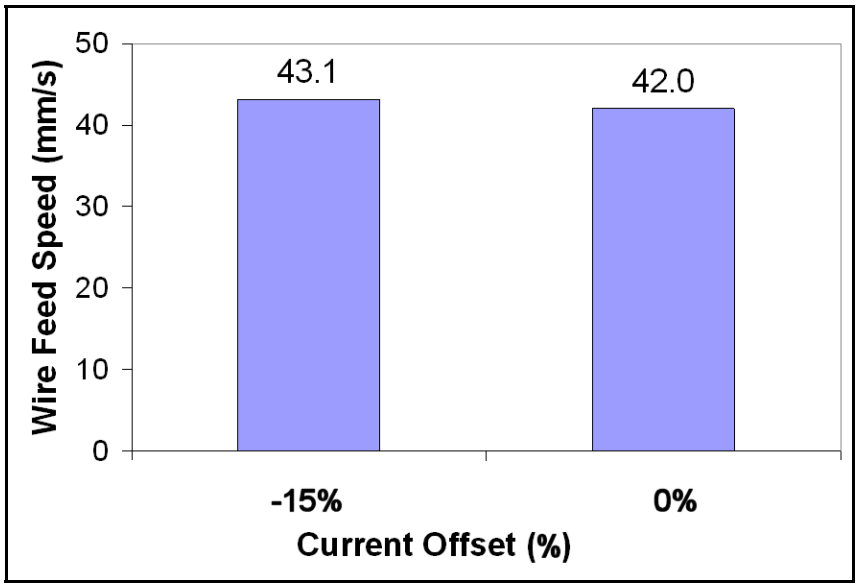

Figure 5-51: The Effect of Trail Current Offset on Wire Feed Speed

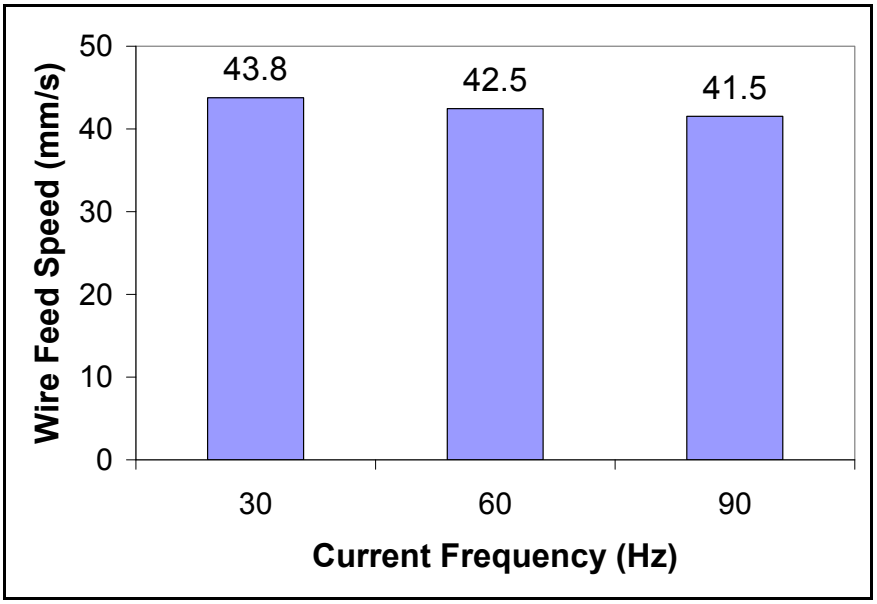

Figure 5-52: The Effect of Trail Current Frequency on Wire Feed Speed

5.5.2 Effects of Waveform Variables on Bead SP Ratio

The Group 2 SP ratio analysis cannot be adequately explained without the use of multi-variable statistical modeling analysis (i.e., future work), and the Group 3 SP ratio analysis yielded no trends. As a result, the evaluation of Group 4 SP ratio analysis was left for future work, after sufficient numerical modeling can be completed.

5.6: Conclusions

Submerged arc welding was used to produce a series of BOP welds. Welds were grouped on the basis of the variables manipulated (heat input or waveform variables), as well as the number of electrodes used (single or tandem). In the case of the BOP welds produced by manipulating heat input variables (Group 1 and Group 2), the heat input values were controlled by changing travel speed. These changes in travel speed complicated the analysis greatly, and trends were determined by comparing differences in molten penetrated or deposited volume rates produced per second of welding. There were several Group 1 welds with unacceptable bead width variation along the welding distance; such unstable bead profiles were the result of extreme variations in voltage, current, and travel speed. The unacceptable beads were not analyzed, and the Group 2 welds were then produced using less extreme ranges of heat input variables. All beads from Group 2, 3, and 4 had acceptable bead profile stability.

When a single electrode was used, increases in current resulted in increased penetration and reinforcement volume rates. Increases in voltage caused a decrease in reinforcement volume rate, but no definite trend was confirmed between voltage and penetration. A polarity shift from DCEN to AC-SQ to DCEP typically reduced reinforcement and increased bead width. At higher current, the same polarity shift also produced a clear increase in penetration.

A useful method of evaluating bead shape (i.e., the SP ratio) was developed. When penetration depth is also considered, the combination provides a good numerical way of qualifying overall bead appearance. It was shown that as travel speed for a single electrode weld was increased, the SP ratio increased also.

When a tandem electrode system was used, a shift in the lead arc polarity from AC-SQ to DCEP was found to reduce lead WFS, while a more significant increase in trail WFS was noted when trail polarity was shifted from AC-SQ to DCEN. The sum of lead and trail WFS values was used to explain the effects of lead and trail polarity on reinforcement. When the lead arc polarity was shifted from AC-SQ to DCEP, the penetration increased. However, a shift from AC-SQ to DCEN trail polarity did not cause a reduction in penetration. It is suspected that the relationship between phase offset and arc attraction / repulsion frequency may be the cause of this trend. To determine this trend definitively, a high speed camera would be required in conjunction with a tandem welding process using an exposed arc, preferably with a consumable electrode (e.g., GMAW). When only direct current was used for both arcs, the weld bead cross-sections were typically offset to the left, presumably due to grounding. This was explored further when the SP ratio values were investigated for the Group 2 weld beads: bead cross-section profile asymmetry artificially raises SP ratio values.

With the BOP welds produced by manipulating the waveform variables (Group 3 and Group 4), cross-section variations were extremely small, and pivot charts yielded no strong trends. It is suspected that even though bead width variation was acceptable for Group 3 and 4 weld beads, the small variations along the cross-section still were of the same magnitude of the variations caused by manipulating the waveform variables. As a result, the only trends produced from Group 3 and 4 welds is the effect of trail electrode WFS, which is synonymous with deposition (i.e., reinforcement). For the single electrode welds, increasing balance decreased WFS (i.e., deposition). Setting the offset to 0.15, and the frequency to 90 Hz, also reduced the WFS. For the tandem electrode welds, WFS was decreased by increasing current balance, offset, and frequency. In all cases,

the actual changes in WFS were very minute. Additionally, because the waveform manipulation variables are closely linked to polarity, it is suspected that performing welds using higher welding currents may cause waveform variable effects to become more apparent.

CHAPTER 6: SUBMERGED ARC WELDING PARAMETERS AND BEAD-ON-PLATE WELD PROPERTIES

In this chapter, sub-size Charpy V-notch (SS-CVN) test specimens were extracted from several BOP welds, to further test the relationships between weld bead cross-section geometric measurements (e.g., penetration area and SP ratio) and notch-toughness results.

In Chapter 5, bead-on-plate (BOP) welds were performed to better understand the relationships between welding parameters and weld bead cross-section geometry. However, the heat input values in many of the welds from Chapter 5 were controlled by manipulating travel speed. As a result, the changes in travel speed affected the cross-section bead geometries too, making it difficult to isolate the effects on geometry from manipulating other welding variables. To compensate for this problem, much of the analysis from Chapter 5 investigated the effects of welding parameters on penetration and reinforcement volumetric rates.

Measuring volumetric rates was critical in understanding the isolated effects of manipulating various welding variables. However, both the initial literature review and the results from Chapter 3 indicated a link between weld bead cross-section geometry (i.e., 2-dimensional measurements) and Charpy V-notch (CVN) impact energies. As a result, comparisons were not made between the volumetric rates and the SS-CVN impact energies. In addition to typical weld bead cross-section measurements (i.e., penetration and reinforcement depths and areas, as well as bead width), the profile shape (i.e., the SP ratio) also was compared with SS-CVN impact energies.

6.1: Experimental Procedure

It was necessary to evaluate the effects of welding parameters and corresponding bead geometries on notch-toughness. However, most of the BOP weld cross-sections possessed penetration depths adequate to accommodate full-size CVN test specimens. As a result, SS-CVN specimens (with a thickness of 5 mm, 0.2 in.) were produced to evaluate the comparative CVN fracture energy values of the various weld beads. While this prevented the evaluation of weld beads with penetration depths less than 5 mm (0.2”), weld beads possessing a wide range of bead geometries, or produced using a great variety of welding variable values, were still tested.

6.1.1 Sub-Size Charpy-V-Notch Specimen Extraction

Mechanical testing was not considered when the BOP welds were first produced. As a result, the beads were placed quite close together, to allow for more welds to be deposited on the same number of weld coupons. Because of the close proximity of the BOP welds to each other, and limited bead length, it was not always possible to extract sub-size coupons from adjacent beads (refer to Figure 6-1, which illustrates a weld coupon at top, and proposed SS-CVN specimen locations below). When combined with the requirement that a minimum bead penetration of 5 mm was required for test specimen extraction, only a limited number of welds underwent SS-CVN evaluation.

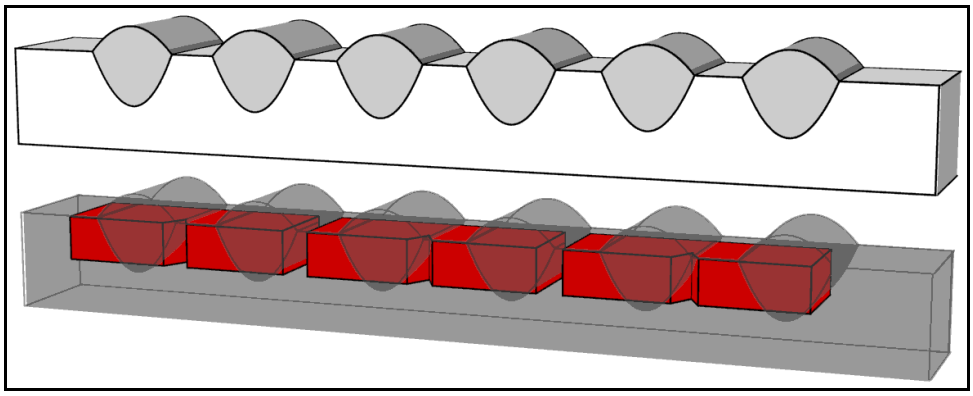

Figure 6-1: Schematic of SS-CVN Specimen Extraction from BOP Weld Coupons

The initial bevel weld work determined connections between weld bead geometry and notch-toughness. Therefore, beads demonstrating extreme geometric values (e.g., largest or smallest penetration area) were selected for SS-CVN evaluation. Beads were selected to best represent high and low values of the following measurements:

- Aspect Ratio (i.e., "penetration depth" / "bead width")
- Area Ratio ("reinforcement area" / "penetration area")
- Reinforcement Area (mm^2)
- Penetration Area (mm^2)
- Total Molten Area (mm^2) (the sum of reinforcement and penetration areas)

The SS-CVN results also were compared with the corresponding weld bead SP ratio values, as were the linear weld bead cross-section measurements (i.e., penetration depth, reinforcement height, and bead width). Table 6-1 to Table 6-4 summarize the beads selected for SS-CVN evaluation, along with their corresponding input welding parameters.

Table 6-1: Group 1 Beads Selected for SS-CVN Evaluation

Weld Bead	Polarity	Current (Amps)	Voltage (Volts)	Travel Speed (mm/s)	Heat Input (kJ/mm)	Frequency (Hz)	Balance (%)	Offset (%)
8	AC-SQ	550	28	10.6	1.5	60	50	0
9				6.2	2.5			
11			32	11.9	1.5			
12				7	2.5			
14		700	28	13.5	1.5			
15				7.8	2.5			
17			32	14.8	1.5			
18				8.9	2.5			
24	DCEP	700	28	7.8	2.5	N/A	N/A	N/A
26			32	8.9	2.5			
32	DCEN		28	7.8	2.5			
34			32	8.9	2.5			

Table 6-2: Group 2 Beads Selected for SS-CVN Evaluation

Weld Bead	LEAD ELECTRODE			TRAIL ELECTRODE			Travel Speed (mm/s)	Heat Input (kJ/mm)	Phase Offset (Deg.)
	Polarity	Current (Amps)	Voltage (Volts)	Polarity	Current (Amps)	Voltage (Volts)			
38	AC-SQ	632	28	AC-SQ	550	28	22.0	1.50	90
39		550	28		632	28			
41		550	28		550	32.2			
46		550	28	DCEN	550	28	20.5		N/A
47		632	28		550	28	22.0		
56	DCEP	632	28	AC-SQ	550	28			
61		550	28		632	32.2	23.7		
62		632	28		550	32.2			
63		550	32.2		632	28			
65		632	28	DCEN	550	28	22.0		
69		632	32.2		550	28	23.7		
72		550	32.2		632	28			

Table 6-3: Group 3 Beads Selected for SS-CVN Evaluation

Weld Bead	Polarity	Current (Amps)	Voltage (Volts)	Travel Speed (mm/s)	Heat Input (kJ/mm)	Frequency (Hz)	Balance (%)	Offset (%)
74	AC-SQ	550	28	10.6	1.5	60	50	15
76							75	0
77								15
78								-15
81							25	-15
82						30	50	0
83								15
84								-15
89							25	15
90								-15
95						90	75	15
96								-15

Table 6-4: Group 4 Beads Selected for SS-CVN Evaluation

Weld Bead	Lead Polarity	Trail Polarity	Lead & Trail Current (Amps)	Lead & Trail Voltage (Volts)	Travel Speed (mm/s)	Heat Input (kJ/mm)	Trail Frequency (Hz)	Trail Balance (%)	Trail Offset (%)
111	DCEP	AC-SQ	550	28	20.6	1.5	30	50	-15
115								25	0
117									-15
118							90	50	0
120									-15
121								75	0
123									-15
124								25	0
126									-15

For consistency with earlier testing, all specimens had their 5 mm notches located at the fusion line (FL) location (refer to Figure 3-9). However, thermal stresses from welding caused the weld coupon top surfaces to become concave. Additional machining then was required to ensure flat SS-CVN specimens, effectively reducing the depth of the remaining bead penetration. As a result, many SS-CVN specimens demonstrated incomplete bead penetration (Figure 6-2).

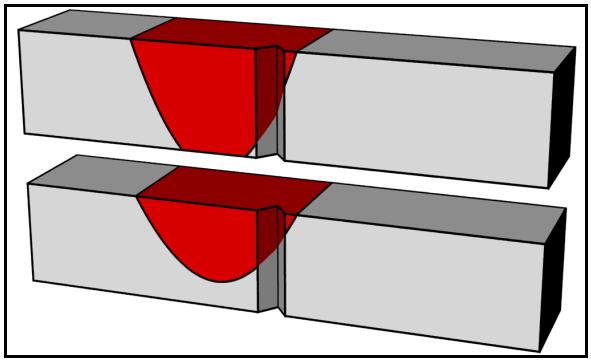

Figure 6-2: SS-CVN Specimen Demonstrating Full Bead Penetration (Top) and SS-CVN Specimen Demonstrating Incomplete Bead Penetration (Bottom). WM is shown in red.

6.1.2 Testing Parameters

CVN testing, sample tolerances, and equipment calibrations were performed in compliance with ASTM A370-03a for 5 mm sub-size specimens [4]. For each combination of weld bead, notch location, and test temperature, three specimens (labeled "a," "b," and "c") were machined and tested. During testing, each specimen was removed from a cooling bath and mounted into the test apparatus. It was critical that each sample was struck by the hammer within five seconds of being removed from the cooling bath, to help ensure that all specimens were tested at a consistent temperature. Failure to impact a specimen within five seconds of its removal from the cooling bath resulted in the test result being rejected. A test result also would be rejected if a tested specimen was not mounted straight in the test apparatus.

All specimens were tested at the Alberta Research Council Millwoods Facility, using a Tinius Olsen CVN tester (S/N 117802), with a 358 Joule maximum capacity. The ductile-to-brittle transition curve changes with CVN specimen thickness [6]. Therefore, base-metal sub-size specimens were tested first, to establish a suitable sub-size specimen test temperature.

6.2: Base Metal Results

Three sub-size base metal specimens were tested at three test temperatures: 0°C (32°F), -20°C (-4°F), and -50°C (-58°F). As per Figure 6-3, the SS-CVN fracture energy values at -20°C and 0°C were very similar, whereas testing at -50°C produced lower impact energies. The similarities in values at the two higher temperatures, with the slight reduction at -20°C, indicates that -20°C should be near the cusp of the transition curve upper-shelf. The error bars represent one standard deviation.

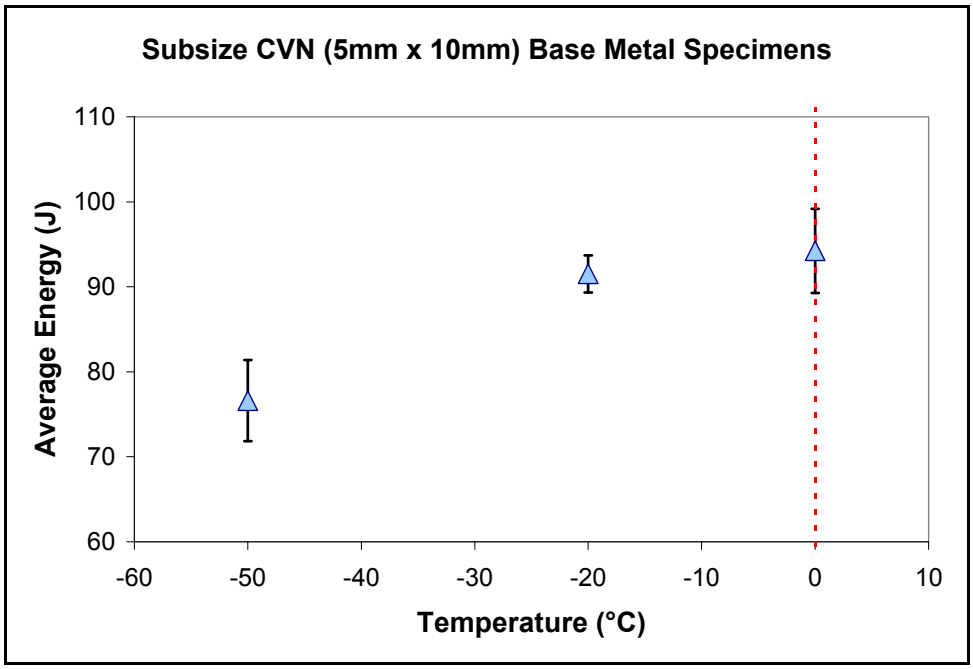

Figure 6-3: The Effect of Test Temperature on 5 mm SS-CVN Test Specimen Results (J)

When sub-size testing was selected as a means of evaluating the weld beads, excessively low total test energy values were a concern. Based on the bevel weld results (Chapter 3), the unaffected base metal SS-CVN specimens should achieve the highest SS-CVN fracture energy values. If the base metal results were too low, it would have been difficult to determine SS-CVN trends between different weld beads. If the average base metal value was 10 joules, it is expected that HAZ CVN values would range from 0 to 10 joules. Considering that CVN fracture energy value standard deviations are typically a few Joules, predicting strong trends would not be possible. However, if the average base metal value was 100 Joules, it is expected that HAZ CVN values would spread out, making trends easier to perceive. With base metal SS-CVN fracture energy values between 90 J and 100 J at the upper shelf, there should be sufficient variation between welded test specimens and the base metal speciements to allow for trends to present themselves.

Therefore, a test temperature of -20°C was selected for the FL specimens. Any detrimental microstructure effects from welding should produce obvious changes in SS-CVN fracture energy values.

6.3: Group 1 SS-CVN "FL" Notch Location Specimens

6.3.1 Initial Comparison of Geometric Values with SS-CVN Fracture Energy Values

The SS-CVN average values were first compared with the geometric area measurements (i.e., area ratio, reinforcement area, penetration area, and total molten area). The corresponding plots are illustrated in Figure 6-5 to Figure 6-7.

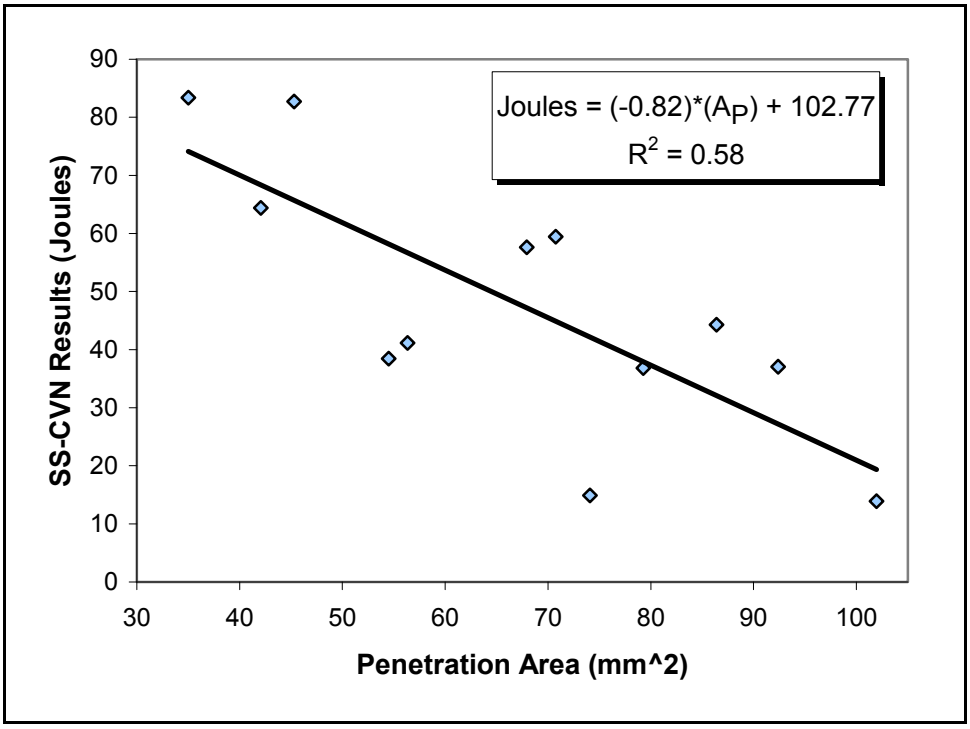

Figure 6-4: The Effect of Penetration Area (mm^2) on SS-CVN Fracture Energies of Group 1 Test Specimens

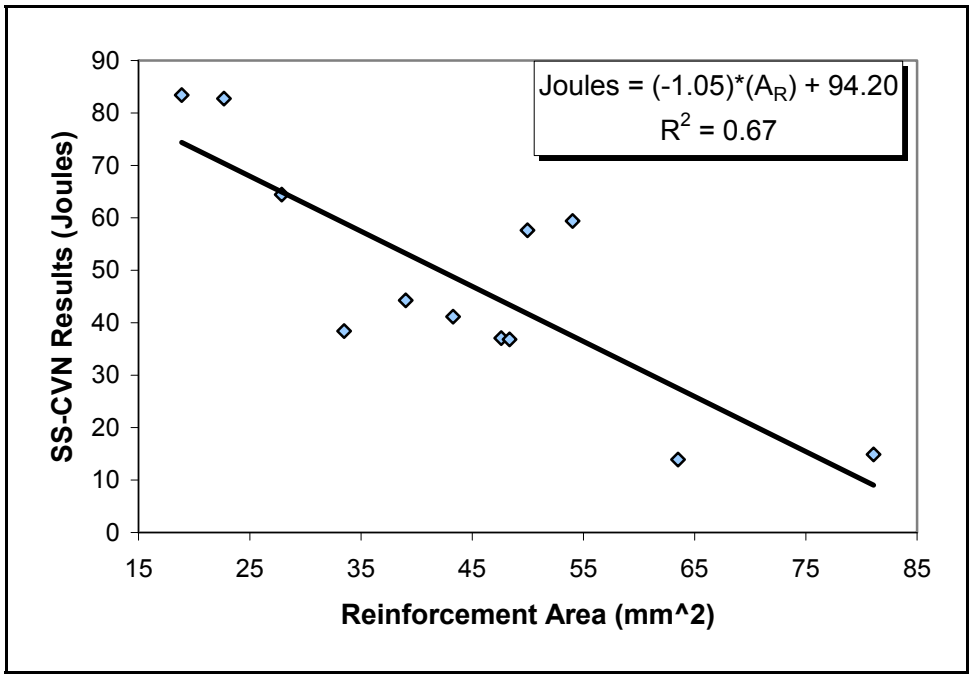

Figure 6-5: The Effect of Reinforcement Area (mm^2) on SS-CVN Fracture Energies of Group 1 Test Specimens

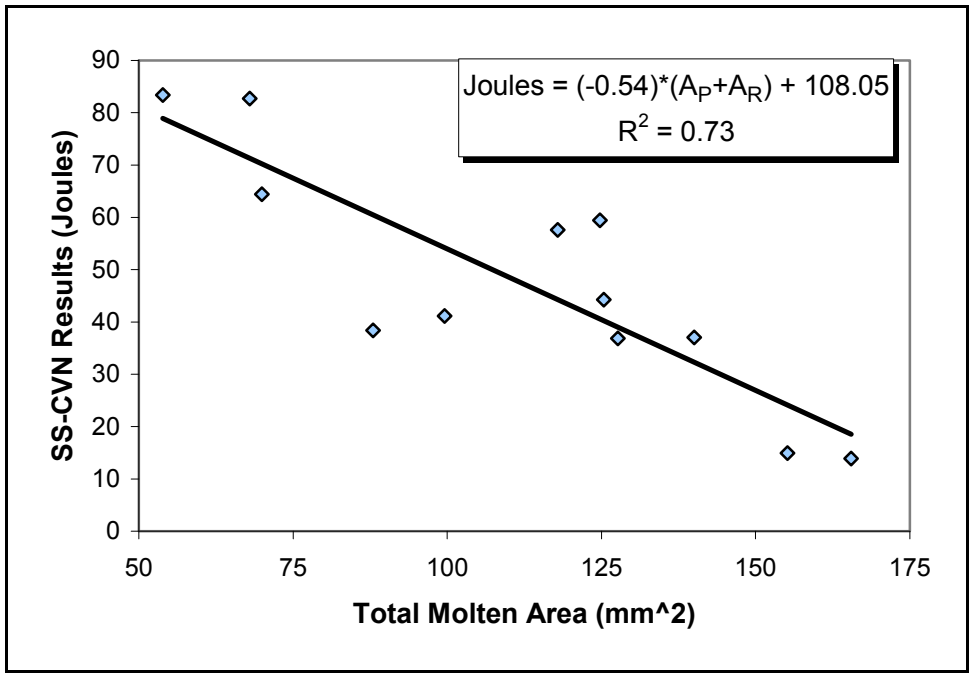

Figure 6-6: The Effect of Total Molten Area (mm^2) on SS-CVN Fracture Energies of Group 1 Test Specimens

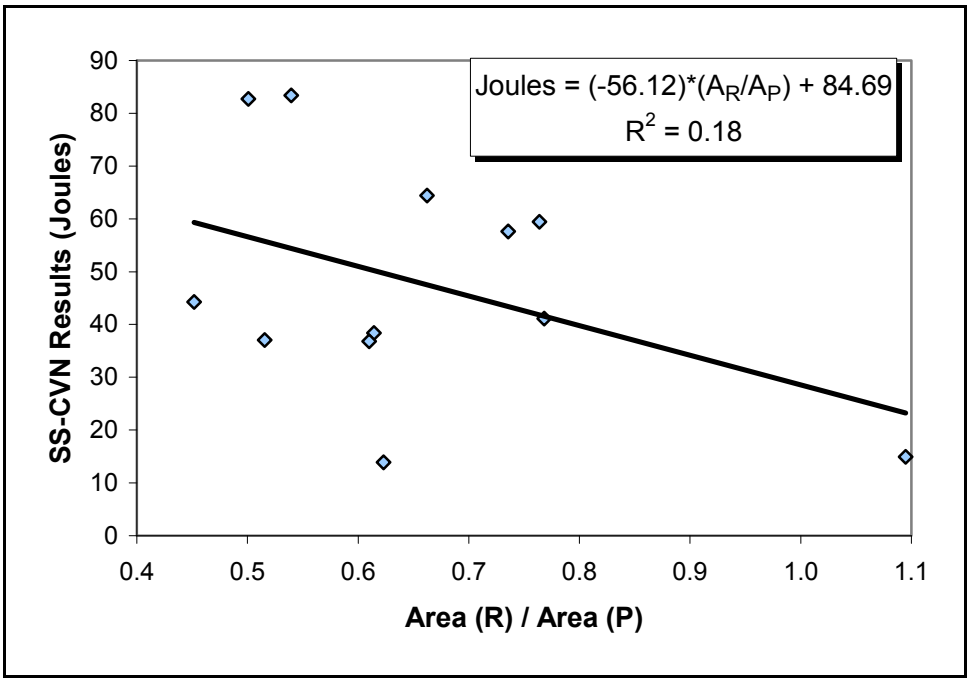

Figure 6-7: The Effect of Area Ratio (A_r/A_p) on SS-CVN Fracture Energies of Group 1 Test Specimens

Figure 6-4 demonstrates a linear relationship between penetration area and SS-CVN fracture energy values; increases in penetration area result in decreased SS-CVN fracture energy values. Such a relationship should be expected. As the penetration area increases, additional heat will be available to the adjacent HAZ material, resulting in the HAZ being exposed to higher temperatures, for longer durations of time. Accordingly, a greater width of adjacent unmelted material will be exposed to the thermal conditions necessary to produce CGHAZ material (i.e., the CGHAZ widens). This wider CGHAZ would cause greater fractions of the SS-CVN notches to pass through it (Section 2.7.1). As the results from Chapter 3 illustrated, increased notch fractions of CGHAZ should result in reduced SS-CVN fracture energy values.

Another linear trend is illustrated in Figure 6-5, showing that greater reinforcement areas resulted in lower SS-CVN fracture energy values. It is believed that as additional molten metal is deposited on top of the weld metal, in close proximity to the HAZ regions, the overall HAZ area should undergo slower cooling rates (and potentially wider areas should reach higher temperatures). By

a similar logic used to explain the trend from Figure 6-4, it makes sense that a greater reinforcement area could result in a larger CGHAZ, which in turn would reduce SS-CVN fracture energy values.

Figure 6-6 illustrates the combined effect of penetration area and reinforcement area on SS-CVN fracture energy values. Because increases in either of the individual areas typically resulted in decreased SS-CVN fracture energy values, it should not be surprising that increases in the combined area produced the same effect.

It should be noted that the variables required to produce large reinforcement areas (i.e., greater heat input) produce large penetration areas too. In other words, it is quite uncommon to achieve large reinforcement areas without achieving large penetration areas (or vice versa). One could potentially argue that because the trend illustrated in Figure 6-8 shows less scatter than the trends from Figure 6-4 and Figure 6-5, there appears to be evidence that both areas contribute to an overall effect on notch-toughness (and to neglect either contribution will result in a weaker trend). However, to further investigate the areas' individual effects, Figure 6-7 was plotted to demonstrate the effect of the area ratio on notch toughness. The figure illustrates no clear trend, which appears to indicate that penetration area and reinforcement area likely affect notch-toughness results via the same mechanism: increased volumes of molten metal will produce wider CGHAZ regions, which in turn will reduce SS-CVN fracture energy values.

While it is helpful to determine relationships between cross-section profile areas and SS-CVN fracture energy, special software is required and/or considerable time is needed to make such geometric measurements accurately. In contrast, recording weld bead cross-section linear measurements (i.e., bead width, penetration depth, and reinforcement height) is extremely straightforward. After the cross-section specimen is etched, only a caliper and a single measurement for each value is required. Therefore, it was important to determine if accurate trends could be determined relying only upon the linear measurements.

Width, penetration depth, and reinforcement height were plotted against SS-CVN fracture energy values in Figure 6-8 through Figure 6-10. The ratio between penetration depth and bead width was also investigated, by plotting these paramters in Figure 6-11.

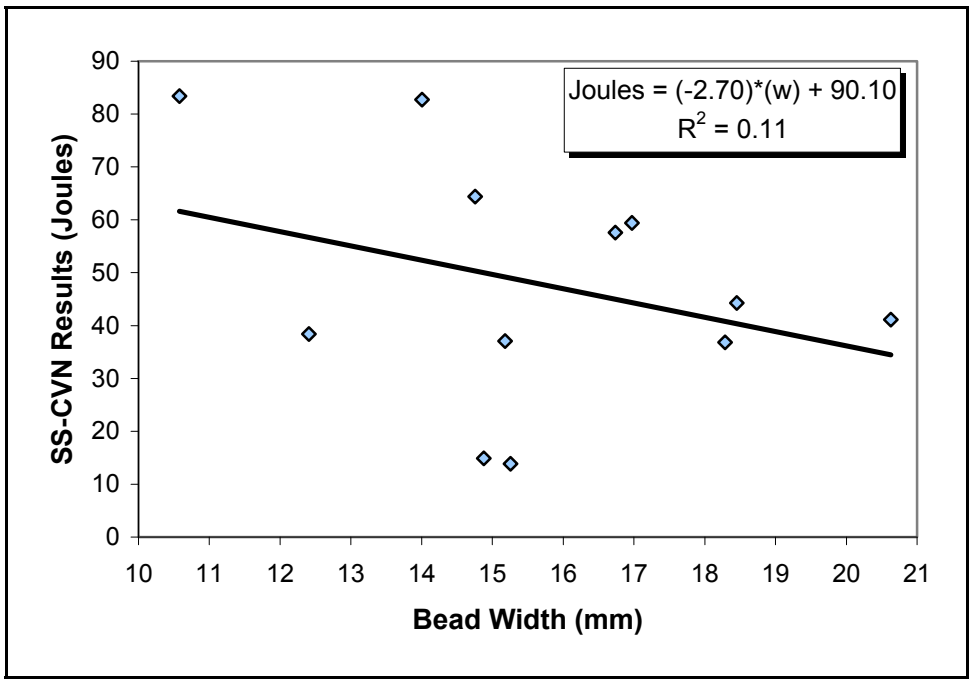

Figure 6-8: The Effect of Bead Width (mm) on SS-CVN Fracture Energies of Group 1 Test Specimens

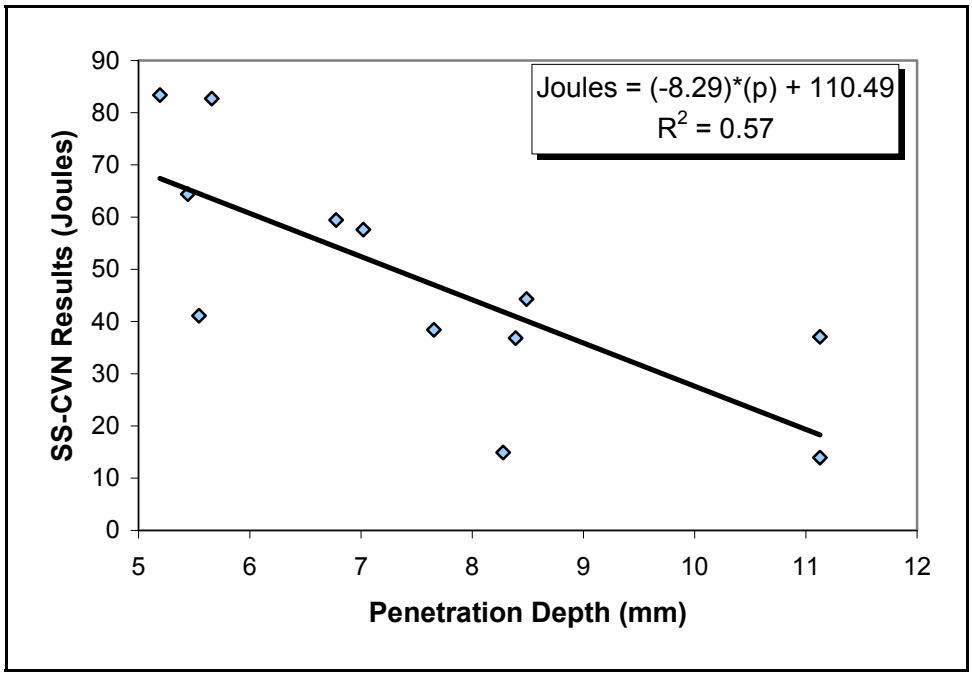

Figure 6-9: The Effect of Penetration Depth (mm) on SS-CVN Fracture Energies of Group 1 Test Specimens

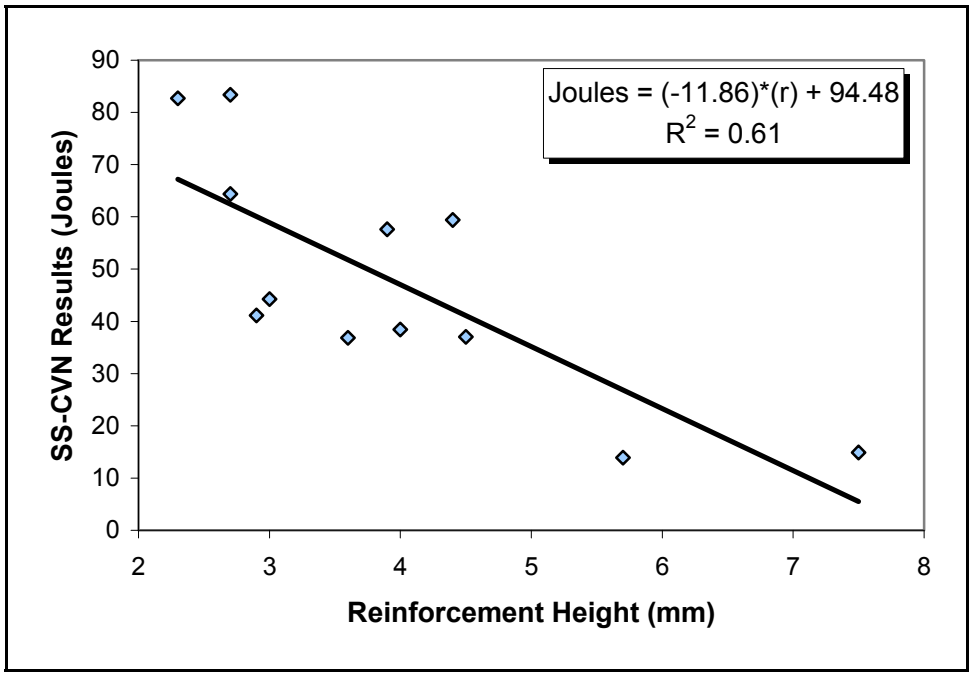

Figure 6-10: The Effect of Reinforcement Height (mm) on SS-CVN Fracture Energies of Group 1 Test Specimens

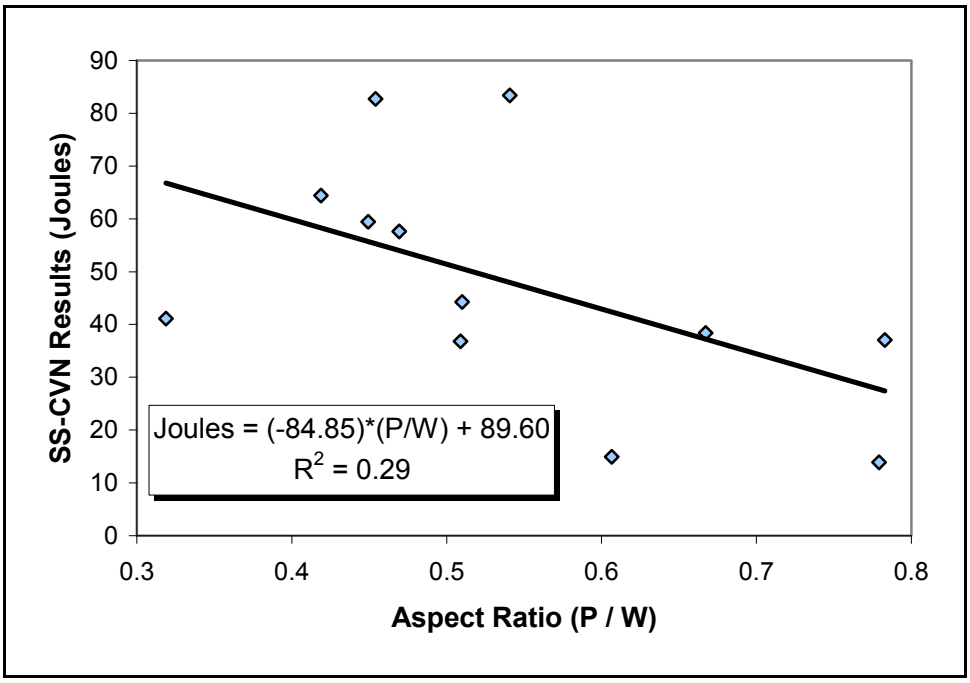

Figure 6-11: The Effect of Aspect Ratio (P/W) on SS-CVN Fracture Energies of Group 1 Test Specimens

Figure 6-8 does not appear to display a relationship between bead width and SS-CVN fracture energy values. This seems reasonable, because there is no theoretical reason for bead width to affect the SS-CVN test results. In particular, bead width does not address heat input (or by extension, the expected CGHAZ width).

Figure 6-9 illustrates the effect of penetration depth on SS-CVN fracture energy values. While an overall linear trend appears to be present, the relationship appears to be quite weak as the figure illustrates several considerable outliers. In contrast, the trend illustrated in Figure 6-10 appears to be stronger, with considerably smaller outlier values. For Figure 6-9 and Figure 6-10, increases in penetration depth or reinforcement height result in overall reductions in SS-CVN fracture energy values. In this respect, the trends of the two figures mimic those demonstrated by the corresponding area-based trends shown in Figure 6-4 and Figure 6-5 respectively.

As the results from Chapter 3 indicated, the fusion line slope at the CVN notch should affect the corresponding CVN test results. It was reasoned that an increased fusion line slope should result from a deeper penetration depth and a reduced bead width. While the effect of aspect ratio (i.e., P/W) was plotted against SS-CVN fracture energy values (Figure 6-11), there does not appear to be a strong relationship between the two.

At first, this was a surprising result, especially because both the literature (Section 2.7.1) and earlier work indicated a strong relationship between SS-CVN fracture energy values and fusion-line slope. However, the relationship from Chapter 3 considered the fusion line slope contained within the CVN test specimen (refer to Figure 3-29 on page 55 in particular). Furthermore, Figure 5-24 (on page 98) illustrates an extreme example of two beads with the same width and same penetration values (and hence, the same aspect ratio), but with very different profile shapes. Because SP ratios provide an indication of penetration shape, it was plotted against SS-CVN fracture energy in Figure 6-12.

As Figure 5-24 shows, a bead with a high SP ratio, with a bulbous cross-section geometry, will present a more rounded fusion line slope at the mid-penetration depth (i.e., from where the SS-CVN specimens were extracted), which in turn should reduce the length of CGHAZ passing through the test specimen notch. This in turn should improve SS-CVN fracture energy values. Alternatively, if a test specimen is removed from a T-shaped weld bead (i.e., one with a low SP ratio), the fusion line passing through the SS-CVN test specimen notch could be extremely steep, resulting in a significant increase in the amount of CGHAZ passing through the notch. As a result, it is expected that a lower SP ratio should result in reduced SS-CVN fracture energy values.

The SP ratio values were plotted against the average SS-CVN fracture energy values (Figure Figure 6-12). Surprisingly, no clear trend was evident.

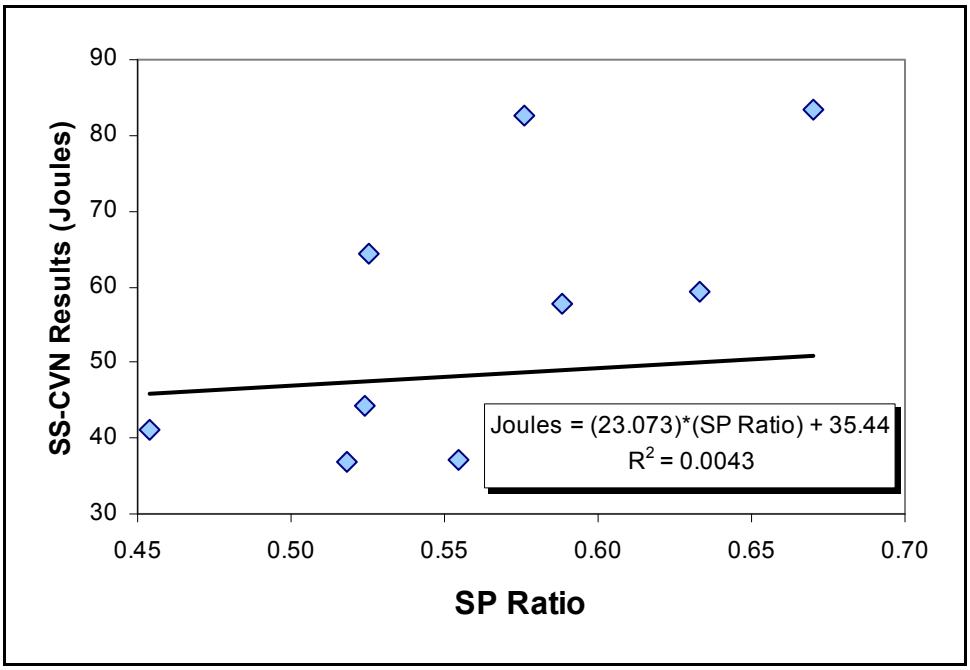

Figure 6-12: The Effect of SP Ratio on SS-CVN Fracture Energies of Group 1 Test Specimens

6.3.2 Comparison of Individual SS-CVN Specimen Geometry to SS-CVN Fracture Energy Values

Based on the literature review (Section 2.7.1) and initial CVN fracture energy tests (Chapter 3), it was expected that there would be a correlation between notch-toughness results and fusion line slope. Fusion line slope was calculated by dividing the penetration depth by half of the bead width, and calculating the inverse tangent value of the quotient. One possible explanation for the poor correlation (Figure 6-11) is that there could be considerable sub-surface bead geometry variation along the weld bead length. Future work would be required to confirm this issue. Each SS-CVN test specimen (i.e., specimen "a," "b," or "c") had its fusion line slope measured prior to testing (Figure 6-13). The values appear to vary by as much as 10°, but when the results were averaged (Figure 6-14) and compared with the initial macroscopic investigation values (Figure 6-15), the average fusion line slopes correspond closely for each weld bead.

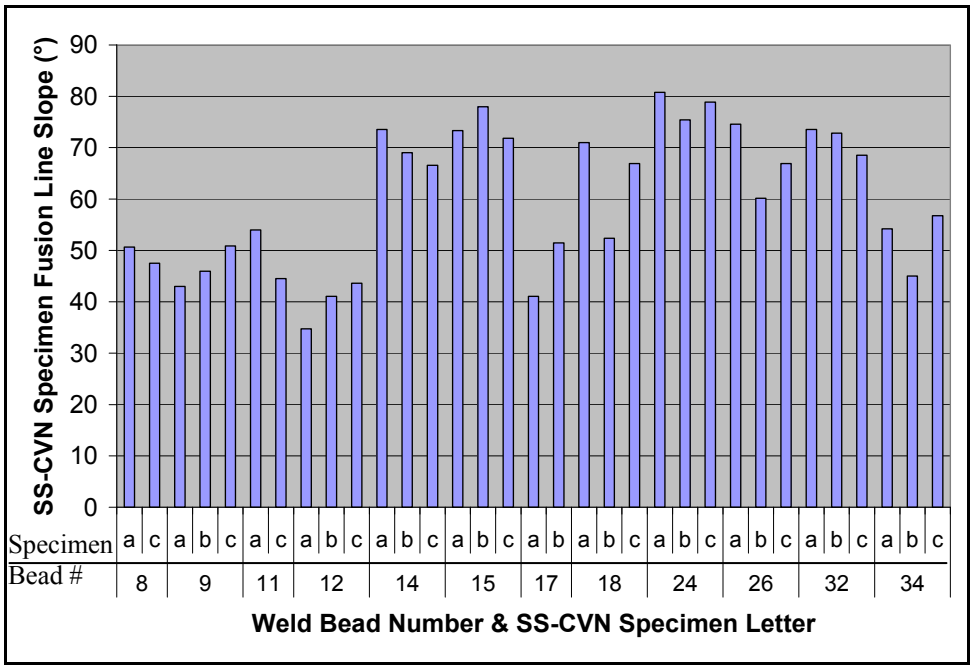

Figure 6-13: Individual SS-CVN Specimen Fusion Line Slope

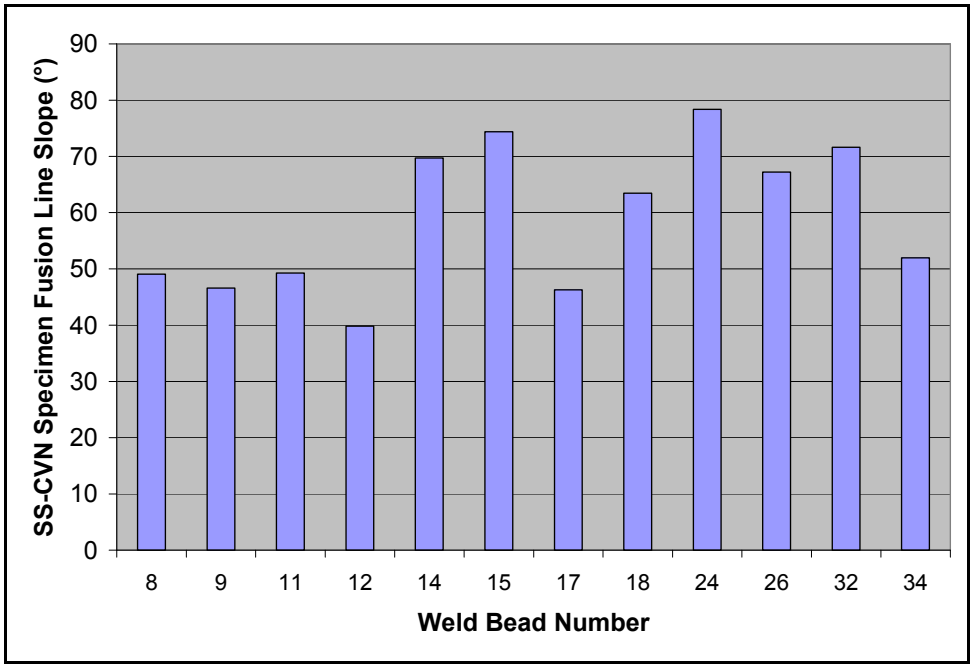

Figure 6-14: Average SS-CVN Specimen Fusion Line Slope (°) for Each Weld Bead

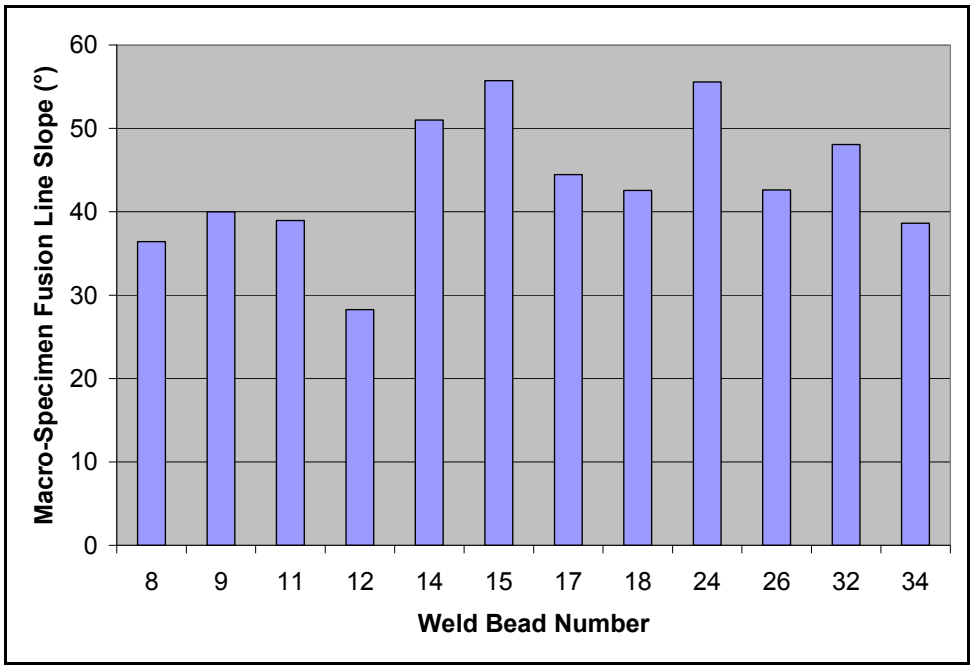

Figure 6-15: Macroscopic-Specimen Fusion Line Slope (°)

While the slope trends in Figure 6-14 and Figure 6-15 are similar, corresponding slope values from individual SS-CVN specimens were consistently higher. The effect is likely because the macroscopic specimen slopes were measured across the entire bead (including the shallowest portion of the penetration curve). The slopes within individual SS-CVN specimens likely avoided the shallow penetration bead bottoms and, hence, steeper slopes were measured (Figure 6-16).

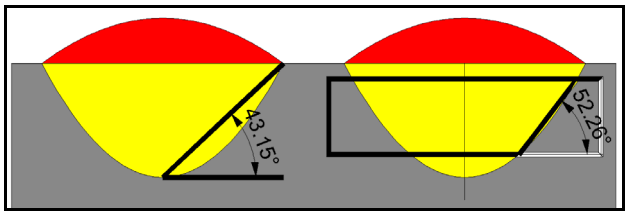

Figure 6-16: Macroscopic Specimen (left) and SS-CVN Specimen[§] (right) Slope Measurement

[§] The rectangle on the right weld bead represents the extraction-location of a SS-CVN specimen.

While Figure 6-11 did not demonstrate a strong trend between average weld bead fusion line slope and SS-CVN fracture energy values, Figure 6-17 was plotted to compare SS-CVN fracture energy values with individual SS-CVN fusion line slope results. There does appear to be a downward trend (i.e., as fusion line slope increases, SS-CVN fracture energy values decrease), which agrees with the literature (Section 2.7.1). However, many specimens do not follow the trend because of significant scatter.

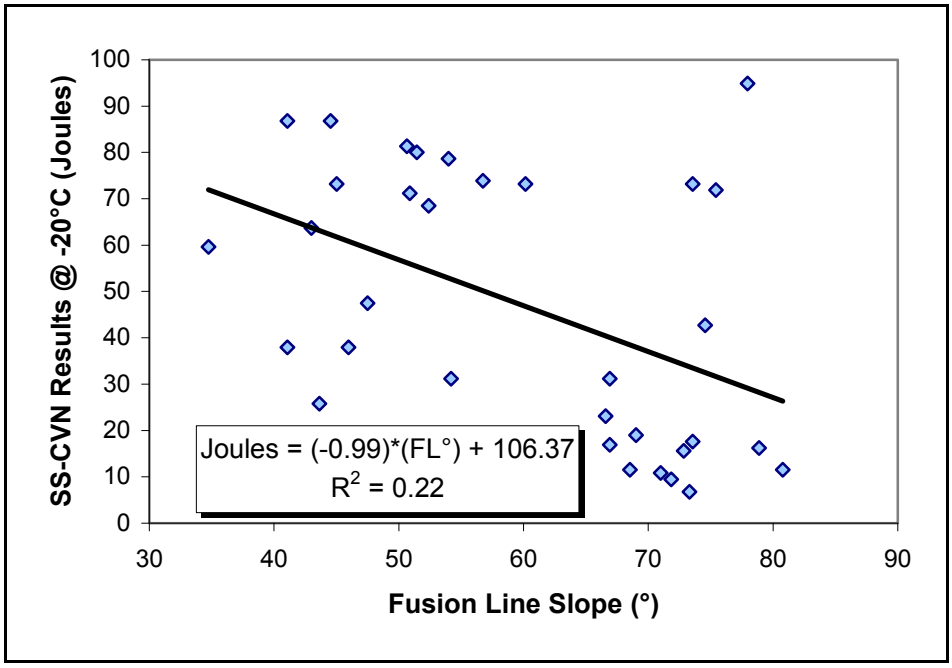

Figure 6-17: The Effect of Fusion Line Slope (°) on SS-CVN Fracture Energy Values at -20°C (Joules)

It should be noted that the Chapter 3 relationships were based not only on fusion line slope, but also on heat affected zone notch placement. While the fusion line appeared to be directly linked to the CVN fracture energy values, there also was a relationship between CVN fracture energy values and the HAZ geometries. Based on the above results, it is inadequate to use only the fusion line slope as a means of predicting SS-CVN fracture energy values.

The remainder of the investigation of Group 1 beads studied the relationships between average SS-CVN fracture energy values from each bead, and variable input parameters. Only tests with two or more successfully-tested specimens were investigated.

6.3.3 Weld Bead Parameters and SS-CVN Fracture Energy Values

Figure 6-18 illustrates the effects of heat input, current, and voltage on SS-CVN test specimens pulled from single-electrode BOP welds. Both average and standard deviations of SS-CVN fracture energy values are listed. Cross-section profiles, corresponding to the values, are illustrated below the bar chart.

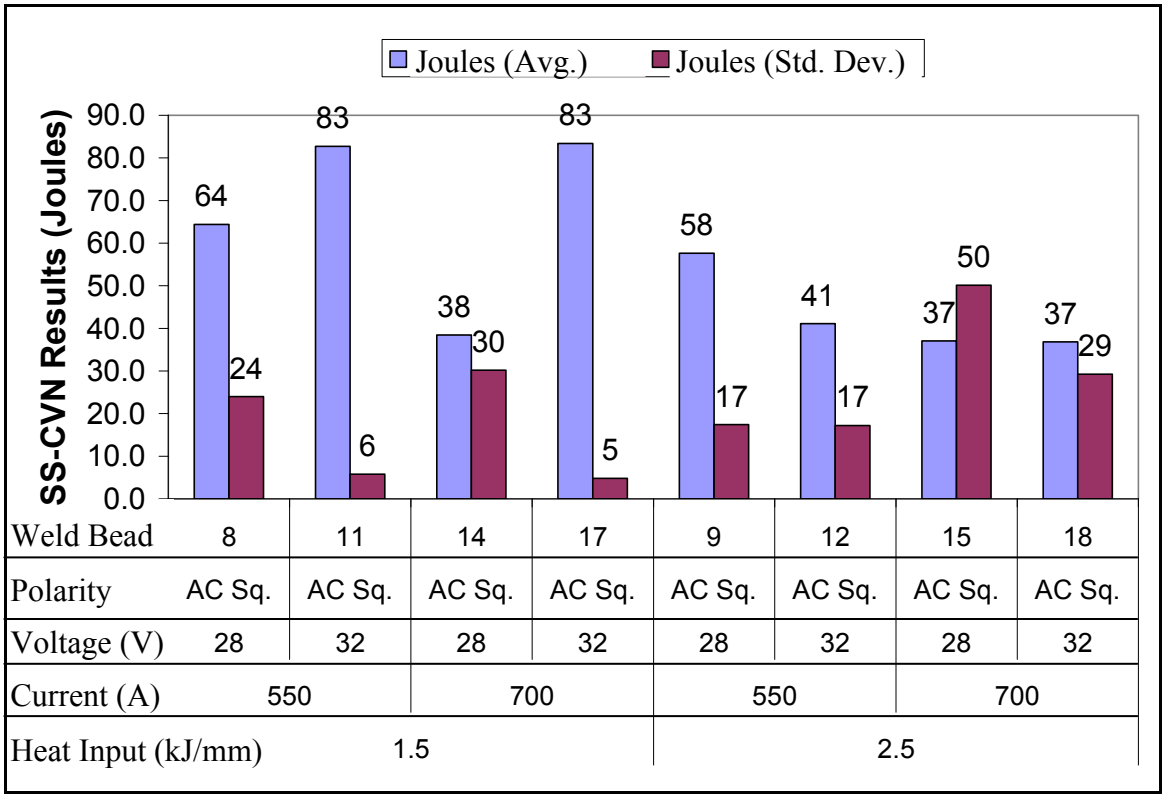

Weld Bead	8	11	14	17	9	12	15	18
Polarity	AC Sq.	AC Sq.	AC Sq.	AC Sq.	AC Sq.	AC Sq.	AC Sq.	AC Sq.
Voltage (V)	28	32	28	32	28	32	28	32
Current (A)	550		700		550		700	
Heat Input (kJ/mm)	1.5				2.5			

Figure 6-18: The Effect of Heat Input, Current and Voltage on SS-CVN Fracture Energy

Overall, notch-toughness decreases as heat input is increased. At lower heat input, an increase in voltage yielded a significant increase in the SS-CVN fracture energy values, while at higher heat input, increasing voltage yielded comparable or slightly worse results. At lower voltage, an increase in current produced lower SS-CVN energies, while at higher voltage, an increase in current yielded comparable results. Such trends indicate that travel speed variations were at least partially responsible. Unfortunately, Figure 6-19 does not illustrates a clear trend.

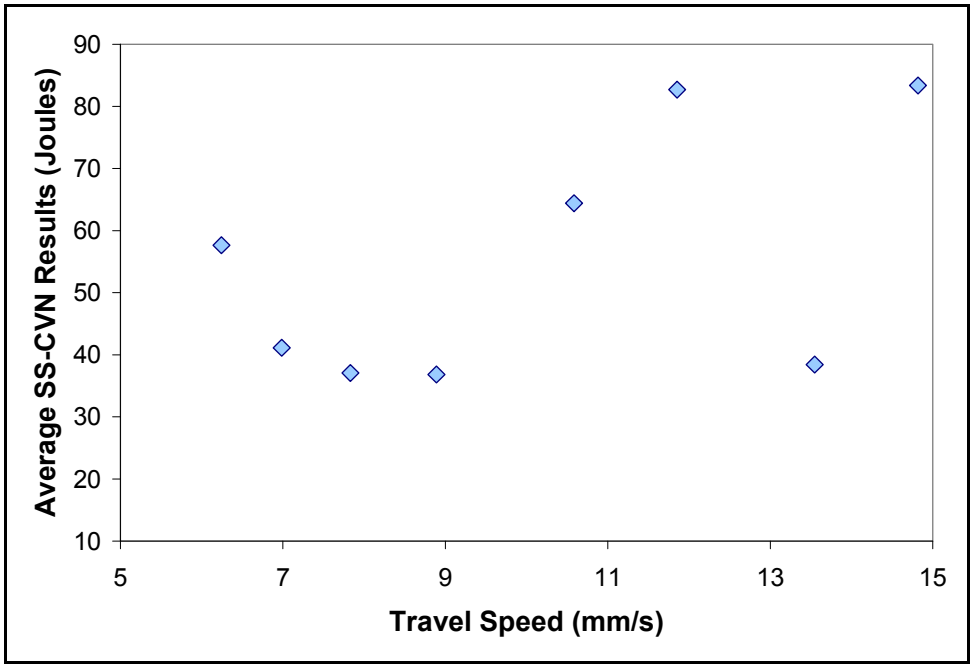

Figure 6-19: The Effect of Travel Speed on Average SS-CVN Fracture Energy (Joules)

The results were then compared with weld bead geometries (bottom portion of Figure 6-18). The general trend confirms that as penetration area increases, toughness decreases. The most obvious exception is bead 12, which has formed the distinct 'T-shape' associated with low SP ratio values. It has already been explained that in theory, a reduced SP ratio (i.e., a 'T-shaped' bead) may have a very steep fusion line slope at the CVN test specimen notch, resulting in reduced SS-CVN fracture energy values. It, therefore, is not surprising that bead 12 should produce poor SS-CVN fracture energy values. Furthermore, the bead

profiles in Figure 6-18 show that both beads 14 and 15 possess steep profiles. Regardless of their SP ratios, steep fusion lines can reduce SS-CVN fracture energy values.

As reinforcement and penetration volumes increase, the HAZ region should thicken. As a result, more of the Charpy test specimen notches should pass through the CGHAZ, resulting in poorer SS-CVN fracture energy values.

The results from different polarities were investigated next (Figure 6-20). The results were obtained from beads with 2.5 kJ/mm heat inputs, and 700 Amp welding currents. Just as before, weld bead cross-sections are illustrated below the bar chart.

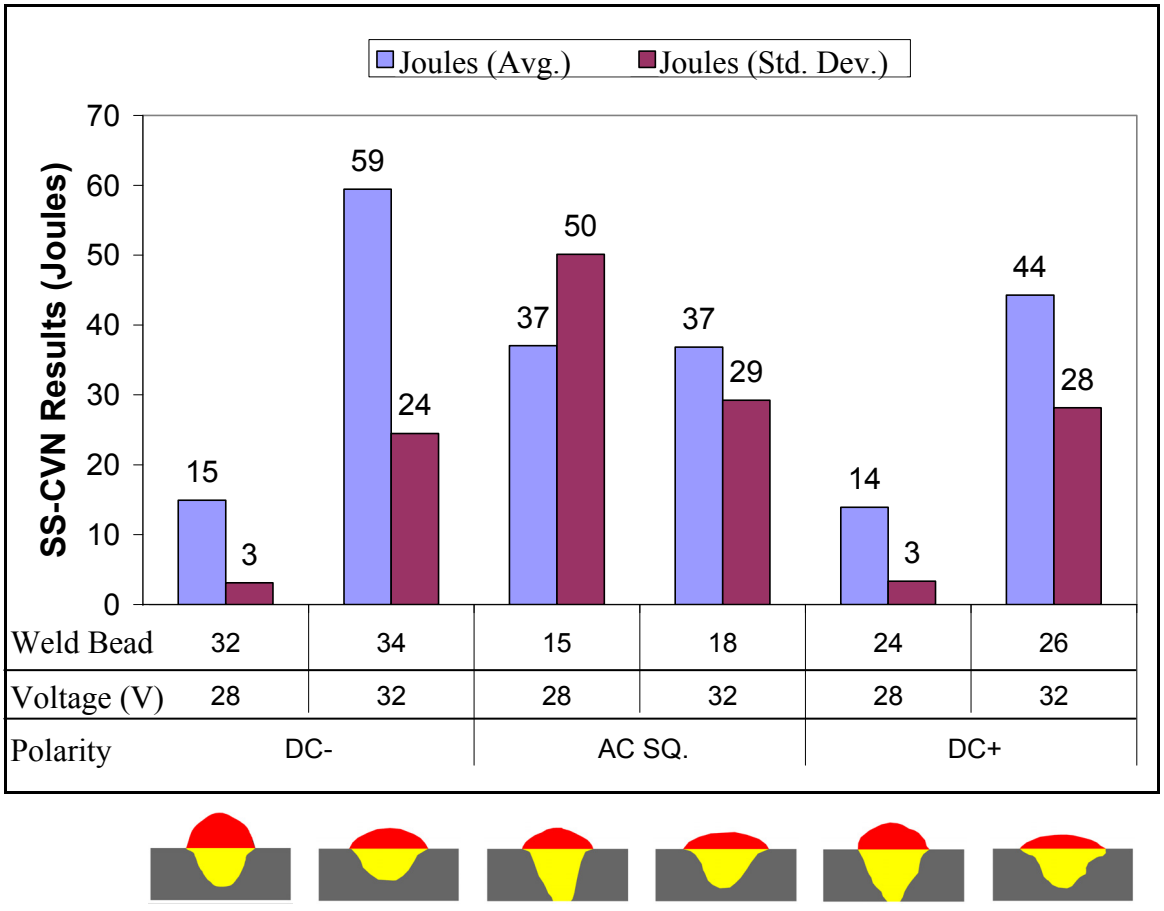

Figure 6-20: The Effect of Polarity and Voltage on SS-CVN Fracture Energy (Joules)

Looking only at the welding parameters, both the DCEN and DCEP beads demonstrated an increase in SS-CVN fracture energy values when voltage was increased. In both cases, this appears to be the result of a reduction in penetration and reinforcement area, which should result in a decrease in HAZ width. At the present time, the trend displayed by the AC-SQ beads (in relation to the trends displayed by the DCEN and DCEP beads) cannot be explained satisfactorily.

6.4: Group 2 SS-CVN "FL" Notch Location Specimens

6.4.1 Initial Comparison of Geometric Values with SS-CVN Fracture Energy Values

The Group 2 SS-CVN specimen average results were plotted against reinforcement area, penetration area, total molten area, and area ratio (Figure 6-21 through Figure 6-23). The SS-CVN fracture energy values were not plotted against reinforcement height or penetration depth, because the plots from the Group 1 bead analysis, showing the area equivalent measurements, appeared to provide stronger trends. Bead width was not considered for the Group 2 analysis because from the Group 1 analysis, there was neither a theoretical explanation for how bead width could affect SS-CVN fracture energy values, nor were there empirical trends. Finally, because of the results from earlier analysis from Section 6.3, neither fusion line nor aspect ratio values were compared to SS-CVN fracture energy values. SP ratio was not compared to the SS-CVN fracture energy values because additional work is required to determine the true relationship of tandem weld variables with SP ratio.

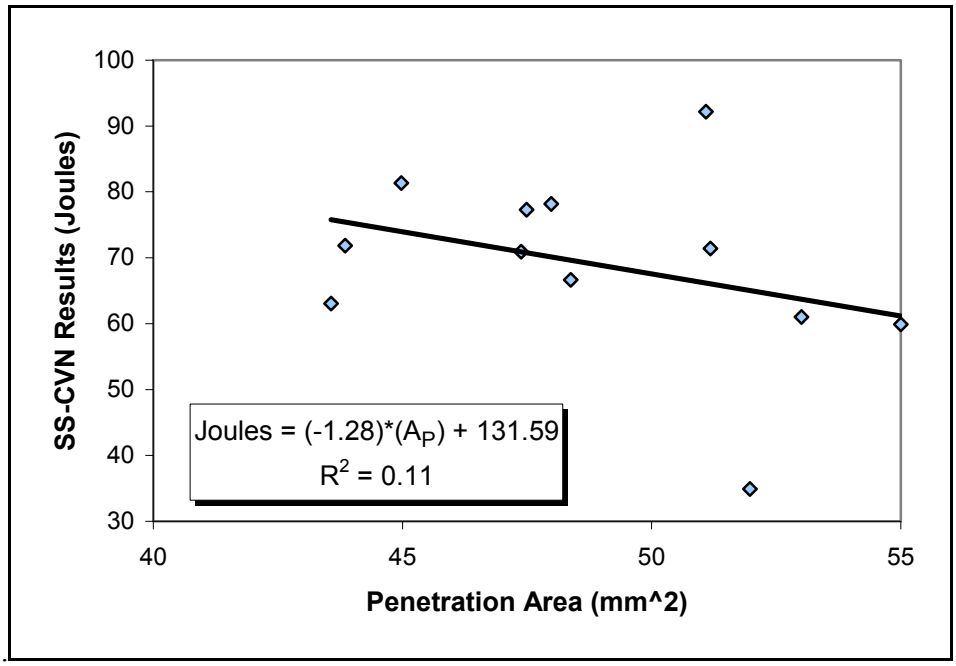

Figure 6-21: The Effect of Penetration Area (mm^2) on SS-CVN Fracture Energies of Group 2 Test Specimens

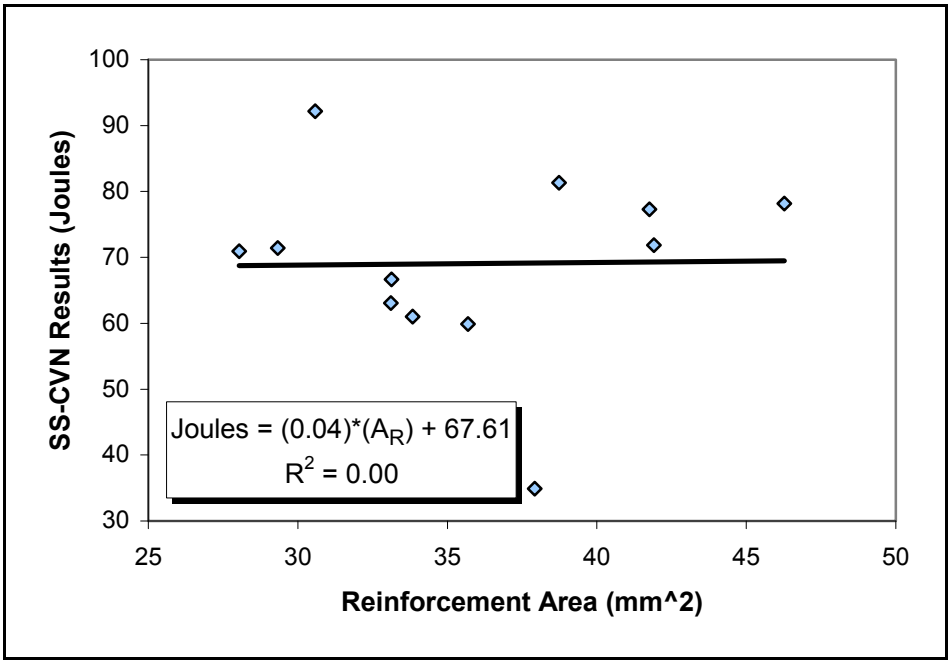

Figure 6-22: The Effect of Reinforcement Area (mm^2) on SS-CVN Fracture Energies of Group 2 Test Specimens

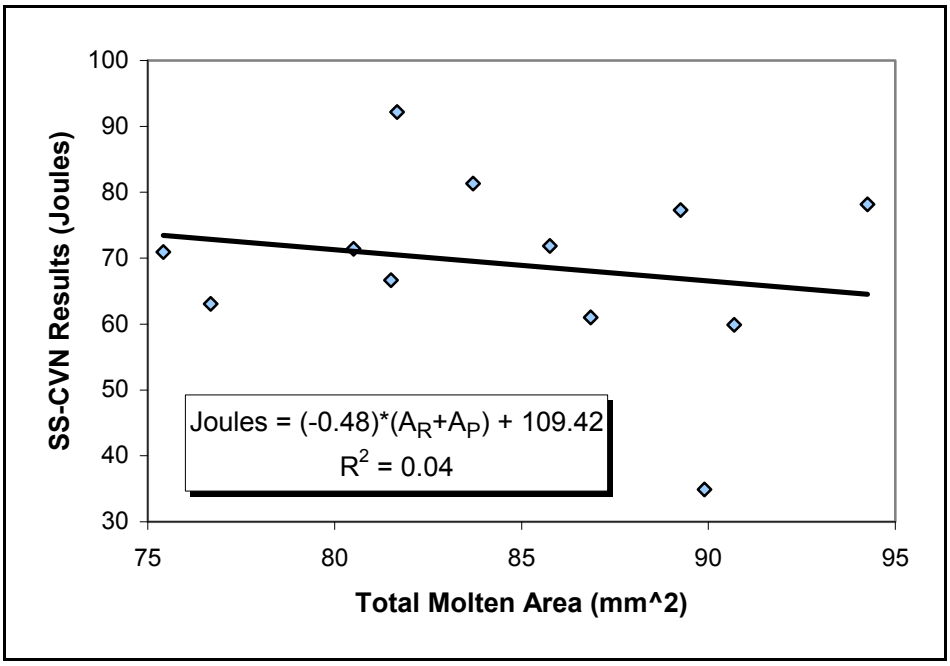

Figure 6-23: The Effect of Total Molten Area (mm^2) on SS-CVN Fracture Energies of Group 2 Test Specimens

As a recap, Figure 6-4 and Figure 6-5 showed that as penetration area and reinforcement area are increased for bead cross-sections, produced using a single-electrode welding process, it is likely that the SS-CVN fracture energy values should decrease as a result. Figure 6-21 and Figure 6-22 fail to show corresponding trends for beads produced using a tandem welding process. Likewise, Figure 6-23 does not show a clear trend linking specific SS-CVN fracture energy changes to the total molten bead cross-section area. It is suspected that the interactive effects of the tandem arcs (which complicated the analysis linking welding variable input values and bead cross-section geometry) was responsible for complicating SS-CVN fracture energy value analysis also. As a result, it is recommended that not only should multi-variable statistical modeling analysis be used to better determine the interactive effects between tandem arc welding variables and the resulting bead cross-section geometry, it also is recommended that additional modeling be used to determine the conditions affecting the SS-CVN fracture energy values.

The effect of area ratios on tandem weld SS-CVN fracture energy values was investigated next (Figure 6-24).

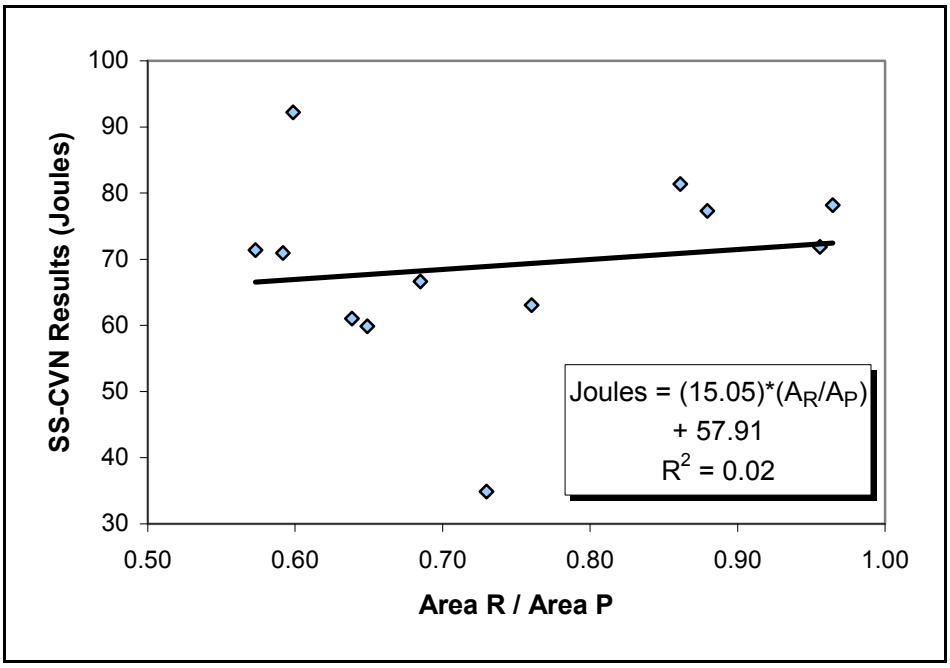

Figure 6-24: The Effect of Area Ratio on SS-CVN Fracture Energies of Group 2 Test Specimens

Upon initial inspection of Figure 6-24, it appears as though there could be a relationship between area ratio and SS-CVN fracture energy values, if the two outlier points (with the highest and lowest SS-CVN fracture energy values) are removed. As a result, Figure 6-25 was produced, which does indicate that as the area ratio is increased, there is a slight increase in SS-CVN fracture energy values. However, Figure 6-25 also indicates that the trend is quite weak. The total heat input for all Group 2 weld beads was 1.5 kJ/mm. It is possible that as the area ratio increases, a greater fraction of the effective heat input is focused at the electrode (i.e., reinforcement area increases). As a result, the effective heat input directly available to melt base metal would decrease (i.e., penetration area decreases). The analysis in Section 6.3 indicates that for a single-electrode weld bead, an increase in either reinforcement area or penetration area decreases SS-

CVN fracture energy values. However, if two separate arcs produce one bead, future work will be required to better understand the effects of the individual arcs on the overall HAZ geometry characteristics.

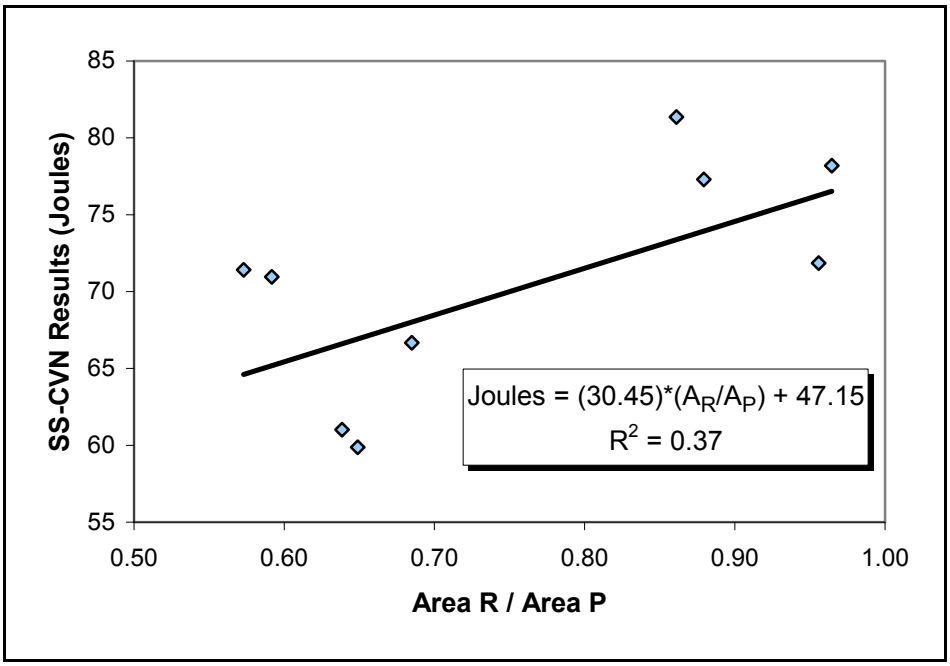

Figure 6-25: The Effect of Area Ratio on SS-CVN Fracture Energies of Group 2 Test Specimens (with Two Outliers Removed)

6.4.2 Weld Bead Parameters and SS-CVN Fracture Energy Values

The SS-CVN fracture energy values were then compared with the input parameters. Based upon the analysis from Chapter 5, it was most beneficial to compare the effects of lead and trail polarities on SS-CVN fracture energy values. Figure 6-26 was produced using beads with a 632 Amp lead current, 500 Amp trail current, and 28 Volt lead and trail voltages.

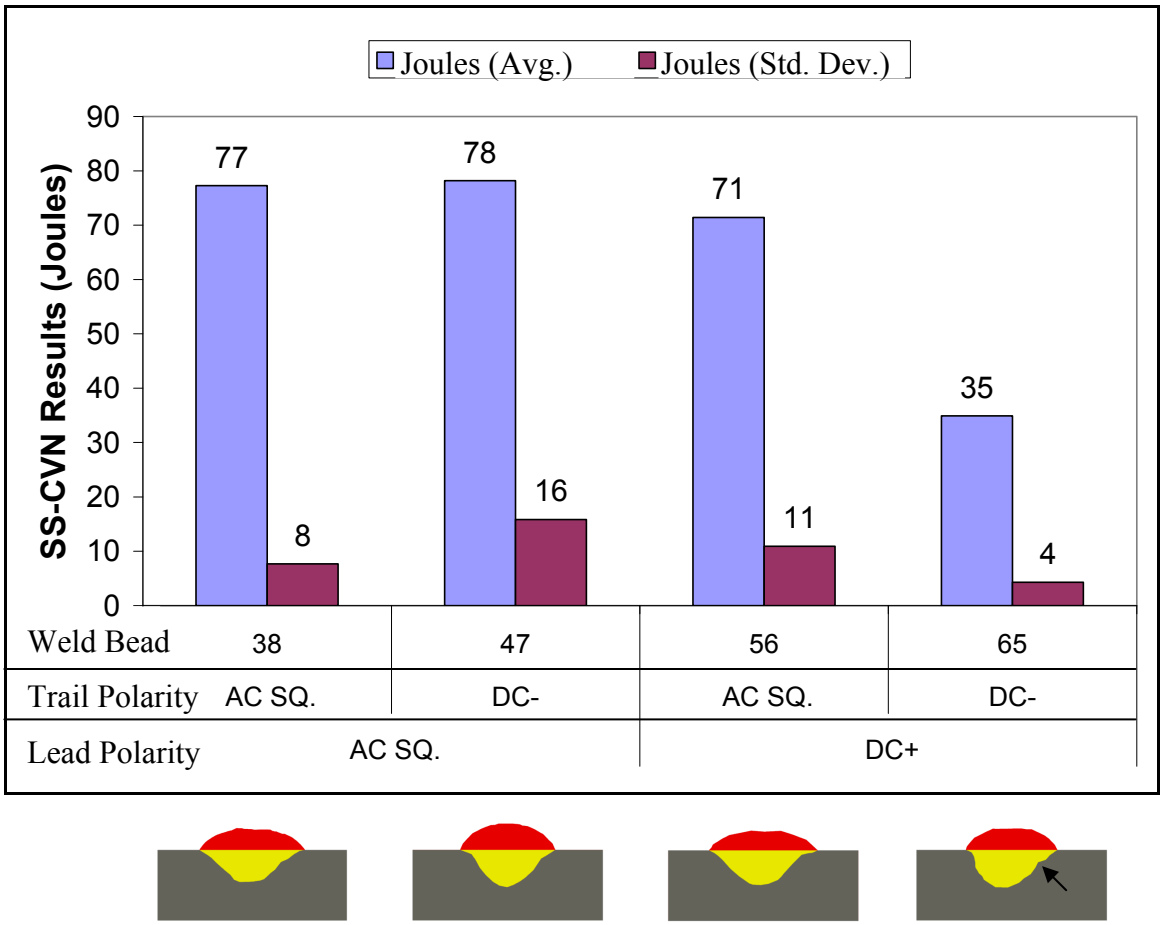

Figure 6-26: The Effect of Lead and Trail Polarities on SS-CVN Fracture energy values

Figure 6-26 illustrates that changing the polarity did not seem to affect the SS-CVN fracture energy values unless the DCEP lead arc, DCEN trail arc polarity combination was selected. The beads at the bottom of Figure 6-26 demonstrate that while the bead reinforcement and penetration areas are comparable, the DCEP/DCEN specimen (weld bead 65) demonstrated a penetration bead that was offset to the side. This observation is consistent with the results from Chapter 5. The weld bead 65 SS-CVN specimens were notched at the right fusion line, which was shallower. This would have placed less of the SS-CVN notch in the CGHAZ, which seems counterintuitive. However, bead 65 has a fusion line indent (Figure 6-26, as indicated by the arrow) located near the mid-penetration depth, which is where the notches would have been located. Heat affected zones typically form parabolic boundaries, regardless of bead shape. As a result, if a notch is located at

a fusion line indent, the HAZ will be "deeper" there, resulting in more of the notch passing through CGHAZ. If bead 65 had irregular fusion line shapes along the duration of the bead, the notches would have passed through more CGHAZ, resulting in poorer fracture energy values. Once again however, multi-variable statistical modeling analysis is recommended to better connect welding variable input values, weld bead cross-section geometry, and SS-CVN fracture energy values.

6.5: Group 3 SS-CVN "FL" Notch Location Specimens

Because the cross-section geometry measurements for the Group 3 specimens yielded extremely small variations, comparisons between their SS-CVN fracture energy values and geometric measurements did not yield visible trends. As a result, the Group 3 specimen notch-toughness values were compared only to their welding variable input values (Figure 6-27).

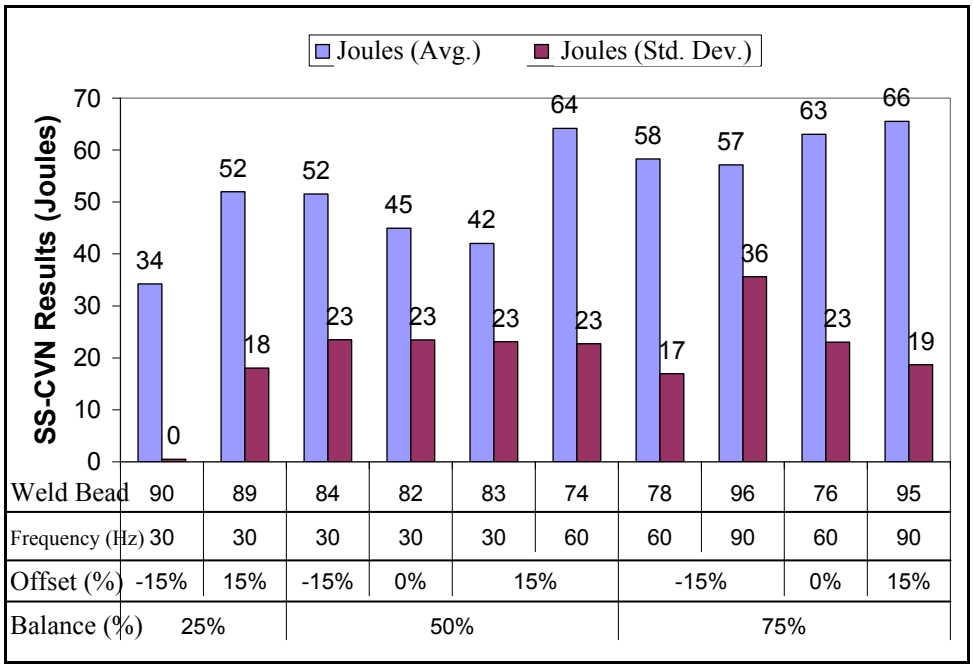

Figure 6-27: The Effect of Balance, Offset, and Frequency on SS-CVN Fracture Energy

The weld beads were sampled based on initial cross-section geometry rankings. Unfortunately, as later analysis revealed, any cross-section geometry trends were too small to be considered statistically valid. As a result, the SS-CVN test specimen sampling was not conducive to comparing the SS-CVN fracture energy Values to the waveform parameters.

For example, there appears to be no trend between offset and SS-CVN fracture energy values. While samples 82, 83, and 84 demonstrate that an increase in offset reduced SS-CVN fracture energy values, the specimen pairs 76 and 78, and 96 and 95, demonstrate the opposite trend. In both cases, the notch-toughness value changes consistent with the trend were smaller than the standard deviation of the test samples.

Additionally, samples produced using 30 Hz current frequency typically produced lower SS-CVN fracture energy values. However, the same specimens typically coincided with 25% and 50% balance. There appears to be a slight correlation that SS-CVN fracture energy increases with balance, especially when the balance is set to 75%.

Overall, there were no trends determined between waveform variables and SS-CVN fracture energy values. There are indications that a frequency of 30 Hz may produce poorer fracture energy values, and a balance of 75% may improve fracture energy values, but without performing additional SS-CVN tests, it is not possible to discern strong trends.

6.6: Group 4 SS-CVN "FL" Notch Location Specimens

Like the Group 3 specimens, the Group 4 specimens did not demonstrate large cross-section geometry variations. As such, their SS-CVN fracture energy values were not compared against geometric measurements (Figure 6-28).

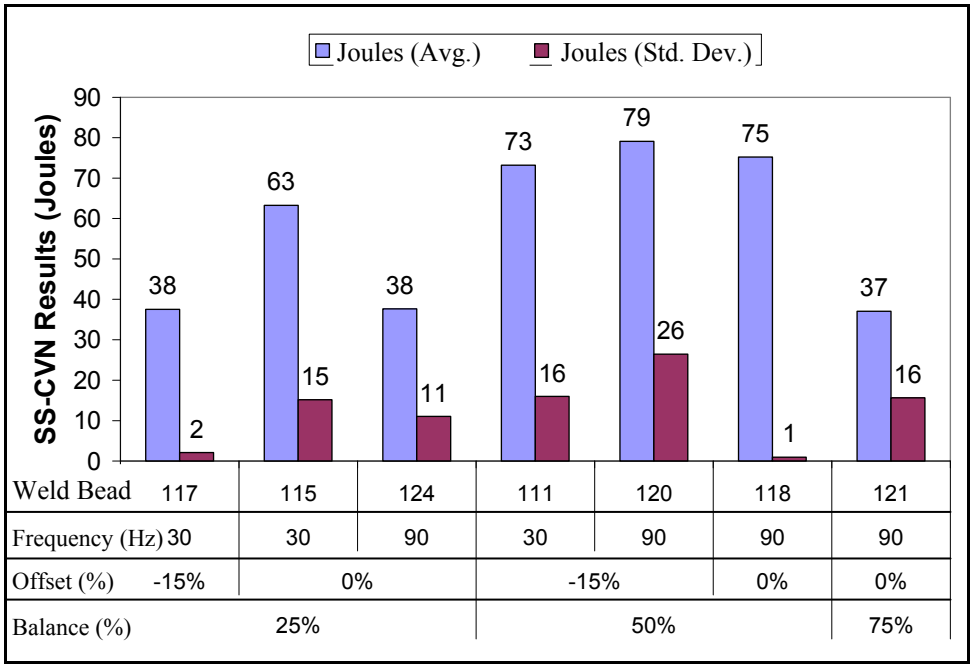

Figure 6-28: The Effect of Trail Balance, Offset, & Frequency on SS-CVN Fracture Energy

Similar to the Group 3 welds, the Group 4 weld beads were sampled based on initial cross-section geometry rankings. Once again, because cross-section geometry trends were too small to be considered statistically valid, the corresponding SS-CVN test specimen sampling was not ideal for analysis.

From the current data, there are no trends that show a strong correlation between trail arc waveform variable and SS-CVN fracture energy values. There are indications that the best toughness results are achieved with a 50% balance, but again, additional testing will be required to determine any trends with confidence.

6.7: Group 1 SS-CVN Analysis Revisited

Because of the variables and variable ranges used to produce the Group 1 welds, clear trends were observed linking input variables and weld bead cross-section geometries. This is in contrast with the Group 3 and 4 welds, which demonstrated limited bead geometry variations with changes to welding input values.

Initial analysis also illustrated trends linking both bead geometry and choice input variables to the notch-toughness fracture energy values. Thus far, the empirical results have been confirmed by established theory (with the exception of the unexplained absence of a visible trend between SP ratio and notch-toughness fracture energy values). This is in contrast to the Group 2 welds, which will undergo future multi-variable statistical modeling to make sense of the data acquired thus far.

As a result, the Group 1 weld beads formed the only suitable candidate for additional analysis, in an attempt to solidify the understanding between welding variable input values, weld bead geometry, and notch-toughness fracture energy values.

Scatter plots (Figure 6-4 through Figure 6-13) were used to initially evaluate potential relationships between weld bead cross-section geometry and SS-CVN fracture energy values. Some of the plots displayed obvious trends, whereas other plots did not display any recognizable relationship between the variables plotted. In all cases, however, there was a significant number of deviating points on the plots, which warranted additional analysis. In particular, the poor correlation between SP ratio and SS-CVN fracture energy values is perplexing, especially because the theoretical relationship lends itself to subsequent analysis of Figure 6-18. As a result, Figure 6-4 through Figure 6-12 were plotted, with the different welding variable input values represented by different scatter plot point symbols. As a result, additional insight was provided linking welding variable input, bead cross-section geometry, and SS-CVN fracture energy values. While most of the plots did not provide additional insight, a select few are presented and explained below. All of the re-plotted graphs are included in Appendix A.

Figure 6-4 illustrates a general trend in which an increased penetration area was accompanied by reduced SS-CVN fracture energy values. However, when the results for Figure 6-4 were separated on the basis of voltage (Figure 6-29), a trend became obvious. For equivalent penetration areas, the beads produced using the

higher voltage values achieved superior notch-toughness fracture energy values. When the AC-SQ cross-section profiles are inspected again (Figure 5-12 on Pg. 86, and Figure 5-21 on Pg. 95), it is clear to see that for the 1.5 kJ/mm and 2.5 kJ/mm beads[**], increased voltage typically resulted in reduced penetration areas (especially when a current of 700 Amps was used). As per earlier explanations, this is a result of the higher voltage value being accompanied by a greater travel speed (to maintain the heat input). To produce two beads, using different voltages, with the same penetration area, a greater heat input is required for the bead produced using the higher voltage. This is counter-intuitive, because greater heat input is often associated with wider heat affected zones (especially the CGHAZ). If the beads produced with the greater voltage then require a higher heat input to achieve the same penetration area, it would be expected that those beads would achieve poorer notch-toughness fracture energy values. Because this is not the case, an alternative factor has affected the SS-CVN fracture energy results.

When only the beads produced using AC-SQ were evaluated (Figure 6-30), there appeared to be a good downward trend for the beads produced using 28 volts. Unfortunately, there does not appear to be a trend for the beads produced using the higher 32 volts. As a result, it cannot be stated with confidence that voltage has a significant effect on toughness, for bead cross-sections of comparable penetration areas.

[**] Because a minimum weld bead cross-section penetration depth of 5mm was required for SS-CVN specimen extraction, it was not possible to evaluate the notch-toughness of any beads produced using a 0.5 kJ/mm heat input.

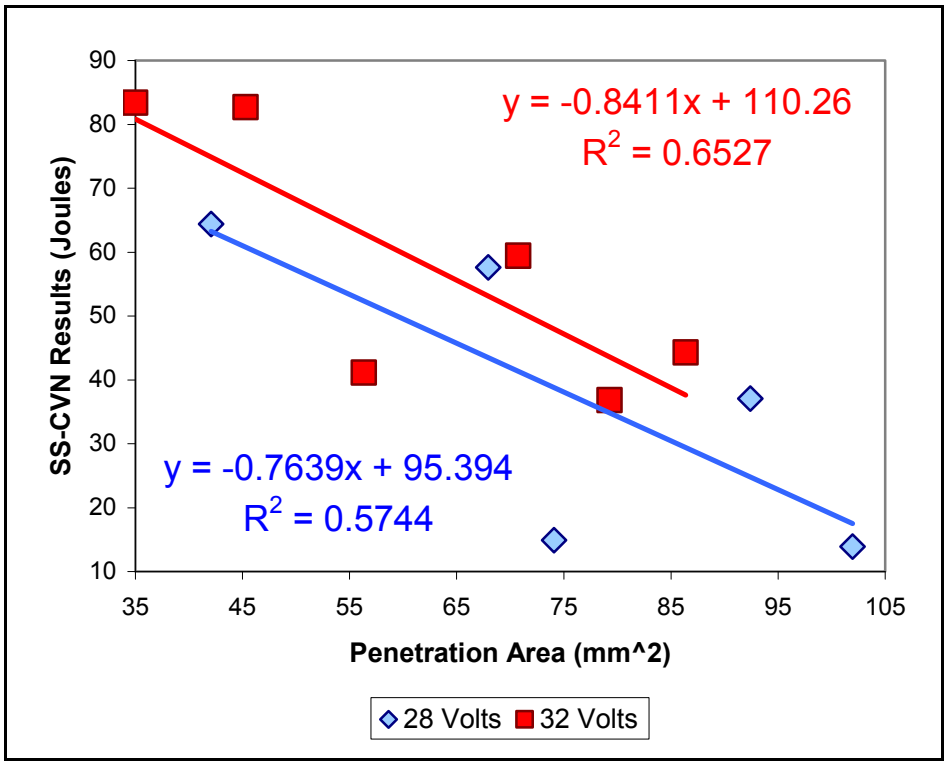

Figure 6-29: The Effect of Voltage and Penetration Area on SS-CVN Fracture Energy

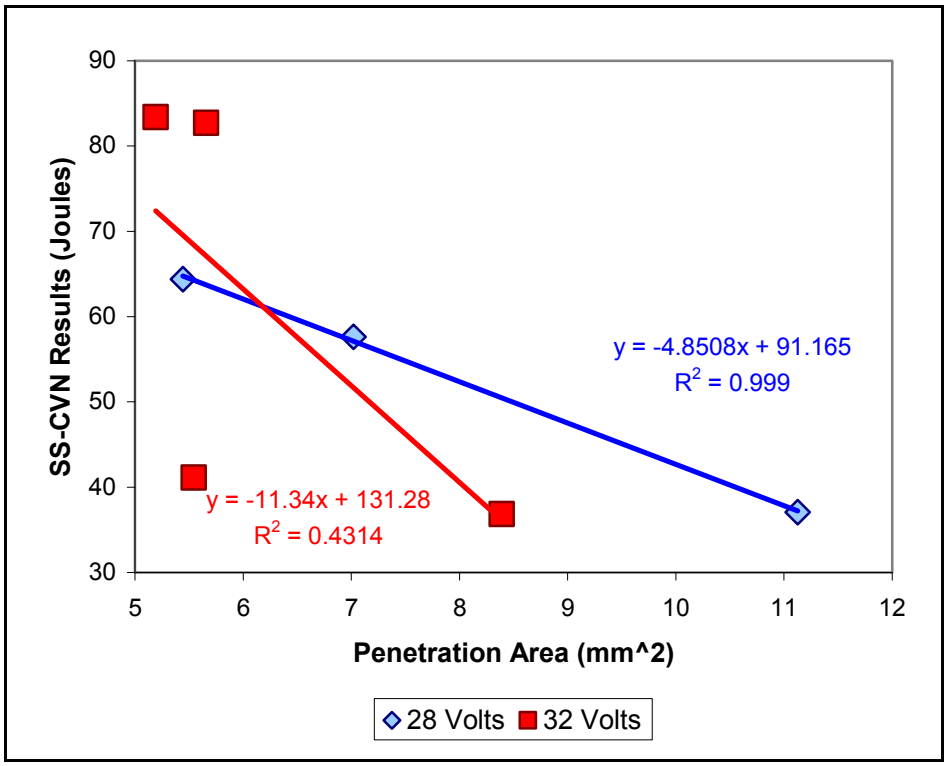

Figure 6-30: The Effect of Voltage and Penetration Area on SS-CVN Fracture Energy Values for Beads Produced Using AC-SQ Polarity

Two additional figures were produced, comparing the effects of SP ratio and SS-CVN fracture energy values, while separating the plot points on the basis of current and heat input (Figure 6-31 and Figure 6-32 respectively). For both figures, only the beads produced with AC-SQ polarity were considered, as the beads produced using DC polarities did not follow the same trends.

It has already been established that, theoretically, a large SP ratio produces a bulbous weld, whereas a small SP ratio produces a 'T-shaped' weld. If a CVN notch passes through the fusion line of the narrow portion of a T-shaped weld, the FL will be near-vertical, and much of the notch will sample the CGHAZ (i.e., CVN fracture energy will decrease). Alternatively, as SP ratio increases, a more bulbous bead will ensure that less CGHAZ is sampled by the CVN notch, resulting in increased CVN fracture energy. However, thus far, there has not been any empirical evidence to support this theory relating SP ratio to notch-toughness fracture energy values.

Figure 6-31 illustrates that for both current values, an increase in SP ratio does in fact correspond to higher SS-CVN fracture energy values. Additionally, as current is increased, the trendline is shifted to the right. As a result, if a larger current value is used, a higher SP ratio is required to achieve the same SS-CVN fracture energy values. As a result, if two beads have comparable SP ratio values, the bead produced using a larger current likely has lower notch-toughness. However, for two beads produced using different currents to have the same SP ratio, it would be necessary to modify voltage and travel speed. As a result, the effect of heat input was investigated (Figure 6-32).

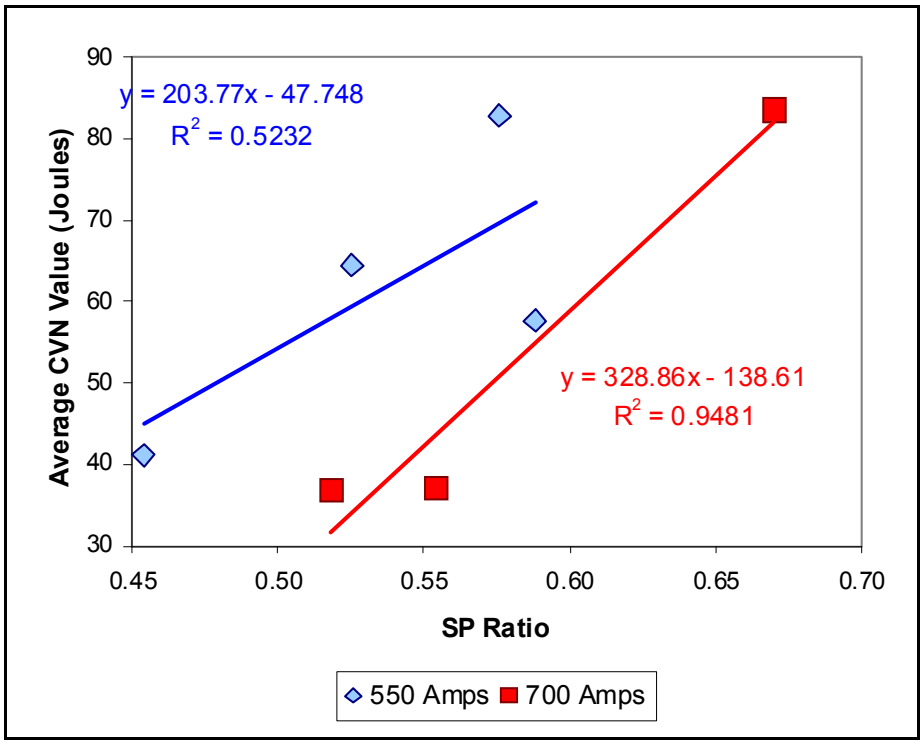

Figure 6-31: The Effect of Amperage and SP Ratio on Average SS-CVN Fracture Energy (Joules) (for Group 1 Welds)

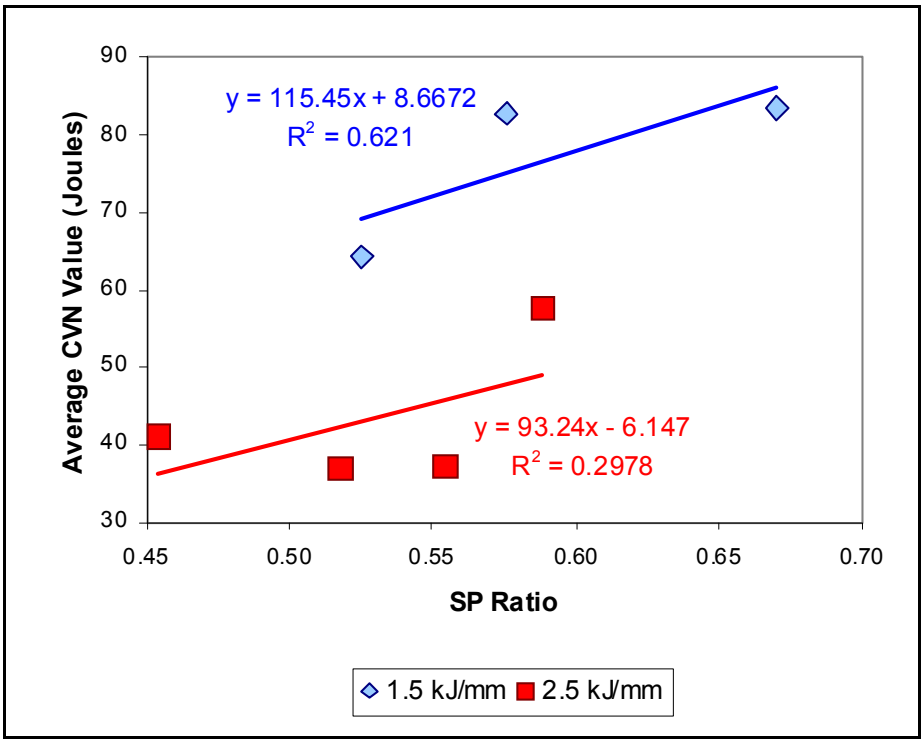

Figure 6-32: The Effect of Heat Inputand SP Ratio on Average SS-CVN Fracture Energy (Joules) (for Group 1 Welds)

Figure 6-32 shows that for individual heat inputs, there is a slight increase in SS-CVN fracture energy values as SP ratio is increased. Furthermore, for two beads with comparable SP ratios, the bead produced using a lower heat input would be expected to have superior notch-toughness. As current and heat input increase, generally, a larger HAZ is produced (and in particular, the CGHAZ should become wider).

As a result, Figure 6-32 shows that the penetration bead profile shape (i.e., the weld bead geometry) affects the SS-CVN fracture energy values, but so does the HAZ geometry. When trying to optimize CVN fracture energy results for weldments, it should now be obvious that the weld bead geometry and the HAZ geometry both must be considered.

6.8: Conclusions

Because SS-CVN testing was not possible for all weld beads, welds were sampled on the basis of their cross-section geometries. The Group 1 weld beads, which were produced using a single arc process, and by manipulating the heat input variables (i.e., voltage, current, travel speed, and polarity), were investigated first. The Group 1 fracture energy values demonstrated no strong relationship to aspect ratio, area ratio, or bead width. There was, however, a trend linking SS-CVN fracture energies to penetration and reinforcement lengths and areas. As penetration or reinforcement was increased, fracture energy values typically decreased. This would have been the result of a greater heat input producing a wider HAZ. As a result, greater portions of specimen notches would have passed through the CGHAZ, effectively decreasing the SS-CVN fracture energy values.

When the weld beads were undergoing significant variable and geometry changes, fusion line slope did not appear to be a good indicator of notch-toughness. However, when beads had comparable sizes and shapes, fusion line slope could

be used to predict differences in the results. As the fusion line slope was increased, the corresponding CVN fracture energy values decreased.

When multiple polarities were investigated, increases in voltage were found to drastically increase notch-toughness results. However, these voltage increases were accompanied by reductions in penetration, which would have both decreased HAZ width and resulted in shallower fusion lines. Once again, it is suspected that better results were the result of SS-CVN specimen notches passing through reduced CGHAZ regions.

The Group 2 test specimens, which were produced using a tandem arc process while manipulating the heat input variables, were analyzed next. With the Group 2 test specimens, there was no clear link between SS-CVN fracture energy values and aspect ratio, reinforcement area, penetration area, or total molten area. Additionally, while an initial plot appeared to display a relationship between area ratio and SS-CVN fracture energy, subsequent removal of two outlier data points from the plot contradicted such a relationship. If such a trend did exist, there would currently be no theory to satisfactorily account for such a relationship. Future work will be required to better explain HAZ formation mechanisms of tandem arc weld beads.

When the polarities were manipulated, the DCEP lead / DCEN trail polarity resulted in a bead that was non-symmetric across the weld centreline. While the specimens were notched at the shallower slope, which should have reduced the length of notch passing through the CGHAZ and, hence, should have increased toughness, the results were actually poorer. It is suspected that because of a characteristic fusion line indent along the weld bead, a greater fraction of the notch still passed through CGHAZ, resulting in the lower fracture energy values.

Analyzed next were the Group 3 and Group 4 weld beads, which were produced by changing waveform manipulation variables (i.e., balance, offset, and frequency) for single and tandem arc welding processes respectively. Because there were not strong trends established between waveform parameters and weld

bead geometry, the SS-CVN fracture energy values for both the Group 3 and Group 4 weld beads were not related to weld bead cross-sections. Overall, there were no trends determined between waveform variables and SS-CVN fracture energy values, but there are indications that a frequency of 30 Hz may produce poorer fracture energy values, and a balance of 75% may improve fracture energy values. Additional testing would be required to confirm that these indications are actually trends.

When an earlier Group 1 scatter plot (Figure 6-4) was re-plotted (Figure 6-29), such that data points were separated based upon the various welding variable input values, there was some evidence to suggest that for weld beads with equal penetration areas, increased welding voltage may increase fracture energy values. However, when only beads produced using AC-SQ polarity were investigated (Figure 6-30), the trend did not appear to be present any longer.

When the effects of bead SP ratio on CVN fracture energy values were investigated, it was found that when the plotted data was grouped either on the basis of current or heat input, there was a clear trend linking increased SP ratio values to improved notch-toughness. Additionally, when results were plotted for beads demonstrating equal SP ratios, it was shown that beads produced using reduced current or heat input will demonstrate improved notch-toughness. Because greater heat input is traditionally associated with wider CGHAZ regions (which has poor toughness), the above results form a strong argument that both the bead profile shape (i.e., SP ratio) and HAZ geometry must be considered for the proper optimization of CVN fracture energy values for weldments.

CHAPTER 7: OVERALL CONCLUSIONS

As pipeline operating conditions continue to become more extreme, it becomes increasingly important to not only ensure superior pipeline strength, but also superior toughness. Submerged arc welding (SAW), being a favorable welding process for mill pipe welding, was the focal point of this investigation. As Charpy-V notch (CVN) testing is an industry standard for evaluating notch-toughness, it formed the basis for weld evaluation.

The first welds performed were bevel tandem welds, which best recreated production welds that would be used to form and connect real pipes. Two bevel welds were performed on grade X80 steel, with a modified V-groove. Balance was manipulated for both the lead and trail arcs, after which the two welds underwent evaluation via CVN testing, hardness testing, and optical microscopy. By changing only balance, the total heat input was unaffected, even though the fraction of heat input supplied by either direct current electrode negative (DCEN) or direct current electrode positive (DCEP) polarity changed.

Initial evaluation illustrated that notch placement had a major influence on the relative CVN fracture energy values. At the macroscopic level, the fracture energy values varied considerably when the notch was located at the WM, FL, FL+2, or FL+5 locations (refer to Figure 3-8). The CVN results were lowest when the notch was placed at the FL location.

Additional differences were noted based upon the linear fraction of the notch passing through the various heat affected zones (HAZ). Typically, as the fraction of coarse-grain heat affected zone (CGHAZ) increased, the CVN fracture energy decreased. If the weld bead had a shallower fusion line, the corresponding CVN specimen notch would contain a smaller fraction of CGHAZ material, thus improving the CVN fracture energy values. Therefore, by controlling the bead shape, it should be possible to control the CVN fracture energy values. Because

toughness was linked to bead geometry, it then became necessary to gain a better understanding of the effects of welding variables on weld bead geometry.

There is a very large number of welding variables that can now be controlled and manipulated, many of which affect bead cross-section size and shape. To evaluate a large number of variables practically, bevel welding was no longer practical. As a result, a series of bead-on-plate (BOP) welds were performed. BOP welds were extremely advantageous for rapid screening and accurate analysis. Not only did the BOP welds require no machining and no tack or root welds, but the simpler welding setup also reduced some potential sources of error (e.g., precise electrode tip placement relative to the bevel geometry). Additionally, it became possible to quickly calculate the amount of base metal melted (by measuring the penetration area) and the amount of weld metal deposited (by measuring the reinforcement area). Such accurate measurements are not possible with the complex geometries of bevel welds.

Due to material availability, a series of BOP welds were performed on 11.1 mm (0.438") thick grade X70 steel. Four groups of welds were produced, with each group using either single or tandem welding processes, and by varying either heat-input or waveform manipulation variables.

When using a single-electrode welding process, increases in current promoted higher deposition and penetration. Greater voltage reduced deposition. Shifting the polarity from Direct Current Electrode Negative (DCEN) to Square-Wave Alternating Current (AC-SQ) to Direct Current Electrode Positive (DCEP) also reduced deposition, in addition to increasing bead width. At higher currents, a shift to DCEP clearly increased penetration as well. Changing the waveform manipulation variables did not produce clear trends regarding welding bead geometry, though the preliminary work indicated that increasing balance decreased wire feed speed (i.e., deposition). Setting the offset to 15%, and the frequency to 90 Hz, also reduced the wire feed speed. Because the waveform

manipulation variables are closely linked to polarity, it is proposed that relationships may be clearer at higher welding currents.

The tandem welding process was investigated next. Shifting the lead arc polarity from AC-SQ to DCEP reduced the lead WFS slightly, while a shift in trail polarity from AC-SQ to DCEN produced a more significant WFS increase. Shifting the lead polarity to DCEP also increased penetration (which also conforms to the literature). However, shifting the trail polarity to DCEN increased penetration. It is suspected that the greater penetration was caused by waveform interaction from tandem arcs shifting polarity. When a DCEP lead arc was combined with an AC-SQ trail arc, increasing the current balance decreased the trail WFS. Greater trail current offset and frequency also reduced the trail WFS. Additionally, when a DCEP lead polarity arc was combined with a DCEN trail polarity arc, the bead penetration areas were offset to one side, indicating grounding issues.

Overall, changing the heat input variables produced the greatest variation in weld bead cross-section geometry and shape, while changing the waveform manipulation variables produced very minor changes in geometry and shape. During this investigation, the SP ratio was introduced, and was used as a simple means to quantify weld bead profile shape. The SP ratio is calculated by dividing the width of the bead, at the mid-penetration cross-section location, by the bead width at the weld coupon's surface. There was a strong correlation between SP ratio and travel speed for single electrode weld beads: increases in travel speed increased the SP ratio (resulting in a more bulbous bead shape). For tandem welding processes, the relative capacity of the lead and trail arcs to penetrate into base metal affected the SP ratio.

Several weld beads had sub-size CVN test specimens extracted and tested at -20°C. With the single electrode welds, test results typically decreased as penetration and reinforcement areas increased. It is suspected that these trends are the result of narrower HAZ regions resulting in less CGHAZ passing through

the notch roots. Fusion line slopes could be helpful in predicting SS-CVN test results when beads have comparable sizes and shapes. However, fusion line cannot be used to predict test results when evaluating beads with a large range of shapes and sizes. Trends were not established for manipulating waveform variables, but initial tests indicate that a frequency of 30 Hz promoted poor test results, while a balance of 75% improved test results.

The tandem weld beads, produced by manipulating the heat input variables, demonstrated no trends linking cross-section geometry to SS-CVN fracture energy values. Whereas the corresponding trends for the single electrode weld beads were noticeable, the absence of such trends indicate that the HAZ formation was more complicated and deserves additional investigation in future work. Also, changes in lead and trail polarities produced negligible SS-CVN test result differences, except for the DCEP lead, DCEN trail combination, which produced lower results. There are indications that a 50% balance improved test results.

Finally, as the bead profile shape became more bulbous, (i.e., the SP ratio increased), there was a general increase in SS-CVN fracture energy values within specimens produced either using the same current or the same heat input. Additionally, as either current or heat input was increased, the SS-CVN fracture energy values decreased. For the heat input increase in particular, this is presumably caused by greater CGHAZ width, and by extension, the SS-CVN notch passing through a greater portion of CGHAZ material. In other words, to optimize the notch-toughness of weld beads, both the geometry of the weld bead, and the geometry of the HAZ regions must be considered.

CHAPTER 8: FUTURE WORK

In this study, the effect of welding variables on weld bead cross-section geometry was studied, as were the effects of bead cross-section geometry on sub-size Charpy V-notch test results.

When the "heat input" variables were manipulated, heat input was controlled by changing the travel speed. However, the test results showed a wide variety of bead geometries produced using the same heat inputs, while the many different travel speeds confounded variable-geometry trends. In future investigations, it is recommended that travel speed be controlled instead of heat input.

At 550 Amps and 28 Volts, there were no clear relationships between waveform variables and bead cross-section geometry. However, frequency, balance, and offset are all related to electrode polarity. Increased current values may amplify the effects of polarity changes on bead cross-section geometry. It is therefore recommended that different combinations of voltage and current be used to determine the effects of waveform variables on bead cross-section geometry.

When tandem welds were performed, questions presented themselves regarding the effects of interacting welding arcs. While the process does not normally use alternating current (and direct current electrode negative) current, gas metal arc welding (GMAW) may be an excellent welding process to investigate the interactions of tandem arcs, primarily due to the exposed arcs. Deeper investigation of the effects of arc physics on arc interactions (i.e., buoyancy, Lorenz forces, surface tension, etc.) may be helpful. Furthermore, the use of statistical modeling could help determine the interactions of lead and trail current and voltage values, as well as their separate and combined effects on the overall bead cross-section profile shapes (i.e., SP ratio).

For future researchers wishing to produce a tandem bevel weld, it is recommended to first use the parameters from bead 44 (Table 5-7). If deeper penetration is required, the lead current should be increased; additional

deposition will require moderate increases in trail current, as well as an increased trail contact-tip-to-work distance (i.e., electrode "stickout"). The lead current should always exceed the trail current.

The power sources provided an internal data acquisition system, Command Centre, which was capable of recording current and voltage during the welds. However, all values were positive, regardless of polarity, implying that root mean square (RMS) values were recorded. Additionally, while the power source manuals explain how balance, offset, and frequency affect power source output, no confirmation was performed during this investigation. The use of a data acquisition system and/or an oscilloscope could determine the true effects of balance, offset, and frequency on the amplitude and duration of current at both polarities of an AC square-wave waveform.

Finally, as the investigation indicated, both the profile shape (i.e., SP ratio) and the heat affected zone (HAZ) geometry must be considered for the optimization of CVN notch-toughness results. It is therefore critical for future work to map out the effects of welding parameters on HAZ geometries. If possible, it would be beneficial if large deposition rates could be achieved alongside narrow CGHAZ bands.

REFERENCES

1) Antaki, G.A., Piping and Pipeline Engineering: Design, Construction, Maintenance, Integrity, and Repair. Marcel Dekker Inc., 2003.

2) Aran, A., Gulec, S., "Fracture Toughness Studies in Different Regions of Weld Heat Affected Zones on a C-Mn Steel." Journal of Materials Science Letters. Volume 3: pp. 512 – 514. 1984.

3) ASME Boiler and Pressure Vessel Code, Section II – Materials (2007) (pp:). American Society of Mechanical Engineers. Online version available at: http://knovel.com/web/portal/browse/display?_EXT_KNOVEL_DISPLAY_bookid=1777&VerticalID=0

4) ASTM Standard A370, 2003a, "Standard Test Methods and Definitions for Mechanical Testing of Steel Products." ASTM International. 2003.

5) Bai, D., Cooke, M.A., Asante, J., Dorricott, J., United States Patent No. 6,682,613 B2, Process for Making High Strength Micro-Alloy Steel. 2002.

6) Benzerga, A.A., Tvergaard, V., Needleman, A., "Size Effects in the Charpy V-Notch Test. International Journal of Fracture. Volume 116: pp. 275 - 296. 2002.

7) Chandel, R.S., Bala, S.R., "Relationship Between Submerged-Arc Welding Parameters and Weld Bead Size." Schweiβen un Schneiden. Volume 40: pp. 88 - 91. 1988.

8) Collins, L., EVRAZ Inc. NA. Private communication. 5 May 2008.

9) Easterling, K., Introduction to Physical Metallurgy of Welding. 2nd ed., Butterworth-Heinemann Ltd. 1992.

10) Fairchild, D.P., Crawford, M.D., Cheng, W., Macia, M.L., Nissley, N.E., Ford, S.J., Lillig, D.B., Sleigh, J., "Girth Welds for Strain-Based Design Pipelines." International Offshore and Polar Engineering Conference. Vancouver. 2008.

11) Fisher, K., "Subarc Technology Breakthrough: Technology Increases SAW Deposition Rates." Welding Design and Fabrication. pp. 28 - 31. March 2002.

12) Gladman, T., The Physical Metallurgy of Microalloyed Steels. The Institute of Materials. London. 1997.

13) Grist, F.J., Farrell, W., Lawrence, G.S., "Power Sources for Welding." ASM Handbook Volume 6 – Welding, Brazing, and Soldering. Online Edition. ASM International. 1998.

14) Gupta, P.C., Ghose, P.K., Sharma, S.K., "Effect of Polarity on Melting Rate in Submerged Arc Welding." Indian Welding Journal. Volume 19 (3): pp. 228 - 233. 1987.

15) Hamad, F., EVRAZ Inc. NA. Private communication.

16) Hamad, F., Collins, L., Volkers, R., "Effects of GMAW Procedure on the Heat-Affected Zone (HAZ) Toughness of X80 (Grade 550) Linepipe" (Paper IPC2008-64097). International Pipeline Conference. Calgary. 2008.

17) Hauser, D., "Gas Tungsten Arc Welding (TIG Welding)." ASM Handbook Volume 6- Welding, Brazing, and Soldering. 9th ed. ASM International. 1983.

18) Hicken, G.K., Campbell, R.D., Daumeyer, G.J., Madigan, R.B., Marburger, S.J., Young, B., "Gas Tungsten Arc Welding." AWS Welding Handbook – Volume 2: Welding Processes Part 1 (8th edition). American Welding Society. Miami. 1990.

19) Hillenbrand, H.G., Kalwa, C., Liessem, A., "Technological Solutions for Ultra-High Strength Gas Pipelines." Super High Strength Steels, 1st International Conference, Rome. 2005.

20) Hinkel, J.E., "Long Stickout Welding – A Practical Way to Increase Deposition Rates." Welding Journal. Miami. Volume 47 (11): 869 – 874. 1968.

21) Holliday, D.B., Carter, S.R., DeFreitas, L., Fink, D.A., Folkening, R.W., Hodson, D.D., Mann, R.H., "Gas Metal Arc Welding." AWS Welding Handbook – Volume 2: Welding Processes Part 1 (8th edition). American Welding Society. Miami. 1990.

22) Ito, Y., Ikeda, M., Yamauchi, N., "High Speed Welding by the Two-Electrodes Submerged-Arc Tandem Method." The Sumitomo Search. Volume 5 (5): 8 - 15.

23) Jackson, C.E. "The Science of Arc Welding." Welding Journal. Miami. Volume 39 (4): 129s – 140s. 1960.

24) Jackson, C.E., Shrubsall, A.E., "Control of Penetration and Melting Ratio with Welding Technique." 33rd National Fall Meeting, AWS. Philadelphia. 1952.

25) James F. Lincoln Welding Foundation, "Properties of Materials." The Procedure Handbook of Arc Welding 14th Edition. James F. Lincoln Welding Foundation. 2000.

26) Jiluan, P., Arc Welding Control. Woodhead Publishing Limited. Cambridge, England. 2003.

27) Khan, Md. I., Welding Science & Technology. New Age International Publishers. 2007.

28) Kielhorn, W.H., Adonyi, Y., Holdren, R.L., Horrocks, R.C., Nissley, N.E., "Survey of Joining, Cutting, and Allied Processes." AWS Welding Handbook – Volume 1: Welding Science and Technology. American Welding Society. Miami. 2001.

29) Kimura, A., Suzuki, T., Jincho, M., Matsui, H., "Dependence of Ductile-Brittle Transition Behavior on the Size of Charpy Specimen and the Location of V-Notch in the HAZ of Welded A533B PVS." Small Specimen Test Techniques, ASTM STP 1329. 1998.

30) Komizo, Y. "Progress in Structural Steels for Bridge and Linepipe." Transactions of JWRI. Volume 35 (1). 2006.

31) Koo, J.Y., Luton, M.J., Bangaru, N.V., Petkovic, R.A., Fairchild, D.P., Petersen, C.W., Asahi, H., Hara, T., Terada, Y., Sugiyama, M., Tamehiro, H., Komizo, Y., Okaguchi, S., Hamada, M., Yamamoto, A., Takeuchi, I., "Metallurgical Design of Ultra-High Strength Steels for Gas Pipelines." Electronic Design. Volume 52 (2): 2 - 10. 2004.

32) Kou, S., "Heat Flow in Welding." Welding Metallurgy, 2nd Edition. Wiley Interscience. Hoboken, New Jersey. 2003.

33) Kubli, R.A., Shrubsall, H.I., "Multipower Subermreged-Arc Welding of Pressure Vessels and Pipe." Welding Journal. pp. 1128 – 1135. November 1956.

34) Lauzhadis, A.I., 1969, "Certain Features of Arc Welding with High Frequency Current," Avt. Svarka (Automatic Welding), 1969(4), pp. 51-56.

35) LeRoy, D., "Submerged Arc Welding." ASM Handbook Volume 6 – Welding, Brazing and Soldering. 9th ed. ASM International. 1983.

36) Liessem, A., Erdelen-Peppler, M., "A Critical View on the Significance of HAZ Toughness Testing" (Paper IPC04-0315). International Pipeline Conference. Calgary. 2004.

37) Lincoln Electric, “How to Make Single Electrode Submerged Arc Welds.” Technical Bulletin C5.600. 1994.

38) Lincoln Electric, “Making Submerged Arc Welds in the Flat and Horizontal Positions.” Technical Bulletin C5.620. 1999.

39) Lincoln Electric, “Power Wave AC/DC 1000 Operator’s Manual.” 2004.

40) Lincoln Electric, “Tandem Arc Welds.” Technical Bulletin C5.640. 1998.

41) Linnert, G.E., “Welding Methods and Processes.” Welding Metallurgy Volume 1 (4th edition). American Welding Society. Miami. 1994.

42) Lochhead, J.C., Rodgers, K., The Practical Welding Engineer. American Welding Society. Miami. 2000.

43) Moran, S.P., Erbe, D.J., Herwig, W.E., Hoffman, W.E., Hsu, C., Reynolds, J.O., “Arc Welding Power Sources.” AWS Welding Handbook Volume 2 – Welding Processes Part 1 (9th Edition). American Welding Society. Miami. 2004.

44) NACE Standard MR0175 / ISO Standard 15156, 2003, “Petroleum and Natural Gas Industries - Materials for Use in H2S-containing Environments in Oil and Gas Production - Parts 1, 2 and 3 (Includes Technical Circulars and Technical Corrigenda).” NACE International. 2003.

45) Nugent, R.M., Dybas, R.J., Hunt, J.F., Meyer, D.W., “Submerged Arc Welding.” AWS Welding Handbook – Volume 2: Welding Processes Part 1 (8th edition). American Welding Society. Miami. 1990.

46) Patchet, B.M., Welding Metallurgy, The Metals Blue Book – Welding Filler Metals. 2nd ed. CASTI Pub. and American Welding Society (AWS), 1998.

47) Penniston, C., EVRAZ Inc. NA. Private Communication. 10 Aug 2009.

48) Poorhaydari-Anaraki, K., “Microstructure and Property Examination of the Weld HAZ in Grade 100 Microalloyed Steel,” (PhD Dissertation, University of Alberta). 2005.

49) Rasanen, B., Tenkula, J., “Phase Changes in the Welded Joints of Constructional Steels.” Scandinavian Journal of Metallurgy. Volume 1 (2): pp. 75 – 80.

50) Shehata, M.T., Boyd, J.D., “Quantitative Correlations Between Toughness and Microstructure for Commercial Line Pipe Steel.” Advances in the Physical Metallurgy and Applications of Steels. Liverpool, England. pp. 229 – 236. Sep. 21 – 24, 1981.

51) Smartt, H.B., “Transfer of Heat and Mass to the Base Metal in Gas-Metal Arc Welding.” ASM Handbook Volume 6 - Welding, Brazing, and Soldering. Online Edition. ASM International. 1998.

52) Smith, N.J., McGrath, J.A., Gianetto, J.A., Orr, R.F. “Microstructure / Mechanical Property Relationships of Submerged Arc Welds in HSLA 80 Steel.” Welding Journal. pp. 112 – 120. March 1989.

53) Swain, R.A., Zentner, H.K., Hunt, J.F., Scott, J.R., “Submerged Arc Welding.” AWS Welding Handbook Volume 2 – Welding Processes Part 1 (9th Edition). American Welding Society. Miami. 2004.

54) Tsai, C.L., Tso, C.M., “Heat Flow in Fusion Welding.” ASM Handbook Volume 6 - Welding, Brazing, and Soldering. Online Edition. ASM International. 1998.

55) Weman, K., “Chapter 7: Submerged Arc Welding.” Welding Process Handbook. CRC Press, Cambridge, England. 2003.

56) Wilson, J.L., Claussen, G.E., Jackson, C.E., “The Effect of I^2R Heating on Electrode Melting Rate.” Welding Journal. pp. 1 - 8. January 1956.

57) Yarmuch, M.A.R., Patchett, B. M., “Variable AC Polarity GTAW Fusion Behavior in 5083 Aluminum.” Welding Journal. v86 (7): pp. 196 - 200. 2007.

58) Yarmuch, M.A.R., “Effect of Welding Parameters on the Plasma Transferred Arc Welding (PTAW) Process for Autogenous Beads and 410SS-WC Overlay” (MSc Thesis, University of Alberta). 2005.

APPENDIX A: SUPPLEMENTARY GROUP 1 SCATTER PLOTS

In Section 6.3, a series of scatter plots were produced (Figure 6-4 to Figure 6-12), comparing the effects of individual weld bead cross-section geometry values on the corresponding SS-CVN fracture energy values. While some of the scatter plots illustrate linear trends, the chart points consistently show significant scatter from the trends.

As a result, many of the plots were re-plotted, with the points distinguished based upon welding variable input values (e.g., voltage or current values). A small number of these new plots were included for additional analysis in Section 6.7. This Appendix contains all of the re-plotted charts.

8.1: Re-Evaluation of Figure 6-4 (The Effect of Penetration Area on SS-CVN Fracture Energy)

Figure 6-4 illustrates the effect of penetration area on SS-CVN fracture energy values. Figure A- through A-5 show the effect of distinguishing the points from Figure 6-4 based upon current, voltage, polarity, power, and heat input values respectively. Whereas the other figures do not reveal any new trends from Figure 6-4, Figure A-2 appears to show a relationship between voltage, penetration area, and SS-CVN fracture energy values. If welds possess the same penetration area, the weld bead produced using a greater voltage appears tp produce a greater SS-CVN fracture energy value. Figure A-2 was, therefore, included in Section 6-7 for further analysis.

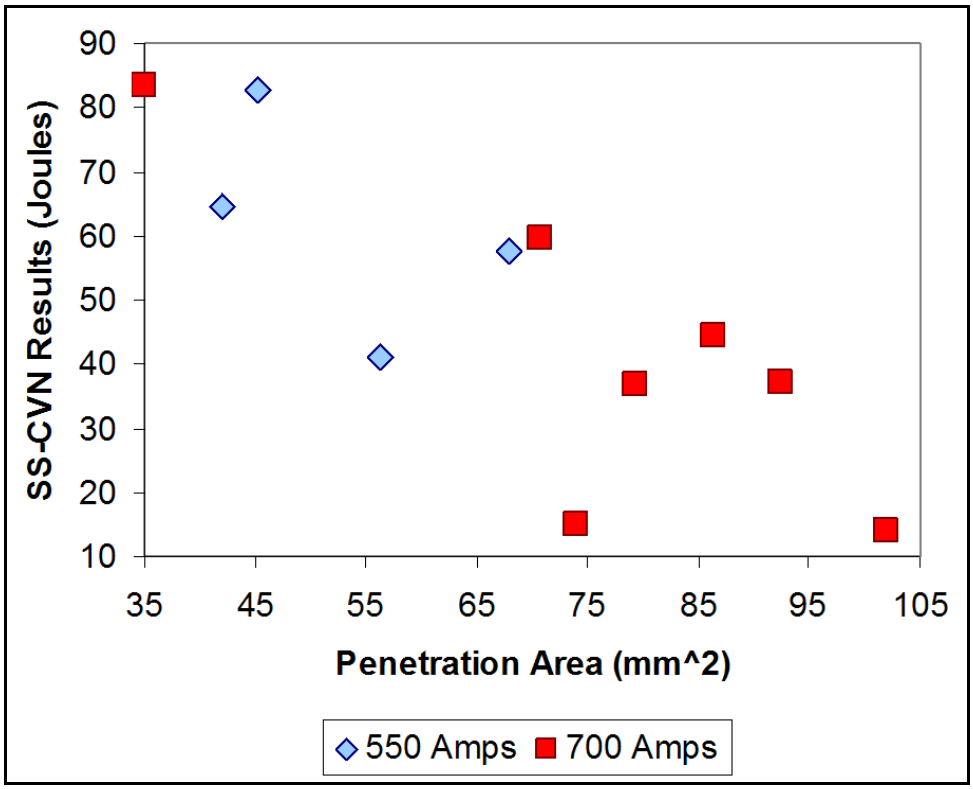

Figure A-1: Effect of Current & Penetration Area on SS-CVN Fracture Energy

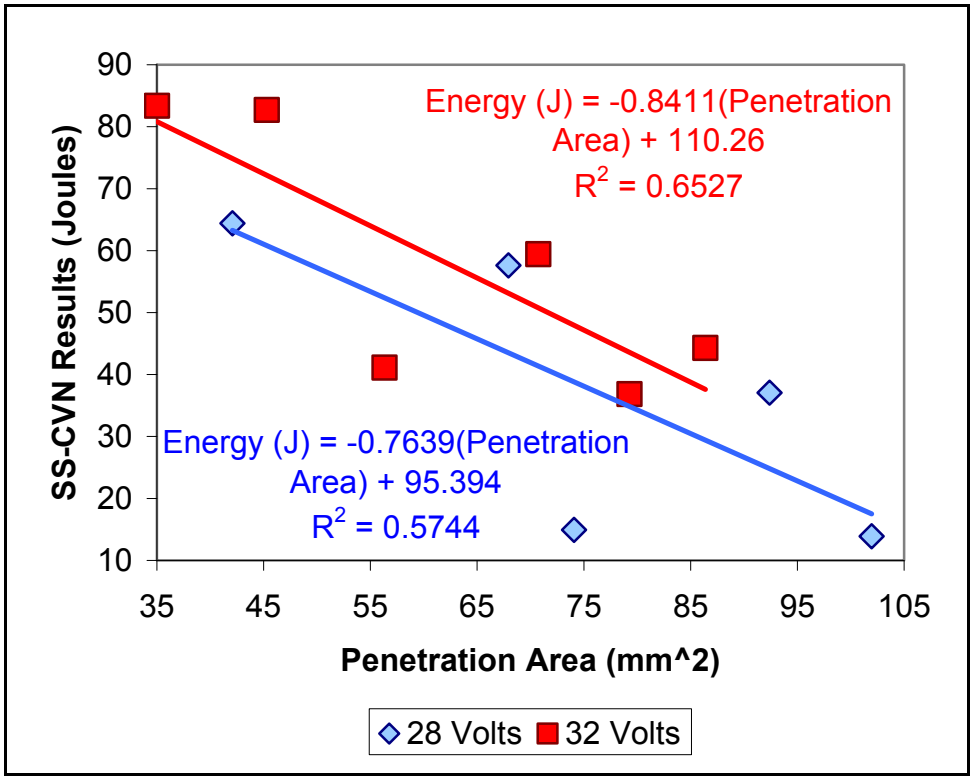

Figure A-2: Effect of Voltage & Penetration Area on SS-CVN Fracture Energy

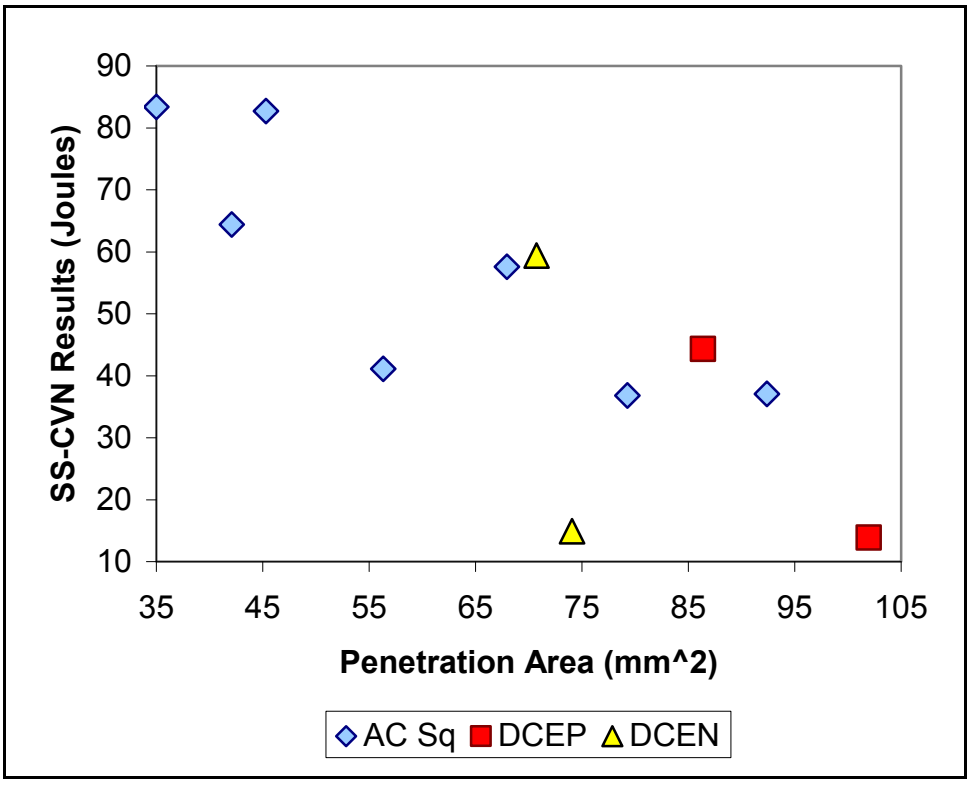

Figure A-3: Effect of Polarity & Penetration Area on SS-CVN Fracture Energy

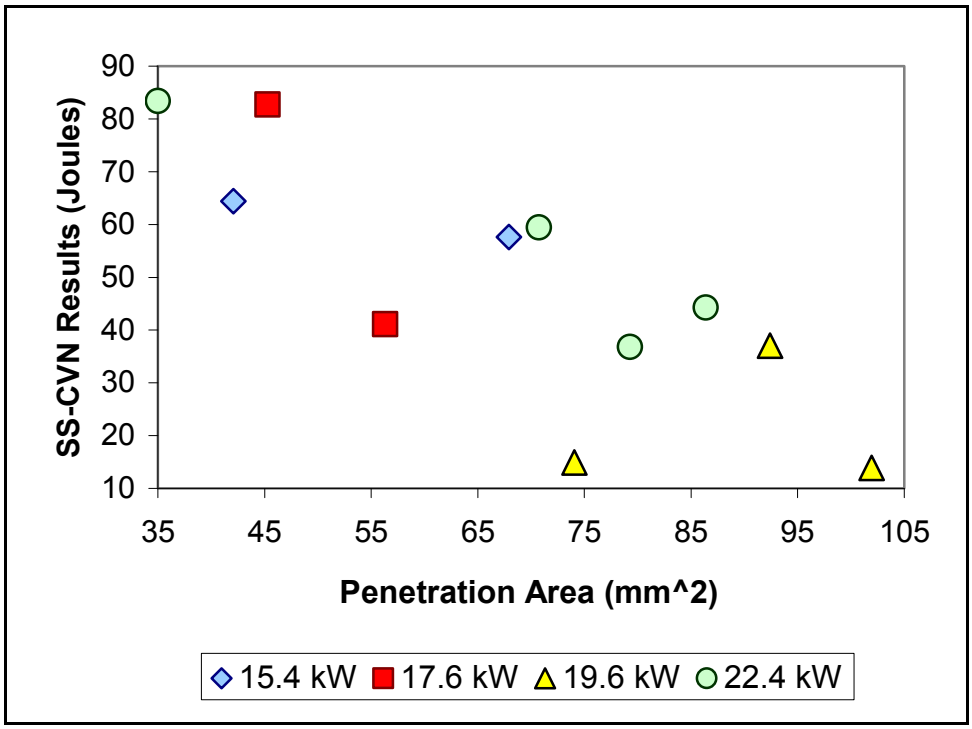

Figure A-4: Effect of Power (VxA) & Penetration Area on SS-CVN Fracture Energy

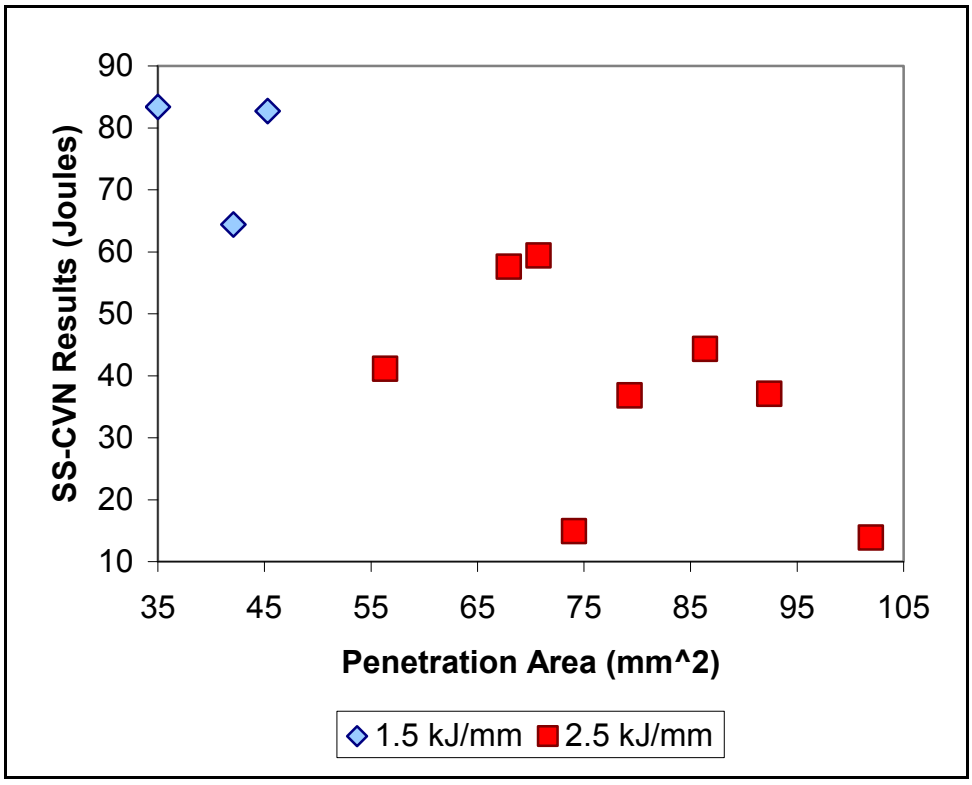

Figure A-5: Effect of Heat Input & Penetration Area on SS-CVN Fracture Energy

8.2: Re-Evaluation of Figure 6-5 (The Effect of Reinforcement Area on SS-CVN Fracture Energy)

Figure 6-5 illustrates the effect of reinforcement area on SS-CVN fracture energy values. Figure A- through A-10 show the effect of distinguishing the points from Figure 6-5 based upon current, voltage, polarity, power, and heat input values respectively. The figures do not reveal any new trends from Figure 6-5, and as such, were not included in Section 6.7 for additional analysis.

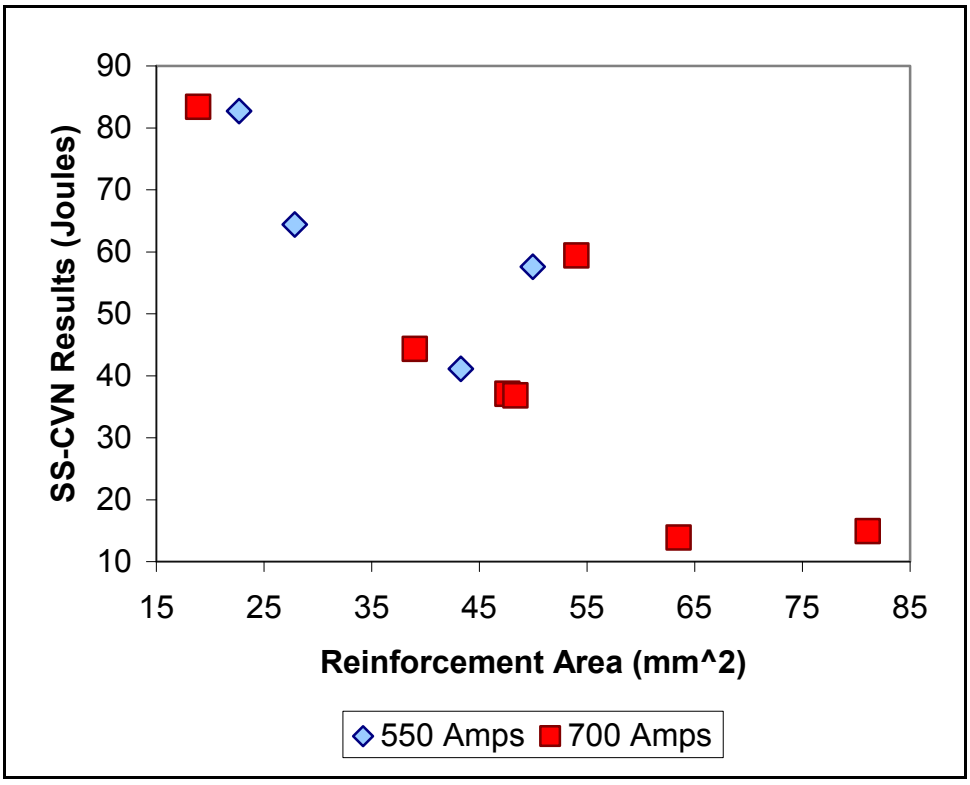

Figure A-6: The Effect of Current and Reinforcement Area on SS-CVN Fracture Energy

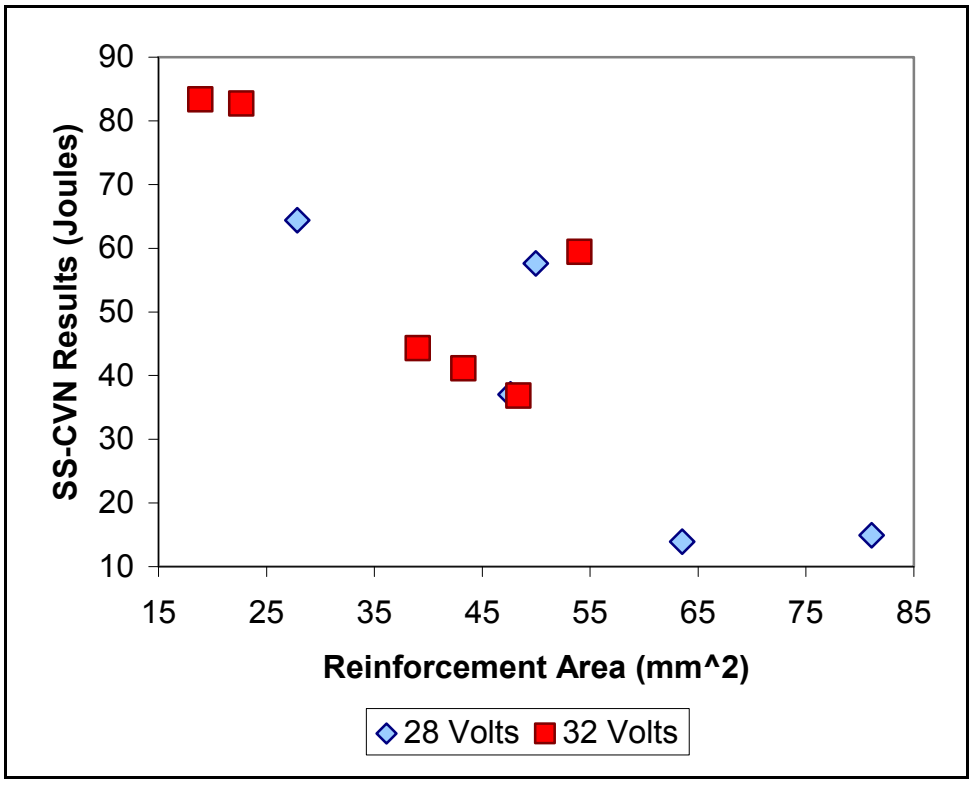

Figure A-7: The Effect of Voltage and Reinforcement Area on SS-CVN Fracture Energy

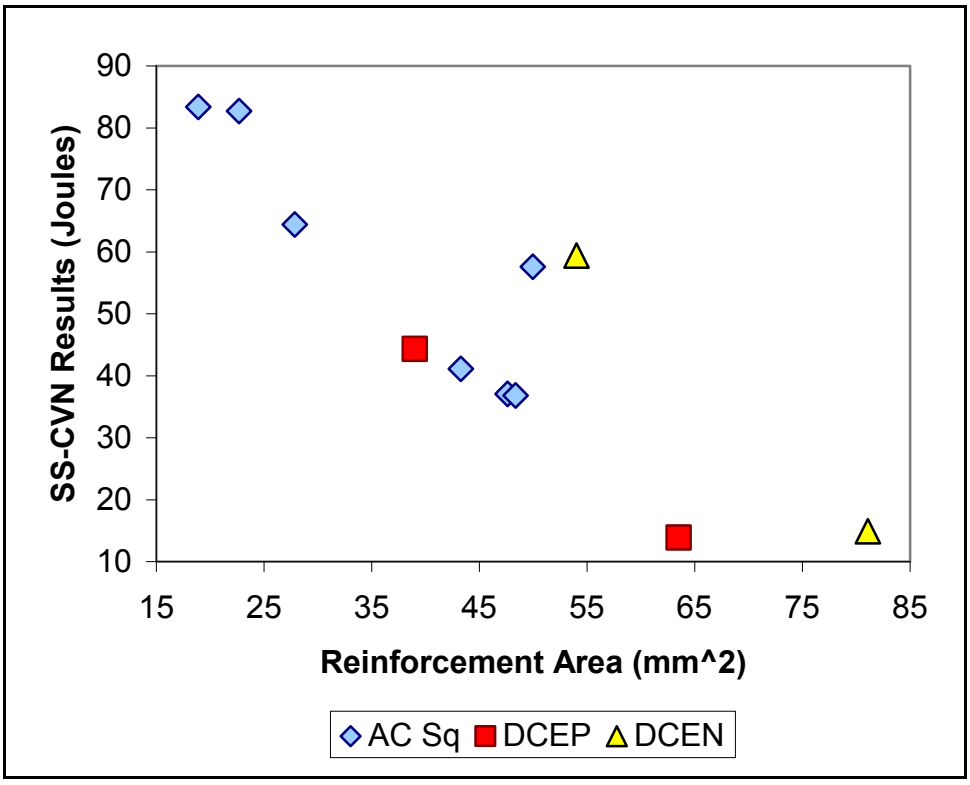

Figure A-8: The Effect of Polarity and Reinforcement Area on SS-CVN Fracture Energy

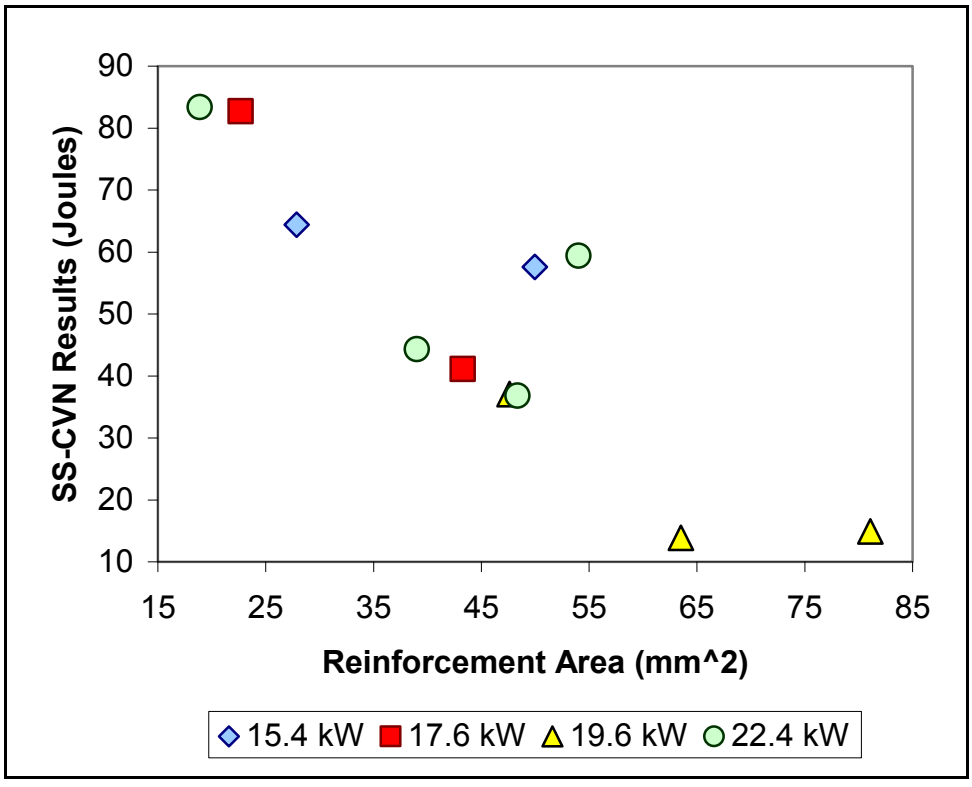

Figure A-9: The Effect of Power (VxA) & Reinforcement Area on SS-CVN Fracture Energy

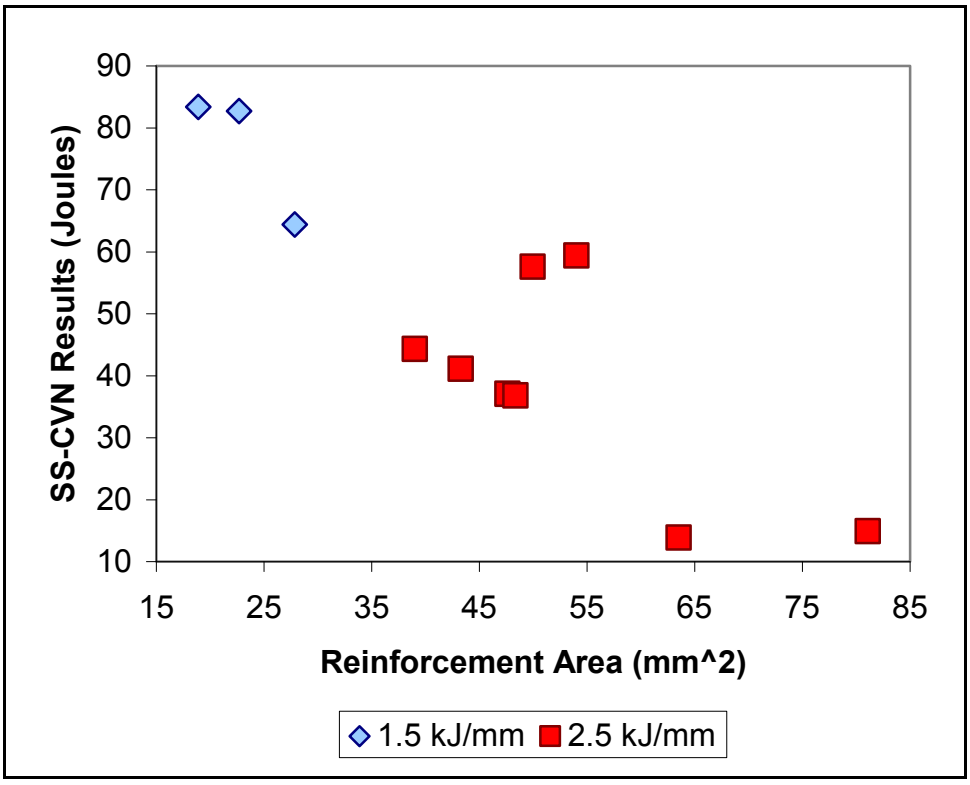

Figure A-10: The Effect of Current and Reinforcement Area on SS-CVN Fracture Energy

8.3: Re-Evaluation of Figure 6-6 (The Effect of Total Molten Area on SS-CVN Fracture Energy)

Figure 6-6 illustrates the effect of total molten area (i.e., the sum of penetration area and reinforcement area) on SS-CVN fracture energy values. Figure A- through A-15 show the effect of distinguishing the points from Figure 6-6 based upon current, voltage, polarity, power, and heat input values respectively. The figures do not reveal any new trends from Figure 6-6, and as such, were not included in Section 6.7 for additional analysis.

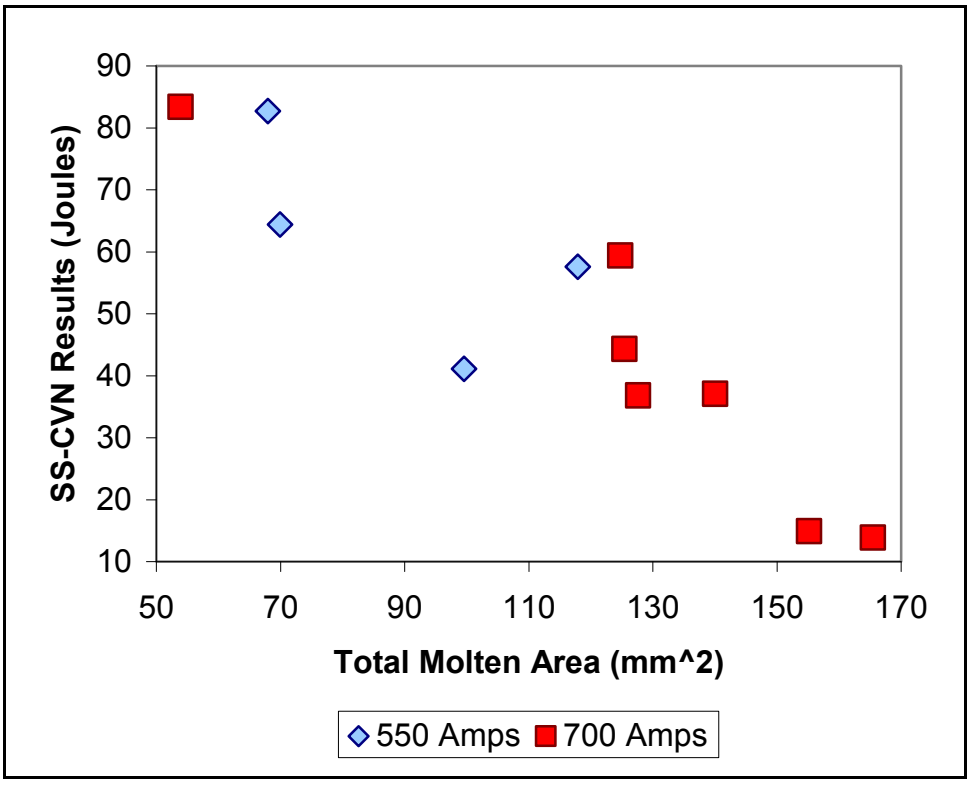

Figure A-11: The Effect of Current and Total Molten Area on SS-CVN Fracture Energy

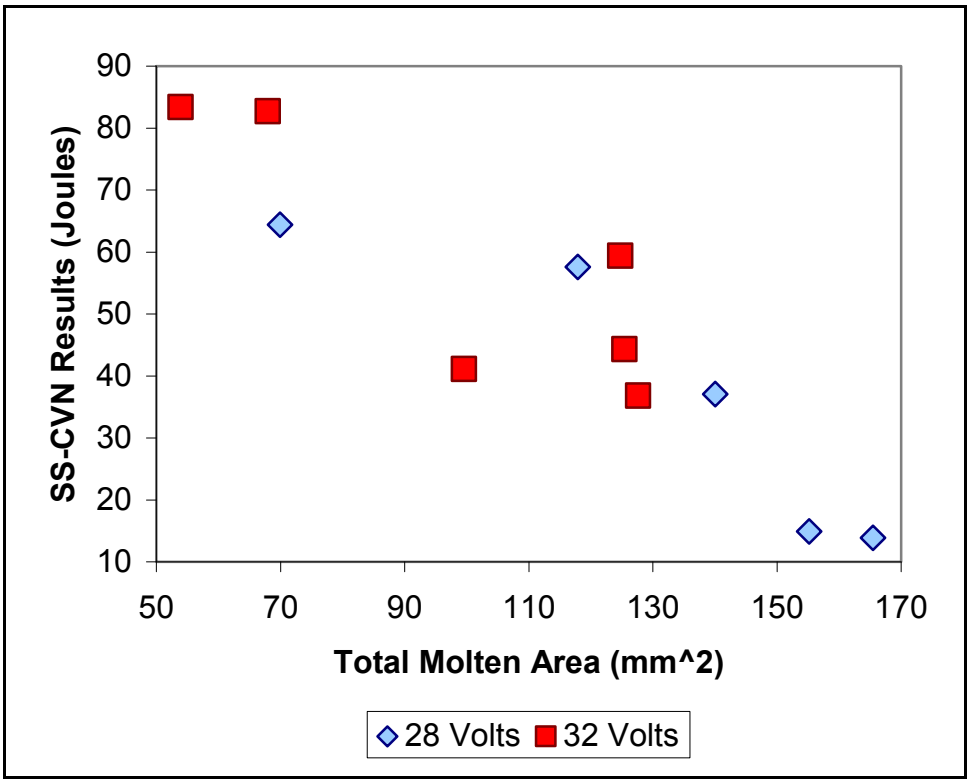

Figure A-12: The Effect of Voltage and Total Molten Area on SS-CVN Fracture Energy

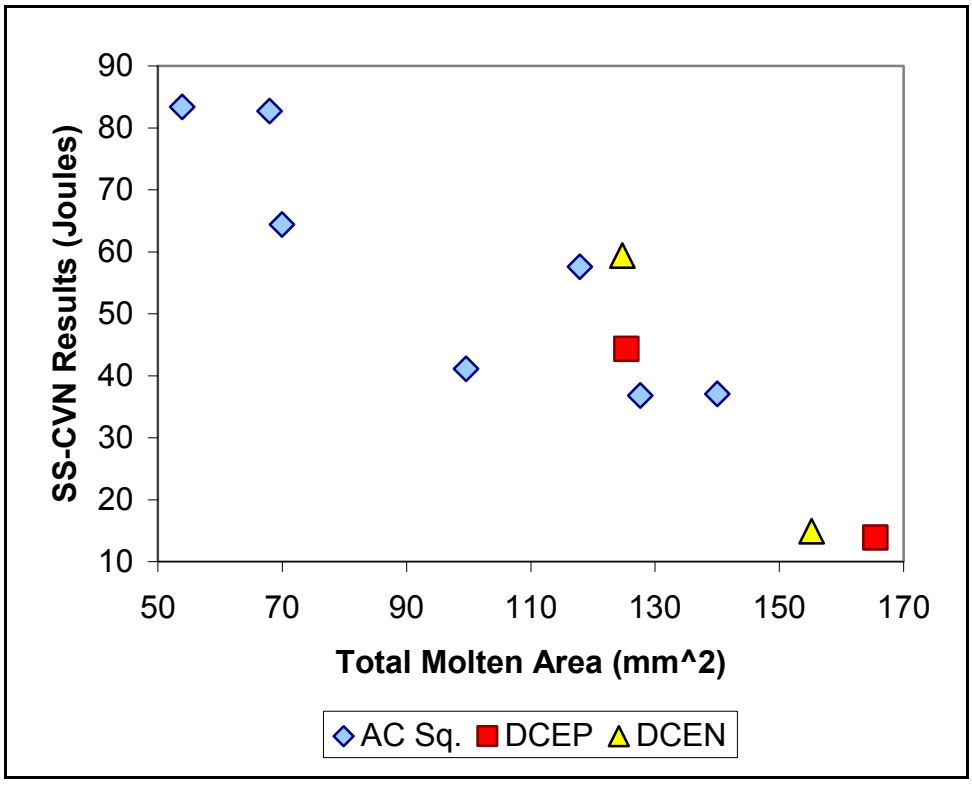

Figure A-13: The Effect of Polarity and Total Molten Area on SS-CVN Fracture Energy

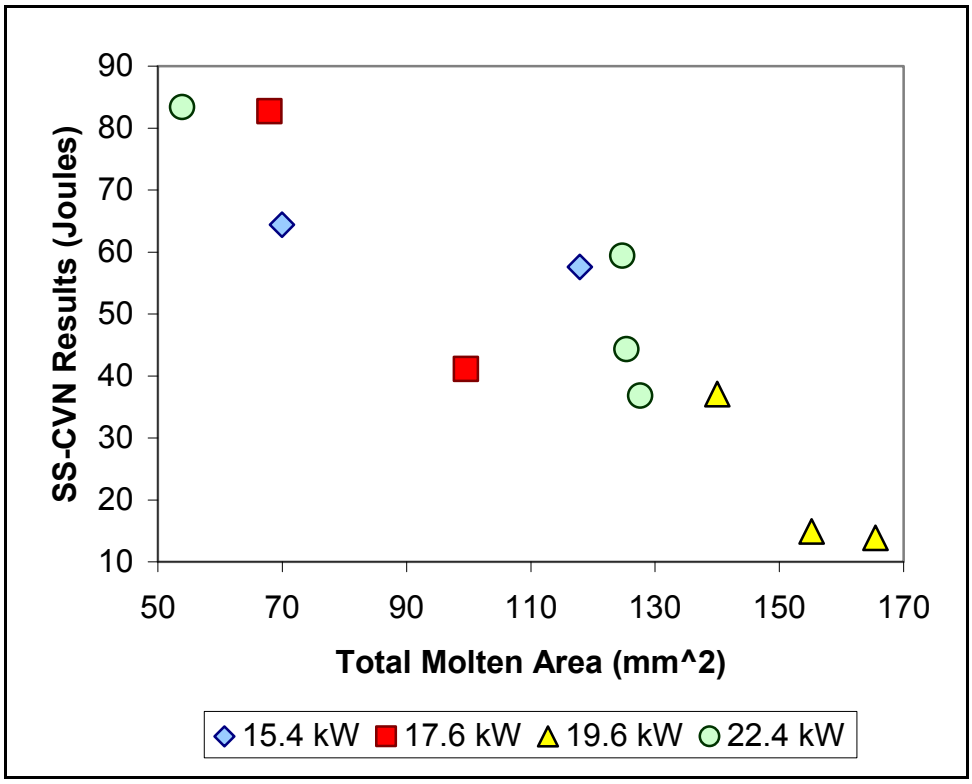

Figure A-14: The Effect of Power (VxA) and Total Molten Area on SS-CVN Fracture Energy

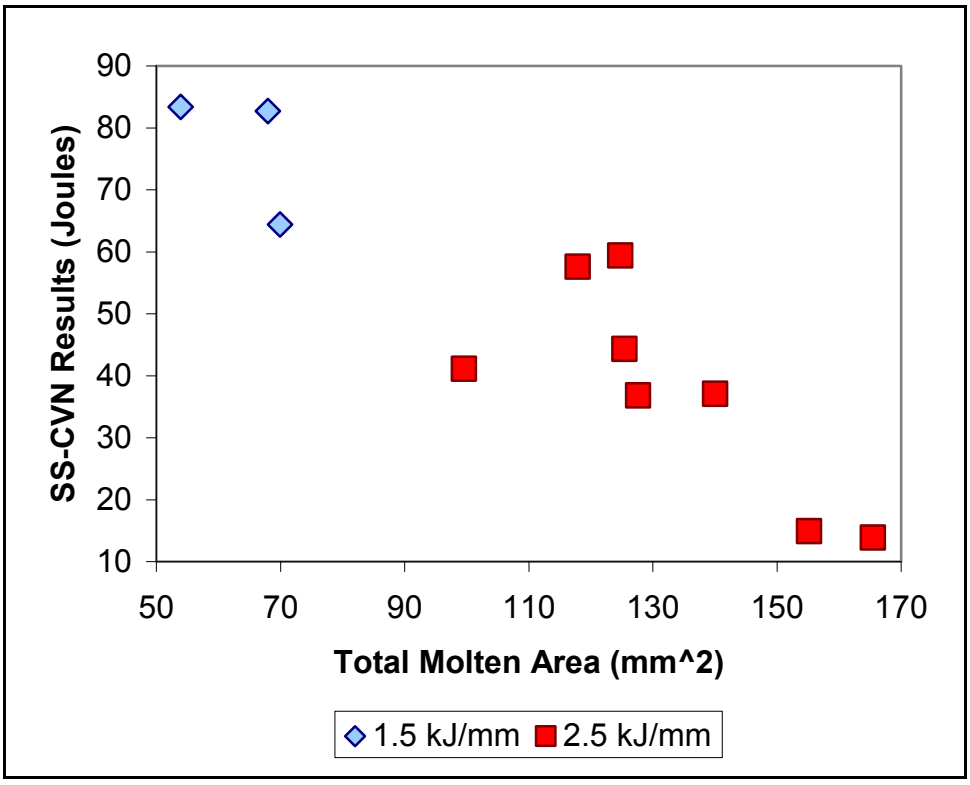

Figure A-15: The Effect of Heat Input and Total Molten Area on SS-CVN Fracture Energy

8.4: Re-Evaluation of Figure 6-7 (The Effect of Area Ratio on SS-CVN Fracture Energy)

Figure 6-7 illustrates the effect of molten area ratio (i.e., the area ratio, divided by the penetration area) on SS-CVN fracture energy values. Figure A- through A-20 show the effect of distinguishing the points from Figure 6-7 based upon current, voltage, polarity, power, and heat input values respectively. Figure A-16 appears to show that for welds produced using a 550 Amp current, an increase in area ratio should result in a reduction of SS-CVN fracture energy values. However, the same figure shows no trend for welds produced using a 700 Amp current. As a result, the figure did not undergo additional analysis. The remaining figures do not reveal any new trends from Figure 6-7, and as such, were not included in Section 6.7 for additional analysis either.

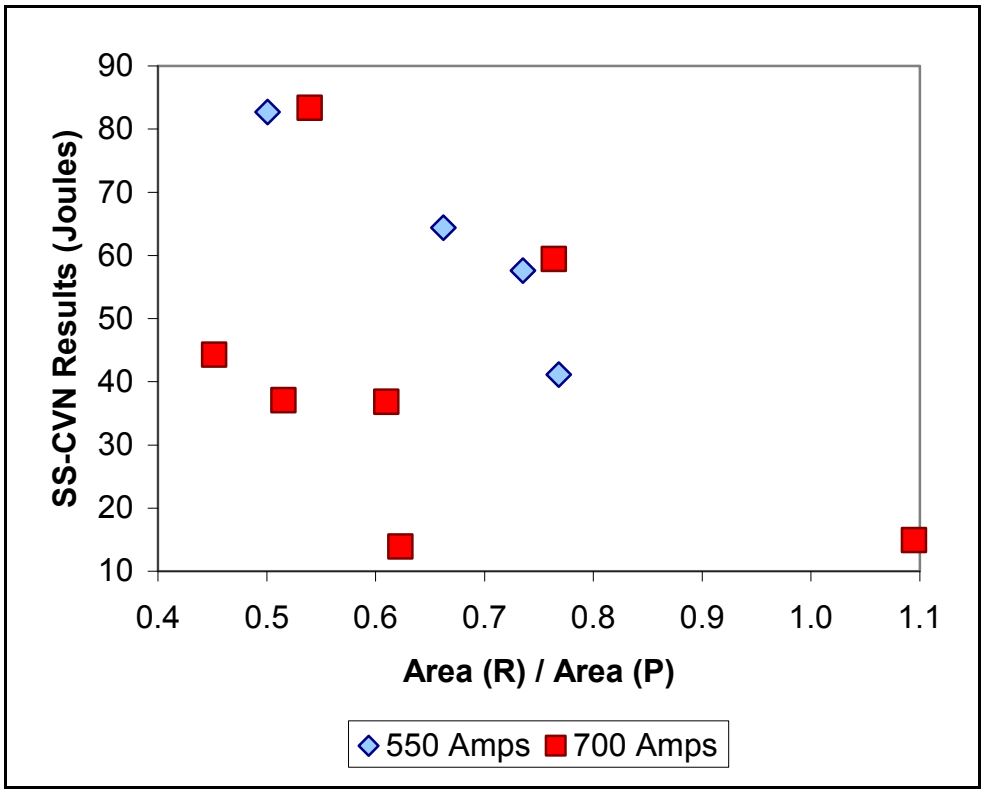

Figure A-16: The Effect of Current and Area Ratio on SS-CVN Fracture Energy

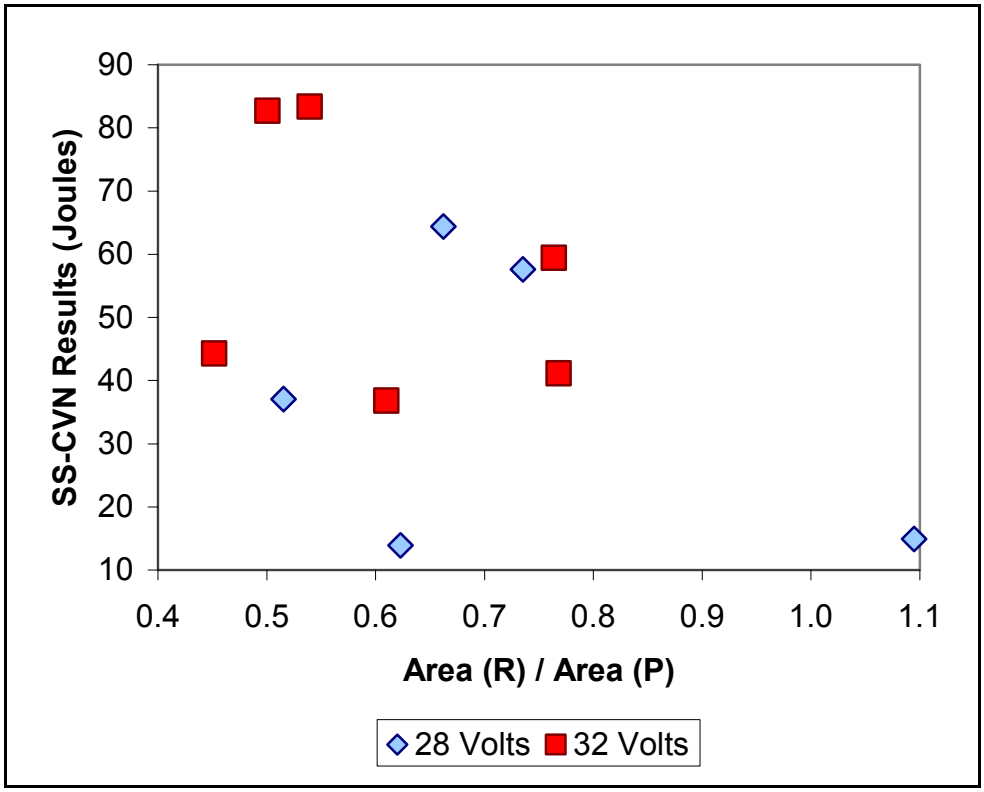

Figure A-17: The Effect of Voltage and Area Ratio on SS-CVN Fracture Energy

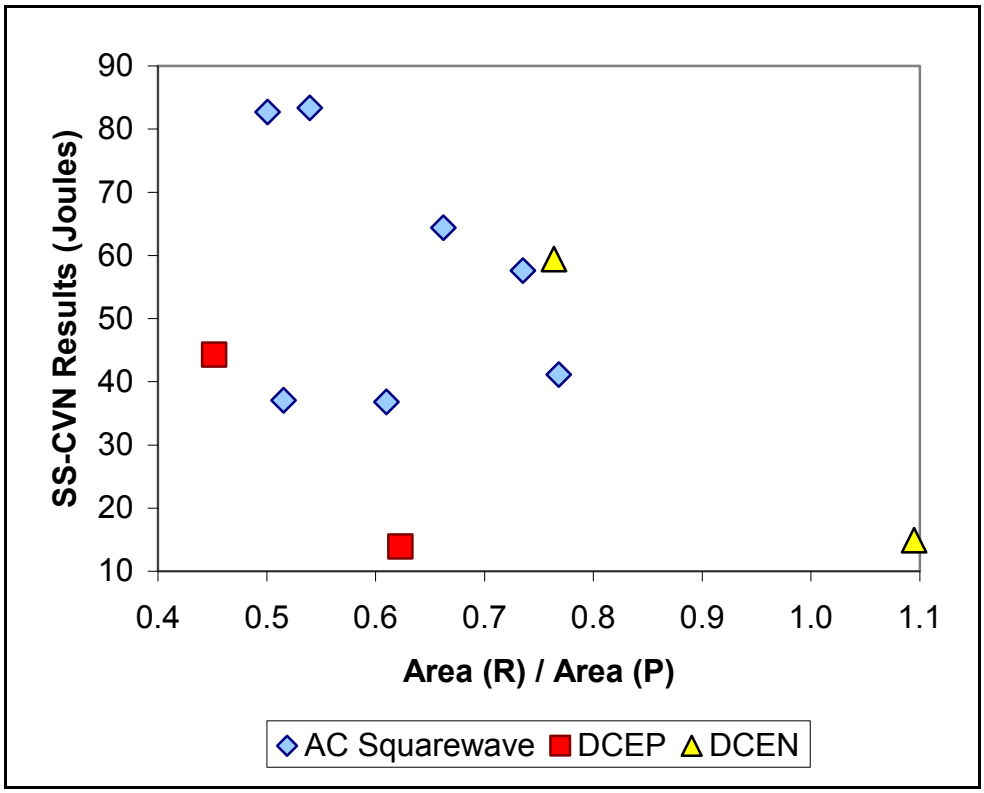

Figure A-18: The Effect of Polarity and Area Ratio on SS-CVN Fracture Energy

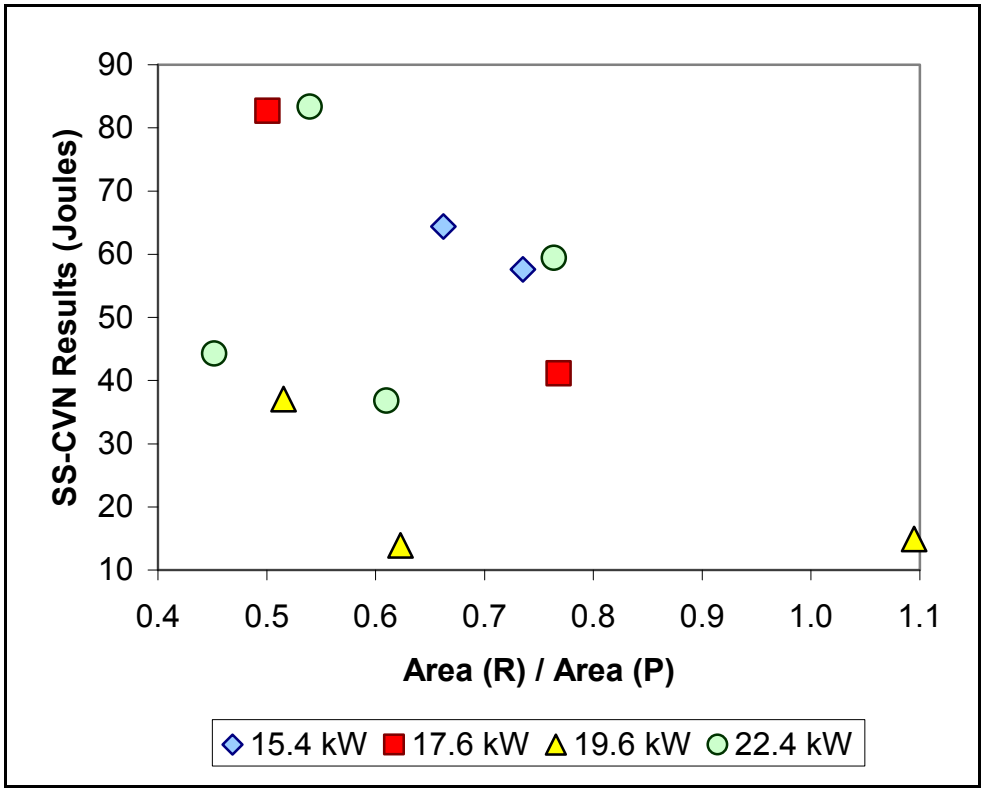

Figure A-19: The Effect of Power (VxA) and Area Ratio on SS-CVN Fracture Energy

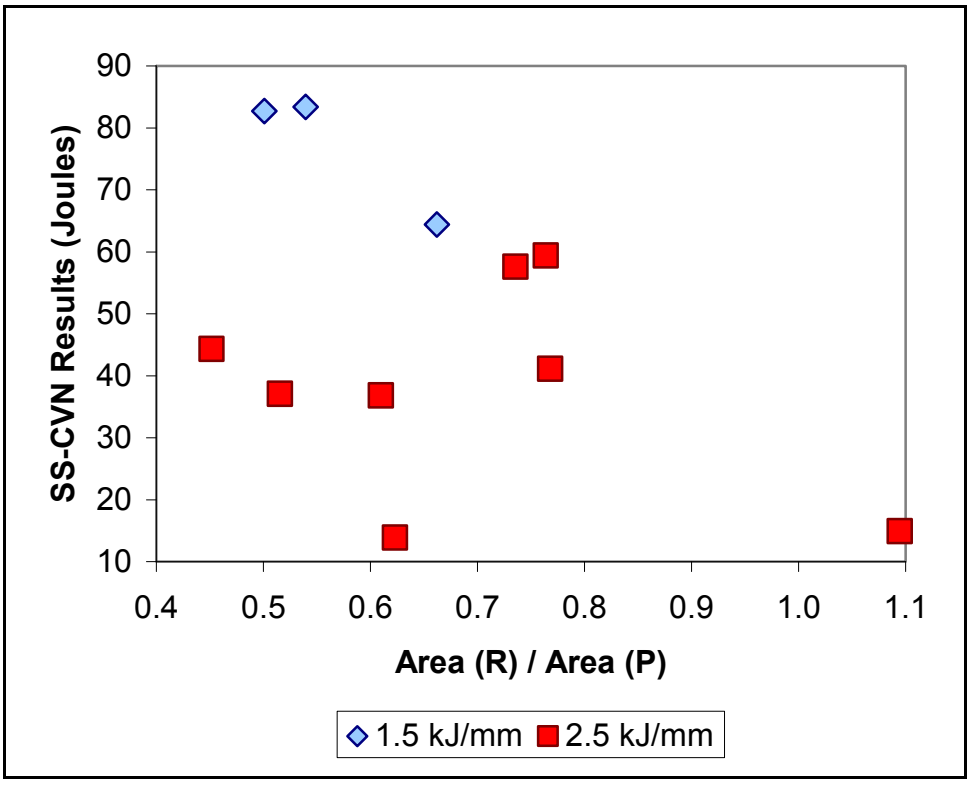

Figure A-20: The Effect of Heat Input and Area Ratio on SS-CVN Fracture Energy

8.5: Re-Evaluation of Figure 6-8 (The Effect of Bead Width on SS-CVN Fracture Energy)

Figure 6-8 illustrates the effect of bead width on SS-CVN fracture energy values. Figure A- through A-25 show the effect of distinguishing the points from Figure 6-8 based upon current, voltage, polarity, power, and heat input values respectively. Figure A-21 shows that as bead width is increased for welds produced using 550 amps, there appears to be a reduction in SS-CVN fracture energy. Also, Figure A-22 shows that a decrease in SS-CVN fracture energy as bead width is increased for welds produced using 32 volts. However, no trends were shown in the two figures for beads produced using 700 amps or 28 volts respectively. As a result, the figures did not undergo additional analysis in Section 6.7. The remaining figures do not reveal any new trends from Figure 6-8, and as such, were not included in Section 6.7 for additional analysis either.

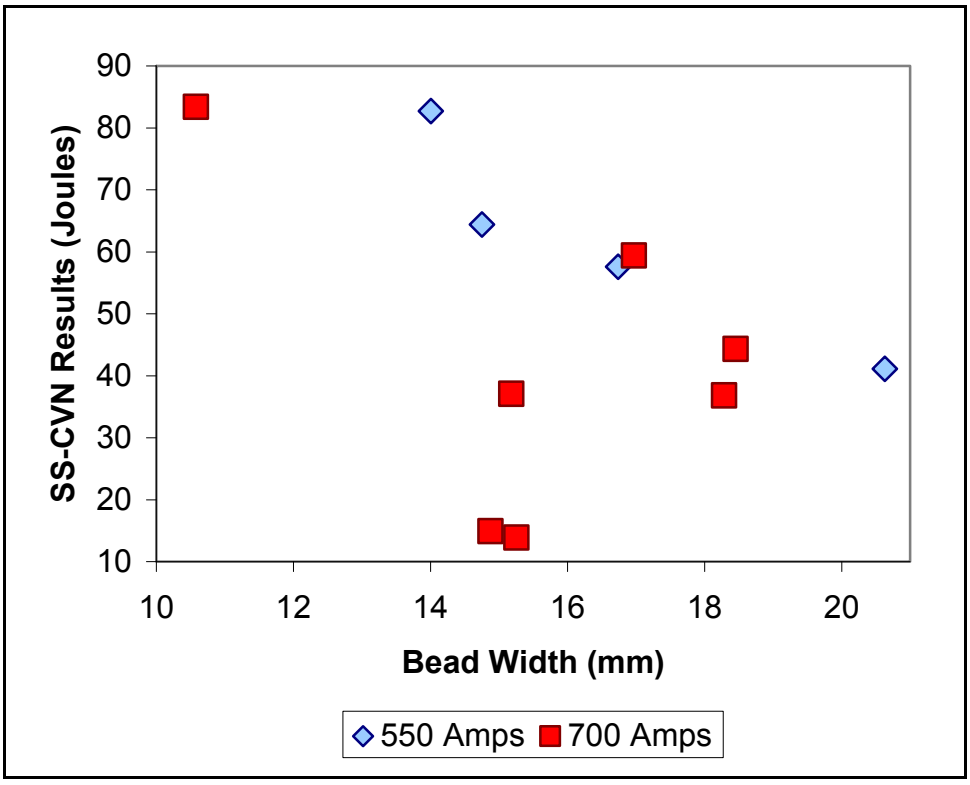

Figure A-21: The Effect of Current and Bead Width on SS-CVN Fracture Energy

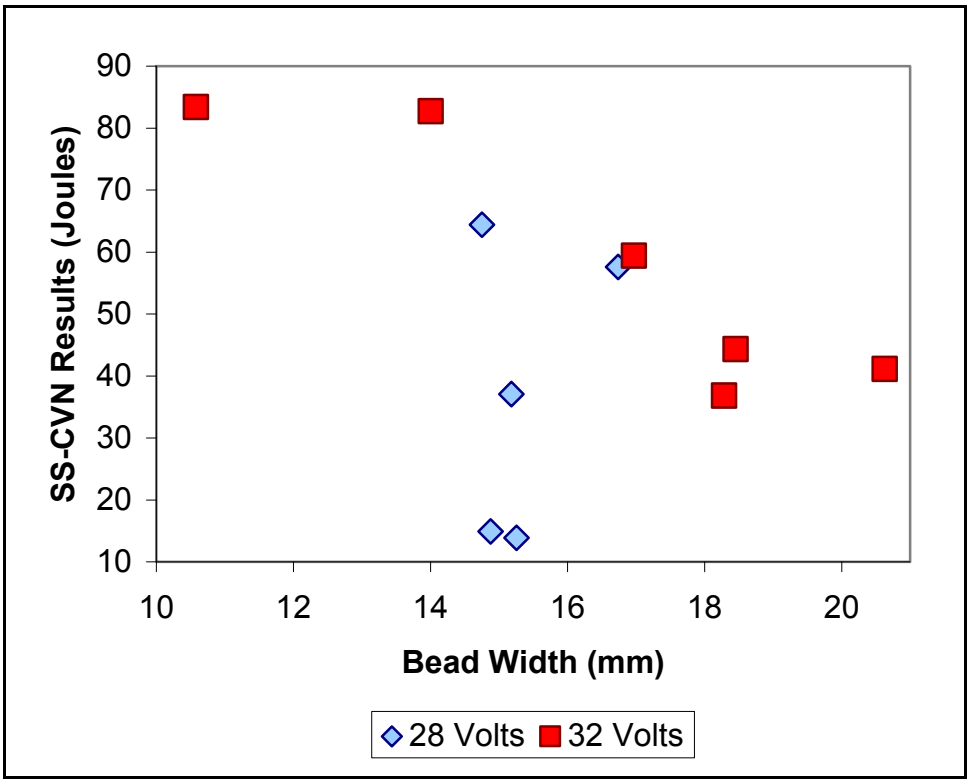

Figure A-22: The Effect of Voltage and Bead Width on SS-CVN Fracture Energy

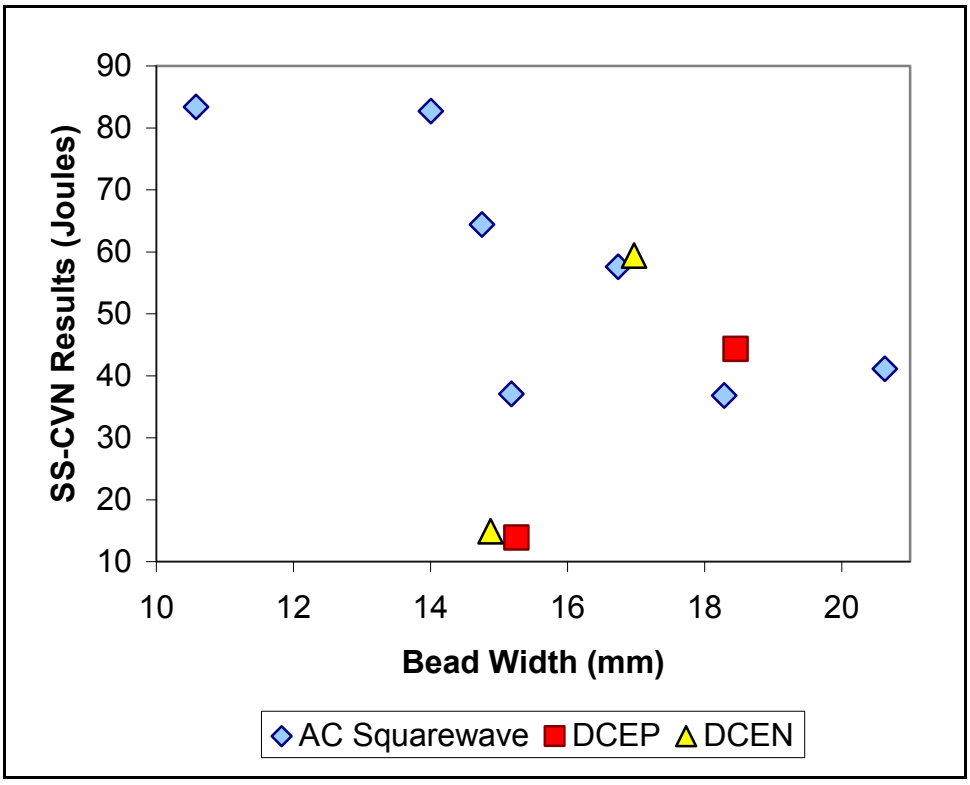

Figure A-23: The Effect of Polarity and Bead Width on SS-CVN Fracture Energy

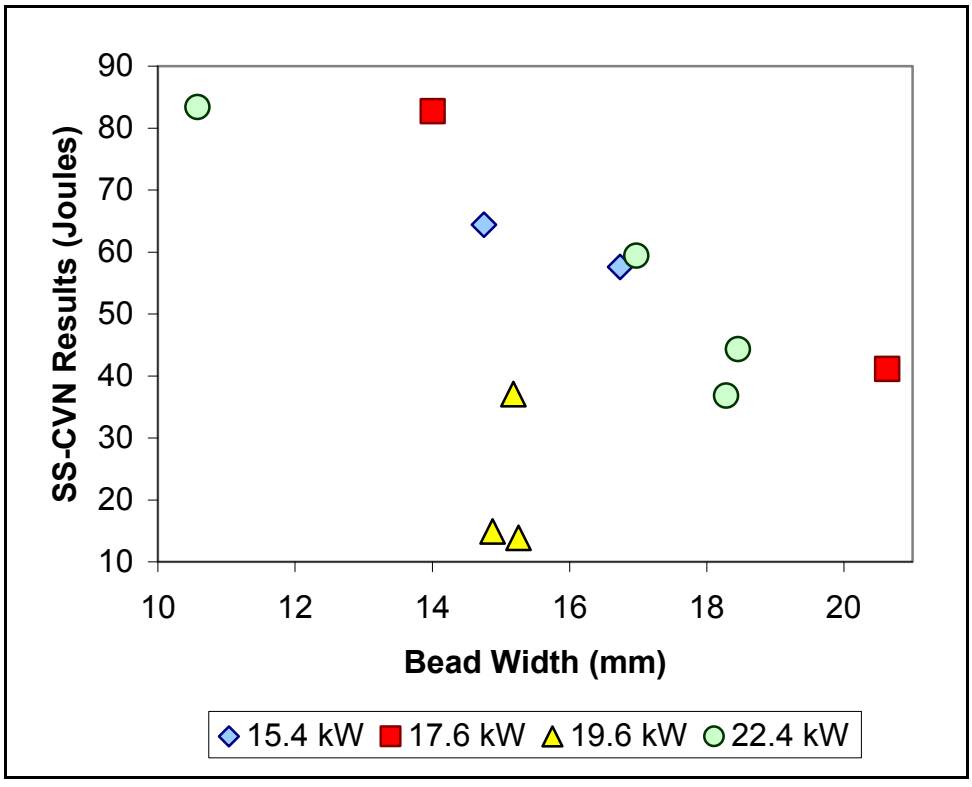

Figure A-24: The Effect of Power (VxA) and Bead Width on SS-CVN Fracture Energy

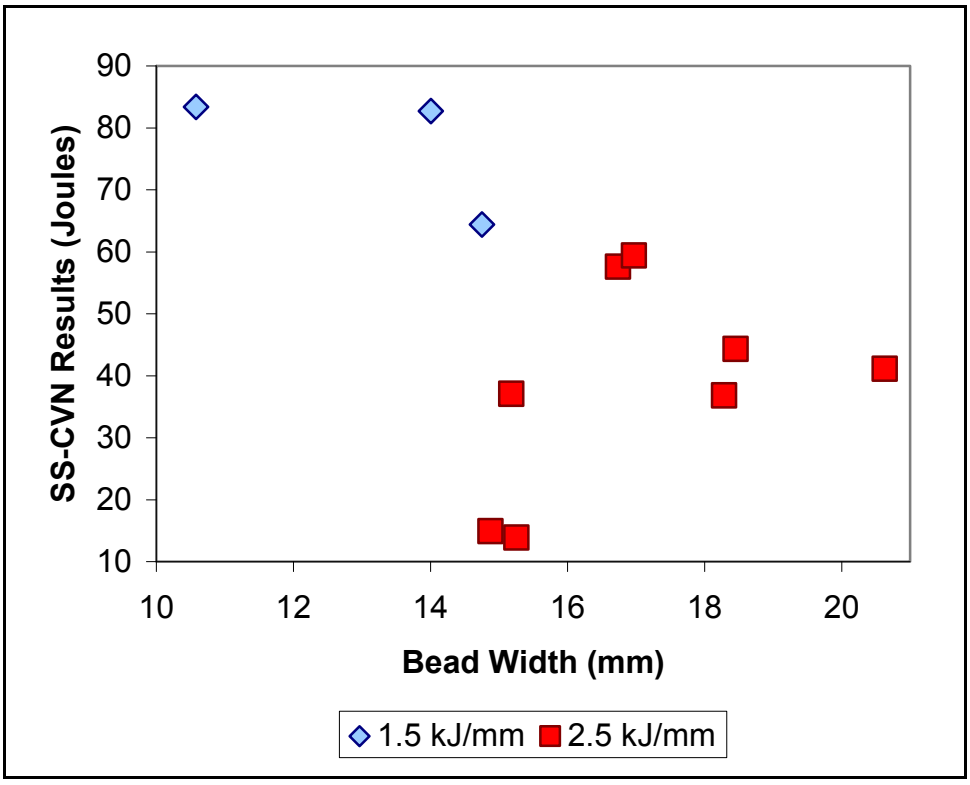

Figure A-25: The Effect of Heat Input and Bead Width on SS-CVN Fracture Energy

8.6: Re-Evaluation of Figure 6-9 (The Effect of Penetration Depth on SS-CVN Fracture Energy)

Figure 6-9 illustrates the effect of penetration depth on SS-CVN fracture energy values. Figure A- through A-30 show the effect of distinguishing the points from Figure 6-9 based upon current, voltage, polarity, power, and heat input values respectively. The figures do not reveal any new trends from Figure 6-9, and as such, were not included in Section 6.7 for additional analysis.

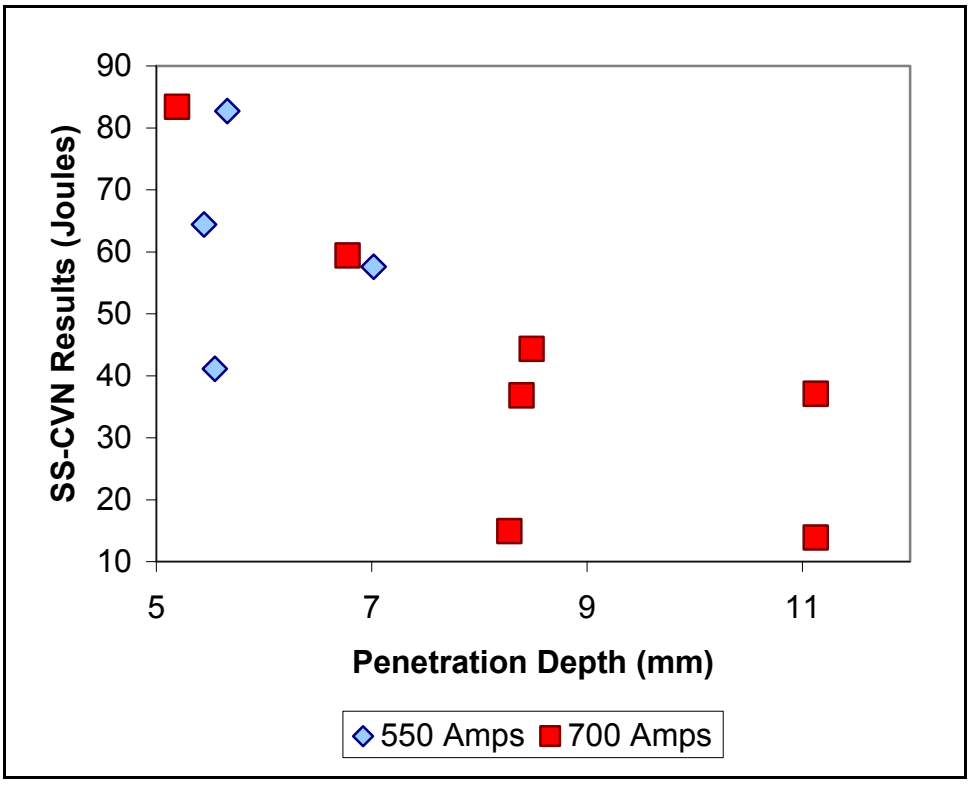

Figure A-26: The Effect of Current and Penetration Depth on SS-CVN Fracture Energy

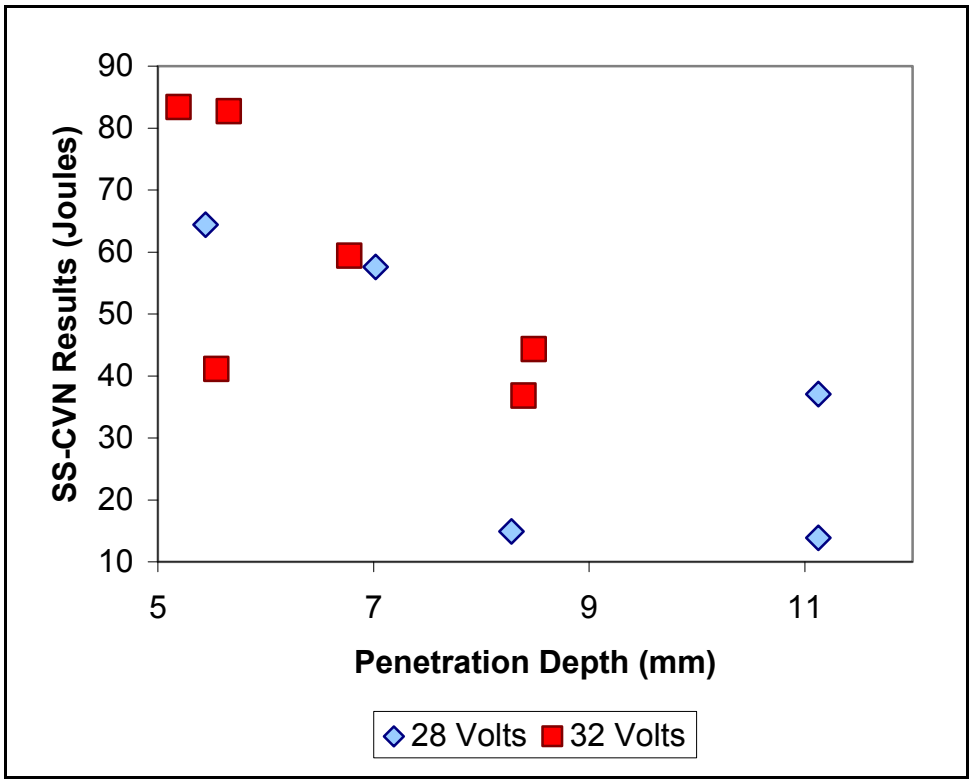

Figure A-27: The Effect of Voltage and Penetration Depth on SS-CVN Fracture Energy

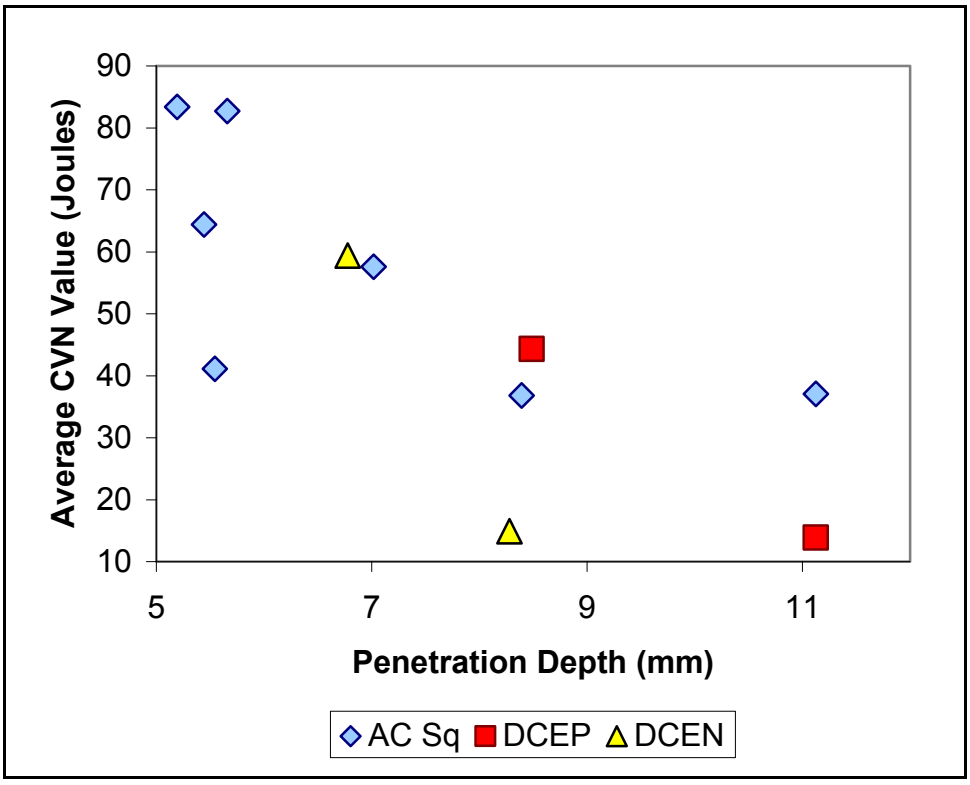

Figure A-28: The Effect of Polarity and Penetration Depth on SS-CVN Fracture Energy

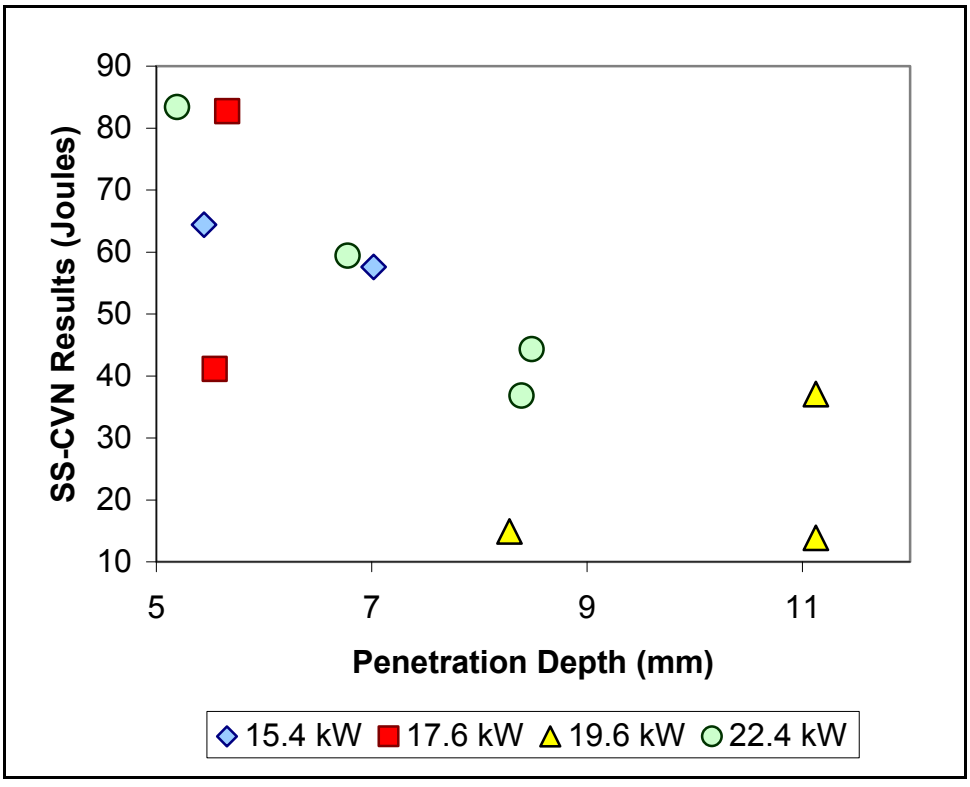

Figure A-29: The Effect of Power (VxA) and Penetration Depth on SS-CVN Fracture Energy

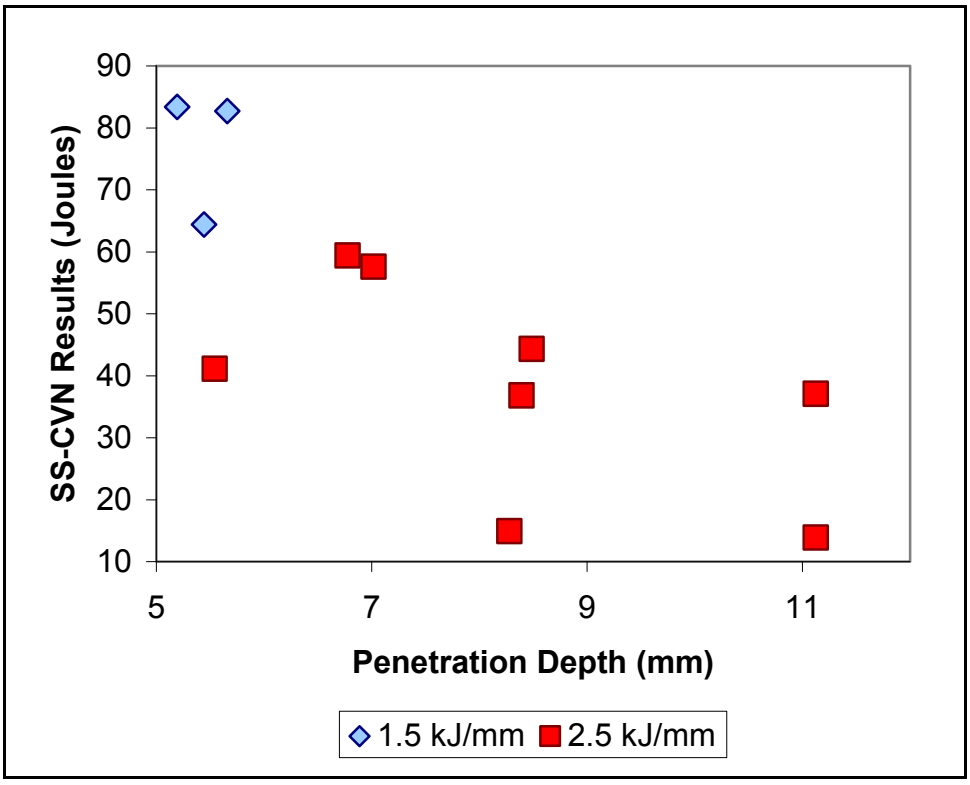

Figure A-30: The Effect of Heat Input and Penetration Depth on SS-CVN Fracture Energy

8.7: Re-Evaluation of Figure 6-10 (The Effect of Reinforcement Height on SS-CVN Fracture Energy)

Figure 6-10 illustrates the effect of reinforcement height on SS-CVN fracture energy values. Figure A-31 through A-31 show the effect of distinguishing the points from Figure 6-10 based upon current, voltage, polarity, power, and heat input values respectively. Figure A-32 appears to show that for weld beads produced using 28 volts, an increase in reinforcement height should reduce the SS-CVN fracture energy values. However, because there is no trend for the beads produced using 32 volts, the figure was not included in Section 6.7 for additional analysis. The remaining figures do no reveal any new trends for Figure 6-10, and as such, were not included in Section 6.7 either.

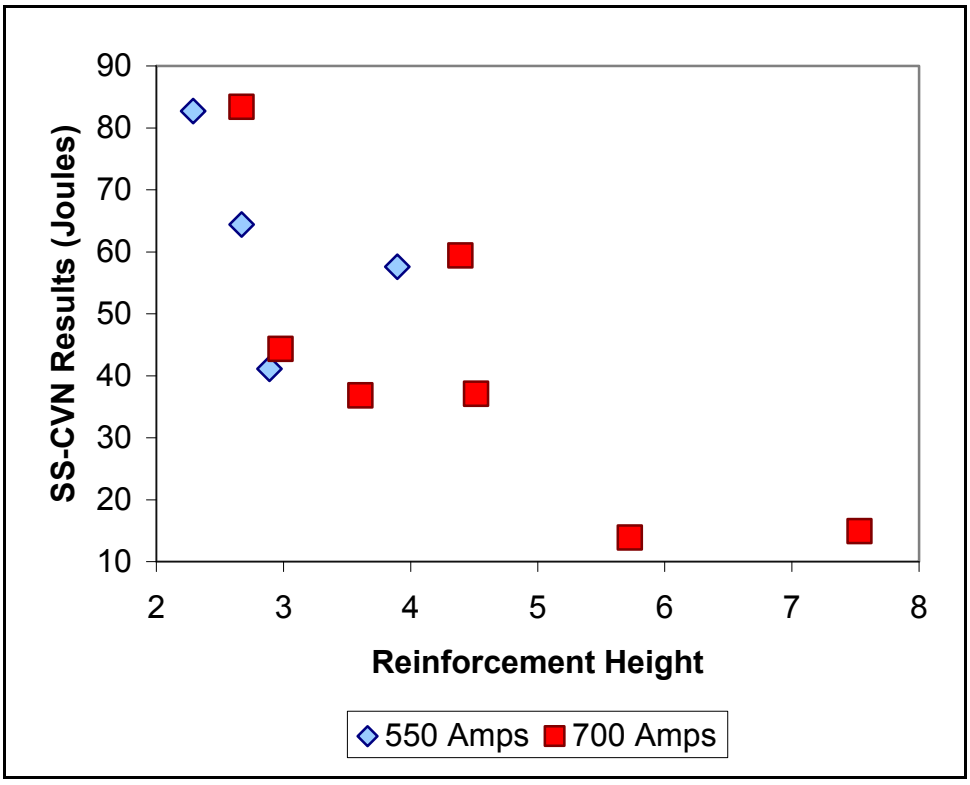

Figure A-31: The Effect of Current and Reinforcement Height on SS-CVN Fracture Energy

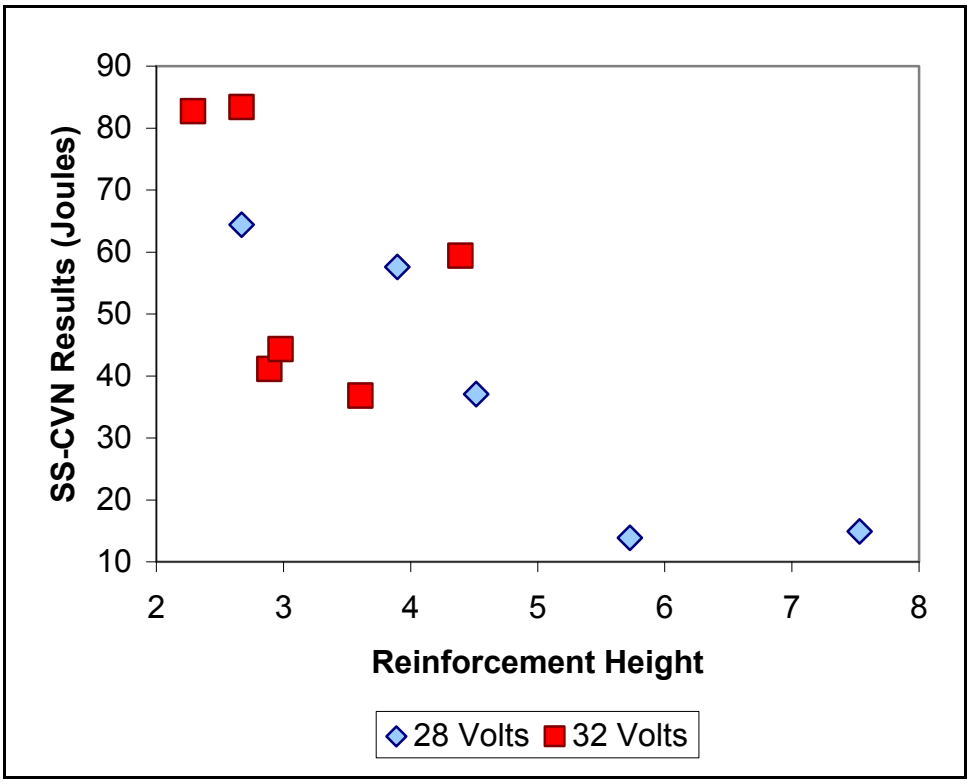

Figure A-32: The Effect of Voltage and Reinforcement Height on SS-CVN Fracture Energy

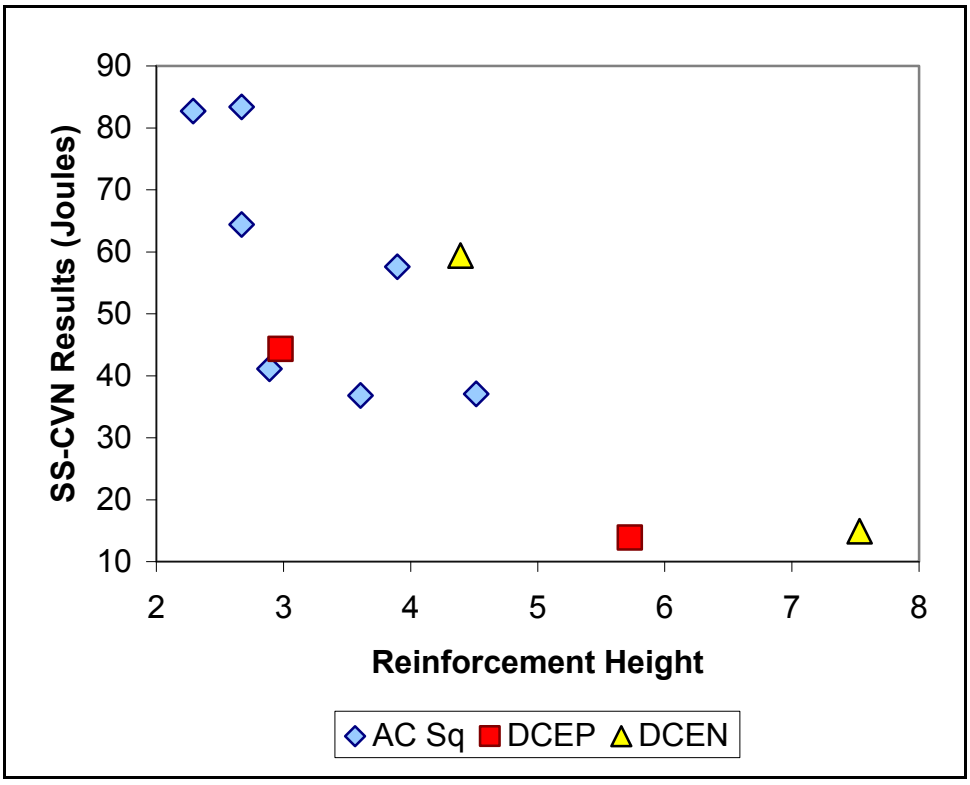

Figure A-33: The Effect of Polarity and Reinforcement Height on SS-CVN Fracture Energy

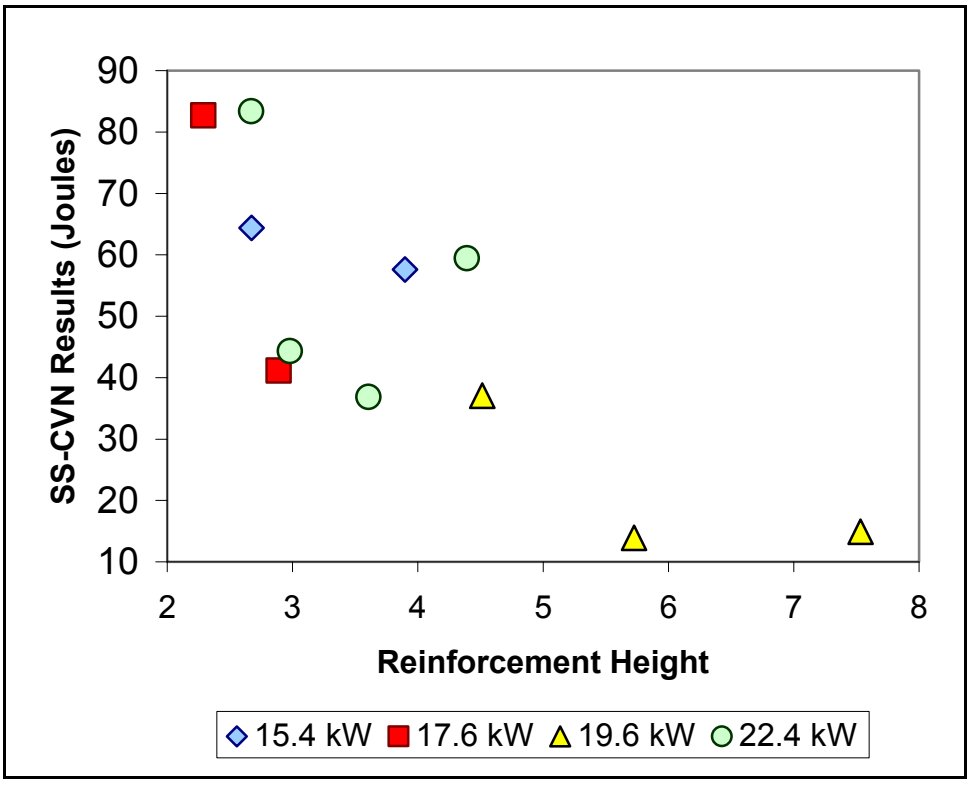

Figure A-34: The Effect of Power (VxA) and Reinforcement Height on SS-CVN Fracture Energy

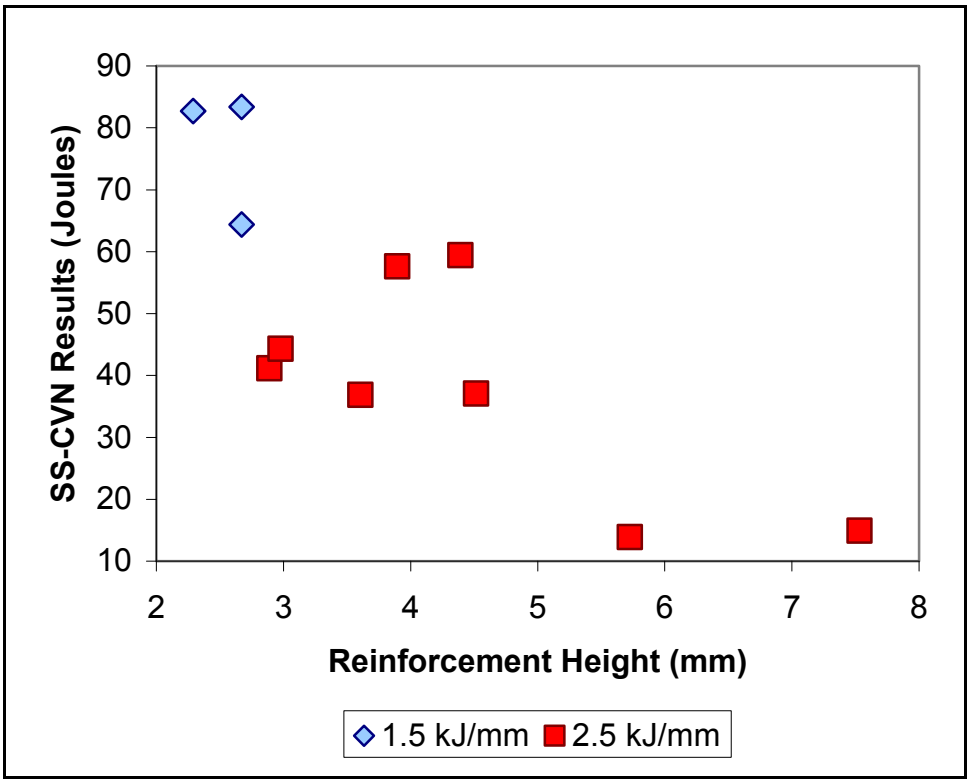

Figure A-35: The Effect of Heat Input and Reinforcement Height on SS-CVN Fracture Energy

8.8: Re-Evaluation of Figure 6-11 (The Effect of Aspect Ratio on SS-CVN Fracture Energy)

Figure 6-11 illustrates the effect of aspect ratio on SS-CVN fracture energy values. Figure A-36 through A-40 show the effect of distinguishing the points from Figure 6-11 based upon current, voltage, polarity, power, and heat input values respectively. The figures do no reveal any new trends for Figure 6-11, and as such, were not included in Section 6.7.

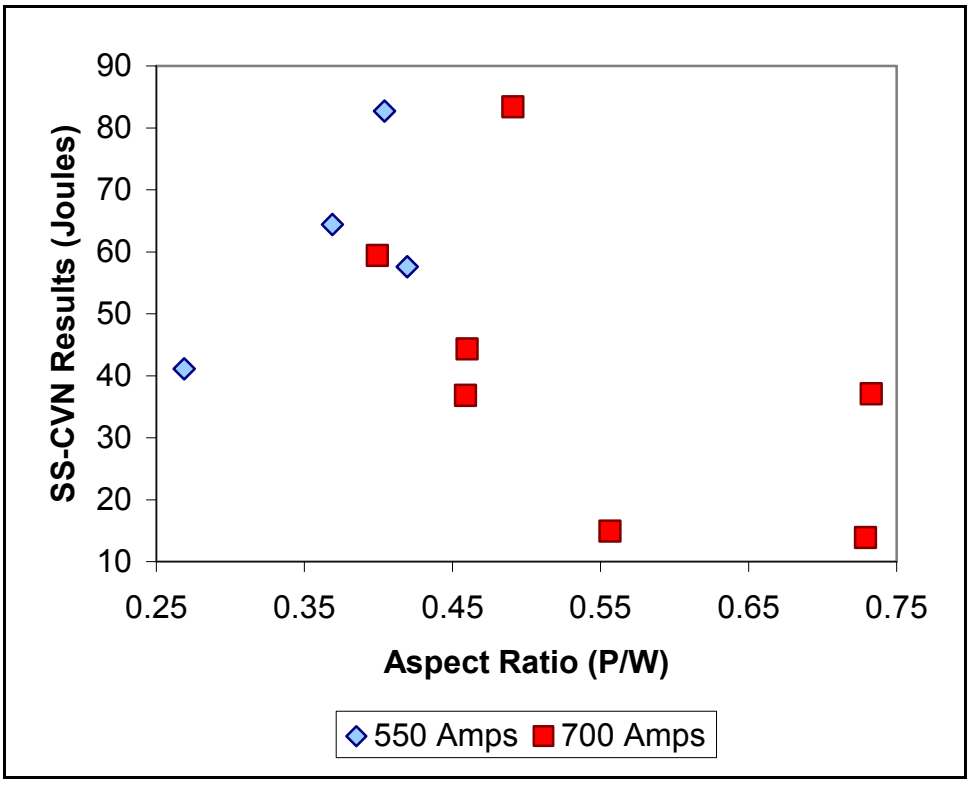

Figure A-36: The Effect of Current and Aspect Ratio on SS-CVN Fracture Energy

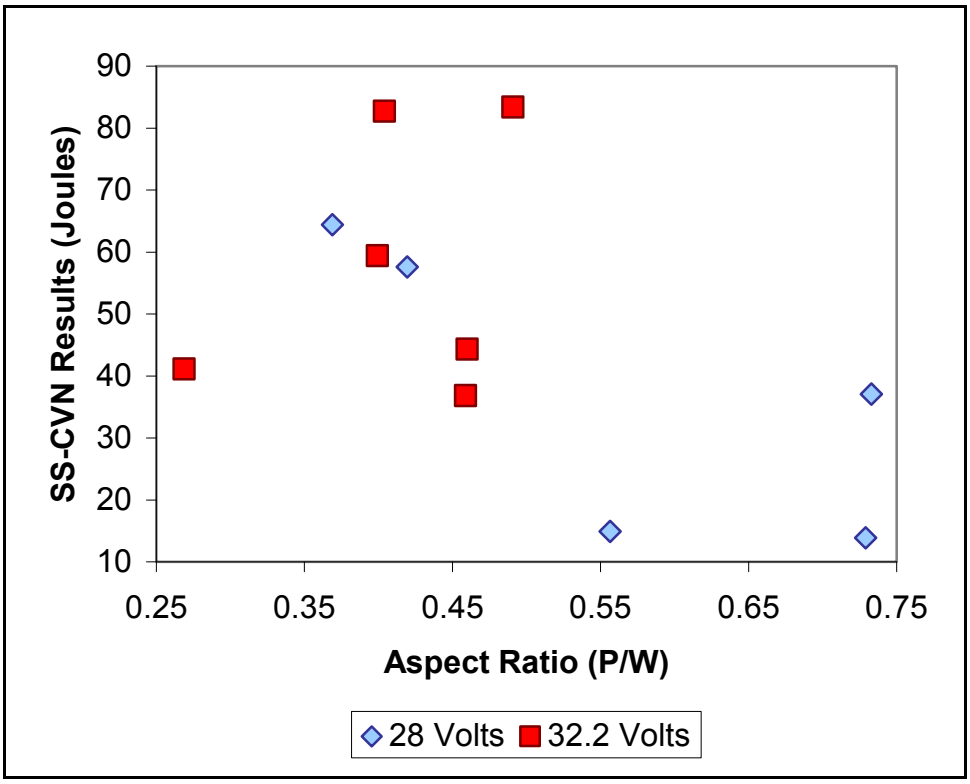

Figure A-37: The Effect of Voltage and Aspect Ratio on SS-CVN Fracture Energy

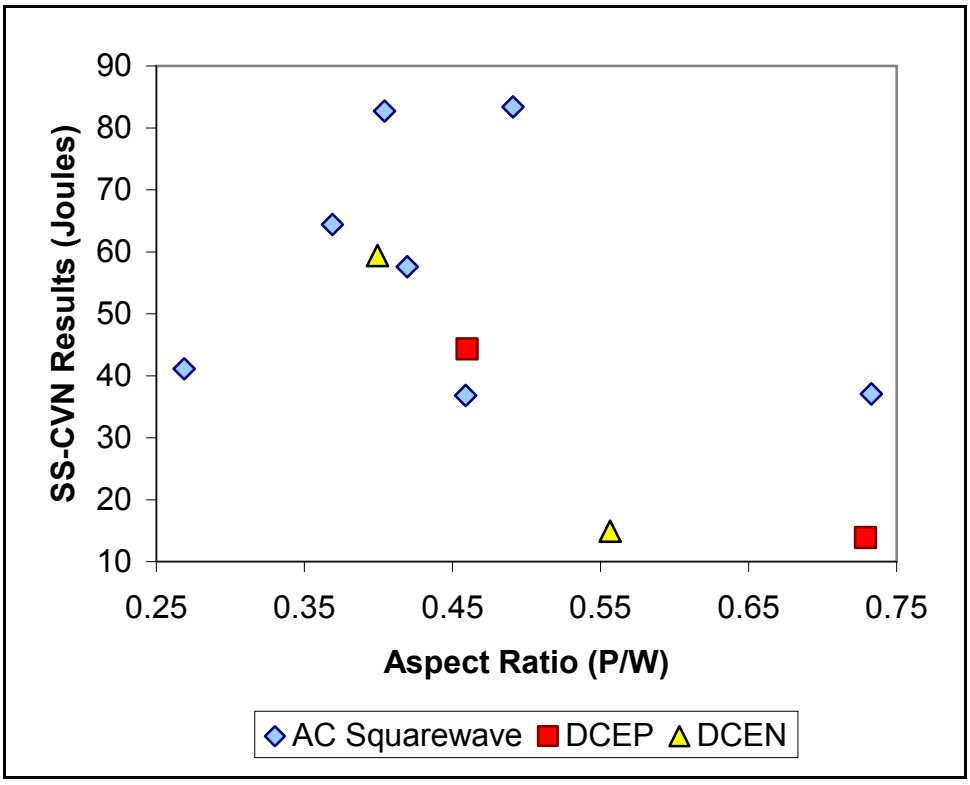

Figure A-38: The Effect of Polarity and Aspect Ratio on SS-CVN Fracture Energy

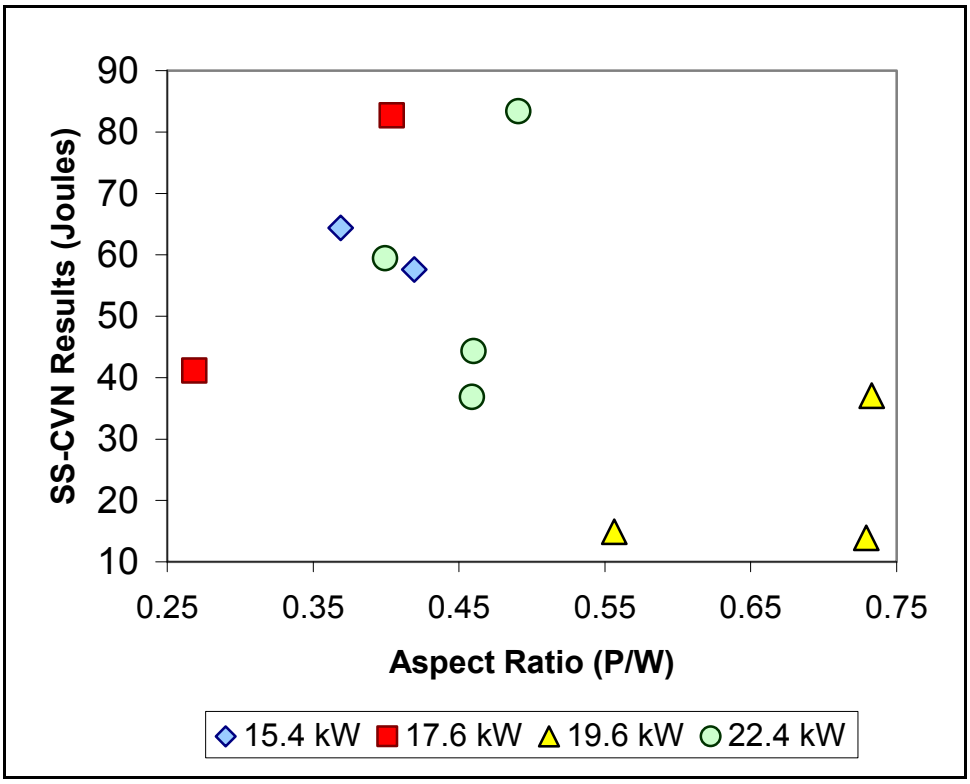

Figure A-39: The Effect of Power (VxA) and Aspect Ratio on SS-CVN Fracture Energy

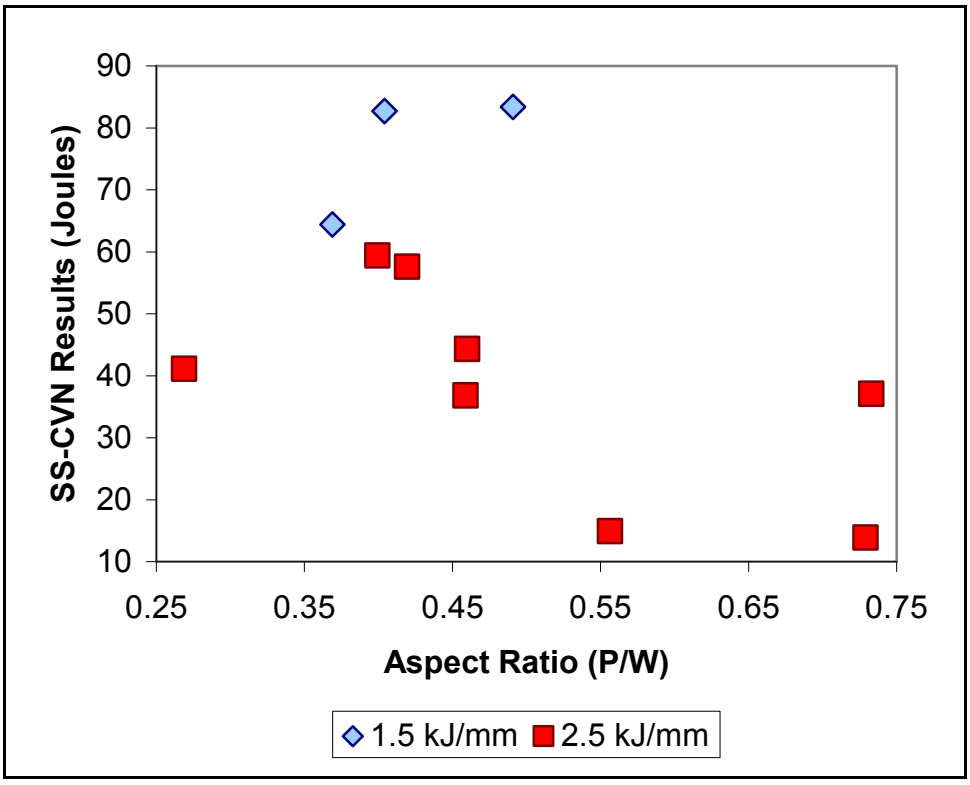

Figure A-40: The Effect of Heat Input and Aspect Ratio on SS-CVN Fracture Energy

8.9: Re-Evaluation of Figure 6-12 (The Effect of SP Ratio on SS-CVN Fracture Energy)

Figure 6-12 illustrates the effect of SP ratio on SS-CVN fracture energy values. Figure A-41 through A-45 show the effect of distinguishing the points from Figure 6-12 based upon current, voltage, polarity, power, and heat input values respectively.

Figure A-42 appears to illustrate two separate trends: an increase in SP ratio appears to coincide with a reduction in SS-CVN fracture energy values for welding beads produced using 28 volts, whereas it coincides with an increase in energy values for beads produced using 32 volts. No theoretical explanation could satisfy the two divergent trends, and it was assumed that the apparent trends were merely coincidental. As such, Figure A-42 was not included in Section 6.7.

Figure A-43 appears to show a general increase in SS-CVN fracture energy with increases of SP ratio values, but only for beads produced using AC-SQ polarity. However, the trends shown by the beads produced using DCEP and DCEN could not be explained, and, therefore, the figure was not included for additional analysis in Section 6.7. However, the chart did show that the outliers from Figures A-41 and A-45 were from welds produced using direct current polarity. As a result, Figures A-41 and A-45 were re-plotted again, using only the data from welds produced using AC-SQ polarity (Figure A-46 and A-47 respectively).

Figure A-46 shows that as SP ratio is increased, beads produced using the same current should possess increased SS-CVN fracture energy values. Additionally, Figure A-47 shows a similar pair of trends for weld beads with the same heat input values. As a result, both figures were included in Section 6.7 for additional analysis.

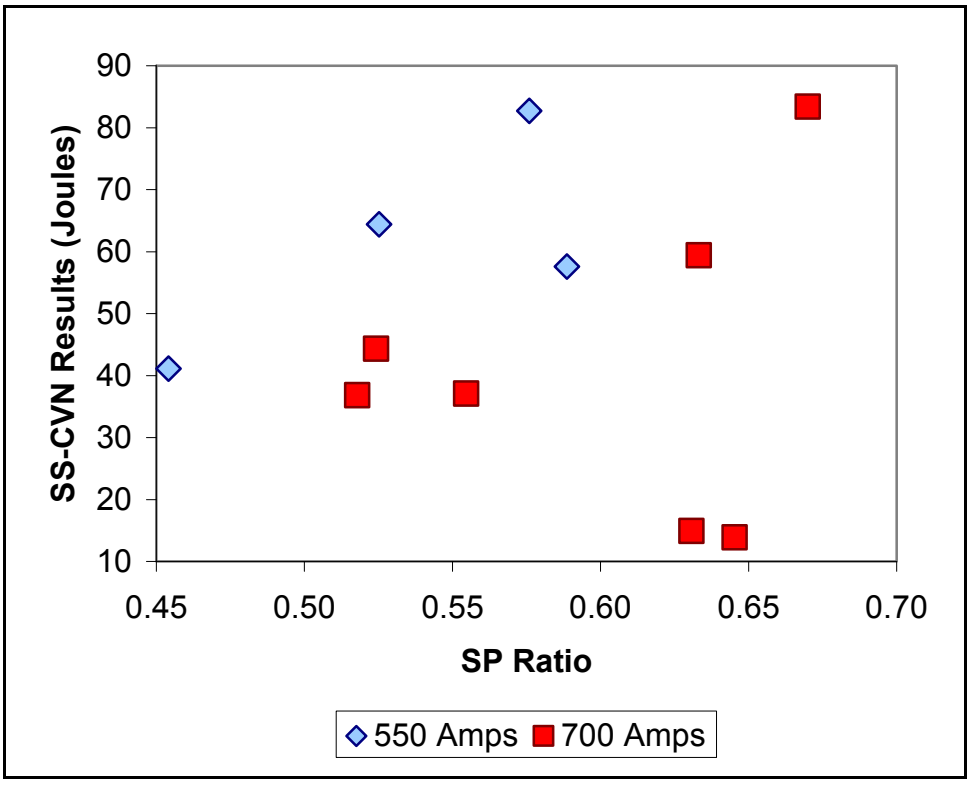

Figure A-41: The Effect of Current and SP Ratio on SS-CVN Fracture Energy

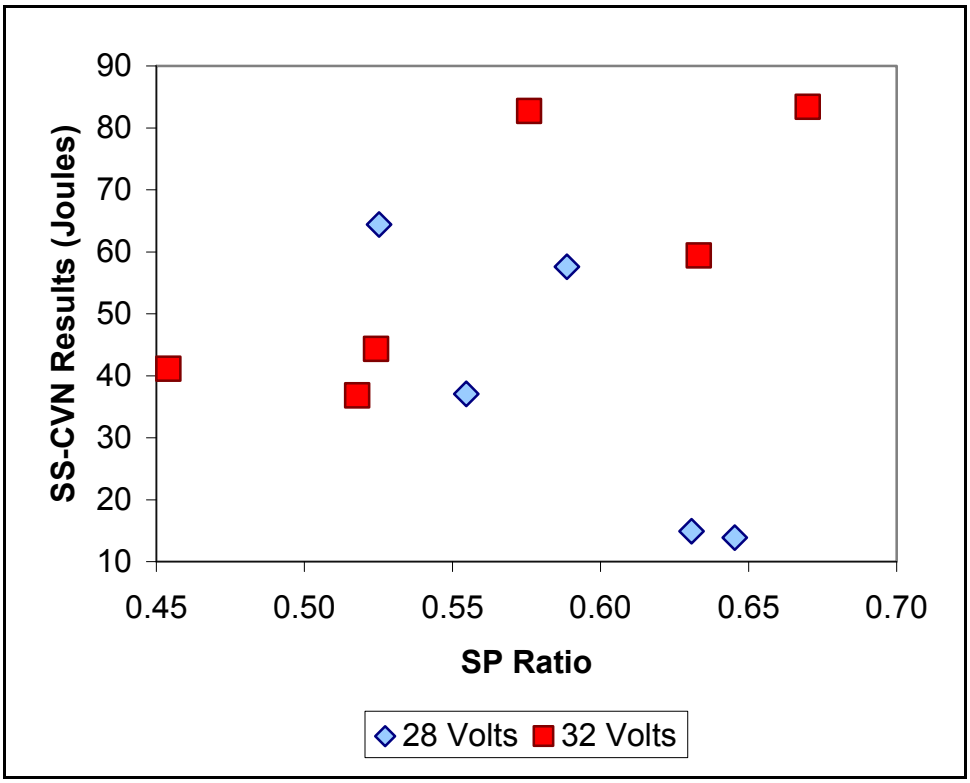

Figure A-42: The Effect of Voltage and SP Ratio on SS-CVN Fracture Energy

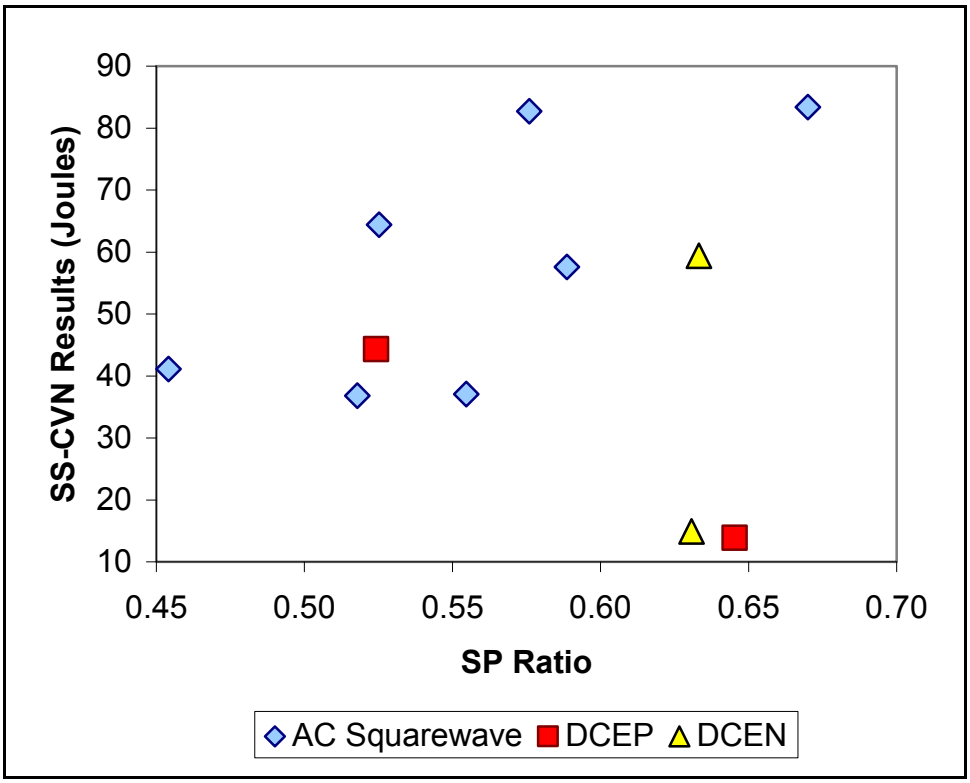

Figure A-43: The Effect of Polarity and SP Ratio on SS-CVN Fracture Energy

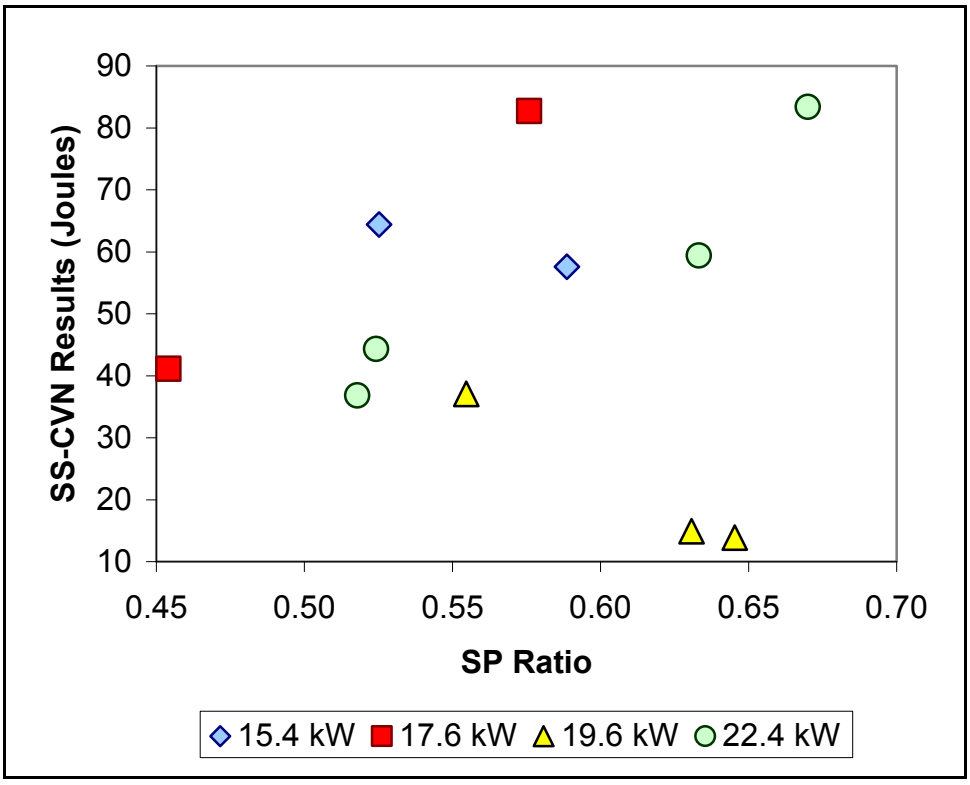

Figure A-44: The Effect of Power (VxA) and SP Ratio on SS-CVN Fracture Energy

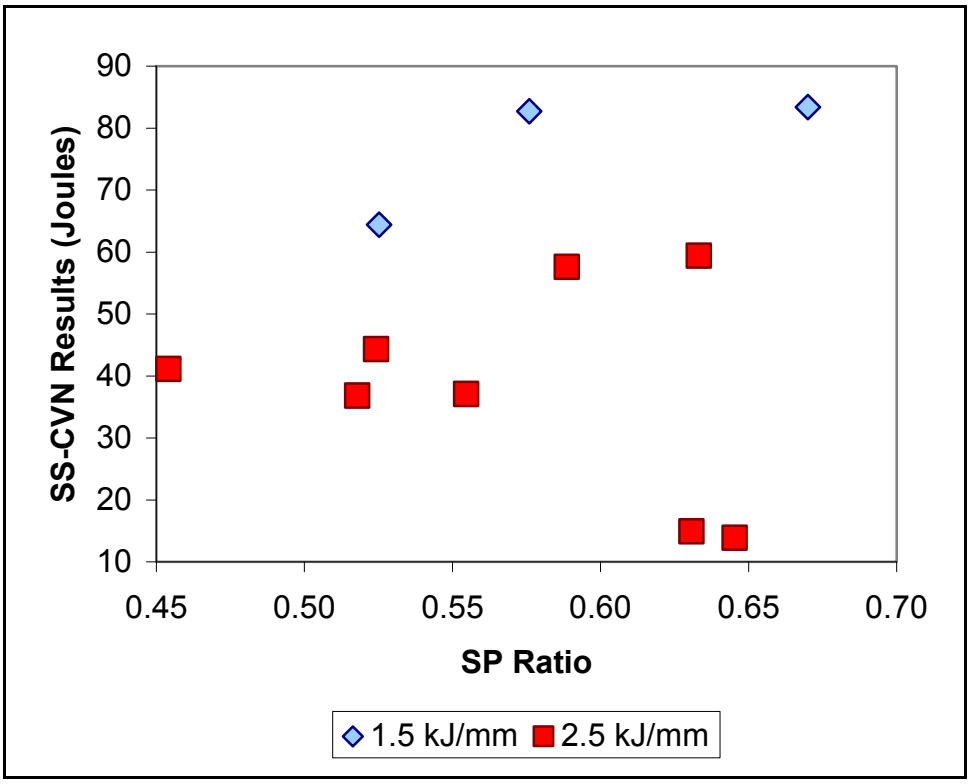

Figure A-45: The Effect of Heat Input and SP Ratio on SS-CVN Fracture Energy

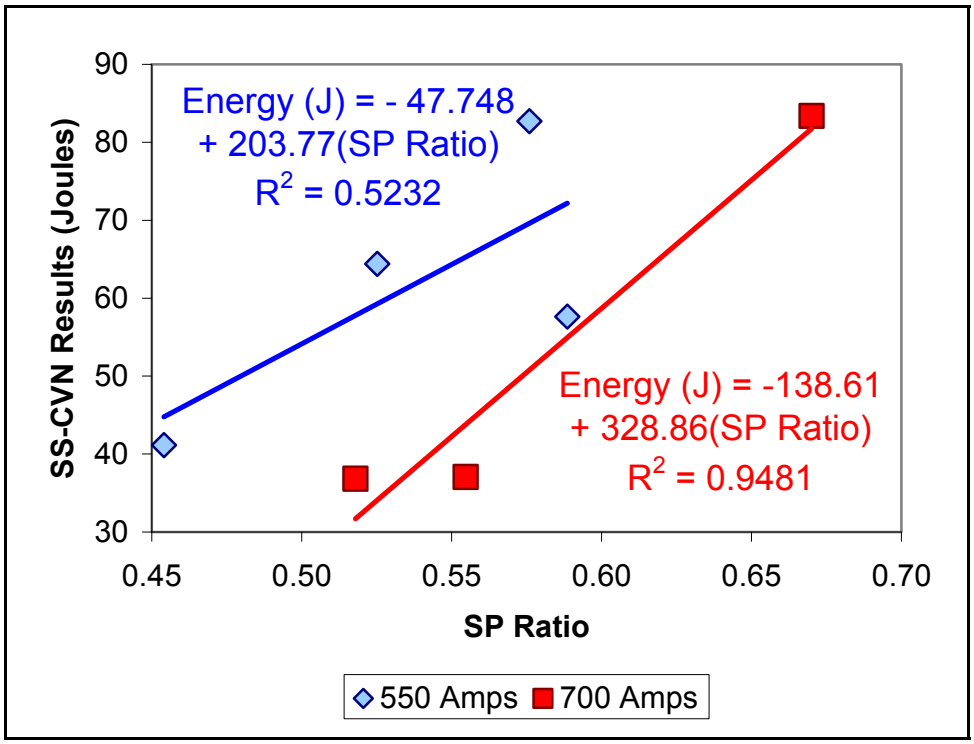

Figure A-46: The Effect of Current and SP Ratio on SS-CVN Fracture Energy, from Welds Produced Using AC-SQ Polarity

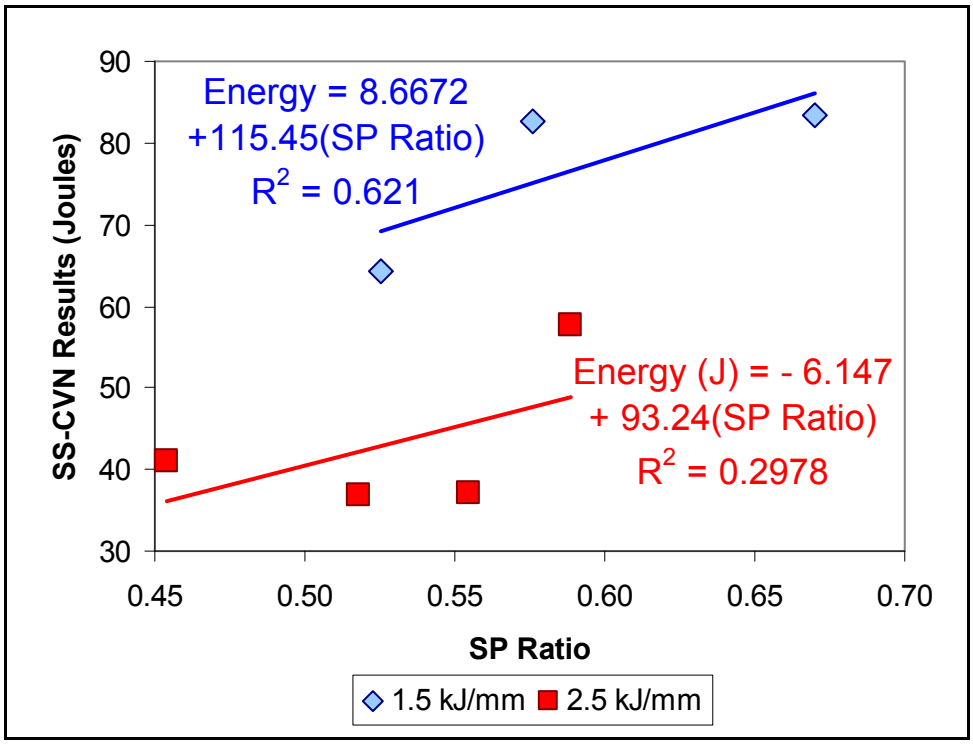

Figure A-47: The Effect of Heat Input and SP Ratio on SS-CVN Fracture Energy, from Welds Produced Using AC-SQ Polarity